Journal of Biomedicine and Biotechnology

Molecular Image-Guided Theranostic and Personalized Medicine 2012

Guest Editors: Hong Zhang, Mei Tian, Enzhong Li, Yasuhisa Fujibayashi, Lie-Hang Shen, and David J. Yang

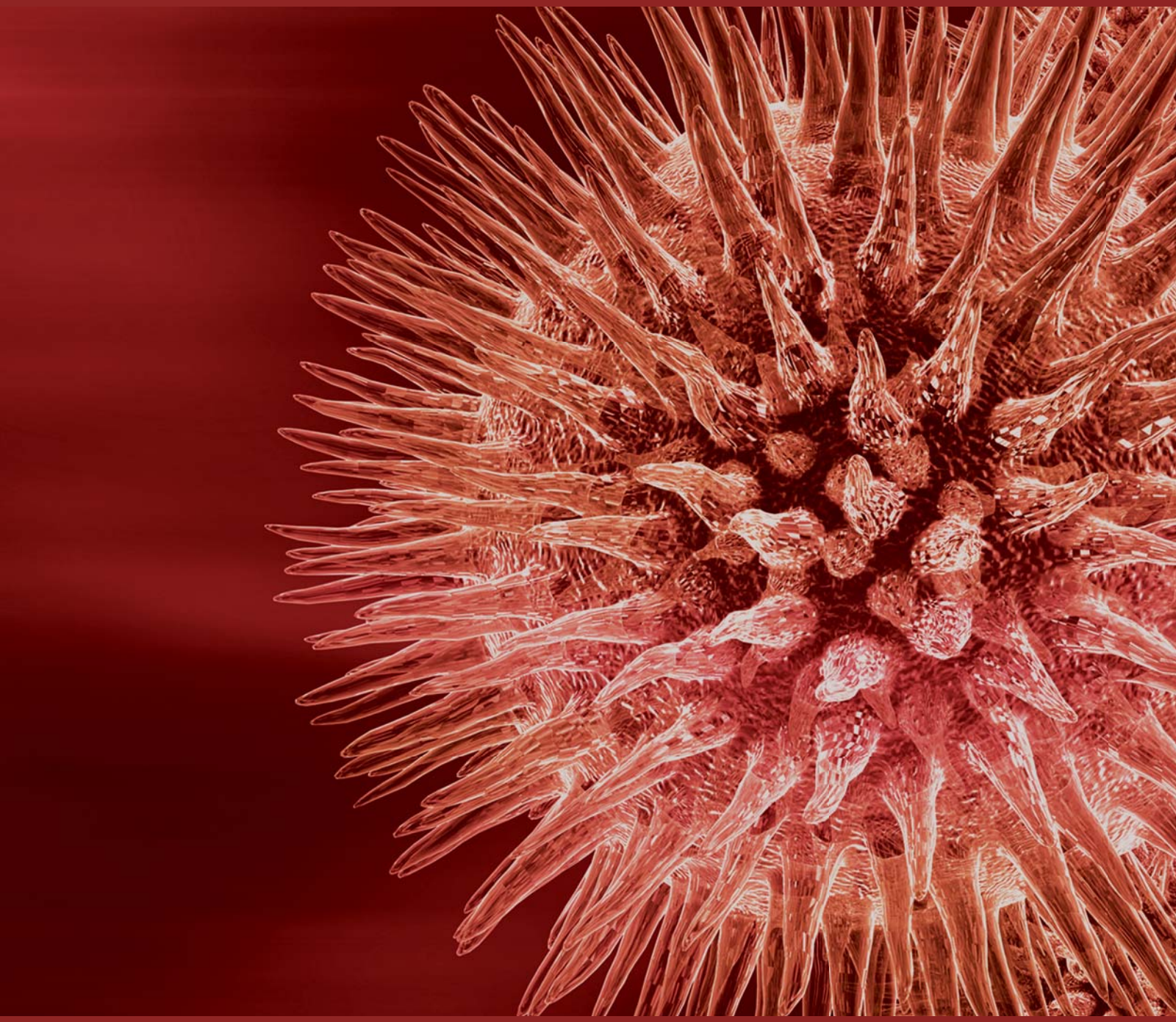

Molecular Image-Guided Theranostic and Personalized Medicine 2012

Journal of Biomedicine and Biotechnology

Molecular Image-Guided Theranostic and Personalized Medicine 2012

Guest Editors: Hong Zhang, Mei Tian, Enzhong Li, Yasuhisa Fujibayashi, Lie-Hang Shen, and David J. Yang

Editorial Board

The editorial board of the journal is organized into sections that correspond to the subject areas covered by the journal.

Biophysics

Miguel Castanho, Portugal
P. Bryant Chase, USA
Kuo-Chen Chou, USA
Rizwan Khan, India
Ali A. Khraibi, Saudi Arabia
Rumiana Koynova, USA
Serdar Kuyucak, Australia
Jianjie Ma, USA
S. B. Petersen, Denmark
Peter Schuck, USA
Claudio M. Soares, Portugal

Cell Biology

Omar Benzakour, France
Sanford I. Bernstein, USA
Phillip I. Bird, Australia
Eric Bouhassira, USA
Mohamed Boutjdir, USA
Chung-Liang Chien, Taiwan
Richard Gomer, USA
Paul J. Higgins, USA
Pavel Hozak, Czech Republic
Xudong Huang, USA
Anton M. Jetten, USA
Seamus J. Martin, Ireland
Manuela Martins-Green, USA
Shoichiro Ono, USA
George Perry, USA
M. Piacentini, Italy
George E. Plopper, USA
Lawrence Rothblum, USA
Michael Sheetz, USA
James L. Sherley, USA
G. S. Stein, USA
Richard Tucker, USA
Thomas van Groen, USA
Andre Van Wijnen, USA
Steve Winder, UK
Chuanyue Wu, USA
Bin-Xian Zhang, USA

Genetics

Adewale Adeyinka, USA
Claude Bagnis, France
J. Birchler, USA
Susan Blanton, USA
Barry J. Byrne, USA
R. Chakraborty, USA
Domenico Coviello, Italy
Sarah H. Elsea, USA
Celina Janion, Poland
J. Spencer Johnston, USA
M. Ilyas Kamboh, USA
Feige Kaplan, Canada
Manfred Kayser, The Netherlands
Brynn Levy, USA
Xiao Jiang Li, USA
Thomas Liehr, Germany
James M. Mason, USA
Mohammed Rachidi, France
Raj S. Ramesar, South Africa
Elliot D. Rosen, USA
Dharambir K. Sanghera, USA
Michael Schmid, Germany
Markus Schuelke, Germany
Wolfgang Arthur Schulz, Germany
Jorge Sequeiros, Portugal
Mouldy Sioud, Norway
Rongjia Zhou, China

Genomics

Vladimir Bajic, Saudi Arabia
Margit Burmeister, USA
Settara Chandrasekharappa, USA
Yataro Daigo, Japan
J. Spencer Johnston, USA
Vladimir Larionov, USA
Thomas Lufkin, Singapore
Joakim Lundeberg, Sweden
John L. McGregor, France
John V. Moran, USA
Yasushi Okazaki, Japan
Gopi K. Podila, USA
Momiao Xiong, USA

Immunology

Hassan Alizadeh, USA
Peter Bretscher, Canada
Robert E. Cone, USA
Terry L. Delovitch, Canada
Anthony L. DeVico, USA
Nick Di Girolamo, Australia
Don Mark Estes, USA
Soldano Ferrone, USA
Jeffrey A. Frelinger, USA
John Robert Gordon, Canada
James D. Gorham, USA
Silvia Gregori, Italy
Thomas Griffith, USA
Young S. Hahn, USA
Dorothy E. Lewis, USA
Bradley W. McIntyre, USA
R. Lee Mosley, USA
Marija Mostarica-Stojković, Serbia
Hans Konrad Muller, Australia
Ali Ouaissi, France
Kanury V. S. Rao, India
Yair Reisner, Israel
Harry W. Schroeder, USA
Wilhelm Schwaeble, UK
Nilabh Shastri, USA
Yufang Shi, China
Piet Stinissen, Belgium
Hannes Stockinger, Austria
J. W. Tervaert, The Netherlands
Graham R. Wallace, UK

Microbial Biotechnology

Jozef Anné, Belgium
Yoav Bashan, Mexico
Marco Bazzicalupo, Italy
Nico Boon, Belgium
Luca Simone Cocolin, Italy
Peter Coloe, Australia
Daniele Daffonchio, Italy
Han de Winde, The Netherlands
Yanhe Ma, China
Bernd H. A. Rehm, New Zealand
Angela Sessitsch, Austria

Microbiology

D. Beighton, UK
Steven R. Blanke, USA
Stanley Brul, The Netherlands
Isaac K. O. Cann, USA
Stephen K. Farrand, USA
Alain Filloux, UK
Gad Frankel, UK
Roy Gross, Germany
Hans-Peter Klenk, Germany
Tanya Parish, UK
Gopi K. Podila, USA
Frederick D. Quinn, USA
Didier A. Raoult, France
Isabel Sá-Correia, Portugal
P. L. C. Small, USA
Michael Thomm, Germany
H. C. van der Mei, The Netherlands
Schwan William, USA

Molecular Biology

Rudi Beyaert, Belgium
Michael Bustin, USA
Douglas Cyr, USA
K. Iatrou, Greece
Lokesh Joshi, Ireland
David W. Litchfield, Canada
Wuyuan Lu, USA
Patrick Matthias, Switzerland
John L. McGregor, France
S. L. Mowbray, Sweden
Elena Orlova, UK
Yeon-Kyun Shin, USA
William S. Trimble, Canada
Lisa Wiesmuller, Germany
Masamitsu Yamaguchi, Japan

Oncology

Colin Cooper, UK
F. M. J. Debruyne, The Netherlands
Nathan Ames Ellis, USA
Dominic Fan, USA
Gary E. Gallick, USA
Daila S. Gridley, USA
Xin-yuan Guan, Hong Kong
Anne Hamburger, USA
Manoor Prakash Hande, Singapore
Beric Henderson, Australia
Steve B. Jiang, USA
Daehee Kang, Republic of Korea
Abdul R. Khokhar, USA
Rakesh Kumar, USA
Macus Tien Kuo, USA
Eric W. Lam, UK
Sue-Hwa Lin, USA
Kapil Mehta, USA
Orhan Nalcioglu, USA
P. J. Oefner, Germany
Allal Ouhtit, Oman
Frank Pajonk, USA
Waldemar Priebe, USA
F. C. Schmitt, Portugal
Sonshin Takao, Japan
Ana Maria Tari, USA
Henk G. Van Der Poel, The Netherlands
Haodong Xu, USA
David J. Yang, USA

Pharmacology

Abdel A. Abdel-Rahman, USA
M. Badr, USA
Stelvio M. Bandiera, Canada
Ronald E. Baynes, USA
R. Keith Campbell, USA
Hak-Kim Chan, Australia
Michael D. Coleman, UK
J. Descotes, France
Dobromir Dobrev, Germany
Ayman El-Kadi, Canada
Jeffrey Hughes, USA
Kazim Husain, USA
Farhad Kamali, UK
Michael Kassiou, Australia
Joseph J. McArdle, USA
Mark J. McKeage, New Zealand
Daniel T. Monaghan, USA
T. Narahashi, USA
Kennerly S. Patrick, USA
Vickram Ramkumar, USA
Michael J. Spinella, USA
Quadiri Timour, France
Todd W. Vanderah, USA
Val J. Watts, USA

Plant Biotechnology

Prem L. Bhalla, Australia
J. R. Botella, Australia
Elvira Gonzalez De Mejia, USA
H. M. Häggman, Finland
Liwen Jiang, Hong Kong
Pulugurtha Bharadwaja Kirti, India
Yong Pyo Lim, Republic of Korea
Gopi K. Podila, USA
Ralf Reski, Germany
Sudhir Kumar Sopory, India

Toxicology

Michael Aschner, USA
Michael L. Cunningham, USA
Laurence D. Fechter, USA
Hartmut Jaeschke, USA
Youmin James Kang, USA
M. Firoze Khan, USA
Pascal Kintz, France
R. S. Tjeerdema, USA
Kenneth Turteltaub, USA
Brad Upham, USA

Virology

Contents

Hindawi Publishing Corporation
Journal of Biomedicine and Biotechnology
Volume 2012, Article ID 747416, 2 pages
doi:10.1155/2012/747416

Editorial

Molecular Imaging-Guided Theranostics and Personalized Medicine

Hong Zhang,[1] Mei Tian,[2] Enzhong Li,[3] Yasuhisa Fujibayashi,[4] Lie-Hang Shen,[5] and David J. Yang[2]

[1] *Department of Nuclear Medicine, Second Affiliated Hospital of Zhejiang University School of Medicine, 88 Jiefang Road, Zhejiang, Hangzhou 310009, China*
[2] *Department of Experimental Diagnostic Imaging, University of Texas MD Anderson Cancer Center, 1515 Holcombe Boulevrd, P.O. Box 59 Houston, TX 77030, USA*
[3] *Department of Health Sciences, National Natural Science Foundation of China, Beijing, China*
[4] *National Institute of Radiological Sciences, Chiba, Japan*
[5] *Isotope Application Division, Institute of Nuclear Energy Research, 1000, Wenhua Road, Jiaan Village, Taoyuan County, Longtan Township 32546, Taiwan*

Correspondence should be addressed to Hong Zhang, dyang@mdanderson.org

Received 20 May 2012; Accepted 20 May 2012

Molecular imaging agents and a parallel progress in instrumentation of imagining technology have demonstrated to be effective in improving diagnosis, prognosis, planning, and monitoring of personalized medication. Molecular imaging modalities include positron emission tomography (PET), single photon emission computed tomography (SPECT), magnetic resonance imaging (MRI), computed tomography (CT), ultrasound (US), and optical (Raman, quantum dots, bioluminescence). Among these imaging modalities, PET and SPECT agents could provide target specific information as well as function, pathway activities, and cell migration in the intact organism. Furthermore, the radiotracer could noninvasively assess diseases treatment endpoints which used to rely almost exclusively on biopsies and histopathological assays. New leads on the development of personalized theranostic (image and treat) agents would allow more accuracy in the selection of patients who may respond to treatment.

Topics covered in this special issue include advances in biomarkers in preclinical drug discovery, PET/CT and SPECT/CT in disease management, image-guided therapy approach of diseases, imaging technology in drug development, and progress in instrumentation of imaging technology. For instance, upregulation of transporter expressions has often been observed in tumor cells to facilitate their accelerated rates of uptake. Advances in biomarkers in transporter system-based imaging in oncology and neurological diseases such as amino acid (FL. Kong et al.), glucose (YH. Zhang et al.) and dopaminergic (LH. Shen et al.; HF. Hou et al.) transporters were reported. These biomarkers showed that specific uptake in lesions compared to clinic imaging agent. In addition, these biomarkers were capable to be labeled with theranostic isotopes for personalized medication.

Most tumors have a considerable proportion of hypoxic cells that are resistant to radio/chemotherapy, with a high propensity to metastasize, and result in worse therapeutic outcome. The contribution by M. Ali et al. and H. Fuji report their newly developed ^{99m}Tc-N4-NIM and ^{125}I-IPOS probes for tumor hypoxia. The preclinical findings showed that these biomarkers could image tumor hypoxia by SPECT. The ability to quantify tissue hypoxia would allow the physicians to select patients for additional or alternative treatment regimens that would circumvent the ominous impact of hypoxia. Along this line, L. Jiang and coworkers report the peptide based radiotracer targeting tumor angiogenesis via VEGF integrin alpha(v) beta3. J. Sims-Mourtada and co-workers report ^{131}I-labeled derivatives of the sonic hedgehog (HH) protein for detection of cancer cells via HH receptors. Molecular imaging of cancer stem cell trafficking was reported by T. Xia and co-workers.

Hybrid molecular imaging modalities (PET/CT, SPECT/CT) provide high-sensitivity functional and high resolution

anatomical imaging, which are important in design personalized treatment. To avoid radiation exposure from multiple slices-CT, K. Tang and co-workers report a reduction of CT tube voltage from 120 kv to 80 kv, the radiation dose could be reduced by 32–42% without losing low-contrast detectability. F. Chao and H. Zhang report the value of using PET/CT in the staging of nonsmall cell lung cancer. Y. Hu and co-workers report the application of PET/CT in assessment of treatment outcome. The application of SPECT/CT in the differential diagnosis of bone metastasis (Y. Zhang et al.) and Parkinson's disease (L. Wang et al.) was reported. Miyake K and co-workers report the application of FDG, MET, and FLT-PET/CT for the management of gliomas. L. Yang and co-workers report the value of using myocardial contrast echocardiography quantitative analysis during adenosine stress over visual analysis before therapy in acute coronary pain. The quantitative analysis correlates well with thrombosis in myocardial infarction.

In summary, molecular imaging could integrate metabolomics and chemical biology. Molecular imaging agents could characterize target expressions, understand the disease progression, prediction for drug response and toxicity, staging, grading, and micrometastasis, and support animal studies. This special issue provides a platform of efficacy of personalized medication from molecular imaging technology which may have high impact on drug discovery, delivery, and development.

Hong Zhang
Mei Tian
Enzhong Li
Yasuhisa Fujibayashi
Lie-Hang Shen
David J. Yang

Hindawi Publishing Corporation
Journal of Biomedicine and Biotechnology
Volume 2012, Article ID 639562, 8 pages
doi:10.1155/2012/639562

Research Article

Detection of Canonical Hedgehog Signaling in Breast Cancer by 131-Iodine-Labeled Derivatives of the Sonic Hedgehog Protein

Jennifer Sims-Mourtada,[1,2] David Yang,[3] Izabela Tworowska,[2] Richard Larson,[4] Daniel Smith,[4] Ning Tsao,[3] Lynn Opdenaker,[5] Firas Mourtada,[1,4] and Wendy Woodward[4]

[1] *Helen F. Graham Cancer Center, Christiana Care Hospital, Newark, DE 19713, USA*
[2] *RadioMedix, Inc., Houston, TX 77042, USA*
[3] *Department of Experimental Diagnostic Imaging, The University of Texas MD Anderson Cancer Center, Houston, TX 77030, USA*
[4] *Department of Radiation Oncology, The University of Texas MD Anderson Cancer Center, Houston, TX 70030, USA*
[5] *Department of Biological Sciences, University of Delaware, Newark, DE 19716, USA*

Correspondence should be addressed to Jennifer Sims-Mourtada, jsimsmourtada@christianacare.org

Received 29 February 2012; Revised 23 April 2012; Accepted 7 May 2012

Academic Editor: Lie-Hang Shen

Activation of hedgehog (HH) pathway signaling is observed in many tumors. Due to a feedback loop, the HH receptor Patched (PTCH-1) is overexpressed in tumors with activated HH signaling. Therefore, we sought to radiolabel the PTCH-1 ligand sonic (SHH) for detection of cancer cells with canonical HH activity. Receptor binding of ^{131}I-SHH was increased in cell lines with high HH pathway activation. Our findings also show that PTCH-1 receptor expression is decreased upon treatment with HH signaling inhibitors, and receptor binding of ^{131}I-SHH is significantly decreased following treatment with cyclopamine. *In vivo* imaging and biodistribution studies revealed significant accumulation of ^{131}I-SHH within tumor tissue as compared to normal organs. Tumor-to-muscle ratios were approximately 8 : 1 at 5 hours, while tumor to blood and tumor to bone were 2 : 1 and 5 : 1, respectively. Significant uptake was also observed in liver and gastrointestinal tissue. These studies show that ^{131}I-SHH is capable of *in vivo* detection of breast tumors with high HH signaling. We further demonstrate that the hedgehog receptor PTCH-1 is downregulated upon treatment with hedgehog inhibitors. Our data suggests that radiolabeled SHH derivatives may provide a method to determine response to SHH-targeted therapies.

1. Introduction

The association between the hedgehog (HH) pathway and cancer was initially established by the identification of heterozygous mutations affecting the membrane receptor PATCHED-1 (PTCH-1), resulting in abnormal activation of HH signaling in basal cell carcinoma and neural tumors [1, 2]. Recently, several studies have shown ligand-dependent constitutive activation of the HH signaling pathway in many solid tumors including prostate, breast, ovarian, esophageal, gastric, and lung cancers. Sonic (SHH) ligand secreted from tumor cells can have a growth-promoting effect on both tumor and stroma cells [1–7]. Furthermore, HH signaling has been implicated in resistance to radiation and chemotherapy through regulation of survival proteins, cell cycle, DNA repair, and drug transport [8–10]. A recent report demonstrated that HH signaling can impair ionizing radiation-induced checkpoints, resulting in increased survival and genomic instability following radiation therapy [11].

Canonical activation of HH activity occurs when secreted SHH binds to and inhibits the cell surface receptor PTCH-1. This binding relieves the PTCH-1-mediated suppression of the transmembrane protein SMOOTHENED (SMO) leading to multiple intracellular events that result in the stabilization, nuclear translocation, and activation of the Gli family of transcription factors (Gli-1, 2, and 3) [12, 13]. Transcriptional targets of Gli include genes controlling cell cycle, cell adhesion, signal transduction, vascularization, and apoptosis [14]. PTCH-1 is also a target of this pathway

[15], providing feedback for HH signaling. Thus, PTCH-1 expression is increased on cells with active HH signaling.

PTCH-1 is overexpressed in many epithelial-derived cancers, when compared to adjacent normal tissue, and its expression is usually correlated to overexpression of other HH pathway members. Immunohistochemical analysis of breast carcinomas revealed overexpression of SHH, PTCH-1, and Gli-1 in breast cancer specimens, compared to adjacent normal tissue [16]. Expression of HH pathway members in breast cancer has been shown to correlate with progesterone receptor expression, high proliferative index of Ki67 lymph node metastasis and clinical grade [16, 17].

Inhibition of HH signaling in animal models of cancer has shown promising effects. Currently, multiple classes of HH inhibitors are under clinical development at several major pharmaceutical companies [18]. However, there is presently no noninvasive method to screen for potential candidates who may benefit from HH-targeted therapies or to follow inhibition of HH signaling *in vivo*. Here, we report the synthesis and characterization of an iodinated derivative of SHH that targets PTCH-1 receptor expression. This approach has several advantages for imaging of HH expression. One, there is a feedback loop that results in increased transcription and membrane localization of PTCH-1 in cells with active HH signaling [15]. Additionally, the N-terminal fragment of SHH is internalized by receptor-mediated endocytosis of the PTCH-1 receptor. The degree of receptor internalization has been associated to the levels of active HH signaling [19].

2. Materials and Methods

2.1. Cell Lines and Antibodies. Human breast cancer cell lines were obtained from ATCC and cultured in Dubelco's modified eagles media, supplemented with 10% (vol : vol) fetal bovine serum and 1% antibiotic-antimycotic at 37°C in a humidified atmosphere containing 5% carbon dioxide. The rat breast cancer cell line 13762 was derived from a tumor induced in Fischer-344 rat by giving an oral dose of 7,12-dimethyl-benz[a]anthracene [20]. The cells were cultured in RPMI-1640 medium, supplemented with 10% (vol : vol) fetal bovine serum and 1% antibiotic-antimycotic at 37°C in a humidified atmosphere containing 5% carbon dioxide. Cyclopamine was obtained from LC labs. Cells were treated with 10–40 μM cyclopamine resuspended in ethanol and diluted in normal culture media for the indicated time points. Control cells were treated with ethanol only. Gli-1 (H-300), Patched-1 (C-20), and B-actin (C-2) antibodies were purchased from Santa Cruz Biotechnologies. Alexa-555 and 488 secondary antibodies were purchased from Molecular Probes. HRP-conjugated secondary antibodies were purchased from Jackson Labs.

2.2. Protein Purification and Iodination. A recombinant derivative of the 19.5 kDa human N-terminal SHH protein was purified from the *E. coli* strain BL21/DE3/PLysS (Stratagene, La Jolla, CA) expressing a pCOLDII vector (Genescript) that contains the wild-type cDNA encoding amino acid residues Cys 24 to Gly 197 of human SHH (accession number NP_000184) [21] linked to an N-terminal sequence encoding six consecutive histidine residues and an Asp-Asp-Asp-Asp-Lys enterokinase cleavage site. The SHH protein was purified using a nickel-based resin (Ni-NTA fast start kit, Qiagen), and resuspended in buffer containing 20 mM phosphate, 150 mM NaCl, and 0.1% Triton-X-100 pH 5.0. BSA protein (Sigma Aldrich) was used as a control and was resuspended in PBS at a pH of 7.4. The proteins were subsequently labeled with iodine-131 (Perkin Elmer) using the Iodogen method [22]. Briefly, 10–20 μg of protein was reacted with Na ^{131}I, (Perkin Elmer) in glass tubes pre-coated with 5-6 mg Iodogen (Sigma Aldrich) for 10–15 min at room temperature. The labeled proteins were purified using a sephadex P-10 column (Sigma Aldrich) preloaded with phosphate buffer pH 5.0 or pH 7.4. Radiochemical purity was determined by radio-thin-layer chromatography (Waterman No. 1, Sigma-Aldrich), with 0.9% NaCl as the eluant.

2.3. Western Blotting. Control or cyclopamine-treated cells were lysed with radioimmunoprecipitation assay (RIPA) buffer, and protein concentrations were determined using the BCA assay (Pierce). Western blot analysis using 40 μg of protein was performed as previously described [23].

2.4. Immunofluorescence. Cells were fixed with methanol at −20°C for 5 min, washed twice with PBS, and blocked for 1 hour with 10% goat serum at room temperature. Antibodies were added at dilutions ranging from 1 : 50 to 1 : 200, overnight at 4°C. Slides were washed 3 times with PBS and secondary antibodies were added at a dilution of 1 : 5000 for 1 hour at room temperature. Slides were washed 3x with PBS, and stained with Prolong Gold antifade reagent containing DAPI (Invitrogen). Slides were analyzed on a Zeiss AxioObserver Z1 Microscope, and images were processed using AxioObserver software. For analysis of nuclear Gli-1, 100 cells were counted per sample from three independent stainings. Cells were scored positive for nuclear Gli1 staining if they demonstrated intensive, predominantly nuclear Gli-1.

2.5. Cellular Proliferation Assay. Cells were seeded at a density of 5,000 to 10,000 cells per well in 96 well plates and grown overnight. Media was removed and replaced with culture media containing 10 μM cyclopamine or ethanol. Cells were cultured for additional 48 hours, and proliferation was measured using the MTT-based cell proliferation assay (Biotinum).

2.6. Cellular Binding Assays. Cells were plated at a density of 50,000–100,000 cells per well in 12 well plates and allowed to grow overnight. For inhibition studies, cells were treated with 10–20 μM cyclopamine or ethanol and allowed to grow for the indicated time. Culture media was removed and replaced with RPMI media containing 0.1–10 nM ^{131}I-SHH. Cells were grown for 1-2 hours, media was removed and collected and the cells washed 3 times with PBS and trypsinized. Media

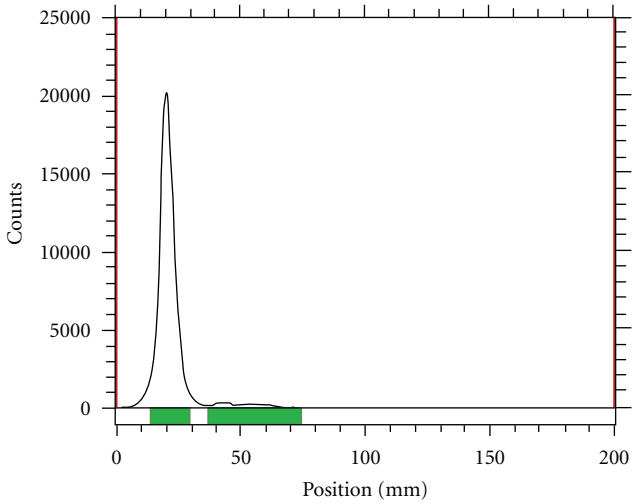

Figure 1: Radiochemical purity of 131I-SHH was >95%. Radiochemical purity was determined by radio TCL with normal saline as the mobile phase.

and cells were counted in a gamma counter. Scatchard plots were generated using Graph pad software. Bmax (binding sites per cell) and kD were determined for each sample using data from three separate experiments. To control for specificity, cellular uptake studies were performed with 100-fold excess unlabeled SHH.

2.7. Animal Model. Six-week-old female Fischer 344 rats (150–175 g) (Harlan Sprague-Dawley, Inc., Indianapolis, IN) were used. Xenografts were generated from the rat mammary cell line 13762 by subcutaneous inoculation of 1 million cells in the right flank. Biodistribution and imaging studies were performed 10–14 days after inoculation when the tumors reached approximately 1–1.5 cm in diameter. All experiments were performed under authorization by the University of Texas MD Anderson Cancer Center Institutional Animal Care and Use Committee (IACUC).

2.8. Gamma Scintigraphy Studies. On the day of the study, rats were anesthetized with Isofluorane, and a tail vein cannula was inserted. Approximately 250 μCi of the radiolabeled tracer (^{131}I-SHH or ^{131}I-BSA) was delivered via tail vein injection. ^{131}I images were acquired using a Siemens MCAM gamma camera with a high energy LP (HELP) collimator and a photopeak centered around 364 keV. Anesthetized animals were placed onto the camera, and counts were acquired for 10 min. Images were acquired at 30 min, 1 hour, 2 hours, 5 hours, and 24 hours following tail vein injection. Image files were saved in DICOM format and exported to Image J software (National Institute of Health, Bethesda MD) for further processing.

2.9. Biodistribution and Dosimetry Studies. Rats were anesthetized with Isofluorane, and a tail vein cannula was inserted. Approximately 20 μCi of the ^{131}I-SHH was delivered via tail vein injection. *In vivo* biodistribution studies were performed at 0.5, 2, and 5 hours after intravenous administration of ^{131}I-SHH. Mice were sacrificed at the indicated time points ($n = 3$) and organs were excised. Organs were weighted, and radioactivity was counted in a gamma counter. Percent injected dose per gram was determined. Absorbed dose for each target organ was estimated using the OLINDA/EXM 1.1 software program (Vanderbilt University) with the adult male model. Rat biodistribution data were extrapolated to humans using an assumed rat weight of 150 g and the mass of each organ in the MIRD 70 kg adult male model as input to Equation 8 of AAPM Primer 71 [24]. Human organ time-activity curves were fitted to a monoexponential function using the OLINDA/EXM software to calculate individual organ residence times, from which the human dosimetry of ^{131}I-SHH was then estimated.

3. Results

3.1. Radiolabeling. The SHH protein was radiolabeled with ^{131}Iodine at specific activities up to 740 GBq/g. Radiochemical yields of 40–65% were obtained. Radiochemical purity of >95% was determined by radio-thin-layer chromatography, (Figure 1).

3.2. Cellular Binding Assays. Cell-binding studies were performed in breast cancer cell lines with varying HH pathway activity. Cellular uptake (Figure 2(a)) correlated with nuclear Gli-1 staining (Figure 2(b)) as well as PTCH-1 receptor expression (Figure 2(c)). Cell uptake increased over time and was blocked with 100-fold excess cold SHH protein confirming receptor specificity (Figure 2(d)). To determine if the uptake ^{131}I-SHH could be modified after HH signaling inhibition, we treated breast cancer cells with a 10–20 μM dose of cyclopamine, a commercially available SMO inhibitor [25]. As shown in Figure 3(a), cyclopamine treatment resulted in a significant decrease in proliferation, which is directly correlated with pretreatment Gli-1 levels. A decrease of PTCH-1 protein levels was observed after treatment with cyclopamine by western blotting and immunofluorescence (Figures 3(b) and 3(c)). Scatchard analysis revealed a fivefold decrease in surface PTCH-1 receptor expression after treatment with cyclopamine (Figure 3(d)). Consistent with these findings, a 50% reduction in uptake of radiolabeled SHH was observed in cells treated with cyclopamine (Figure 3(e)). These results suggest the potential to follow response to HH pathway inhibition using radiolabeled SHH.

3.3. Biodistribution and Dosimetry Studies. Based on the baseline expression of HH signaling proteins and tumor growth characteristics, *in vivo* studies were carried out using xenografts from the rat mammary cell line 13762 in Fischer rats. The 13762 model was chosen due to its efficiency of tumor growth and its high canonical HH signaling, evidenced by high protein expression of PTCH and Gli-1 as well as the ligand (Figure 4). This cell line also demonstrated high *in vitro* uptake of the tracer. The results, shown in Table 1, reveal significant tumor uptake with tumor-to-muscle ratios of 8 : 1 at 5 hours, while tumor to blood and

Table 1: Biodistribution of ^{131}I-SHH.

	30 min		2 Hr		5 Hr	
Organ	% ID/g	% S.E.M.	% ID/g	% S.E.M.	% ID/g	% S.E.M.
Blood	5.5	0.3	3.1	1.4	2.7	0.3
Heart	1.9	0.9	1.9	0.2	0.8	0.3
Lung	4.8	0.4	2.3	0.3	2.0	0.3
Thyroid	2.2	0.0	2.0	0.3	1.4	0.3
Pancreas	2.9	0.1	2.0	0.3	1.2	0.3
Liver	55.2	4.8	30.6	2.7	21.3	4.4
Spleen	27.7	3.9	12.6	1.6	6.7	1.5
Kidney	15.1	1.6	10.3	0.3	8.6	1.5
Stomach	6.1	0.6	5.9	1.0	2.4	0.6
Sm intestine	4.1	0.2	3.6	1.0	1.6	0.2
Lg intestine	2.2	0.2	1.7	0.5	1.5	0.4
Muscle	1.2	0.1	0.9	0.2	0.5	0.3
Bone	1.9	0.2	1.7	0.2	0.8	0.3
Tumor	2.8	0.3	3.7	0.2	3.9	0.1
Tumor : muscle	2.4		4.4		8.1	
Tumor : bone	1.5		2.2		4.7	
Tumor : lung	0.6		1.6		2.0	
Tumor : blood	0.5		1.2		1.5	

Table 2: Radiation dose estimates of reference adults of ^{131}I-SHH from rats.

Target organ	mSv/MBq
Small intestine	9.65×10^{-02}
Stomach wall	9.62×10^{-02}
Kidneys	6.34×10^{-01}
Liver	4.07×10^{-01}
Lungs	8.78×10^{-02}
Muscle	4.46×10^{-02}
Pancreas	1.73×10^{-01}
Red marrow	3.91×10^{-02}
Osteogenic cells	9.15×10^{-02}
Skin	1.60×10^{-02}
Spleen	4.93×10^{-01}
Thyroid	1.01×10^{-01}
Urinary bladder wall	1.09×10^{-02}
Total body	2.95×10^{-01}

tumor to bone were 2 : 1 and 5 : 1, respectively. Significant uptake of ^{131}I-SHH was also observed in the liver and kidney. Uptake was also observed in the thyroid and gastrointestinal tract, which may be due in part to dehalogenation that is common with iodinated proteins. Dosimetric studies showed kidneys, liver, and spleen to be the dose-limiting organs. Organ dose estimates are shown in Table 2. Higher absorbed doses may be due to dehalogenation and could potentially be mitigated by blocking absorption of free iodine in a clinical setting.

3.4. Gamma Scintigraphy. Planar imaging studies were conducted with ^{131}I-SHH to test the potential of imaging PTCH-1 receptor expression in a rat model of breast cancer. Fisher rats bearing tumor xenografts of the cell line 13762, a chemically induced rat breast cancer line, were injected with 250 μCi of ^{131}I-SHH. Planar scintigraphy was conducted at 30 min, 2, 5, and 24 hours. Studies were performed with iodinated BSA as a control for nonspecific uptake. Tumor accumulation of the tracer was observed at 30 min and increased up to 5 hours. As shown in Figure 5, the tumor is clearly visualized in the rat injected with ^{131}I-SHH, but absent in the animal injected with ^{131}I-BSA. Plasma dehalogenation is also observed, with appearance of radioiodine uptake in the thyroid and stomach visualized at 2 hours and increasing on later images. The thyroid, liver, and stomach were also visualized on the animal injected with ^{131}I-BSA, further suggesting that the uptake in these organs is due to free iodine that is a result of dehalogenation of the iodinated protein.

4. Discussion

Our findings show that expression of the PTCH-1 receptor is increased in breast cancer cells with canonical HH signaling and that surface PTCH-1 receptor expression is decreased upon treatment with the SMO inhibitor cyclopamine. This decrease correlated to a decrease in uptake of ^{131}I-SHH. These studies are in agreement with previous studies that report direct gene regulation of PTCH-1 by Gli-1 [26] and correlation of Gli-1 activity to PTCH-1 expression [1, 27]. Furthermore, treatment of cancer cells with small molecule

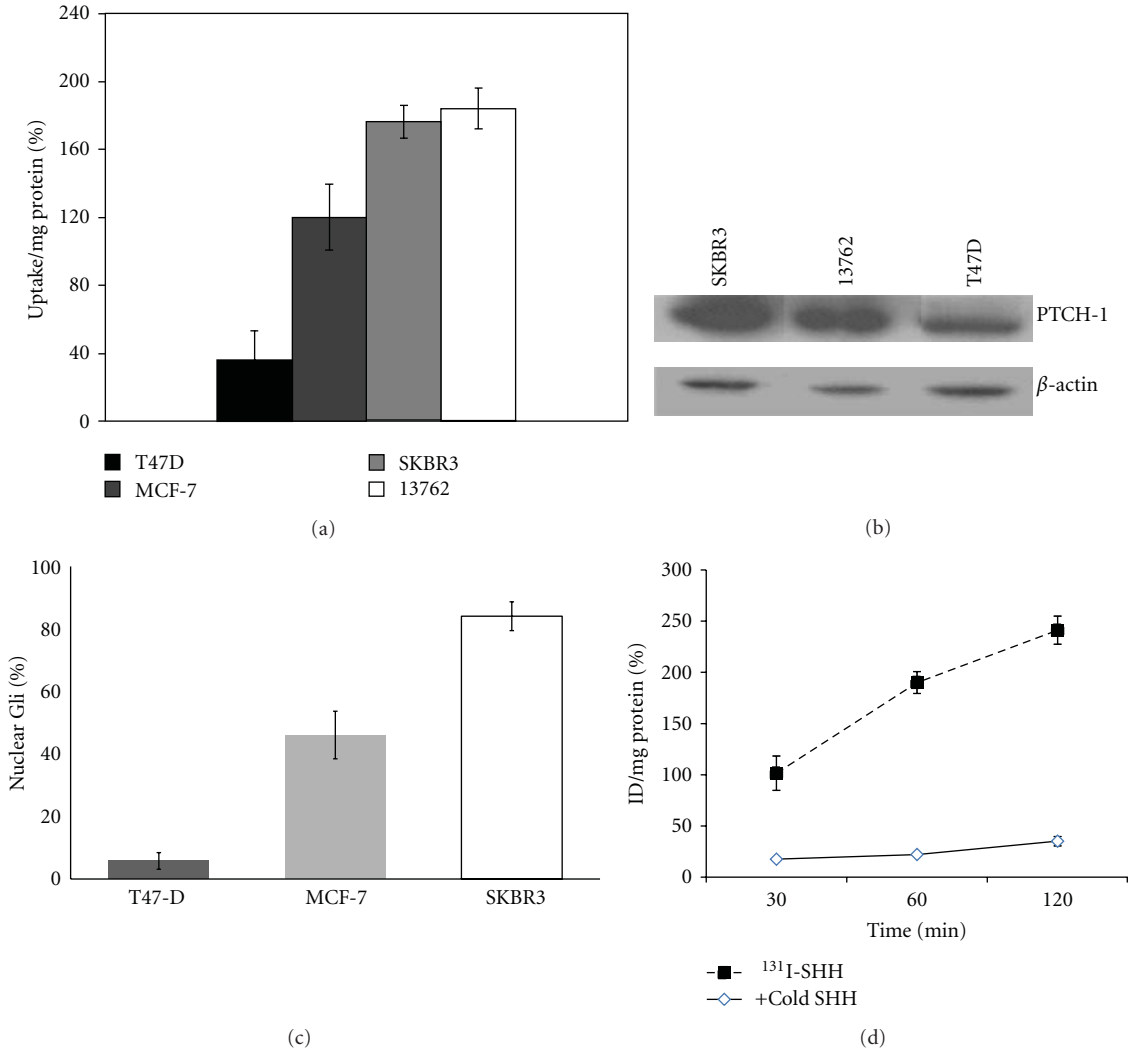

Figure 2: (a) Cellular uptake of ^{131}I-SHH in breast cancer cell lines at one hour. Data is represented as the % injected dose (cpm (cells)/cpm (media))/mg protein. (b) Western blot showing expression of PTCH-1 in breast cancer cell lines. Cellular uptake of ^{131}I-SHH is correlated with expression of the PTCH-1 receptor. (c) Nuclear Gli-1 expression in breast cancer cell lines. Data is expressed as number of cells with intense nuclear Gli-1 staining. (d) Time course showing increased accumulation of ^{131}I-SHH in SKBR3 cancer cells with time. Uptake was blocked by 100-fold excess cold SSH.

inhibitors of SMO, which block canonical HH signaling, was shown to decrease PTCH-1 mRNA expression [28].

These studies suggest that binding of radiolabeled HH to surface PTCH-1 receptors can differentiate tumors with active ligand-dependent HH signaling, and this feature can be used to image hedgehog activity in tumors. Preliminary imaging studies show that ^{131}I-SHH is capable of *in vivo* delineation of breast tumors with high HH signaling. In these preliminary imaging studies using ^{131}I-SHH we find that in addition to tumor uptake, ^{131}I-SHH exhibited high uptake in the spleen and gastrointestinal organs. This uptake potentially arises from deiodination of the tracer as high gastrointestinal uptake was also observed with an iodinated BSA control protein [29]. Furthermore, HH signaling has been shown to increase activity of deiodinases [30], which could potentially increase dehalogenation of ^{131}I-labeled compounds in tumors with active HH signaling. Higher absorbed doses in the intestines, liver, and spleen may be due to dehalogenation and could potentially be mitigated by blocking absorption of free iodine in a clinical setting. It is common to use saturated potassium iodide solution (SSKI) to prevent radiation exposure to thyroid and stomach due to deiodination in clinic settings. However, we cannot rule out possible specific uptake of ^{131}I-SHH in the GI-tract as there are reports of low-level PTCH-1 expression in normal epithelia in the intestine and liver [31]. Likewise, low-level PTCH-1 expression has also been reported in lymphocytes and follicular dendritic cells present in the spleen [32] during immune responses.

While ligand-dependent hedgehog signaling has been reported in breast cancer and numerous other cancers, heterozygous mutations affecting the membrane receptor

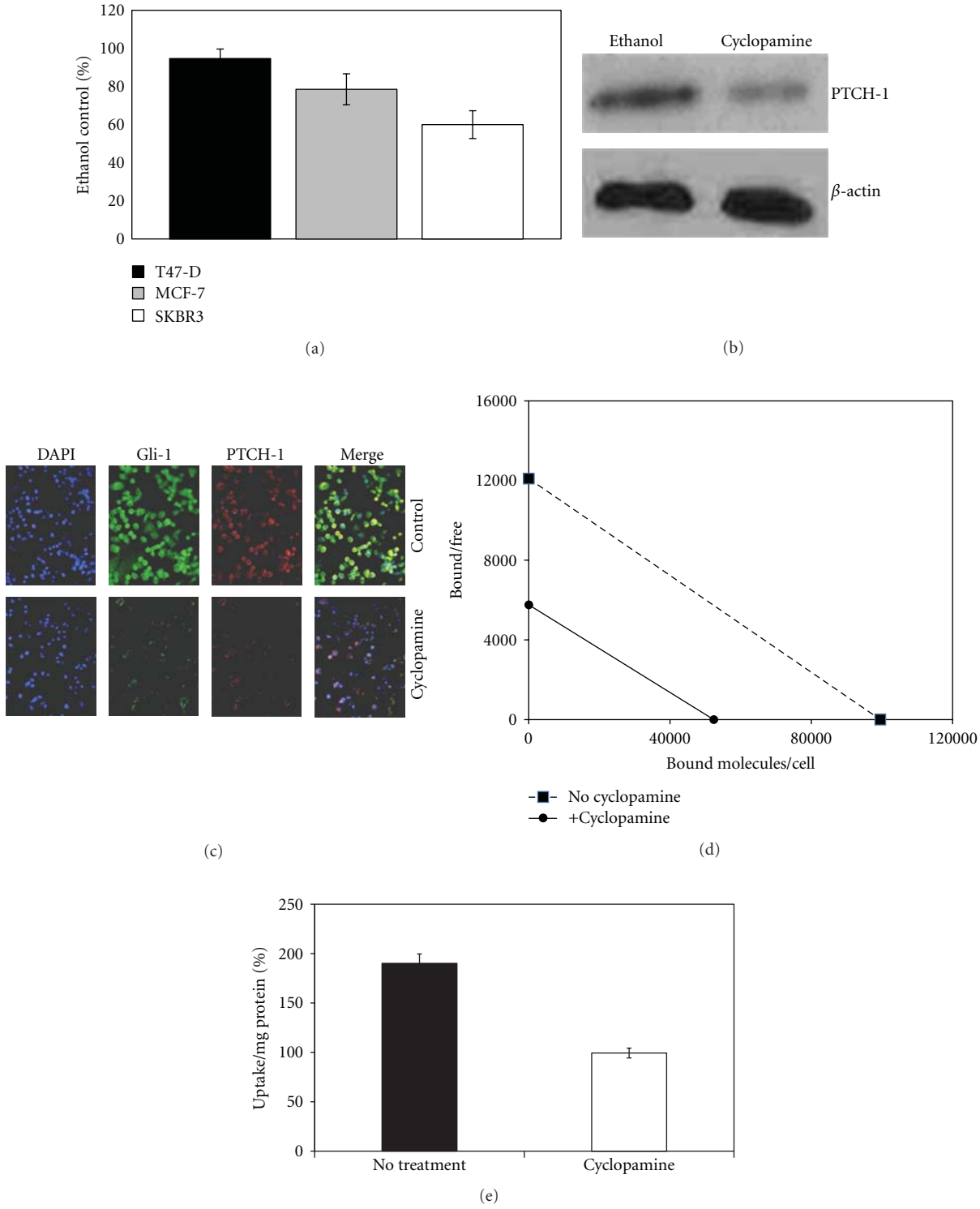

Figure 3: (a) MTT assay showing decrease in proliferating cells after treatment with 20 μM cyclopamine for 48 hours. Data is expressed as % of control (ethanol treatment only). (b) Western blot showing decrease in PTCH-1 expression in SKBR3 cells treated with 20 μM cyclopamine as compared to cells treated with ethanol only. (c) Immunofluorescence showing decrease in PTCH-1 and Gli-1 (nuclear and cytoplasmic) 24 hours after treatment with cyclopamine. (d) Scatchard analysis of ^{131}I-SHH binding to the surface of SKBR3 cell lines with and without treatment with 10 μM cyclopamine. There is a 5-fold decrease in surface PTCH-1 receptor expression 48 hours after treatment. (e) Reduced cellular uptake of ^{131}I-SHH in the PTCH-1 receptor positive breast cancer cell line SKBR3 with and without treatment with the HH inhibitor cyclopamine.

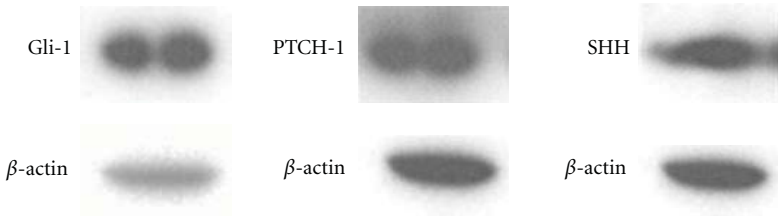

Figure 4: Western blot showing strong expression of SHH, PTCH-1, and Gli-1 in 13762 cells. β-actin is included as a control for protein level.

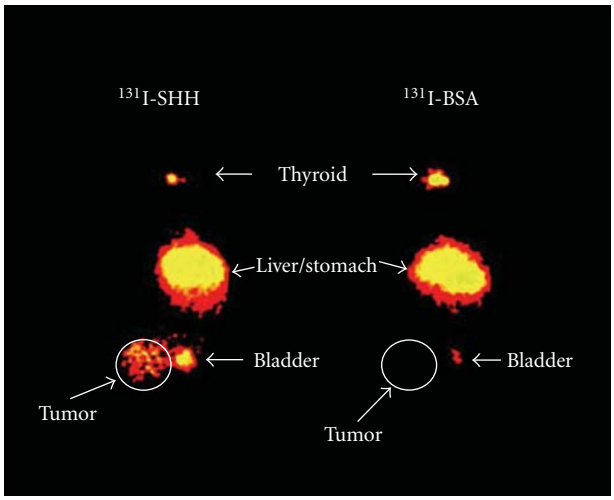

Figure 5: Planar image of Fischer 344 rats bearing breast cancer xenografts approximately 2 hours after injection of ^{131}I-SHH or ^{131}I-BSA. Tumor accumulation of the tracer is only observed in the rat injected with ^{131}I-SHH. The thyroid, stomach, and liver are also visible in both animals.

PTCH-1 have been directly linked to carcinogenesis in basal cell carcinoma and neural tumors [1, 2]. In many cases, these mutations result in truncation of the PTCH-1 receptor and loss of the SMO-binding inhibitory domain. However, in some cases the N-terminal extracellular ligand-binding domain is still expressed [33]. Therefore, while ^{131}I-SHH was shown to detect canonical HH activation in our studies, it is still unclear whether this method could also be used to determine hedgehog activation that results from PTCH-1 inactivating mutations.

5. Conclusions

Our data suggests that surface PTCH-1 receptor expression is correlated to canonical HH activity, and its expression is downregulated by small molecule inhibitors of HH signaling. We propose that radiolabeled SHH derivatives can be used to detect active HH signaling by noninvasive imaging. Furthermore, radiolabeled SHH derivatives may provide a method to determine *in vivo* response to hedgehog-targeted therapies.

Acknowledgments

This work was supported by the National Institutes of Health/National Cancer Institute Grant RO1 CA138230-01.

References

[1] E. B. Harmon, A. H. Ko, and S. K. Kim, "Hedgehog signaling in gastrointestinal development and disease," *Current Molecular Medicine*, vol. 2, no. 1, pp. 67–82, 2002.

[2] A. E. Bale and K. P. Yu, "The hedgehog pathway and basal cell carcinomas," *Human Molecular Genetics*, vol. 10, no. 7, pp. 757–762, 2001.

[3] D. M. Berman, S. S. Karhadkar, A. Maitra et al., "Widespread requirement for Hedgehog ligand stimulation in growth of digestive tract tumours," *Nature*, vol. 425, no. 6960, pp. 846–851, 2003.

[4] D. N. Watkins and C. D. Peacock, "Hedgehog signalling in foregut malignancy," *Biochemical Pharmacology*, vol. 68, no. 6, pp. 1055–1060, 2004.

[5] S. P. Thayer, M. P. di Magliano, P. W. Heiser et al., "Hedgehog is an early and late mediator of pancreatic cancer tumorigenesis," *Nature*, vol. 425, no. 6960, pp. 851–856, 2003.

[6] X. Ma, T. Sheng, Y. Zhang et al., "Hedgehog signaling is activated in subsets of esophageal cancers," *International Journal of Cancer*, vol. 118, no. 1, pp. 139–148, 2006.

[7] J. W. Theunissen and F. J. De Sauvage, "Paracrine hedgehog signaling in cancer," *Cancer Research*, vol. 69, no. 15, pp. 6007–6010, 2009.

[8] J. Sims-Mourtada, J. G. Izzo, J. Ajani, and K. S. C. Chao, "Sonic Hedgehog promotes multiple drug resistance by regulation of drug transport," *Oncogene*, vol. 26, no. 38, pp. 5674–5679, 2007.

[9] J. Sims-Mourtada, J. G. Izzo, S. Apisarnthanarax et al., "Hedgehog: an attribute to tumor regrowth after chemoradiotherapy and a target to improve radiation response," *Clinical Cancer Research*, vol. 12, no. 21, pp. 6565–6572, 2006.

[10] Z. Shafaee, H. Schmidt, W. Du, M. Posner, and R. Weichselbaum, "Cyclopamine increases the cytotoxic effects of paclitaxel and radiation but not cisplatin and gemcitabine in hedgehog expressing pancreatic cancer cells," *Cancer Chemotherapy and Pharmacology*, vol. 58, no. 6, pp. 765–770, 2006.

[11] J. M. Leonard, H. Ye, C. Wetmore, and L. M. Karnitz, "Sonic Hedgehog signaling impairs ionizing radiation—induced checkpoint activation and induces genomic instability," *Journal of Cell Biology*, vol. 183, no. 3, pp. 385–391, 2008.

[12] P. W. Ingham and A. P. McMahon, "Hedgehog signaling in animal development: paradigms and principles," *Genes and Development*, vol. 15, no. 23, pp. 3059–3087, 2001.

[13] L. Ruel, R. Rodriguez, A. Gallet, L. Lavenant-Staccini, and P. P. Thérond, "Stability and association of Smoothened, Costal2 and fused with Cubitus interruptus are regulated by Hedgehog," *Nature Cell Biology*, vol. 5, no. 10, pp. 907–913, 2003.

[14] J. W. Yoon, Y. Kita, D. J. Frank et al., "Gene expression profiling leads to identification of GLI1-binding elements in target genes and a role for multiple downstream pathways in GLI1-induced cell transformation," *The Journal of Biological Chemistry*, vol. 277, no. 7, pp. 5548–5555, 2002.

[15] P. Dai, H. Akimaru, Y. Tanaka, T. Maekawa, M. Nakafuku, and S. Ishii, "Sonic hedgehog-induced activation of the Gli1 promoter is mediated by GLI3," *The Journal of Biological Chemistry*, vol. 274, no. 12, pp. 8143–8152, 1999.

[16] M. Kubo, M. Nakamura, A. Tasaki et al., "Hedgehog signaling pathway is a new therapeutic target for patients with breast cancer," *Cancer Research*, vol. 64, no. 17, pp. 6071–6074, 2004.

[17] Y. Xuan and Z. Lin, "Expression of Indian Hedgehog signaling molecules in breast cancer," *Journal of Cancer Research and Clinical Oncology*, vol. 135, no. 2, pp. 235–240, 2009.

[18] C. Mas and A. Ruiz i Altaba, "Small molecule modulation of HH-GLI signaling: current leads, trials and tribulations," *Biochemical Pharmacology*, vol. 80, no. 5, pp. 712–723, 2010.

[19] J. P. Incardona, J. H. Lee, C. P. Robertson, K. Enga, R. P. Kapur, and H. Roelink, "Receptor-mediated endocytosis of soluble and membrane-tethered sonic hedgehog by patched-1," *Proceedings of the National Academy of Sciences of the United States of America*, vol. 97, no. 22, pp. 12044–12049, 2000.

[20] D. J. Yang, K. D. Kim, N. R. Schechter et al., "Assessment of antiangiogenic effect using 99mTc-EC-endostatin," *Cancer Biotherapy and Radiopharmaceuticals*, vol. 17, no. 2, pp. 233–246, 2002.

[21] D. P. Baker, F. R. Taylor, and R. B. Pepinsky, "Purifying the hedgehog protein and its variants," *Methods in Molecular Biology*, vol. 397, pp. 1–22, 2007.

[22] C. M. Lahorte, C. van de Wiele, K. Bacher et al., "Biodistribution and dosimetry study of 123I-rh-annexin V in mice and humans," *Nuclear Medicine Communications*, vol. 24, no. 8, pp. 871–880, 2003.

[23] J. Sims-Mourtada, J. G. Izzo, J. Ajani, and K. S. C. Chao, "Sonic Hedgehog promotes multiple drug resistance by regulation of drug transport," *Oncogene*, vol. 26, no. 38, pp. 5674–5679, 2007.

[24] D. J. Macey, L. E. Williams, H. B. Breitz, A. Liu, T. K. Johnson, and P. B. Zanzonico, "A primer for radioimmunotherapy and radionuclide therapy," Tech. Rep. 7, AAPM Nuclear Medicine Committee, American Association of Physicists in Medicine, 2001.

[25] Y. J. Chen, J. Sims-Mourtada, J. Izzo, and K. S. C. Chao, "Targeting the hedgehog pathway to mitigate treatment resistance," *Cell Cycle*, vol. 6, no. 15, pp. 1826–1830, 2007.

[26] M. H. Shahi, M. Afzal, S. Sinha et al., "Regulation of sonic hedgehog-GLI1 downstream target genes PTCH1, Cyclin D2, Plakoglobin, PAX6 and NKX2.2 and their epigenetic status in medulloblastoma and astrocytoma," *BMC Cancer*, vol. 10, article 614, 2010.

[27] M. Katano, "Hedgehog signaling pathway as a therapeutic target in breast cancer," *Cancer Letters*, vol. 227, no. 2, pp. 99–104, 2005.

[28] G. Shaw and D. M. Prowse, "Inhibition of androgen-independent prostate cancer cell growth is enhanced by combination therapy targeting Hedgehog and ErbB signalling," *Cancer Cell International*, vol. 8, article 3, 2008.

[29] K. A. Krohn, L. C. Knight, J. F. Harwig, and M. J. Welch, "Differences in the sites of iodination of proteins following four methods of radioiodination," *Biochimica et Biophysica Acta*, vol. 490, no. 2, pp. 497–505, 1977.

[30] M. Dentice, C. Luongo, S. Huang et al., "Sonic hedgehog-induced type 3 deiodinase blocks thyroid hormone action enhancing proliferation of normal and malignant keratinocytes," *Proceedings of the National Academy of Sciences of the United States of America*, vol. 104, no. 36, pp. 14466–14471, 2007.

[31] T. Mazumdar, J. DeVecchio, T. Shi, J. Jones, A. Agyeman, and J. A. Houghton, "Hedgehog signaling drives cellular survival in human colon carcinoma cells," *Cancer Research*, vol. 71, no. 3, pp. 1092–1102, 2011.

[32] R. Sacedón, B. Díez, V. Nuñez et al., "Sonic hedgehog is produced by follicular dendritic cells and protects germinal center B cells from apoptosis," *Journal of Immunology*, vol. 174, no. 3, pp. 1456–1461, 2005.

[33] J. Li, J. Wang, Y. Liu, and W. Wang, "Analysis of mutation in exon 17 of PTCH in patients with nevoid basal cell carcinoma syndrome," *Molecular Biology Reports*, vol. 37, no. 1, pp. 359–362, 2010.

Hindawi Publishing Corporation
Journal of Biomedicine and Biotechnology
Volume 2012, Article ID 806731, 7 pages
doi:10.1155/2012/806731

Research Article

Effectiveness of Myocardial Contrast Echocardiography Quantitative Analysis during Adenosine Stress versus Visual Analysis before Percutaneous Therapy in Acute Coronary Pain: A Coronary Artery TIMI Grading Comparing Study

Lixia Yang,[1,2] Yuming Mu,[2] Luiz Augusto Quaglia,[3] Qi Tang,[2] Lina Guan,[2] Chunmei Wang,[2] and Ming Chi Shih[4,5]

[1] *Department of Image Center, Xuhui Central Hospital, Shanghai 200031, China*
[2] *Department of Echocardiography, Center of Medical Ultrasound, The First Affiliated Hospital of Xinjiang Medical University, Xinjiang Urumqi 830011, China*
[3] *Faculty of Medical Sciences, State University of Campinas (UNICAMP), 13083 Campinas, SP, Brazil*
[4] *Department of Radiology, The University of Chicago, Chicago, IL 60637, USA*
[5] *Instituto Israelita de Ensino e Pesquisa Albert Einstein, 05652 São Paulo, SP, Brazil*

Correspondence should be addressed to Yuming Mu, yuming.mu@hotmail.com

Received 29 February 2012; Revised 19 April 2012; Accepted 19 April 2012

Academic Editor: David J. Yang

The study aim was to compare two different stress echocardiography interpretation techniques based on the correlation with thrombosis in myocardial infarction (TIMI) flow grading from acute coronary syndrome (ACS) patients. Forty-one patients with suspected ACS were studied before diagnostic coronary angiography with myocardial contrast echocardiography (MCE) at rest and at stress. The correlation of visual interpretation of MCE and TIMI flow grade was significant. The quantitative analysis (myocardial perfusion parameters: A, β, and $A \times \beta$) and TIMI flow grade were significant. MCE visual interpretation and TIMI flow grade had a high degree of agreement, on diagnosing myocardial perfusion abnormality. If one considers TIMI flow grade <3 as abnormal, MCE visual interpretation at rest had 73.1% accuracy with 58.2% sensitivity and 84.2% specificity and at stress had 80.4% accuracy with 76.6% sensitivity and 83.3% specificity. The MCE quantitative analysis has better accuracy with 100% of agreement with different level of TIMI flow grading. MCE quantitative analysis at stress has showed a direct correlation with TIMI flow grade, more significant than the visual interpretation technique. Further studies could measure the clinical relevance of this more objective approach to managing acute coronary syndrome patient before percutaneous coronary intervention (PCI).

1. Introduction

Acute myocardial infarction (AMI) is one of the major problems influencing public health, and PCI is one of the most effective method to reduce myocardial ischemia, ventricular remodeling and restore myocardial functions after AMI [1]. TIMI flow grade was at first related to a postthrombosis's coronary flow status measured by coronary angiography, where a totally obstructed flow receive grade 0 and a totally opened artery grade 3 [2]. Nowadays these flow grading is applied in others circumstances, supporting clinical decisions about PCI and making TIMI risk one of reference standards in ACS clinical management [3, 4].

Despite the clinical role of coronary flow in the prediction of myocardial ischemia, coronary angiography power of visualization is restricted to blood vessels with diameter >100 μm, which is not so accurate for collateral vessels and capillaries assessment, consequently not accurate for myocardial perfusion data.

Recently, the confirmation of myocardial microvascular integrity before PCI procedure becomes one of important concerns to achieve better survival and functional recovery of myocardium [5], and myocardial contrast-enhanced echocardiography (MCE) can assess the myocardial blood volume changes at stress using adenosine for accurately and

securely evaluating of myocardial microvascular perfusion in a real-time manner. This technique, which became more popular in clinical practice [6, 7], detects contrast microbubble at the capillary level within the myocardium and, thus, has the potential to assess tissue viability and the duration of the contrast effects [8].

MCE has been used for the determination of functional relevance of coronary stenoses of intermediate angiographic severity and is at least equivalent to single-photon emission computed tomography (SPECT) in microvascular disease and ACS evaluation, with a tendency toward higher sensitivity [9, 10].

Otherwise, MCE has a great advantage as a bedside technique and can be used early in patients presenting with acute heart failure to rapidly assess left ventricular (LV) function (regional and global) and perfusion (rest and stress) [11, 12].

There is no research data comparing TIMI flow grade with MCE perfusion in acute patients, neither comparing a quantitative and a visual MCE analysis for this purpose. So the objective of the study is to validate MCE as a useful tool for predict coronary flow dysfunctions and determinate which MCE analysis technique is more accurate.

2. Methods

2.1. Patients. The study was conducted during the period of March to December 2008, consisted of 41 patients (34 men, 36–69 years old and mean age 54 ± 10.8) who were diagnosed as acute coronary syndrome (ACS) highly elected for a PCI treatment. From the final population, 30 patients had acute myocardial infarction (AMI) confirmed. Diagnosis of ACS and AMI was based on the criteria by International Society of Cardiology and World Health Organization.

All patients underwent rest and hyperemic stress real-time myocardial contrast echocardiography (RT-MCE) before coronary angiography (CAG). All the diseases arteries had stents implanted with the blood flow of each reached 3 in TIMI flow grade after PCI. Baseline characteristics of the patients are listed in Table 1. This study was approved by the Ethics Committee of the First Affiliated Hospital of Xinjiang Medical University, and all of the patients provided written informed consent forms before their enrollment in the study.

2.2. Contrast Agent Administration. The contrast agent Sonovue (BRACCO Imaging B. V., Switzerland) is a suspension of microbubbles whose active product is sulphur hexafluoride, an innocuous gas eliminated through the respiratory system. The product is presented in the form of particles that activate when added to a saline solution and shaken vigorously for 30 seconds. A total amount of 2 mL was administered intravenously using an infusion pump at the rate of 1 mL/min. Then, 5 mL saline solution was added at the same rate. No adverse effects occurred in using the contrast agent.

2.3. Hyperemic Stress. Adenosine was the clinical stress agent preferred due to the efficient vasodilatation effect, the rapid effect and short half-life, and the modest chronotropic and inotropic effects. When resting RT MCE cine loops had been captured, adenosine was administered intravenously at a rate of 140 g/kg/min for up to 6 minutes. After 2.5 minutes of infusion, destruction-replenishment sequences were repeated in all apical views. Heart rate and rhythm were monitored continuously, and blood pressure and 12-lead electrocardiogram recorded every minute. All patients underwent the examinations in the research protocol, and no side effects occurred during these procedures.

Table 1: Demographic and clinical characteristics of 41 patients.

Variable	Value
Age (years)	54 ±10.8
Men	34 (82.9%)
Previous coronary angioplasty	0
Previous coronary bypass	0
Hypertension (*n*)	26 (63.4%)
Diabetes mellitus (*n*)	15 (36.6%)
Smokers (*n*)	28 (68.3%)
AMI	30
ACS	11
Diseased arteries	44
Left anterior descending	22 (50.0%)
Left circumflex coronary artery	7 (15.9%)
Right coronary artery	15 (34.1%)
Single-vessel disease	28
Multivessel disease	8
TIMI flow of diseased arteries before PCI <3	40 (90.9%)
TIMI flow of diseased arteries after PCI <3	0
Left ventricular ejection fraction (%)	47 ± 5
Left ventricular end diastolic volume (mL)	129 ± 41
Left ventricular end systolic volume (mL)	66 ± 32

Data presented as mean ± SD, unless otherwise noted; data in parentheses are percentages.
TIMI: thrombolysis in myocardial infarction; AMI: acute myocardial infarction; ACS: acute coronary syndrome.

2.4. Echocardiographic Image Acquisition. Echocardiography was performed within 48 hours before PCI, using a Philips iE 33 unit with S5 sound, the transmitting and receiving frequency was 1.8 MHz and 3.6 MHz, respectively. RT-MCE was performed using the technique of power modulation with the angiographic mode, which used a combination of low (0.08) and high (1.7) mechanical indexes. After obtaining an adequate acoustic window, the depth was adjusted so that only the left ventricle filled the image sector. The gain was adjusted to the limit until we began to see tissue noise. Then the contrast agent was infused as above. When a good signal was seen in the myocardium, a high (1.7) mechanical index impulse was given to destroy the contrast agent. Soon after, a low (0.08) mechanical index of RT-MCE was switched on, the myocardial contrast replenishment was visualized. Images of the apical 2-, 3-, and 4-chamber views were acquired for up to 15 cardiac cycles after the flash sequence was obtained and stored for offline evaluation later.

2.5. Assessment of RT-MCE. The MCE data of rest and stress cine loops were transferred to an offline computer workstation for analysis using Q-Lab (version 6.0, Philips Ultrasound) and performed by two independent researchers; both blinded to the results of CAG. The myocardial segments from the apical 2-, 3- and 4-chamber views were divided into 16 segments according to the standard segmentation scheme recommended by American Society of Echocardiography (ASE) [13]. Malm's et al. method [14] was adopted on analyzing the relationship between myocardial segments and CA. There were three segments (the basal, the middle, and the apical) within each wall of the anterior, inferior in apical 2-chamber, anterior interventricular septum and post in apical 3- chamber, and lateral and post interventricular septum in apical 4- chamber. Totally, 646 segments were analyzed among 41 patients. For qualitative analysis of myocardial perfusion the visual interpretation was used considering the degree of perfusion: the uniform distribution of contrast scored 1, no uniform scored 0.5, and no visualization scored 0. The quantitative analysis region of interest (ROI, 5 mm × 5 mm) was placed in the middle of each myocardial segment by using Qlab software quantitatively analyzing the reperfusion curve of real-time acoustic radiography. The mean value of three measurements was taken for the parameters in each region (Figure 1). Plots of contrast intensity versus time were constructed and fitted to an exponential function, $y = A(1 - e - \beta t)$ [15]. The plateau of signal intensity (A) and the slope of maximum signal intensity rise (β) were measured, and the product of $A \times \beta$ was computed. Then the mean value of A, β, and $A \times \beta$ in each segment was calculated. A, β, and $A \times \beta$ represent myocardial blood volume, myocardial blood flow velocity, and myocardial blood flow, respectively. The segmental MCE parameters and their vasodilator reserves (stress-rest ratios) were recorded, named for A-reserve (stress A/rest A), β-reserve (stress β/rest β), and $A \times \beta$-reserve (stress $A \times \beta$/rest $A \times \beta$) [16].

2.6. Coronary Angiography. Selective coronary angiography on device INNOVA 2000 (GE, USA) was performed in all patients within 48 hours of the MCE. An independent experienced observer blinded to the MCE data analyzed the coronary angiograms. The coronary TIMI flow grading was expressed, using digital substation angiography, which was equipped with the function of image counting. AMI and ACS results underwent TIMI flow grading according to TIMI study group [2].

2.7. Reproducibility of the Measurements. The visual interpretation scoring and quantitative assessment of blood flow parameters were conducted by two doctors blindly. We randomly selected 50 segments of the patients to assess the inter- and intra-observer agreement.

2.8. Statistical Analysis. Categorical variables were expressed as number (%) of myocardial segments and quantitative variables as mean ± standard deviation (SD). The comparisons for categorical data were performed by Wilcoxon signed ranks test and consistency test by *Kappa*. Univariate ANOVA or Welch tests that are similar to ANOVA were used for quantitative data. The Dunnett's *T3* test was used for comparison between any two groups [17]. Spearman-rank correlation was used to analyze the correlation between visual interpretation perfusion score, perfusion parameters and TIMI flow grade. Inter- and intra-observer reproducibility of ordered variables agreement was assessed by *Kappa* [18]. For quantitative variables, interclass correlation coefficient (ICC) was used with reproducibility considered perfect if the ICC was between 0.81 and 1.0. The statistical analysis was done using the Statistical Package for Social Sciences, version 13.0 for windows (SPSS, Inc., Chicago, IL, USA). All results were considered to be statistically significant when the P value was less than 0.05.

3. Results

3.1. Coronary Angiography. From 41 patients that underwent coronary angiography, 36 were elected for PCI, 28 had single-vessel disease, and 8 were multivessel. The blood flow of coronary artery was determined by the TIMI flow grade classification. There are 8 vessels in TIMI flow grade 0. There are 12 vessels in TIMI flow grade 1. There are 20 vessels in TIMI flow grade 2. There are 4 vessels in TIMI flow grade 3. All the diseases arteries (36 patients) had stents implanted with the blood flow of each reached 3 in TIMI flow grade after PCI.

3.2. RT-MCE Assessments before PCI. In the 41 patients, 123 vessels were selected. A total of 656 myocardial segments from the apical 2-, 3-, and 4-chamber views were imaged. 89 non-analyzable segments comprising 41 basal segments. 567 segments were analyzable and had clear images being used for MCE qualitative and quantitative analysis at rest and at stress. 271 segments were fed by the diseased arteries, in which 198 by LAD, 28 by LCx and 45 by RCA.

3.3. Visual Interpretation (Qualitative Analysis). The number of myocardial segments analysed by MCE in each TIMI flow grade were shown in Tables 2 and 3 (rest and stress). There was a positive correlation between MCE and TIMI flow grade ($rs = 0.691$, P values <0.001) at rest. There was a positive correlation between MCE and TIMI flow grade ($rs = 0.738$, P values <0.001) at stress. On diagnosing myocardial perfusion abnormality, MCE at rest and at stress had a high degree of agreement comparing with TIMI flow grade (*Kappa* = 0.687, P values <0.001) and (*Kappa* = 0.827, P values <0.001).

3.4. Quantitative RT-MCE Assessment. The results of myocardial perfusion parameters (A, β, and $A \times \beta$) before PCI at rest and at stress were shown in Table 4.

The differences in A, β, and $A \times \beta$ values at rest between any of two groups were different and statistically significant ($W = 382.13$, 192.61, and 450.96 resp., P values <0.001). These results also apply to the stress group ($W = 499.64$, 318.15, and 601.17 resp., P values <0.001). A, β, and $A \times \beta$

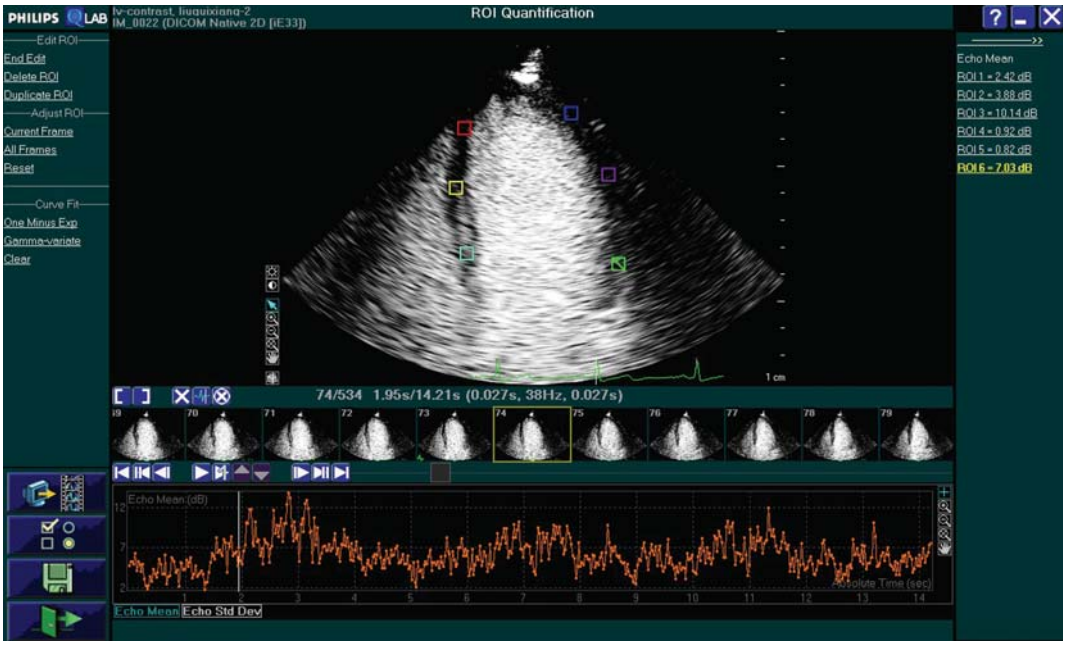

Figure 1: Region of interest (ROI, 5 mm × 5 mm) was placed in the middle of the six myocardial segments, and the ROI was tracked manually to assure its center position in each segment. The reperfusion curves of acoustic contrast intensity versus time were constructed automatically with QLab software. The specific values of signal intensity peak (A), the slope of slope of curve (β), and perfusion volume ($A \times \beta$) were acquired.

Table 2: MCE visual interpretation at rest among TIMI flow grades before PCI n (%).

MCE visual interpretation	TIMI flow grades			
	Grade 0	Grade 1	Grade 2	Grade 3
0	31 (64.6)	9 (11.7)	8 (6.7)	9 (2.8)
0.5	10 (20.8)	46 (59.7)	38 (31.9)	42 (13.0)
1	7 (14.6)	22 (28.6)	73 (61.3)	272 (84.2)
Total	48	77	119	323

TIMI: thrombolysis in myocardial infarction trial; PCI: percutaneous coronary intervention.
MCE visual interpretation at rest and TIMI flow grade correlated positively, $rs = 0.691$, $P < .001$.
PCI: percutaneous coronary intervention; TIMI: thrombolysis in myocardial infarction trial.
Grades 0, 1, and 2 were abnormal, grade 3 was normal for TIMI grade. MCE Visual Interpretation 0 and 0.5 were abnormal, and 1 was normal for MCE Visual Interpretation.
On diagnosing myocardial perfusion abnormality TIMI flow grade and MCE Visual Interpretation at rest had a high degree of agreement, *Kappa* = .687, $P < .001$.

Table 3: MCE visual interpretation among at stress TIMI flow grades before PCI n (%).

MCE visual interpretation	TIMI flow grades			
	Grade 0	Grade 1	Grade 2	Grade 3
0	41 (85.4)	26 (33.8)	14 (11.8)	10 (3.1)
0.5	6 (12.5)	44 (57.1)	56 (47.1)	44 (13.6)
1	1 (2.1)	7 (9.1)	49 (41.2)	269 (83.3)
Total	48	77	119	323

TIMI, thrombolysis in myocardial infarction trial; PCI, percutaneous coronary intervention.
MCE Visual Interpretation at stress and TIMI flow grade correlated positively, $rs = 0.738$, $P < .001$.
PCI, percutaneous coronary intervention; TIMI, thrombolysis in myocardial infarction trial.
Grades 0, 1, and 2 were abnormal, grade 3 was normal for TIMI grade. MCE Visual Interpretation 0 and 0.5 were abnormal, and 1 was normal for MCE Visual Interpretation.
On diagnosing myocardial perfusion abnormality TIMI flow grade and MCE Visual Interpretation at stress had a completely consistent, *Kappa* = .827, $P < .001$.

values at rest and at stress increased linearly with the TIMI flow grading, and the means of the parameters correlated with TIMI flow grade ($rs = 0.741$, 0.528, and 0.715 for A, β, and $A \times \beta$, P values <0.001, and $rs = 0.872$, 0.767 and 0.845 for A, β, and $A \times \beta$, P values <0.001, resp.).

If one considers TIMI grade <1 is abnormal, MCE Visual Interpretation (at rest/at stress) had 72.0%/65.5% accuracy with 85.4%/97.9% sensitivity and 70.7%/62.6% specificity respectively. If one considers TIMI grade <2 is abnormal, MCE Visual Interpretation (at rest/at stress) had 77.7%/76.7% accuracy with 76.8%/93.6% sensitivity and 78.1%/71.9% specificity, respectively. If one considers TIMI grade <3 is abnormal, MCE Visual Interpretation (at rest/at stress) had 73.1%/80.4% accuracy with 58.2%/76.6% sensitivity and 84.2%/83.3% specificity, respectively (see Table 5).

The correlation between the trend of A-reserve, β-reserve, $A \times \beta$-reserve, and TIMI grade are shown in Figure 2.

3.5. Reproducibility of the Measurements. For MCE visual interpretation, a high degree of intraobserver agreement (*Kappa* = 0.79, $P = 0.08$) and interobserver agreement

Table 4: Comparison of myocardial perfusion parameters at rest and stress among TIMI flow grades.

Myocardial perfusion parameters	TIMI flow grades					
	Grade 0	Grade 1	Grade 2	Grade 3	W^*	P
A (db):						
rest	$1.06 \pm 0.02^{*\S\dagger}$	$3.17 \pm 0.08^{*\S}$	$4.49 \pm 0.32^{*}$	5.29 ± 0.47	382.13	.000
stress	$1.01 \pm 0.06^{*\S\dagger}$	$3.09 \pm 0.11^{*\S}$	$4.83 \pm 0.09^{*}$	$5.71 \pm 0.53^{*}$	499.64	.000
β (s−1):						
rest	$0.13 \pm 0.02^{*\S\dagger}$	$0.17 \pm 0.03^{*\S}$	$0.24 \pm 0.03^{*}$	0.28 ± 0.01	192.61	.000
stress	$0.11 \pm 0.06^{*\S\dagger}$	$0.23 \pm 0.05^{*\S\#}$	$0.57 \pm 0.04^{*\#}$	$0.71 \pm 0.09^{*}$	318.15	.000
A × β (db/S):						
rest	$0.14 \pm 0.01^{*\S\dagger}$	$0.54 \pm 0.03^{*\S}$	$1.08 \pm 0.02^{*}$	1.39 ± 0.04	450.96	.000
stress	$0.11 \pm 0.01^{*\S\dagger}$	$0.71 \pm 0.01^{*\S\#}$	$2.75 \pm 0.09^{*\#}$	$4.05 \pm 0.11^{*}$	601.17	.000
A-reserve	$0.95 \pm 0.08^{*\S\dagger}$	$0.98 \pm 0.07^{*\S}$	$1.08 \pm 0.07^{*}$	1.09 ± 0.05	452.14	.000
β-reserve	$0.85 \pm 0.02^{*\S\dagger}$	$1.36 \pm 0.02^{*\S}$	$2.37 \pm 0.03^{*}$	2.54 ± 0.05	267.82	.000
A × β-reserve	$0.79 \pm 0.02^{*\S\dagger}$	$1.31 \pm 0.03^{*\S}$	$2.55 \pm 0.06^{*}$	3.11 ± 0.05	539.74	.000

A: indicates myocardial blood volume; β: myocardial blood flow velocity; A × β: myocardial blood flow; A-reserve: stress A/rest A; β-reserve: stress β/rest β; A × β-reserve: stress A × β/rest A × β; TIMI: thrombolysis in myocardial infarction trial.
The correlation between the means of A, β, and A × β at rest and TIMI grade reached significant (rs = 0.741, 0.528, and 0.715, resp., P values <.001).
The correlation between the means of A, β, and A × β at stress and TIMI grade reached significant (rs = 0.872, 0.767, and 0.845 for A, β, and A × β, resp., P values <.001).
$^*P < .001$ versus TIMI grade 3.
$^{\S}P < .001$ versus TIMI grade 2.
$^{\dagger}P < .001$ versus TIMI grade 1.
$^{\#}P < .001$ versus parameter in rest.
*Welch tests.

Table 5: Accuracy, sensitivity, and specificity of abnormal in MCE Visual Interpretation at rest and stress with different TIMI flow grades as abnormal (%).

TIMI flow grades	Accuracy	Sensitivity	Specificity
Grade <1:			
rest	72.0	85.4	70.7
stress	65.6	97.9	62.6
Grade <2:			
rest	77.7	76.8	78.1
stress	76.7	93.6	71.9
Grade <3:			
rest	73.1	58.2	84.2
stress	80.4	76.6	83.3

TIMI: thrombolysis in myocardial infarction trial.
TIMI grade <1, grade 0 was abnormal, grades 1, 2, and 3 were normal for TIMI grade. TIMI grade <2, grades 0 and 1 were abnormal, grades 2 and 3 were normal for TIMI grade. TIMI Grade <3, grades 0, 1, and 2 were abnormal, grade 3 was normal for TIMI grade.

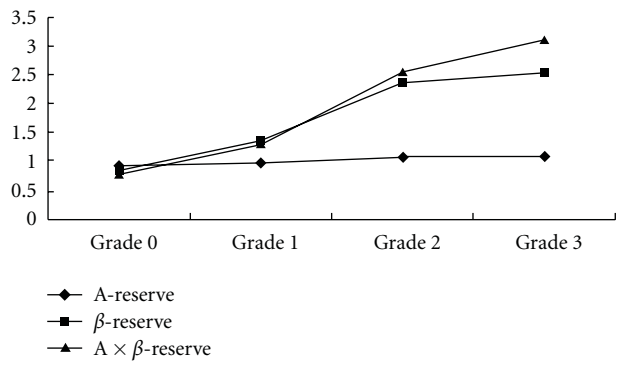

Figure 2: Trend of intergroup reserve of MEC parameters among groups of each coronary artery TIMI grade.

Table 6: Reproducibility of quantitative assessment of myocardial perfusion parameters.

	A	β	A × β
Intraobserver r_i	0.950	0.820	0.873
Interobserver r_i	0.950	0.869	0.851

(*Kappa* = 0.76, P = 0.09) was observed. The intraobserver reproducibility of A, β, and $A \times \beta$ was perfect. The ICCs were 0.950, 0.820, and 0.873 for, A, β, and $A \times \beta$, respectively. The interobserver agreement was perfect for A, and $A \times \beta$, with ICCs being 0.950, 0.869, and 0.851 for A, β, and $A \times \beta$, respectively (Table 6).

4. Discussion

The results of visual interpretation and parametric quantification of MCE and TIMI flow grade were not totally similar and the correlation was quite different. Using MCE visual interpretation scoring method, the changes in cardiac imaging can be directly observed with unaided eyes, and the PCI preoperative microcirculation status can be preliminarily evaluated. The results of MCE visual interpretation at rest and stress had a positive correlation with TIMI flow grade. It indicated that visual interpretation could reflect myocardial perfusion and TIMI flow grade as well. However, the results

of the quantitative analysis from our study expressed by the myocardial perfusion parameters (A, β, and $A \times \beta$) can directly reflect the status of blood perfusion and coronary TIMI flow grade even more accurate and precise than visual analysis.

With the help of this parametric quantification, this could overcome the limitations of visualization and part of operator dependency bias.

Malm's et al. [14] study demonstrate that the importance of quantitative assessment of RT-MCE by myocardial perfusion parameters β (velocity) and $A \times \beta$ (Volume $\times$ velocity) has more influence in prediction of coronary artery stenosis. In the mean time, study from Li et al. [19] showed that when there were no collateral circulation patencies, β, and $A \times \beta$ decreased with the aggravation of coronary artery stenosis. Through quantitative analysis of myocardial perfusion parameters, we observed that β and $A \times \beta$ value increased at rest and being more exponential at stress to TIMI flow grading level reaching at least 1–3 folds. It also indicated that perfusion injury became severe with the decrease of β value (velocity) more accentually, confirming the importance of pathophysiology of steal phenomenon from coronary artery flow, more evident at stress.

Even though TIMI flow grade and MCE focused on different ways to look at the same physiopathology, the epicardical coronary tree flow had a great concordance with myocardial flow measured by MCE, inferring that in acute patients TIMI's grading still has a good accuracy as a perfusion-deficit predictor. However, there were two patients where TIMI grade was abnormal and MCE was normal, possibly because collateral microcirculation takes place in those patients. There were no data that supports a conservative treatment for then, despite clinical evidence that percutaneous interventions without myocardial ischemia leads to a worst prognostic tendency [20, 21].

For the ACS patients screening before PCI, the MCE technique could raise more necessary evidence for clinician in evaluating the status of myocardial perfusion give the data of possible improvements of preoperative myocardial microvascular perfusion and also filtering case for correct treatment choice.

In conclusion, MCE parametric quantification had a positively correlation with TIMI flow grading and can qualitatively and quantitatively assess the myocardial perfusion more accurately than the visual one. The technique of MCE can work as a beneficial tool aiding before coronary angiography to predict TIMI risk and help clinical decision.

5. Limitations

The limitations of the study include no data about MCE side effects and the level of acceptability by the patients and the absent of traditional perfusion gold standards, like fractional flow reserve (FFR) or Rubidium nuclear imaging.

The improvements of the myocardial perfusion has not been further investigated by conducting follow-up visits 3–6 months after the surgery, which will be improved in the future studies.

Acknowledgment

The research was supported by the Science and Technology Planning Project Grant of Urumqi Municipality of the Xinjiang Uygur Autonomous Region "The Application of Myocardial Contrast Echocardiography on the Assessment of Myocardial Microcirculation Perfusion" (no. G06131001). All the authors have no conflict of interests in this study, reveal in a statement with any (1) financial interests or arrangements with a company whose product was used in a study or is referred to in a paper, (2) any financial interests of arrangement with a competing company, (3) any direct payment to an author(s) from any source for the purpose of writing the paper, and (4) any other financial connections, direct or indirect, or other situations that might raise the question of bias in the work reported or the conclusions, implications, or opinions stated-including pertinent commercial or other sources of funding for the individual author(s) or for the associated department(s) or organization(s), personal relationships, or direct academic competition. They would like to express their gratitude to the doctors from the Cardiovascular Department and the Echocardiography Department of the First Affiliated Hospital, Xinjiang Medical University, for their contributions and support to this study.

References

[1] J. Shiraishi, Y. Kohno, T. Sawada et al., "Predictors of nonoptimal coronary flow after primary percutaneous coronary intervention with stent implantation for acute myocardial infarction," *Journal of Cardiology*, vol. 55, no. 2, pp. 217–223, 2010.

[2] H. S. Mueller, A. Dyer, and M. A. Greenberg, "The thrombolysis in myocardial infarction (TIMI) trial. Phase I findings," *New England Journal of Medicine*, vol. 312, no. 14, pp. 932–936, 1985.

[3] G. De Luca, N. Ernst, F. Zijlstra et al., "Preprocedural TIMI flow and mortality in patients with acute myocardial infarction treated by primary angioplasty," *Journal of the American College of Cardiology*, vol. 43, no. 8, pp. 1363–1367, 2004.

[4] E. Appelbaum, A. J. Kirtane, A. Clark et al., "Association of TIMI Myocardial Perfusion Grade and ST-segment resolution with cardiovascular magnetic resonance measures of microvascular obstruction and infarct size following ST-segment elevation myocardial infarction," *Journal of Thrombosis and Thrombolysis*, vol. 27, no. 2, pp. 123–129, 2009.

[5] K. Wei and S. Kaul, "The coronary microcirculation in health and disease," *Cardiology Clinics*, vol. 22, no. 2, pp. 221–231, 2004.

[6] L. Galiuto, G. Locorotondo, L. Paraggio et al., "Characterization of microvascular and myocardial damage within perfusion defect area at myocardial contrast echocardiography in the subacute phase of myocardial infarction," *European Heart Journal*, vol. 13, no. 2, pp. 174–180, 2012.

[7] S. S. Abdelmoneim, A. Basu, M. Bernier et al., "Detection of myocardial microvascular disease using contrast echocardiography during adenosine stress in type 2 diabetes mellitus:

prospective comparison with single-photon emission computed tomography," *Diabetes and Vascular Disease Research*, vol. 8, no. 4, pp. 254–261, 2011.

[8] E. Modonesi, M. Balbi, and G. P. Bezante, "Limitations and potential clinical application on contrast echocardiography," *Current Cardiology Reviews*, vol. 6, no. 1, pp. 24–30, 2010.

[9] S. S. Abdelmoneim, M. Bernier, A. Dhoble et al., "Diagnostic accuracy of contrast echocardiography during adenosine stress for detection of abnormal myocardial perfusion: a prospective comparison with technetium-99 m sestamibi single-photon emission computed tomography," *Heart and Vessels*, vol. 25, no. 2, pp. 121–130, 2010.

[10] G. Dwivedi, R. Janardhanan, S. A. Hayat, T. K. Lim, and R. Senior, "Comparison between myocardial contrast echocardiography and 99mTechnetium sestamibi single photon emission computed tomography determined myocardial viability in predicting hard cardiac events following acute myocardial infarction," *American Journal of Cardiology*, vol. 104, no. 9, pp. 1184–1188, 2009.

[11] S. A. Hayat and R. Senior, "Myocardial contrast echocardiography in ST elevation myocardial infarction: ready for prime time?" *European Heart Journal*, vol. 29, no. 3, pp. 299–314, 2008.

[12] J. R. Arnold, T. D. Karamitsos, T. J. Pegg et al., "Adenosine stress myocardial contrast echocardiography for the detection of coronary artery disease: a comparison with coronary angiography and cardiac magnetic resonance," *Journal of the American College of Cardiology*, vol. 3, no. 9, pp. 934–943, 2010.

[13] N. B. Schiller, P. M. Shah, M. Crawford et al., "Recommendations for quantitation of the left ventricle by two-dimensional echocardiography. American Society of Echocardiography Committee on Standards, Subcommittee on Quantitation of Two-Dimensional Echocardiograms," *Journal of the American Society of Echocardiography*, vol. 2, no. 5, pp. 358–367, 1989.

[14] S. Malm, S. Frigstad, H. Torp, R. Wiseth, and T. Skjarpe, "Quantitative adenosine real-time myocardial contrast echocardiography for detection of angiographically significant coronary artery disease," *Journal of the American Society of Echocardiography*, vol. 19, no. 4, pp. 365–372, 2006.

[15] K. Wei, A. R. Jayaweera, S. Firoozan, A. Linka, D. M. Skyba, and S. Kaul, "Quantification of myocardial blood flow with ultrasound-induced destruction of microbubbles administered as a constant venous infusion," *Circulation*, vol. 97, no. 5, pp. 473–483, 1998.

[16] G. Korosoglou, K. G. C. Da Silva, N. Labadze et al., "Real-time myocardial contrast echocardiography for pharmacologic stress testing: is quantitative estimation of myocardial blood flow reserve necessary?" *Journal of the American Society of Echocardiography*, vol. 17, no. 1, pp. 1–9, 2004.

[17] P. Y. Chen, *SPSS 13.0 Statistic Software Tutorial*, The People's Medical Publishing House, 2005.

[18] J. R. Landis and G. G. Koch, "The measurement of observer agreement for categorical data," *Biometrics*, vol. 33, no. 1, pp. 159–174, 1977.

[19] Y. Li, Q. Lv, X. F. Wang et al., "Myocardial perfusion in patients with different graded coronary stenosis by real-time myocardial contrast echocardiography," *Chinese Journal of Medical Imaging Technology*, vol. 24, no. 12, pp. 1955–1958, 2008.

[20] K. L. Gould, "Physiological severity of coronary artery stenosis," *American Journal of Physiology*, vol. 291, no. 6, pp. H2583–H2585, 2006.

[21] P. A. L. Tonino, B. De Bruyne, N. H. J. Pijls et al., "Fractional flow reserve versus angiography for guiding percutaneous coronary intervention," *New England Journal of Medicine*, vol. 360, no. 3, pp. 213–224, 2009.

Hindawi Publishing Corporation
Journal of Biomedicine and Biotechnology
Volume 2012, Article ID 262741, 6 pages
doi:10.1155/2012/262741

Research Article

In Vivo Visualization of Heterogeneous Intratumoral Distribution of Hypoxia-Inducible Factor-1α Activity by the Fusion of High-Resolution SPECT and Morphological Imaging Tests

Hirofumi Fujii,[1] Masayuki Yamaguchi,[1] Kazumasa Inoue,[1] Yasuko Mutou,[1] Masashi Ueda,[2] Hideo Saji,[2] Shinae Kizaka-Kondoh,[3] Noriyuki Moriyama,[4] and Izumi O. Umeda[1]

[1] *Functional Imaging Division, National Cancer Center Hospital East, Kashiwa 277-8577, Japan*
[2] *Graduate School of Pharmaceutical Sciences, Kyoto University, Kyoto 606-8501, Japan*
[3] *Graduate School of Bioscience and Biotechnology, Tokyo Institute of Technology, Yokohama 226-8503, Japan*
[4] *Research Center for Cancer Prevention and Screening, National Cancer Center, Tokyo 104-0045, Japan*

Correspondence should be addressed to Izumi O. Umeda, ioumeda@east.ncc.go.jp

Received 1 March 2012; Accepted 24 April 2012

Academic Editor: David J. Yang

Purpose. We aimed to clearly visualize heterogeneous distribution of hypoxia-inducible factor 1α (HIF) activity in tumor tissues *in vivo*. *Methods*. We synthesized of ^{125}I-IPOS, a ^{125}I labeled chimeric protein probe, that would visualize HIF activity. The biodistribution of ^{125}I-IPOS in FM3A tumor-bearing mice was evaluated. Then, the intratumoral localization of this probe was observed by autoradiography, and it was compared with histopathological findings. The distribution of ^{125}I-IPOS in tumors was imaged by a small animal SPECT/CT scanner. The obtained *in vivo* SPECT-CT fusion images were compared with *ex vivo* images of excised tumors. Fusion imaging with MRI was also examined. *Results*. ^{125}I-IPOS well accumulated in FM3A tumors. The intratumoral distribution of ^{125}I-IPOS by autoradiography was quite heterogeneous, and it partially overlapped with that of pimonidazole. High-resolution SPECT-CT fusion images successfully demonstrated the heterogeneity of ^{125}I-IPOS distribution inside tumors. SPECT-MRI fusion images could give more detailed information about the intratumoral distribution of ^{125}I-IPOS. *Conclusion*. High-resolution SPECT images successfully demonstrated heterogeneous intratumoral distribution of ^{125}I-IPOS. SPECT-CT fusion images, more favorably SPECT-MRI fusion images, would be useful to understand the features of heterogeneous intratumoral expression of HIF activity *in vivo*.

1. Introduction

It is very important for the optimization of treatments of tumors to evaluate their features. The features of tumors are usually investigated by pathological examination using some pieces of biopsied specimens. But the pathological findings inside the tumor are often heterogeneous. For example, the expression of human epidermal growth factor receptor 2 (HER2) is often heterogeneous in breast cancer tissues [1]. This means that the degree of HER2 expression can be differently diagnosed according to the biopsy site even in the same tumor. Since, the indication of trastuzumab therapy for breast cancer is determined on the basis of the expression of HER2, the indication of this therapy might also be judged differently according to the biopsy site. To resolve this issue, imaging tests would be useful because they can observe the whole of tumors, unlike pathological tests using biopsied specimens.

There are many studies to evaluate the features of tumors using imaging tests. For example, ^{18}F-fluorodeoxyglucose (FDG) positron emission tomography (PET) has been used to observe glucose metabolism in tumors [2]. And this imaging test is now routinely performed in the clinical practice. Although these imaging tests could image the whole

of tumors, they usually failed to visualize the heterogeneity of tumors due to their poor spatial resolution.

But recent advances in imaging devices and image processing methods have enabled to provide excellent images with high spatial resolution. And it has been also reported that the superimposition of images showing functional information on morphological images such as CT and MRI is quite useful to understand the features of tumors [3]. We will be able to investigate heterogeneous features inside tumors more precisely by using these techniques, and the obtained results will contribute to the optimization of cancer therapy.

Tumor hypoxia is one of the main reasons for the resistance to anticancer therapy such as radiotherapy and chemotherapy [4, 5]. The oxygen partial pressure is heterogeneously distributed in tissues since it depends on intratumoral vasculature [6]. It is difficult to diagnose this heterogeneity in oxygen partial pressure in cancer tissues by biopsied specimens. In some studies, oxygen partial pressure in tumors was measured by inserting an oxygen electrode [7]. But this method is rather invasive and not easy to repeat due to patients' pain. It is also difficult to investigate its heterogeneous distribution in the tumor. Therefore, it is expected to visualize the heterogeneous intratumoral distribution of oxygen partial pressure by *in vivo* imaging tests with high spatial resolution.

Although immunohistological staining by pimonidazole is often used in experimental studies, its clinical application is impossible because pimonidazole cannot be injected into humans due to its toxicity.

Overexpression of hypoxia inducible factor (HIF) partially contributes to the resistance to antitumor therapies under hypoxic conditions [8]. We are interested in evaluating HIF activity as a surrogate of direct measuring of oxygen partial pressure. Recently, an idea where HIF activity is evaluated utilizing the stability of oxygen-dependent degradation (ODD) domain in HIF was reported in the field of optical imaging. And HIF activity was successfully visualized using an optical probe obtained by the fusion of ODD and protein transduction domain (PTD) [9, 10]. As the clinical application of optical imaging techniques is quite limited, its translation in the field of nuclear medicine is expected.

Kudo et al. imaged HIF-1-active tumor hypoxia using a similar chimeric protein probe, ^{123}I-IPOS, a conjugate of ^{123}I-labeled 3-iodobenzoyl norbiotinamide (IBB) and a fusion protein consisting of PTD, ODD, and streptavidin (POS) using a planar gamma camera [11, 12]. Although they could image the tumor itself as a mass, it was difficult to visualize the intratumoral heterogeneous distribution of ^{123}I-IPOS due to poor spatial resolution. Recently, we found that intratumoral heterogeneous distribution of radioactive IPOS might be imaged by using a single-photon-emission computed tomography (SPECT) scanner dedicated for small animal imaging, instead of planar gamma camera [13].

In this study, we aimed to clearly visualize heterogeneous intratumoral localization of ^{125}I-IPOS *in vivo* using fusion imaging methods of high-resolution SPECT and morphological imaging tests such as computed tomography (CT) and magnetic resonance imaging (MRI). And we tried to confirm the usefulness of these fusion images in the diagnosis of heterogeneous features inside tumors.

2. Materials and Methods

2.1. Synthesis of ^{125}I-IPOS. POS was overexpressed in *Escherichia coli* and purified, as previously reported [11]. Purified POS was dissolved in Tris-HCl buffer, pH 8.0. Sodium [^{125}I] iodine (629 GBq/mg as I) was purchased from Perkinelmer Japan. 3-Iodobenzoyl norbiotinamine (IBB) was prepared as described previously [14] and labeled with ^{125}I. ^{125}I-IPOS was obtained by the incubation of ^{125}I-IBB and POS for 1 hour. ^{125}I-IPOS was purified using a Sephadex G-50-filled spin column.

2.2. Animal Tumor Model. Five-week-old female C3H/He mice were purchased from Japan SLC (Hamamatsu, Japan). They were kept at 12/12 h dark-light cycles and were fed *ad libitum*. FM3A mouse breast cancer cells (5×10^6 cells) were subcutaneously implanted into a thigh of a mouse. These mice were used for the experiments 2 weeks after the inoculation. Implanted tumors in this model showed good affinity to IPOS in our previous study [13]. All animal experiments were carried out after the approval by the Ethical Committee for Animal Experiments of our institute.

2.3. Biodistribution of ^{125}I-IPOS. ^{125}I-IPOS (2.0 MBq/30 μg/0.2 mL) was intravenously injected into each mouse via its tail vein. The mice were sacrificed 24 hours after the injection because our previous study revealed that ^{125}I-IPOS accumulated well enough for SPECT imaging [11]. Whole-organ specimens were removed immediately and weighed, and their radioactivity was measured by a dose calibrator (IGC-7, Aloka, Tokyo, Japan) or an autowell gamma counter (ARC-380CL, Aloka).

2.4. Immunohistochemistry and Autoradiography of Excised Tumors. ^{125}I-IPOS (2.0 MBq/30 μg/0.2 mL) was intravenously injected into mice via their tail veins. Pimonidazole (60 mg/kg) was intravenously injected into these mice 1 h before the dissection. These mice were sacrificed 24 h after the injection of ^{125}I-IPOS. The excised tumors were embedded in OCT compound (Sakura Finetek Japan, Tokyo, Japan), frozen, and cut into 6 μm thick sections for hematoxylin-eosin (H&E) staining and fluorescent immunostaining of pimonidazole, and 20 μm thick sections for autoradiography (ARG) using a cryomicrotome (CM 3050S, Leica Instruments, Wetzlar, Germany). For fluorescent immunostaining of pimonidazole, FITC-conjugated mouse IgG_1 monoclonal antibody (Chemicon, Temecula, CA, USA) was treated according to the manufacture's protocol for pimonidazole staining. For ARG, the sliced tumor specimens were placed in contact with an imaging plate (MS2040, Fujifilm, Tokyo, Japan), and the exposed imaging plates were analyzed by an FLA-7000 reader (Fujifilm) and Multi-Gause ver. 3.0 software (Fujifilm).

2.5. SPECT/CT Imaging. High dose of ^{125}I-IPOS (20 MBq/30 μ g/0.2 mL) was intravenously injected into 2 mice via their tail veins. The mice were anesthetized by the inhalation of isoflurane gas 24 hours after the injection. SPECT images were obtained using a SPECT/CT combined scanner dedicated for small animal imaging (NanoSPECT/CT, Bioscan, Washington, D.C., USA). This scanner had 4 detectors with tungsten multipinhole collimators (number of pinholes: 9, the diameter of pinhole: 1.4 mm). First, CT images were acquired by a continuous helical scanning method. The acquisition conditions were as follows: tube voltage: 45 keV, tube current: 177 μA. Then, SPECT images were obtained by a step-and-shoot helical scanning method. The energy window was set between 20 and 36 keV. The acquisition time was set to 5 min for each step. Six steps of 4 detectors, total 24 steps, covered 360 degrees.

The acquired image data of both CT and SPECT were reconstructed by using InVivoScope software (Bioscan). Filtered back-projection algorithms and ordered subset-expectation maximization ones were used for CT image data and for SPECT ones, respectively.

The excised tumor was also imaged using the same SPECT/CT scanner *ex vivo*. The SPECT acquisition time for single step was set to 10 min. Both *in vivo* and *ex vivo* SPECT images superimposed on CT images were compared with each other.

2.6. MR Imaging and Image-Fusion of SPECT and MRI. High-dose ^{125}I-IPOS (20 MBq/30 μg/0.2 mL) was intravenously injected into 2 mice via their tail veins. The mice were anesthetized by mixed gas of isoflurane and nitrogen oxide 24 hours after the injection. After the anesthesia, the mice were put on the special bed that was designed for the fusion imaging of SPECT and MR imaging and immobilized by fastening their extremities to the bed. MR images were acquired using a 3.0T whole-body scanner (Signa HDx, GE Healthcare, Milwaukee, WI, USA) combined with a 3-turn solenoid coil with the internal diameter of 35 mm. The following pulse sequence of 2D fast spin echo was used: TR = 4,000 ms, effective TE = 60.7 ms, echo train length = 8. Field of view was set to $4 \times 4\,\text{cm}^2$ with the matrix size of 256×192. Slice thickness was set to 1 mm. And the total acquisition time was 6 m 40 s. SPECT images were acquired as described above.

SPECT images were superimposed on obtained MR images so that images of markers attached on the cover of the special bed completely overlapped each other on both images.

3. Results

3.1. Biodistribution of ^{125}I-IPOS. The biodistribution of ^{125}I-IPOS in FM3A-bearing mice 24 h after the injection is shown in Figure 1.

^{125}I-IPOS was well accumulated in FM3A tumors implanted in the thigh of mice. The uptake ratio of ^{125}I-IPOS in FM3A tumors was 4.3 ± 0.68% of administered dose/g (mean SD) The reticuloendothelial organs such as liver and spleen showed strong uptake of this probe whereas neck including thyroid gland and muscle showed weak uptake. As a result, tumor-to-blood ratio was as high as 13.1.

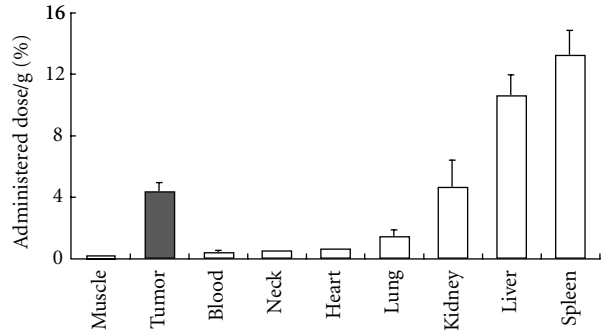

Figure 1: Biodistribution of ^{125}I-POS in FM3A-bearing mice. Administration dose of ^{125}I-POS 2.0 MBq, POS: 30 μg, tumor weight: 0.3–2.3 g, tumor uptake 4.3% AD/g, T/B: 13.1%($n = 5$).

3.2. Immunohistochemistry and Autoradiography of Excised Tumors. ARG tests revealed the heterogeneous ^{125}I-IPOS distribution in FM3A tumors (Figure 2). Fusion imaging of ARG and H&E staining indicated that ^{125}I-IPOS was distributed in viable areas. Fusion imaging of ARG and pimonidazole staining showed the intratumoral location of ^{125}I-IPOS partially overlapped with that of pimonidazole (arrows, Figure 2). But there was discrepancy between the intratumoral location of ^{125}I-IPOS and pimonidazole.

3.3. SPECT/CT Images of FM3A Tumors. As high radioactivity must be accumulated in target tissues to obtain images with excellent spatial resolution, ^{125}I-IPOS with high radioactivity of 22 MBq was administered to each mouse, and *in vivo* SPECT/CT images were acquired. The obtained SPECT images successfully depicted the heterogeneous distribution of ^{125}I-IPOS in FM3A tumors with excellent resolution (Figure 3).

After the acquisition of *in vivo* SPECT images, tumors were excised and weighed and their radioactivity was measured. The radioactivities of both tumors were 0.68 MBq (0.93 g, 0.73 MBq/g) and 1.19 MBq (1.37 g, 0.87 MBq/g), respectively. Then *ex vivo* tumor images were obtained. As *ex vivo* images were obtained with longer acquisition time than *in vivo* ones and there were no surrounding tissues around the tumor tissues that cause scattering of emitted photons in *ex vivo* images, image quality of *ex vivo* images was superior to that of *in vivo* ones. However, *in vivo* images also rather well depicted the heterogeneous intratumoral distribution of ^{125}I-IPOS (Figure 3).

As for the fusion imaging of SPECT and CT, since the tissue contrast inside tumors on CT images was poor, fusion images failed to provide useful information about the features of uptake sites of ^{125}I-POS.

3.4. Fusion Images of SPECT and MRI. MR images could provide more detailed tissue contrast than CT images. As

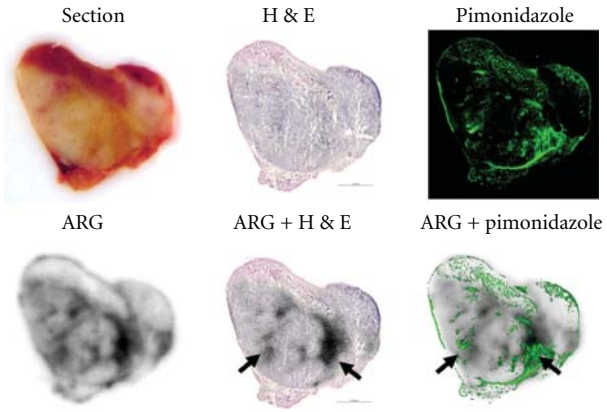

Figure 2: Intratumoral distribution of ^{125}I-POS, pimonidazole. Administration dose of ^{125}I-POS 2.0 MBq, POS: 30 μg, tumor weight: 0.3 g, tumor uptake 5.2%, slice thickness for ARG 20 μm, slice thickness for staining 6 μm.

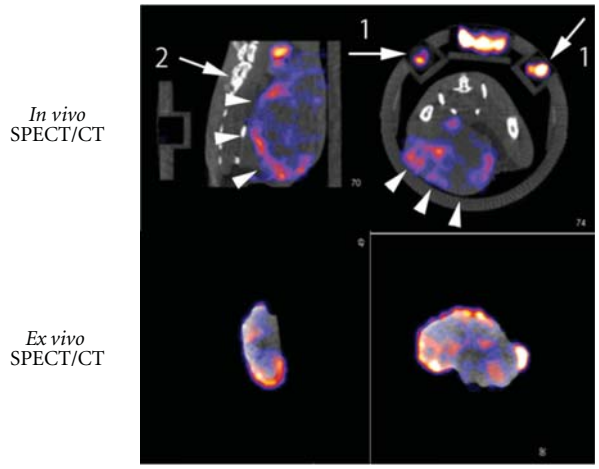

Figure 3: *In vivo* visualization of heterogeneous intratumoral distribution of POS by SPECT/CT. The comparison of *in vivo* SPECT images and *ex vivo* images. Upper raw: *in vivo* SPECT images, lower raw: *ex vivo* SPECT images, left column: sagittal sectional images, right column: axial sectional images. Arrows 1: markers for coregistration, arrows 2: vertebrae, and arrowheads: the tumor.

a result, the superimposition of SPECT images on MR images could give more information about the intratumoral distribution of ^{125}I-IPOS than that on CT images. Figure 4 shows the fusion images of ^{125}I-IPOS SPECT and MR images. As MR images are T2-weighted ones, high signal in the central area of the tumor suggests nonviable tumor tissues. And ^{125}I-IPOS does not accumulate in these high signal areas. SPECT-MR fusion images show that ^{125}I-IPOS is heterogeneously distributed in the low-signal area in the tumor, probably viable tumor areas.

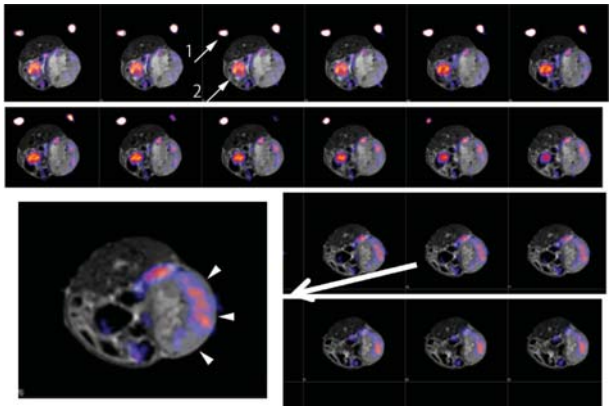

Figure 4: *In vivo* fusion imaging of intratumoral distribution of ^{125}I-POS and MR images. A representative image is enlarged. Arrows 1: markers, arrows 2: urinary bladder, and arrowheads: the tumor.

4. Discussion

We have investigated the precise evaluation of intratumoral localization of HIF activity to establish strategies to optimize cancer treatment.

As the intratumoral distribution of ^{125}I-POS evaluated by ARG partially corresponded with that of pimonidazole, the accumulation of ^{125}I-POS in tumor tissues would be related with tumor hypoxia. The discrepancy can be explained by the facts that HIF activates in the milder hypoxic areas, compared with hypoxic areas with high affinity to pimonidazole [6]. Currently, some PET probes such as ^{18}F-fluoromisonidazole (FMISO), ^{18}F-fluoro-azomycinarabino-furanoside (FAZA), and ^{62}Cu-diacetyl-bis(N4-methylthiosemicarbazone) (ATSM) are under the clinical investigation [4]. As the intratumoral distribution of these probes directly depends on the oxygen partial pressure in tumor tissues, like pimonidazole, they accumulate well in severe hypoxic areas. On the other hand, it is expected that ^{125}I-POS distributes in the tumor according to HIF activity. Our previous study actually demonstrated by an immunohistological method that intratumoral distribution of ^{125}I-IPOS was well correlated with HIF activity [13].

But it is difficult to clearly visualize this heterogeneity in intratumoral localization of ^{125}I-IPOS *in vivo*.

To resolve this difficult problem, we first examined high-resolution SPECT to precisely depict intratumoral distribution of HIF activity. Then, the obtained SPECT images were superimposed on morphological images such as CT and MRI to add anatomical information to intratumoral distribution of HIF activity.

It is necessary to acquire a lot of counts to obtain high-resolution SPECT images [15]. For this purpose, it is required to accumulate high counts of radioactive compounds in target tissues or to acquire images for a long time. The acquisition time is usually limited by effects of longitudinal changes of biodistribution of radioactive compounds and those of the movement of animal bodies. Therefore, it would be better to consider a method to

accumulate a lot of radioactive compounds in target tissues. More accurately speaking, radioactivity concentration in the target tissues should be high.

We synthesized ^{125}I-IPOS with radioactivity concentration of as high as 100 MBq/mL and injected this high activity of ^{125}I-IPOS (20 MBq/30 μg/0.2 mL) into tumor-bearing mice. As a result, ^{125}I-IPOS could be accumulated in tumor tissues with average radioactivity concentration of 0.8 MBq/g. When these mice were acquired by a SPECT scanner dedicated for small animal imaging, heterogeneous intratumoral distribution of ^{125}I-IPOS was successfully imaged *in vivo* with the total acquisition time of 30 minutes.

After that, *ex vivo* SPECT images of excised tumors were obtained. In *ex vivo* imaging, acquisition time was longer. And statistical noise is reduced by the suppression of scattering and attenuation of gamma rays due to the removal of tissues surrounding a tumor. That is why the image quality of *ex vivo* SPECT images is likely to be superior to of that *in vivo* ones. Considering these factors, *in vivo* SPECT images were never inferior to *ex vivo* ones in the light of the visualization of intratumoral heterogeneity.

Our previous experimental study using ^{111}In reported that the radioactivity concentration larger than 0.2 MBq/mL was needed to image the heterogeneous distribution of radiopharmaceuticals in tissues [16]. Since the energy of photons emitted from ^{125}I is much lower than that from ^{111}In [17], radioactivity concentration higher than 0.2 MBq/mL would be required to depict the heterogeneous distribution in tissues by ^{125}I-labeled compounds. The radioactivity concentration of 0.8 MBq/g, which we obtained in this study, was high enough to visualize the heterogeneous distribution of ^{125}I-labeled compounds.

In the light of the energy of emitted photons and half-life, ^{123}I-labeled compounds are more suitable for clinical nuclear medicine tests than ^{125}I ones. But, to obtain SPECT images with excellent spatial resolution in small animal studies, radioactive probes with high radioactive concentration and specific radioactivity are required [16]. In our country, it is, however, very difficult to get Na^{123}I with high specific radioactivity. That is why we used ^{125}I-labeled compounds in this study.

It is often difficult to evaluate the features of target tissues where radioactive compounds accumulated only by SPECT images due to the lack of anatomical information. The situation is same in the clinical practice. Therefore, superimposition of SPECT images on morphological images such as CT and MRI is actively examined to settle this problem.

In this study, as images of ^{125}I-IPOS were obtained using a SPECT/CT combined scanner, the fusion images of SPECT and CT could be easily obtained using preinstalled software. The superimposition on CT images provided the information about the position of the uptake of ^{125}I-IPOS. But additional information about the pathological features of ^{125}I-IPOS uptake areas was poor because the tissue contrast of CT images was not excellent and the change of CT number inside tumors was minimal.

On the other hand, fusion imaging of SPECT and MRI took a lot of effort. As MR images could not be obtained using a combined scanner with SPECT, it was required to image mice by putting them on a special bed with markers for coregistration [18]. Good tissue contrast of MRI, however, could provide important information about the features of tumor interiors. In this study, SPECT-MRI fusion images successfully suggested that ^{125}I-IPOS was distributed in mainly viable tumor tissues.

There are some problems that must be settled in SPECT-MRI fusion imaging: the accuracy of coregistration, the distortion of images, and so on. But SPECT-MRI fusion images can provide more useful information about the features of tumor interiors than SPECT-CT images. Therefore, SPECT-MRI fusion imaging should be more actively investigated.

The clinical application of fusion images of radioactive IPOS SPECT and morphological imaging tests, especially MRI, will be an important research project in the future. It is expected that the fusion images of radioactive IPOS SPECT and CT or MRI will contribute toward overcoming the resistance to cancer therapy such as radiotherapy and chemotherapy.

5. Conclusion

High-resolution SPECT images successfully demonstrated heterogeneous intratumoral distribution of ^{125}I-IPOS *in vivo*. The superimposition of SPECT images on CT images, more favorably MR images, would be useful to understand the features of heterogeneous intratumoral expression of HIF activity *in vivo*.

Conflict of Interests

The authors declare no conflict of interests.

Acknowledgments

This study was partially supported by Grants-in-Aid from the Japanese Ministry of Education, Culture, Sports, Science and Technology (MEXT) and the Japan Society for the Promotion of Science (JSPS), Health Labour Sciences Research Grant (Research on 3rd Term Comprehensive 10-year Strategy for Cancer Control) from the Japanese Ministry of Health, Labour and Welfare (MHLW) and the National Cancer Center Research and Development Fund.

References

[1] M. Chivukula, R. Bhargava, A. Brufsky, U. Surti, and D. J. Dabbs, "Clinical importance of HER2 immunohistologic heterogeneous expression in core-needle biopsies vs resection specimens for equivocal (immunohistochemical score 2+) cases," *Modern Pathology*, vol. 21, no. 4, pp. 363–368, 2008.

[2] K. Kubota, "From tumor biology to clinical PET: a review of positron emission tomography (PET) in oncology," *Annals of Nuclear Medicine*, vol. 15, no. 6, pp. 471–486, 2001.

[3] R. L. Wahl, L. E. Quint, R. D. Cieslak, A. M. Aisen, R. A. Koeppe, and C. R. Meyer, "'Anatometabolic' tumor imaging: fusion of FDG PET with CT or MRI to localize foci of increased activity," *Journal of Nuclear Medicine*, vol. 34, no. 7, pp. 1190–1197, 1993.

[4] A. R. Padhani, K. A. Krohn, J. S. Lewis, and M. Alber, "Imaging oxygenation of human tumours," *European Radiology*, vol. 17, no. 4, pp. 861–872, 2007.

[5] P. Vaupel and A. Mayer, "Hypoxia in cancer: significance and impact on clinical outcome," *Cancer and Metastasis Reviews*, vol. 26, no. 2, pp. 225–239, 2007.

[6] S. Kizaka-Kondoh and H. Konse-Nagasawa, "Significance of nitroimidazole compounds and hypoxia-inducible factor-1 for imaging tumor hypoxia," *Cancer Science*, vol. 100, no. 8, pp. 1366–1373, 2009.

[7] J. D. Chapman, "Measurement of tumor hypoxia by invasive and non-invasive procedures: a review of recent clinical studies," *Radiotherapy and Oncology*, vol. 20, no. 1, supplement, pp. 13–19, 1991.

[8] G. L. Semenza, "Intratumoral hypoxia, radiation resistance, and HIF-1," *Cancer Cell*, vol. 5, no. 5, pp. 405–406, 2004.

[9] H. Harada, S. Kizaka-Kondoh, and M. Hiraoka, "Optical imaging of tumor hypoxia and evaluation of efficacy of a hypoxia-targeting drug in living animals," *Molecular Imaging*, vol. 4, no. 3, pp. 182–193, 2005.

[10] T. Kuchimaru, T. Kadonosono, S. Tanaka, T. Ushiki, M. Hiraoka, and S. Kizaka-Kondoh, "In vivo imaging of HIF-active tumors by an oxygen- dependent degradation protein probe with an interchangeable labeling system," *PLoS ONE*, vol. 5, no. 12, article e15736, 2010.

[11] T. Kudo, M. Ueda, Y. Kuge et al., "Imaging of HIF-1-active tumor hypoxia using a protein effectively delivered to and specifically stabilized in HIF-1-active tumor cells," *Journal of Nuclear Medicine*, vol. 50, no. 6, pp. 942–949, 2009.

[12] M. Ueda, T. Kudo, Y. Kuge et al., "Rapid detection of hypoxia-inducible factor-1-active tumours: pretargeted imaging with a protein degrading in a mechanism similar to hypoxia-inducible factor-1α," *European Journal of Nuclear Medicine and Molecular Imaging*, vol. 37, no. 8, pp. 1566–1574, 2010.

[13] M. Ueda, T. Kudo, Y. Mutou et al., "Evaluation of ^{125}I-IPOS as a molecular imaging probe for hypoxia-inducible factor-1-active regions in a tumor: comparison among single-photon emission computed tomography/X-ray computed tomography imaging, autoradiography, and immunohistochemistry," *Cancer Science*, vol. 102, no. 11, pp. 2090–2096, 2011.

[14] C. F. Foulon, K. L. Alston, and M. R. Zalutsky, "Synthesis and preliminary biological evaluation of (3-iodobenzoyl) norbiotinamide and ((5-iodo-3-pyridinyl)carbonyl)norbiotinamide: two Radioiodinated biotin conjugates with improved stability," *Bioconjugate Chemistry*, vol. 8, no. 2, pp. 179–186, 1997.

[15] S. R. Cherry, J. A. Sorenson, and M. E. Phelps, *Image Quality in Nuclear Medicine*, Physics in Nuclear Medicine, Saunders, Philadelphia, Pa, USA, 2003.

[16] I. O. Umeda, K. Tani, K. Tsuda et al., "High resolution SPECT imaging for visualization of intratumoral heterogeneity using a SPECT/CT scanner dedicated for small animal imaging," *Annals of Nuclear Medicine*, vol. 26, no. 1, pp. 67–76, 2012.

[17] F. J. Beekman, D. P. McElroy, F. Berger, S. S. Gambhir, E. J. Hoffman, and S. R. Cherry, "Towards in vivo nuclear microscopy: iodine-125 imaging in mice using micro-pinholes," *European Journal of Nuclear Medicine*, vol. 29, no. 7, pp. 933–938, 2002.

[18] M. Yamaguchi, D. Suzuki, R. Shimizu et al., "Precise co-registration of SPECT and MRI for small animal imaging using a common animal bed with external references: visualization of macrophage distribution within inflammatory lymph nodes," in *Proceedings of 18th Meeting of the International Society for Magnetic Resonance in Medicine*, vol. 3963, 2010.

Hindawi Publishing Corporation
Journal of Biomedicine and Biotechnology
Volume 2012, Article ID 828139, 9 pages
doi:10.1155/2012/828139

Research Article

Development of ^{99m}Tc-N4-NIM for Molecular Imaging of Tumor Hypoxia

Mohammad S. Ali,[1] Fan-Lin Kong,[1] Alex Rollo,[1] Richard Mendez,[1] Saady Kohanim,[1] Daniel Lee Smith,[2] and David J. Yang[1]

[1] *Department of Experimental Diagnostic Imaging, The University of Texas MD Anderson Cancer Center, Houston, TX 77030, USA*
[2] *Department of Radiation Physics, The University of Texas MD Anderson Cancer Center, Houston, TX 77030, USA*

Correspondence should be addressed to Mohammad S. Ali, mohammad.ali@mdanderson.org

Received 31 January 2012; Revised 24 March 2012; Accepted 1 April 2012

Academic Editor: Yasuhisa Fujibayashi

The nitro group of 2-nitroimidazole (NIM) enters the tumor cells and is bioreductively activated and fixed in the hypoxia cells. 1,4, 8,11-tetraazacyclotetradecane (N4) has shown to be a stable chelator for ^{99m}Tc. The present study was aimed to develop ^{99m}Tc-cyclam-2-nitroimidazole (^{99m}Tc-N4-NIM) for tumor hypoxia imaging. N4-NIM precursor was synthesized by reacting N4-oxalate and 1,3-dibromopropane-NIM, yielded 14% (total synthesis). Cell uptake of ^{99m}Tc-N4-NIM and ^{99m}Tc-N4 was obtained in 13762 rat mammary tumor cells and mesothelioma cells in 6-well plates. Tissue distribution of ^{99m}Tc-N4-NIM was evaluated in breast-tumor-bearing rats at 0.5–4 hrs. Tumor oxygen tension was measured using an oxygen probe. Planar imaging was performed in the tumor-bearing rat and rabbit models. Radiochemical purity of ^{99m}Tc-N4-NIM was >96% by HPLC. Cell uptake of ^{99m}Tc-N4-NIM was higher than ^{99m}Tc-N4 in both cell lines. Biodistribution of ^{99m}Tc-N4-NIM showed increased tumor-to-blood and tumor-to-muscle count density ratios as a function of time. Oxygen tension in tumor tissue was 6–10 mmHg compared to 40–50 mmHg in normal muscle tissue. Planar imaging studies confirmed that the tumors could be visualized clearly with ^{99m}Tc-N4-NIM in animal models. Efficient synthesis of N4-NIM was achieved. ^{99m}Tc-N4-NIM is a novel hypoxic probe and may be useful in evaluating cancer therapy.

1. Introduction

Recent studies demonstrated that the hypoxic environment induces more malignant neoplastic phenotypes [1]. Disruption of oxygen delivery to tumors could diminish apoptotic potential and increase the chemotherapy/radiation resistance, while an improvement in oxygen delivery to tumors increases tumor sensitivity to radiation and chemotherapy [2–4]. Due to its significant prognostic and therapeutic implication, efforts have been made to invent efficient noninvasive methods to assess the presence and extent of tumor hypoxia because information on the hypoxic fraction in tumors could aid to reveal the mechanisms of aggressive behavior. The success of the endeavor to noninvasively detect the hypoxic fraction of tumor by nuclear molecular imaging such as single-photon emission computed tomography (SPECT) allows physicians to select patients for additional or alternative treatment regimens that may circumvent or overcome the ominous impact of tumor hypoxia and improve disease control [5].

The nitro group of nitroimidazole is enzymatically reduced by ribonucleoside reductase within viable hypoxic cells. This mechanism is well understood through numerous *in vitro* and *in vivo* studies from the past three decades [6]. In aerobic cells the reduced nitroimidazole is immediately reoxidized and washed out rapidly. On the contrary, in cells with low oxygen concentration the reoxidation is slowed, which allows further reductive reactions to take place. This leads to the formation of reactive products that could covalently bind to cell components and thus diffuse more slowly out of the tissue in an oxygen-dependent manner [7]. ^{18}F-Fluoromisonidazole (^{18}F-FMISO) and ^{18}F-fluoroerythronitroimidazole (^{18}F-FETNIM), 2-nitroimidazole analogues, have been used with PET to evaluate tumor

hypoxia, but the chemistries are dependent on a cyclotron to produce ^{18}F in addition to slow serum clearances [8–10].

In an attempt to identify efficient and clinically user-friendly chelator-based hypoxia tracers, our team has developed a new class of ^{99m}Tc hypoxia SPECT tracers based on the nitroimidazole backbone. The nitrogen, oxygen, and sulfur combination has shown to be stable chelators for radiometals [11–18]. The chelator used in this paper is 1,4,8,11-tetraazabicyclohexadecane (N4) which has shown to be a stable chelator for ^{99m}Tc [11, 12]. In addition, N4-chemistry could be easily modified and selectively reacted with halogenated homing compounds. In this paper, the potential use of ^{99m}Tc-N4-NIM as tumor hypoxic imaging agent was evaluated. The advantage of ^{99m}Tc-N4-nitroimidazole over ^{18}F-FMISO and ^{18}F-FETNIM is its easier chemistry and its water solubility that may lead to the rapid clearance of unbounded tracers after intravenous injection.

2. Materials and Methods

2.1. Chemicals and Analysis. All chemicals of analytical grade and solvents of high performance liquid chromatography (HPLC) grade were obtained from Sigma-Aldrich (St. Louis, MO, USA). Nuclear magnetic resonance (NMR) was performed on a Bruker 300-MHz spectrometer (Bruker BioSpin Corporation, Billerica, MA, USA), and mass spectra were performed on a Waters Q-TOF Ultima mass spectrometer (Waters, Milford, MA, USA) at the chemistry core facility at The University of Texas MD Anderson Cancer Center (Houston, TX, USA). Sodium pertechnetate ($Na\,^{99m}TcO_4$) was obtained from a ^{99}Mo/^{99m}Tc generator (Covidien, Mansfield, MA, USA).

2.2. Sodium Salt of 2-Nitroimidazole (Compound 1). The synthetic scheme of N4-NIM is shown in Figure 1. One molar equivalent of NaOH 1 M (0.3864 g, 9.66 mmol, 9.66 mL) was added to 2-nitroimidazole (1.09 g, 9.66 mmol) and warmed 30 minutes at 50°C to dissolve it. If the compound was not dissolved in the solution then NaOH was added drop by drop until the solid was dissolved completely and we continue heating for 15 minutes more. Water was removed on rotary evaporator. Crude compound was dissolved in minimum quantity of water, filtered, and lyophilized. Yield: 5.31 g, (90%).

2.3. Bromopropane Nitroimidazole (Compound 2). In two-neck flask one molar equivalent of Sodium salt of 2-nitroimidazole (2.00 g, 14.7 mmol) in solid form was added in 40 mL of acetonitrile (anhydrous) to dissolve it, then 18-crown-6 (3.88 g, 14.7 mmol) was added to this mixture. In nitrogen atmosphere 12.5 molar equivalent of 1,3-dibromopropane (18.65 mL, 183.76 mmol, 37.09 g) was added to the reaction mixture. The reaction mixture was then refluxed in a nitrogen environment at 50°C overnight. The reaction was filtered to purify the precipitate of NaBr using the 0.22 μM filter paper. Soon after the solvent was evaporated, the crude compound was purified by column chromatography with a $CHCl_3 : CH_3OH$ mixture (v : v, 9 : 1). Yield: 10.45 g (90%).

2.4. N^1, N^4-Dioxylyl-1,4,8,11-Tetraazacyclotetradecane (Compound 3). 1,4,8,11-Tetraazacyclotetradecance (N4) (2.997 g, 14.974 mmol) was dissolved in 50 mL of ethanol (anhydrous) ethanol, and after heating at 50°C, diethyl oxalate (2.188 g, 14.974 mmol, 2.03 mL) was added. The reaction mixture was refluxed for 18 hours at 75°C. The solvent was rotary evaporated and the crude product was dissolved in minimum quantity of ethanol and the turbid solution was filtered with 0.22 μM filter. Crude compound was dissolved in minimum amount of anhydrous ethanol and kept rotating on rotary evaporator for 40 minutes at 40–50°C. The compound was crystallized by adding 200 mL acetone (anhydrous) leaving the solution overnight in the refrigerator to yield white crystals of N^1, N^4-dioxylyl-1,4,8,11-tetraazacyclotetradecane. Yield: 8.64 g (52.04%) Ms (m/z) 255.19 $[M]^+$.

2.5. 1-[3-(2-Nitroimidazole-1-yl)propyl]-(N^1,N^4-Dioxylyl-1,4,8,11-Tetraazacyclotetradecane) (Compound 4). N^1,N^4-dioxylyl-1,4,8,11-tetraazacyclotetradecane (0.5746 g, 2.259 mmol) was placed into the two-neck flask and dissolved in 25 mL of DMF (anhydrous). While heating the solution at 50°C, bromonitroimidazole (0.5329 g, 2.259 mmol) dissolved in 2.0 mL of DMF (anhydrous) was added to the reaction mixture. After adding K_2CO_3 (anhydrous) (0.7805 g; 5.6475 mmol) in 2.5 molar equivalent solid to the reaction mixture, it was refluxed at 70°C overnight. Crude compound was filtered using 0.22 μM filter paper and checked by TLC in chloroform: methanol in an 8 : 2 solvent system. Solvent was then evaporated and crude compound was purified by column chromatography in (8 : 2) of chloroform and methanol. Yield: 6.96 g, (75.86%). Ms (m/z) 408.30 $[M]^+$.

2.6. 1-[3-(2-Nitroimidazole-1-yl)propyl]-(1,4,8,11-Tetraazacyclotetradecane) (Compound 5, N4-NIM). To a 1 equivalent solution of (N4OxaNIM) N^1,N^4-dioxylyl-1,4,8,11-tetraazacyclotetradecane (0.100 g; 0.246 mmol) in 1 mL of water, 10 equivalents of 10 N NaOH (0.246 mL) were added, stirred, and refluxed over night at 75°C. The solvent was evaporated under vacuum, giving off white solid. The crude compound was dissolved in minimum quantity of water and filtered, then purified by sephadex G25 column. The fractions were lyophilized and collected by checking ^{1}H NMR as off white solid. Yield: 0.045 g (52.32%).

2.7. Radiolabeling of N4-NIM with ^{99m}Tc. Radiosynthesis of ^{99m}Tc-N4-NIM was achieved by adding a required amount of ^{99m}Tc-pertechnetate into a kit containing the lyophilized residue of N4-NIM (1 mg) and $SnCl_2$ (100 μg). Final pH of the preparation was 5.5–7.4. Radiochemical purity was determined by TLC and HPLC. Radio-TLC (Waterman No. 1) was obtained by eluting ^{99m}Tc-N4-NIM with acetone and saline, respectively. Radio-HPLC (Waters) was obtained by eluting ^{99m}Tc-N4-NIM on a C-18 reverse phase column (4.5 × 250 mm, 5 μm diameter, Zorbax Extend C 18, Agilant Technologies, Santa Clara, CA, USA) with 8 : 2 acetonitrile: water solution (v : v) using a flow rate of 0.5 mL/minute

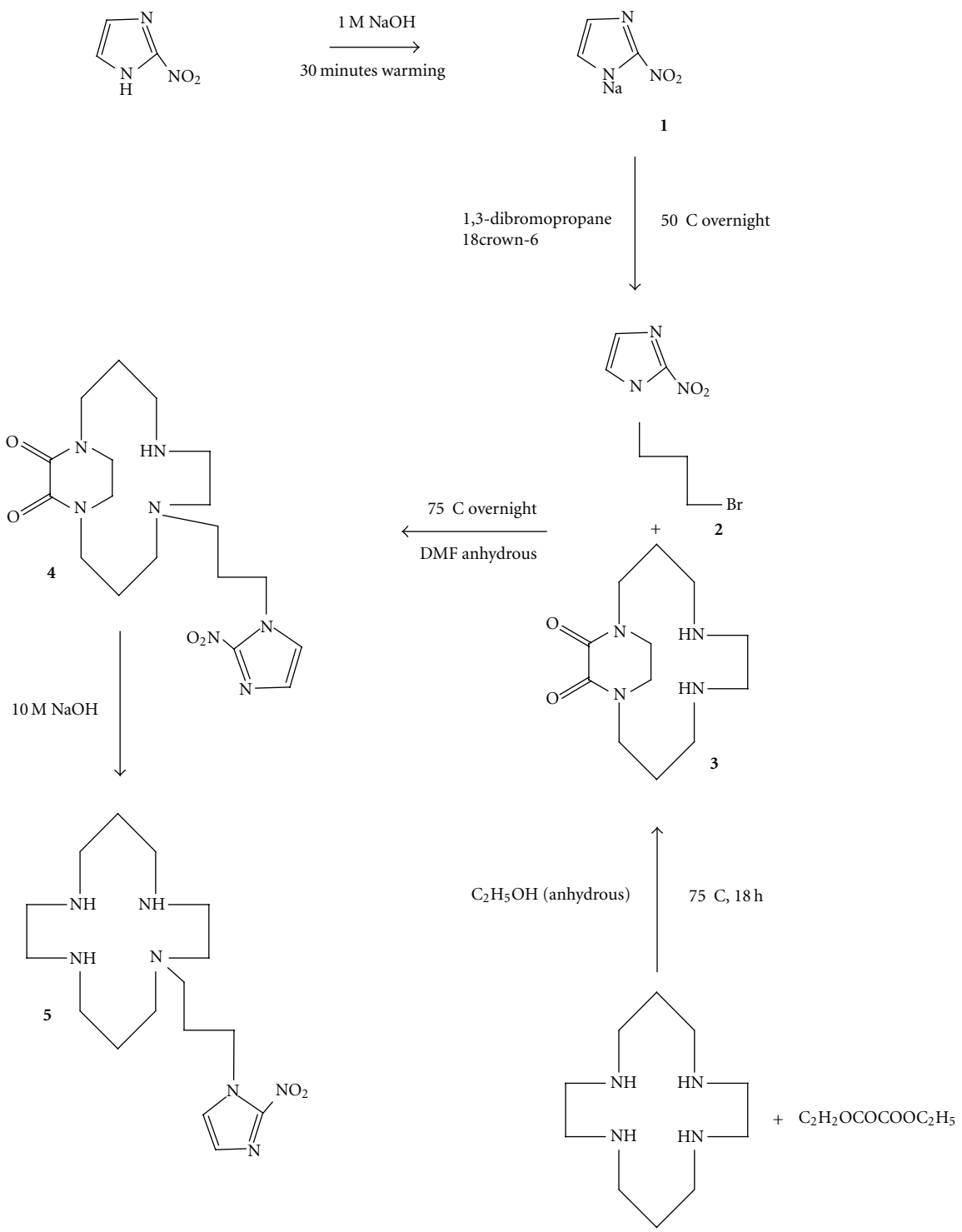

Figure 1: Synthetic scheme of N4-NIM.

at UV 210 and 254 nm. The concentration of ^{99m}Tc-N4-NIM was 1.0 mg/1.96 mCi/500 μL H_2O. The concentration of unlabeled N4-NIM was 1.7 mg/200 μL H_2O.

2.8. Cellular Uptake of ^{99m}Tc-N4-NIM. The 13762 mammary cancer cells and mesothelioma cells (IL-45) were plated to 6-well tissue culture plates that contained 2×10^5 cells/well and incubated with ^{99m}Tc-N4-NIM (0.05 mg/well, 8 μCi/well) and ^{99m}Tc-N4 (0.025 mg/well, 8 μCi/well) for 0–4 hours. After incubation, cells were washed with ice-cold phosphate-buffered solution twice and detached using a treatment of 0.5 mL of trypsin for 5 minutes. Cells were then collected and the radioactivity of the cells was measured in triplicate with a gamma counter. Radioactivity was expressed as mean ± standard deviation percent of cellular uptake (%Uptake).

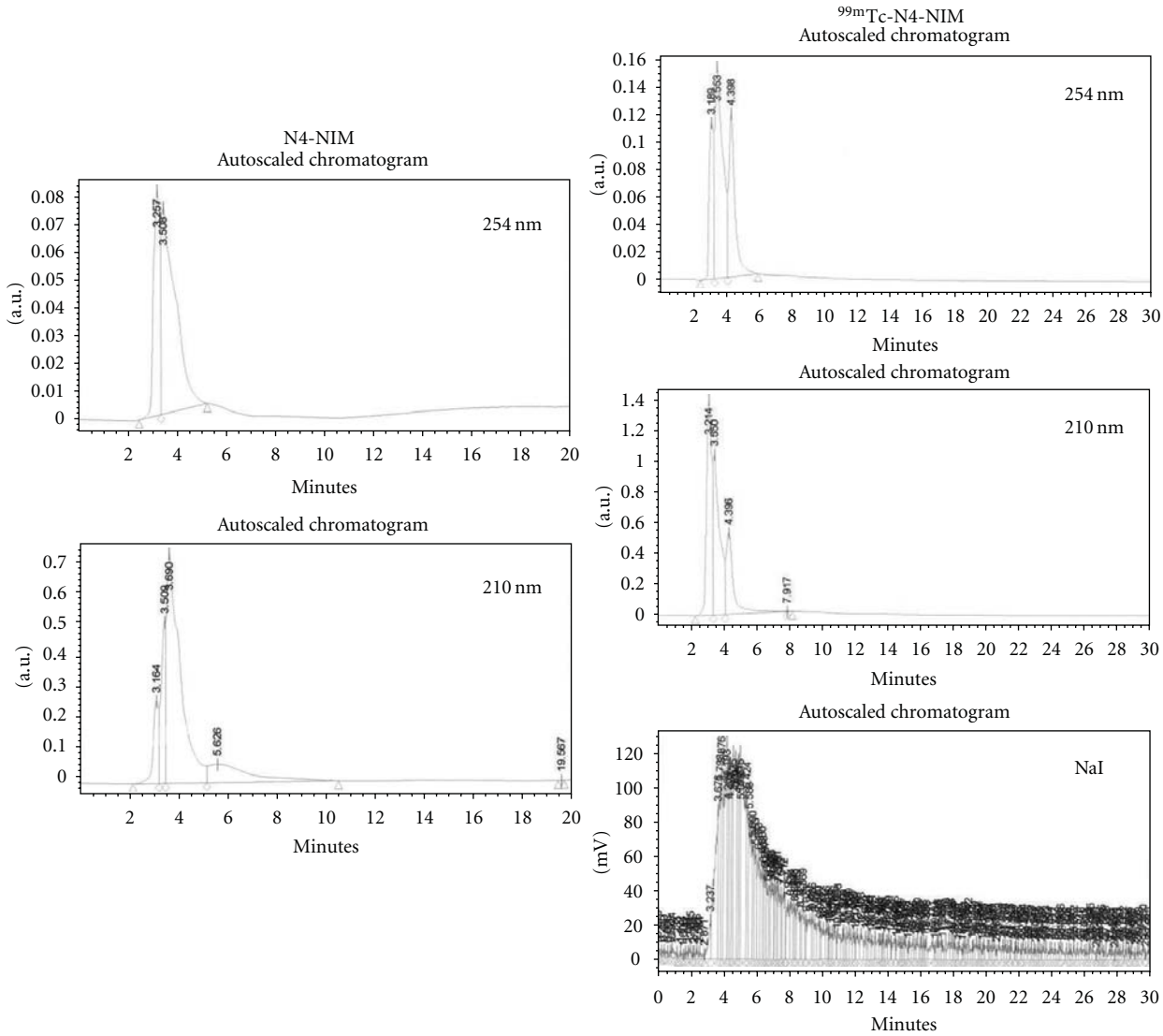

Figure 2: HPLC analysis of N4-NIM (left) and ^{99m}Tc-N4-NIM (right). The purity of both N4NIM and ^{99m}Tc-N4-NIM was 96%.

2.9. Biodistribution and Radiation Dosimetry Estimates of ^{99m}Tc-N4-NIM. The animal experiments were carried out in compliance with the relevant national laws relating to the conduct of animal experimentation. The animal protocol was approved by The University of Texas M. D. Anderson Cancer Center Animal Care and Use Committee (IACUC). Female Fischer 344 rats (150 ± 25 g) (Harlan Sprague-Dawley, Indianapolis, IN) were inoculated subcutaneously with 0.1 mL of mammary tumor cells from the 13762 tumor cell line suspension (10^6 cells/rat, a tumor cell line specific to Fischer rats) into the hind legs using 25-gauge needles. Studies were performed 14 to 17 days after implantation when tumors reached approximately 1 cm diameter. The rats were divided into 3 groups and each rat was injected intravenously with 25 ± 0.5 μCi of ^{99m}Tc-N4-NIM and ^{99m}Tc-N4. Each group was examined at 1 of 3 time points (0.5, 2, or 4 hours after injection). At each time point, the rats were killed and the selected tissues were excised, weighed, and measured for radioactivity by gamma counter. For each sample, radioactivity was expressed as mean percentage of the injected dose per gram of tissue wet weight (%ID/g). Counts from a 1/10 diluted sample of the original injection were used as a reference.

Tumor/nontarget tissue count density ratios were calculated from the corresponding %ID/g values. Olinda software (version 1.1; Vanderbilt University, Nashville, TN, USA) was used to determine dosimetry, based upon preclinical source organ residence time estimates as followed: rat organ distribution data was processed using in-house software to determine residence times (τ) based on AUC. The data was then converted to human residence time estimates using the correction factor for each organ, and subsequent τ values were entered into Olinda software to generate human dose estimates.

2.10. Polarographic pO_2 Measurements of Mammary Tumors. To confirm tumor hypoxia, intratumoral pO_2 measurements

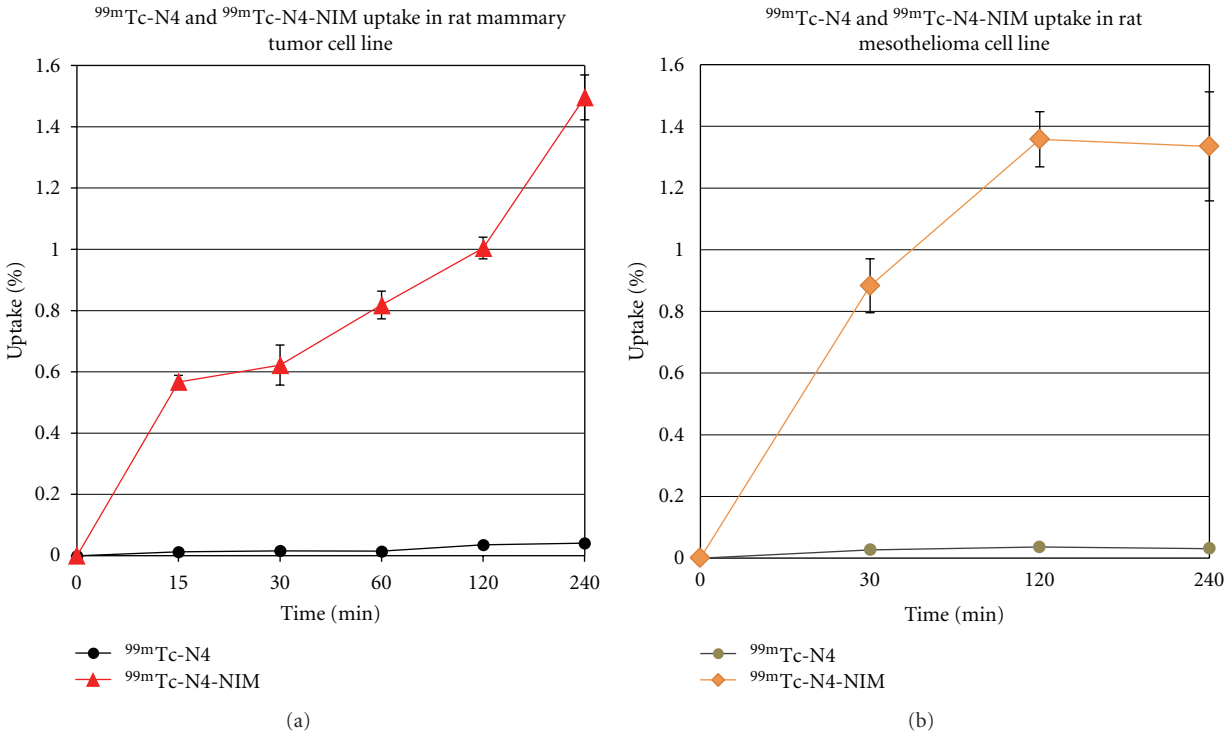

Figure 3: *In vitro* cell uptake studies using rat mammary cancer cells and mesothelioma cells revealed that ^{99m}Tc-N4-NIM had high uptake in both cell lines.

were performed using the Eppendorf computerized histographic system. Twenty to twenty-five pO_2 measurements along each of two to three linear tracks were performed at 0.4 mm intervals on each tumor (40–75 measurements total). Tumor pO_2 measurements were made on three tumor-bearing rats. Using an on-line computer system, the pO_2 measurements of each track were expressed as absolute values relative to the location of the measuring point along the track and as the relative frequencies within a pO_2 histogram between 0 and 100 mmHg with a class width of 2.5 mm.

2.11. Planar Scintigraphic Imaging in Tumor-Bearing Models. Two animal models were created. For Rabbit model, the VX-2 tumor mass was inoculated (im) to the thigh region of male New Zealand white rabbits (2 kg). For rat model, cells from the mammary tumor cell line 13762, suspended in phosphate-buffered solution (10^5 cells/0.1 mL solution per rat), were injected subcutaneously into the right calf muscle of female Fischer 344 rats. Planar scintigraphic imaging of ^{99m}Tc-N4-NIM was performed 12–14 days after inoculation when tumors reached approximately 1 cm in diameter. The animals were anesthetized and injected intravenously with ^{99m}Tc-N4-NIM (0.3 mg/rat, 300 μCi/rat; 1.5 mCi/rabbit), and images were acquired at 30, 120, and 240 minutes after administration of tracers. Planar scintigraphic images were obtained using M-CAM (Siemens Medical Solutions, Hoffman Estates, IL, USA) equipped with a low-energy high-resolution collimator. Computer-outlined regions of interest (ROIs in counts per pixel) between tumor and muscle tissue were used to calculate tumor-to-muscle (T/M) ratios. Percent of injected dose (%ID) in the tumor was also calculated from the reference standard, which was 1/10 of the original injection activity of ^{99m}Tc-N4-NIM.

3. Results

3.1. Chemistry and Radiochemistry. The synthetic scheme is shown in Figure 1. The total synthesis yield of precursor N4-NIM via our 5-step procedure was 14%. The structure and purity of N4-NIM were confirmed by ^{1}H- and ^{13}C-NMR, mass spectra, and HPLC. The N4-NIM ^{1}H-NMR results (D_2O δ, ppm) were as follows: 8.25 (s, H, imidazole ring), 3.74 (s, H, imidazole ring), 3.17–3.25 (t, 2H,CH_2 of propyl group), 3.05–2.91 (t, 2H, CH_2 of propyl group), 2.26–2.76 (m, 2H, CH_2 of propyl group), 2.28–2.48 (m, 14H, CH_2 of N4 ring), and 1.38–1.68 (m, 6H, CH_2 of N4 ring). ^{13}C-NMR results (D_2O δ, ppm) were as follows: 180.27, 173.13, 164.13, 61.48, 54.13, 51.73, 50.20, 49.45, 48.29, 46.61, 24.64, 23.76, and 22.64. Ms (m/z) 377.24 $[M]^+$. In radio-TLC analysis, ^{99m}Tc-N4-NIM did not migrate either in saline or acetone solvent. HPLC analysis showed that the retention time for N4-NIM was 3.506 min and 3.690 min at UV-254 and 210 nm, respectively. N4-NIM was labeled with ^{99m}Tc successfully with high radiochemical purity (>96%) (Figure 2). HPLC analysis showed the retention time for ^{99m}Tc-N4-NIM was 3.663 min (UV-254 nm), 3.650 min (UV-210 nm), and 4.200 min (NaI detector). Because ^{99m}Tc-N4-NIM is a kit product and labeled without any further purification, its radiochemical yield was assumed to be identical to its radio-chemical purity.

Table 1: Biodistribution of ^{99m}Tc-N4 in mammary tumor-bearing rats.

	% of injected dose per gram of tissue weight (n = 3/time, interval, iv)		
	30 min	120 min	240 min
Blood	0.23 ± 0.009	0.04 ± 0.002	0.02 ± 0.002
Heart	0.07 ± 0.005	0.01 ± 0.001	0.01 ± 0.000
Lung	0.20 ± 0.011	0.05 ± 0.002	0.03 ± 0.001
Thyroid	0.25 ± 0.011	0.03 ± 0.002	0.02 ± 0.001
Pancreas	0.07 ± 0.007	0.02 ± 0.002	0.02 ± 0.001
Liver	2.98 ± 0.083	1.14 ± 0.018	0.79 ± 0.026
Spleen	0.35 ± 0.026	0.37 ± 0.007	0.39 ± 0.020
Kidney	2.56 ± 0.101	1.11 ± 0.045	0.65 ± 0.028
Stomach	0.12 ± 0.005	0.02 ± 0.001	0.01 ± 0.000
Intestine	0.25 ± 0.004	0.39 ± 0.048	0.14 ± 0.003
Uterus	0.16 ± 0.014	0.02 ± 0.001	0.01 ± 0.001
Tumor	0.09 ± 0.004	0.03 ± 0.003	0.02 ± 0.001
Muscle	0.05 ± 0.002	0.01 ± 0.000	0.01 ± 0.000
Bone	0.07 ± 0.001	0.02 ± 0.001	0.01 ± 0.000
Brain	0.01 ± 0.000	0.00 ± 0.000	0.00 ± 0.000
Tumor/blood	0.40 ± 0.002	0.78 ± 0.044	0.70 ± 0.008
Tumor/muscle	1.96 ± 0.015	5.32 ± 0.402	3.35 ± 0.147
Tumor/brain	6.19 ± 0.365	11.06 ± 0.667	11.93 ± 0.675

Value shown represents the mean ± standard deviation of data from 3 animals.

3.2. In Vitro Cellular Uptake Assays. The cellular uptake kinetics of ^{99m}Tc-N4-NIM and ^{99m}Tc-N4 in rat mammary tumor cells and rat mesothelioma cells are shown in Figure 3. The uptake for ^{99m}Tc-N4-NIM increased dramatically up to 240 minutes, but this was not the case for the ^{99m}Tc-N4, suggesting that ^{99m}Tc-N4-NIM can enter tumor cells specifically and accumulate rapidly.

3.3. Biodistribution and Radiation Dosimetry Estimates of ^{99m}Tc-N4-NIM. Tissue distribution of ^{99m}Tc-N4 and ^{99m}Tc-N4-NIM is shown in Tables 1 and 2. Biodistribution studies showed that tumor/blood and tumor/muscle count density ratios at 0.5–4 hr gradually increased for ^{99m}Tc-N4-NIM (Table 2). No significant uptake in thyroid and stomach suggests *in vivo* stability of ^{99m}Tc-N4-NIM. The optimal tumor imaging time for ^{99m}Tc-N4-NIM is at 2 hr post-administration of ^{99m}Tc-N4-NIM. Although tumor/blood and tumor/muscle count density ratios at 0.5–4 hr gradually increased for ^{99m}Tc-N4, yet there was almost no tumor uptake (Table 1). Based upon preclinical studies, dosimetry of ^{99m}Tc-N4-NIM was estimated from MIRDose. It is safe to use ^{99m}Tc-N4-NIM in human because the whole body, liver, and effective dose equivalent for the proposed single dose at 20 mCi of ^{99m}Tc-N4-NIM were less than the limits for 3 rem annual and 5 rem total dose equivalent, and other organs of single dose at 5 rem annual and total dose equivalent at 15 rem if the subject did not have any other radiation exposure (Table 3).

Table 2: Biodistribution of ^{99m}Tc-N_4-NIM in mammary tumor-bearing rats.

	% of injected dose per gram of tissue weight (n = 3/time, interval, iv)		
	30 min	2 h	4 h
Blood	0.76 ± 0.06	0.20 ± 0.01	0.16 ± 0.01
Heart	0.26 ± 0.03	0.07 ± 0.01	0.04 ± 0.00
Lung	0.58 ± 0.06	0.17 ± 0.00	0.10 ± 0.00
Thyroid	0.71 ± 0.06	0.17 ± 0.01	0.08 ± 0.00
Pancreas	0.22 ± 0.03	0.06 ± 0.00	0.04 ± 0.01
Liver	0.88 ± 0.05	0.84 ± 0.03	0.51 ± 0.02
Spleen	0.74 ± 0.13	0.42 ± 0.01	0.70 ± 0.02
Kidney	4.92 ± 0.89	4.42 ± 0.06	1.33 ± 0.10
Stomach	0.37 ± 0.04	0.09 ± 0.01	0.03 ± 0.00
Intestine	0.33 ± 0.04	0.15 ± 0.07	0.04 ± 0.01
Uterus	0.61 ± 0.16	0.20 ± 0.11	0.08 ± 0.01
Tumor	0.52 ± 0.02	0.20 ± 0.00	0.08 ± 0.00
Muscle	0.18 ± 0.01	0.04 ± 0.00	0.02 ± 0.00
Bone	0.22 ± 0.08	0.14 ± 0.02	0.03 ± 0.00
Brain	0.04 ± 0.00	0.01 ± 0.00	0.01 ± 0.00
Tumor/blood	0.69 ± 0.02	1.01 ± 0.05	0.98 ± 0.06
Tumor/muscle	2.86 ± 0.19	5.69 ± 0.40	4.88 ± 0.56
Tumor/brain	12.74 ± 2.26	15.51 ± 2.16	15.10 ± 2.47

Values shown represent the mean ± standard deviation of data from 3 animals.

Table 3: Radiation dose estimates for the reference adult for ^{99m}Tc-N4-NIM.

Target organ	rad/mCi	Human dose (mCi)	rad
Organs (5 rem annual/15 rem total)			
Adrenals	$6.56E-03$	20	0.131
Brain	$5.03E-04$	20	0.010
Breasts	$1.22E-03$	20	0.024
Gall bladder wall	$4.28E-03$	20	0.086
Lli wall	$1.53E-03$	20	0.031
Small int	$2.97E-03$	20	0.059
Stomach	$4.19E-03$	20	0.084
Uli wall	$2.74E-03$	20	0.055
Heart wall	$5.50E-03$	20	0.110
Kidneys	$8.20E-02$	20	1.640
Liver	$4.41E-03$	20	0.088
Lungs	$5.05E-03$	20	0.101
Muscle	$1.46E-03$	20	0.029
Pancreas	$8.44E-03$	20	0.169
Bone surfaces	$4.11E-03$	20	0.082
Skin	$8.81E-04$	20	0.018
Testes	$8.11E-04$	20	0.016
Thymus	$1.69E-03$	20	0.034
Thyroid	$9.93E-04$	20	0.020
Urine bladder wall	$1.18E-03$	20	0.024
Uterus	$1.65E-03$	20	0.033
Eff dose	$3.41E-03$	20	0.068
Blood-forming organs (3 rem annual/5 rem total)			
Ovaries	$1.67E-03$	20	0.033
Red marrow	$2.15E-03$	20	0.043
Spleen	$3.27E-02$	20	0.654
Eff dose eq	$9.73E-03$	20	0.195
Total body	$2.26E-03$	20	0.045

3.4. Polarographic Oxygen Microelectrode pO_2 Measurements. Intratumoral pO_2 measurements of mammary tumors indicated the tumor oxygen tension ranged 4.6 ± 1.4 mmHg as compared to normal muscle of 35 ± 10 mmHg. The data indicated that the tumors were hypoxic.

3.5. Planar Scintigraphic Imaging in Tumor-Bearing Models. The selected planar scintigraphic images of tumor-bearing rats and rabbits after ^{99m}Tc-N4-NIM injection are shown in Figures 4 and 5. Tumors could be clearly detected by ^{99m}Tc-N4-NIM. The T/M ratios at 60–120 minutes were 4.1–4.2 in tumor-bearing rats and 2.52–2.98 in tumor-bearing rabbits, respectively.

4. Discussion

The development of new tumor hypoxia agents is clinically desirable for detecting primary and metastatic lesions as well as predicting radioresponsiveness and time to recurrence [10, 19]. None of the contemporary imaging modalities accurately measures hypoxia since the diagnosis of tumor hypoxia requires a pathologic examination. It is often difficult to predict the outcome of a therapy for hypoxic tumor without knowing at least the baseline of hypoxia in each tumor treated. Although the Eppendorf polarographic oxygen microelectrode can measure the oxygen tension in a tumor, this technique is invasive and needs a skillful operator. Additionally, this technique can only be used on accessible tumors (e.g., head and neck, cervical) and multiple readings are needed. Therefore, an accurate and easy method of measuring tumor hypoxia will be useful for patient selection. However, tumor-to-normal tissue uptake ratios vary and depend upon the radiopharmaceuticals used. Therefore, it would be rational to correlate tumor-to-normal tissue uptake ratios with the gold standard Eppendorf electrode measures of hypoxia when new radiopharmaceuticals are introduced to clinical practice.

In biodistribution, ^{99m}Tc-N4-NIM in tumor tissue was decreased as same as ^{99m}Tc-N4 (Tables 1 and 2). This decreased uptake might be due to slower uptake ^{99m}Tc-N4 and ^{99m}Tc-N4-NIM as a function of increased renal excretion. However, the tumor uptake as well as tumor/blood and tumor/muscle ratios in ^{99m}Tc-N4-NIM were higher than that in ^{99m}Tc-N4 group.

Hypoxia-Inducible Factor (HIF)-1α/β heterodimer is a master transcription factor for several genes involved in angiogenesis, glycolysis, pH balance, and metastasis. These HIF-1 target genes help tumors to overcome forthcoming metabolic obstacles as they grow. Under normoxic condition, the HIF-1α subunit is hydroxylated by its specific prolyl-4 hydroxylase 2, given the acronym PHD2, thus stabilizing it under normoxic conditions [20]. *In vitro* cellular uptake assay, the uptake of ^{99m}Tc-N4-NIM in tumor cells increases up to 240 min. However, this assay was performed under normoxic condition. The increased uptake of ^{99m}Tc-N4-NIM in tumor cells under normoxic condition might be due to stabilized HIF-1α. $NaTcO_4$ was reduced to $^{+5}$Tc [O] and bound to the three nitrogens of cyclam. The charge of ^{99m}Tc-N4-NIM is neutral. Cell uptake of ^{99m}Tc-N4-NIM was via passive diffusion.

In our animal model, tumor oxygen tension was determined to be 3.2 to 6.0 mmHg, whereas normal muscle tissue had 30 to 40 mmHg. Although another factor such as anemia may have influenced the level of tumor hypoxia, there was no attempt in identifying this factor. In biodistribution, ^{99m}Tc-N4-NIM in tumor tissue was decreased as same as ^{99m}Tc-N4 (Tables 1 and 2). This decreased uptake might be due to slower uptake of ^{99m}Tc-N4 and ^{99m}Tc-N4-NIM as a function of increased renal excretion. However, the tumor uptake as well as tumor/blood and tumor/muscle ratios in ^{99m}Tc-N4-NIM was higher than those in ^{99m}Tc-N4 group.

Due to better imaging characteristics and lower cost, attempts are made to replace the ^{123}I-, ^{131}I-, ^{67}Ga-, and ^{111}In-labeled compounds with corresponding ^{99m}Tc-labeled compounds when possible. Our radiochemistry data indicated N4-NIM could be labeled with ^{99m}Tc very easily and efficiently at room temperature with high radiochemical purity.

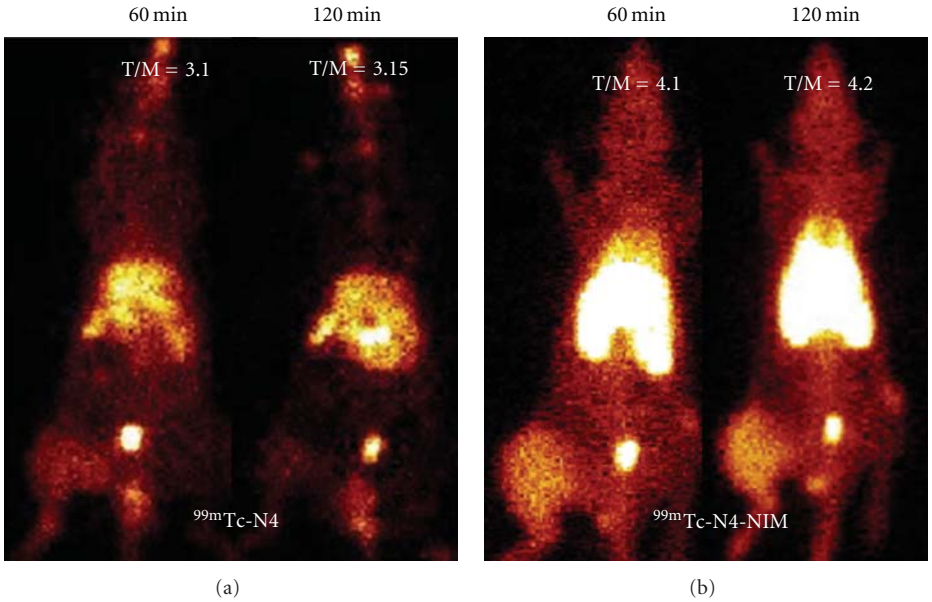

Figure 4: Planar scintigraphy of ^{99m}Tc-N4 and ^{99m}Tc-N4-NIM (400 μCi/rat, iv, acquired 500,000 count) showed higher tumor-to-muscle count density ratio in ^{99m}Tc-N4-NIM compared to that of ^{99m}Tc-N4. The numbers are tumor-to-muscle count density ratios (counts/pixel) at 60–120 min.

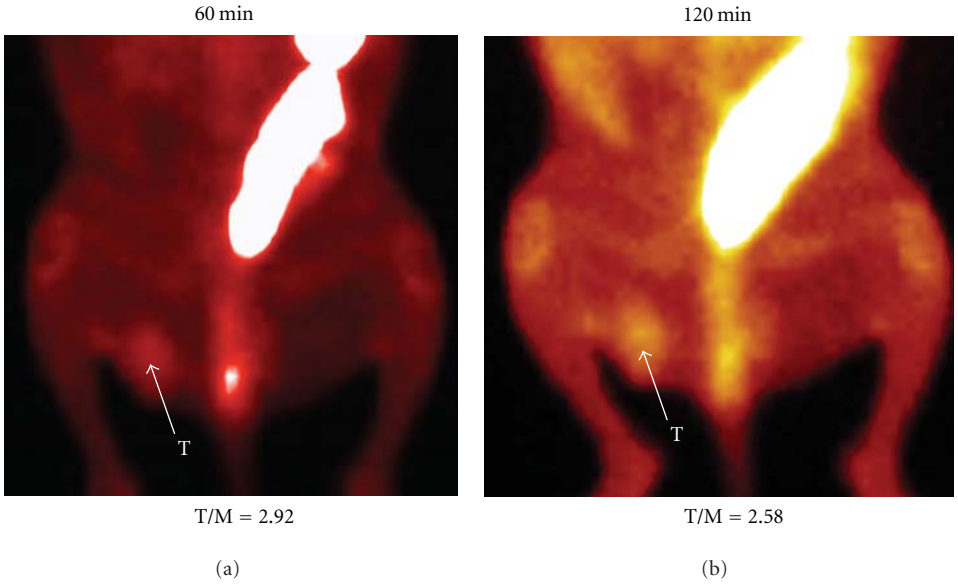

Figure 5: Planar scintigraphy of ^{99m}Tc-N4-NIM (15 mCi/rabbit, iv, acquired 500,000 count) showed higher tumor-to-muscle count density ratio (counts/pixel) at 60 and 120 min.

In vivo tissue distribution studies showed that radiation dosimetry of blood-forming organs was within radiation dose limits. Our planar imaging studies indicate that ^{99m}Tc-N4-NIM is feasible to assess tumor hypoxia.

In summary, N4-NIM kits could be labeled with ^{99m}Tc easily and efficiently, with high radiochemical purity and cost-effectiveness. *In vitro* cellular uptake and scintigraphic imaging studies demonstrated the pharmacokinetic distribution and feasibility of using ^{99m}Tc-N4-NIM for tumor hypoxia imaging.

Acknowledgments

This work was supported in part by a Sponsored Research Grant (MDA LS2005-00012803PL) established between

MDACC and Cell>Point L.L.C. and the J. S. Dunn Foundation. The chemistry analysis and animal research are supported by M. D. Anderson Cancer Center (CORE) Grant NIH CA-16672.

References

[1] B. C. Liang, "Effects of hypoxia on drug resistance phenotype and genotype in human glioma cell lines," *Journal of Neuro-Oncology*, vol. 29, no. 2, pp. 149–155, 1996.

[2] A. J. Giaccia, "Hypoxic stress proteins: survival of the fittest," *Seminars in Radiation Oncology*, vol. 6, no. 1, pp. 46–58, 1996.

[3] T. G. Graeber, C. Osmanian, T. Jacks et al., "Hypoxia-mediated selection of cells with diminished apoptotic potential in solid tumours," *Nature*, vol. 379, no. 6560, pp. 88–91, 1996.

[4] S. Dai, M. L. Huang, C. Y. Hsu, and K. S. C. Chao, "Inhibition of hypoxia inducible factor 1α causes oxygen-independent cytotoxicity and induces p53 independent apoptosis in glioblastoma cells," *International Journal of Radiation Oncology Biology Physics*, vol. 55, no. 4, pp. 1027–1036, 2003.

[5] J. M. Brown, "The hypoxic cell: a target for selective cancer therapy—eighteenth Bruce F. Cain Memorial Award Lecture," *Cancer Research*, vol. 59, no. 23, pp. 5863–5870, 1999.

[6] T. Chu, R. Li, S. Hu, X. Liu, and X. Wang, "Preparation and biodistribution of technetium-99m-labeled 1-(2-nitroimidazole-1-yl)-propanhydroxyiminoamide (N2IPA) as a tumor hypoxia marker," *Nuclear Medicine and Biology*, vol. 31, no. 2, pp. 199–203, 2004.

[7] B. M. Seddon, R. J. Maxwell, D. J. Honess et al., "Validation of the fluorinated 2-nitroimidazole SR-4554 as a non-invasive hypoxia marker detected by magnetic resonance spectroscopy," *Clinical Cancer Research*, vol. 8, no. 7, pp. 2323–2335, 2002.

[8] L. Bentzen, S. Keiding, M. Nordsmark et al., "Tumour oxygenation assessed by 18F-fluoromisonidazole PET and polarographic needle electrodes in human soft tissue tumours," *Radiotherapy and Oncology*, vol. 67, no. 3, pp. 339–344, 2003.

[9] T. Grönroos, L. Bentzen, P. Marjamäki et al., "Comparison of the biodistribution of two hypoxia markers [18F]FETNIM and [18F]FMISO in an experimental mammary carcinoma," *European Journal of Nuclear Medicine and Molecular Imaging*, vol. 31, no. 4, pp. 513–520, 2004.

[10] M. B. Mallia, S. Subramanian, A. Mathur, H. D. Sarma, M. Venkatesh, and S. Banerjee, "Comparing hypoxia-targeting potential of 99mTc(CO) 3-labeled 2-nitro and 4-nitroimidazole," *Journal of Labelled Compounds and Radiopharmaceuticals*, vol. 51, no. 8, pp. 308–313, 2008.

[11] K. M. Herzog, E. Deutsch, K. Deutsch, E. B. Silberstein, R. Sarangarajan, and W. Cacini, "Synthesis and renal excretion of technetium-99m-labeled organic cations," *Journal of Nuclear Medicine*, vol. 33, no. 12, pp. 2190–2195, 1992.

[12] F. L. Kong, M. S. Ali, Y. Zhang et al., "Synthesis and evaluation of amino acid-based radiotracer ^{99m}Tc-N4-AMT for breast cancer imaging," *Journal of Biomedicine and Biotechnology*, vol. 2011, Article ID 276907, 7 pages, 2011.

[13] S. Liu, "The role of coordination chemistry in the development of target-specific radiopharmaceuticals," *Chemical Society Reviews*, vol. 33, no. 7, pp. 445–461, 2004.

[14] S. Liu, "Bifunctional coupling agents for radiolabeling of biomolecules and target-specific delivery of metallic radionuclides," *Advanced Drug Delivery Reviews*, vol. 60, no. 12, pp. 1347–1370, 2008.

[15] K. Ohtsuki, K. Akashi, Y. Aoka et al., "Technetium-99m HYNIC-annexin V: a potential radiopharmaceutical for the in-vivo detection of apoptosis," *European Journal of Nuclear Medicine*, vol. 26, no. 10, pp. 1251–1258, 1999.

[16] C. G. Van Nerom, G. M. Bormans, M. J. De Roo, and A. M. Verbruggen, "First experience in healthy volunteers with technetium-99m L,L-ethylenedicysteine, a new renal imaging agent," *European Journal of Nuclear Medicine*, vol. 20, no. 9, pp. 738–746, 1993.

[17] C. H. Kao, S. P. ChangLai, P. U. Chieng, and T. C. Yen, "Technicium-99m methoxyisobutylisonitrile chest imaging of a small cell lung carcinoma: relation to patient prognosis and chemotherapy response- a preliminary report," *Cancer*, vol. 83, pp. 64–68, 1998.

[18] H. C. Wu, C. H. Chang, M. M. Lai, C. C. Lin, C. C. Lee, and A. Kao, "Using Tc-99m DMSA renal cortex scan to detect renal damage in women with type 2 diabetes," *Journal of Diabetes and Its Complications*, vol. 17, no. 5, pp. 297–300, 2003.

[19] J. M. Brown and A. J. Giaccia, "The unique physiology of solid tumors: opportunities (and problems) for cancer therapy," *Cancer Research*, vol. 58, no. 7, pp. 1408–1416, 1998.

[20] H. Y. Lee, T. Lee, N. Lee et al., "Src activates HIF-1α not through direct phosphorylation of HIF-1α-specific prolyl-4 hydroxylase 2 but through activation of the NADPH oxidase/Rac pathway," *Carcinogenesis*, vol. 32, no. 5, pp. 703–712, 2011.

Hindawi Publishing Corporation
Journal of Biomedicine and Biotechnology
Volume 2012, Article ID 232863, 9 pages
doi:10.1155/2012/232863

Research Article

Molecular Imaging of Mesothelioma with ^{99m}Tc-ECG and ^{68}Ga-ECG

Yin-Han Zhang, Jerry Bryant, Fan-Lin Kong, Dong-Fang Yu, Richard Mendez, E. Edmund Kim, and David J. Yang

Department of Experimental Diagnostic Imaging, The University of Texas MD Anderson Cancer Center, P.O. Box 59, 1515 Holcombe Boulevard, Houston, TX 77030, USA

Correspondence should be addressed to David J. Yang, dyang@mdanderson.org

Received 6 January 2012; Revised 9 February 2012; Accepted 16 February 2012

Academic Editor: Lie-Hang Shen

We have developed ethylenedicysteine-glucosamine (ECG) as an alternative to ^{18}F-fluoro-2-deoxy-D-glucose (^{18}F-FDG) for cancer imaging. ECG localizes in the nuclear components of cells via the hexosamine biosynthetic pathway. This study was to evaluate the feasibility of imaging mesothelioma with ^{99m}Tc-ECG and ^{68}Ga-ECG. ECG was synthesized from thiazolidine-4-carboxylic acid and 1,3,4,6-tetra-O-acetyl-2-amino-D-glucopyranose, followed by reduction in sodium and liquid ammonia to yield ECG (52%). ECG was chelated with ^{99m}Tc/tin (II) and ^{68}Ga/^{69}Ga chloride for *in vitro* and *in vivo* studies in mesothelioma. The highest tumor uptake of ^{99m}Tc-ECG is 0.47 at 30 min post injection, and declined to 0.08 at 240 min post injection. Tumor uptake (%ID/g), tumor/lung, tumor/blood, and tumor/muscle count density ratios for ^{99m}Tc-ECG (30–240 min) were 0.47 ± 0.06 to 0.08 ± 0.01; 0.71 ± 0.07 to 0.85 ± 0.04; 0.47 ± 0.03 to 0.51 ± 0.01, and 3.49 ± 0.24 to 5.06 ± 0.25; for ^{68}Ga-ECG (15–60 min) were 0.70 ± 0.06 to 0.92 ± 0.08; 0.64 ± 0.05 to 1.15 ± 0.08; 0.42 ± 0.03 to 0.67 ± 0.07, and 3.84 ± 0.52 to 7.00 ± 1.42; for ^{18}F-FDG (30–180 min) were 1.86 ± 0.22 to 1.38 ± 0.35; 3.18 ± 0.44 to 2.92 ± 0.34, 4.19 ± 0.44 to 19.41 ± 2.05 and 5.75 ± 2.55 to 3.33 ± 0.65, respectively. Tumor could be clearly visualized with ^{99m}Tc-ECG and ^{68}Ga-ECG in mesothelioma-bearing rats. ^{99m}Tc-ECG and ^{68}Ga-ECG showed increased uptake in mesothelioma, suggesting they may be useful in diagnosing mesothelioma and also monitoring therapeutic response.

1. Introduction

Drug discovery is accelerating due to mapping of molecular targets and the rapid synthesis of high-throughput *in vitro* testing of compounds in their early stage of the drug development process. The development of radiolabeled biochemical compounds, understanding molecular pathways and imaging devices to detect the radioactivity by external imaging, has expanded the use of nuclear molecular imaging studies in drug development. Nuclear molecular imaging provides vascular angiogenesis, cellular translational, and transcriptional information. The important applications in molecular imaging in oncology are at the characterization of tumors (degree of malignancy), optimal dosing determination, differentiation (i.e., inflammation/infection versus recurrence, sensitive versus resistant, low versus high grade), and prediction of treatment response (i.e., select patient who may respond to therapy). Thus, molecular imaging helps to control and monitor dosage for increased safety and effectiveness. The focus of molecular imaging in oncology is to identify tumor-specific markers and apply these markers for evaluation of patient response to treatment. Nuclear molecular imaging could noninvasively assess diseases treatment endpoints which used to rely almost exclusively on biopsies and histopathological assays. ^{18}F-Fluoro-deoxy-glucose (^{18}F-FDG), a gold standard for molecular imaging, utilizes glucose transporters and hexokinase phosphorylated processes for tumor imaging [1]. However, ^{18}F-FDG has several limitations that give rise to false positive/negative results [2]. ^{18}F-FDG has poor differentiation between tumor and inflammation/infection due to its high uptake in granulocytes and macrophages. Therefore, it is amenable to develop a radiotracer as an alternative for better differentiation in tumor imaging.

Glucosamine enters into cells via hexosamine biosynthetic pathway and its regulatory products of glucosamine-6-phosphate mediate insulin activation, downstream signaling, glycosylation, and tumor growth. In the hexosamine pathway, upregulated glucose transporters induce overexpression of glutamine: fructose-6-phosphate amidotransferase (GFAT). GFAT uses the amide group of glutamine to convert fructose 6-phosphate to glucosamine 6-phosphate and forms hexosamine products [3]. Phosphorylated glucosamine interacts with uridine diphosphate (UDP) to form UDPN-acetylglucosamine (UDP-GlcNAc). The dynamic glycosylation of serine or threonine residues on nuclear and cytosolic proteins by O-linked protein N-acetylglucosamine (O-GlcNAc) transferase is abundant in all multicellular eukaryotes. Glycosylation is a part of posttranslational modification and appears to modify a large number of nucleocytoplasmic proteins. O-GlcNAc transferase (OGT) activity is exquisitely responsive to intracellular UDP-GlcNAc and UDP concentrations, which are in turn highly sensitive to glucose concentrations and other stimuli [4]. In cell nucleus, the ubiquitous transcription factor Sp1 is extensively modified by O-GlcNAc. Sp1 becomes hyperglycosylated in response to hyperglycemia or elevated glucosamine [4]. Because O-GlcNAc is involved in hexosamine pathway and nucleus activity, it becomes an attractive imaging agent for differential diagnosis in cancers.

^{68}Ga (89% positron, 68 min half-life) and ^{99m}Tc (140 keV, 6 hrs half-life) are obtained from generators on-site and have significant commercial interest. ^{68}Ga and ^{99m}Tc could provide serial images which are pivotal to clinical applications by positron emission tomography (PET) and single photon emission-computed tomography (SPECT). PET/SPECT/CT is better than PET and SPECT alone because multiple slices by CT and serial images by PET and SPECT provide a better delineation in tumor volumes. L,L-ethylenedicysteine (EC), a family of bisaminoethanethiol, is known to form stable metal complexes [5, 6]. The strong metal complexing property of such EC systems is also applied for labeling of small molecules, proteins, and peptides after conjugation to EC derivatives. EC-technology platform has shown to coordinate radiometals and metals for image-guided target assessment, theranostic applications, and the selection of patient for treatment [7–19].

Mesothelioma is a cancer caused by exposure to asbestos. Asbestos fibers have been shown to alter the function and secretory properties of macrophages, ultimately creating conditions which favor the development of mesothelioma. Following asbestos phagocytosis, macrophages generate increased amounts of hydroxyl radicals which are thought to promote asbestos carcinogenicity. Furthermore, genetic alterations in asbestos-activated macrophages may result in the release of potent mesothelial cell mitogens such as platelet-derived growth factor and transforming growth factor-β which, in turn, may induce the chronic stimulation and proliferation of mesothelial cells after injury by asbestos fibers. Although there have been some modest improvements in prognosis from newer chemotherapies and multimodality treatments, the prognosis for malignant mesothelioma remains poor. The standard approaches such as radiation, chemotherapy, and surgery have been investigated to treat patients with malignant pleural mesothelioma. Treatment of malignant mesothelioma at earlier stages has a better prognosis, but cures are exceedingly rare. Immunohistochemical analysis has shown that GlcNAc-specific binding sites are useful for distinguishing metastatic carcinoma from mesothelioma in human [20]. Subsequently, EC-glucosamine (ECG), a glucose analogue, is developed to trace the glucose transport system and glucosamine binding sites in mesothelioma. ^{99m}Tc-ECG and ^{68}Ga-ECG may assess the staging, restaging, and response monitoring in mesothelioma for early and right medication of this disease.

2. Materials and Methods

2.1. General. All chemicals and solvents were obtained from Sigma-Aldrich (St. Louis, MO). Nuclear magnetic resonance (NMR) was performed on Bruker 300 MHz Spectrometer, and mass spectra were performed on Waters Q-TOF Ultima Mass Spectrometer (Milford, MA) at the core facility at the University of Texas MD Anderson Cancer Center (UTMDACC, Houston, TX). Chemical shifts were reported in δ (ppm) and J values in Hertz. FDG was obtained from Department of Nuclear Medicine at UTMDACC.

2.2. Synthesis of ECG

2.2.1. Step 1: Synthesis of T-G-(Ac)$_4$. To a solution of thiazolidine-4-carboxylic acid (T) (2.6 g, 0.02 mol) in DMF (20 mL) and 5.0 mL trimethylamine, 1-hydroxybenzotriazole hydrate 2.7 g (0.02 mol) was added. After 30 min, 1,3,4,6-tetra-O-acetyl-2-amino-α-D-glucopyranose hydrochloride (G-(Ac)$_4$) (7.7 g, 0.02 mol), N,N′-di-cyclohexylcarbodiimide (DCC; 4.2 g, 0.02 mol), and 4-dimethylaminopyridine (DMAP; 1.2 g, 0.01 mol) were added to the mixture and stirred for overnight at room temperature. The solution was evaporated to dryness at high vacuum. Dichloromethane (CH_2Cl_2) (50 mL) was added to the residual and kept at 4°C for overnight, then filtered. The product was purified with silica gel by eluting with CH_2Cl_2/MeOH (95/5, V/V) to yield white product T-G-(Ac)$_4$ 4.08 g (44.2%). NMR and mass spectrometry were used to confirm the structure of T-G-(Ac)$_4$.

2.2.2. Step 2: Reduction Reaction. Sodium was added piece by piece to a solution of T-G-(Ac)$_4$ (4.08 g, 8.8 mmol) in liquid ammonia (170 g). The color of the solution was slowly changed to dark blue. After 30 minutes, a little of ammonium chloride was added. The liquid ammonia was removed by reduced pressure. The residual solid was triturated with methanol (100 mL). The solid was then filtered and washed with additional methanol (50 mL) to yield crude product 4.16 g. To obtain analytical pure ECG, the crude product (0.1 g) was dissolved in 1.0 mL of HCl (0.1 N) and purified with sephadex column by eluting with H_2O. The aqueous fractions were combined and lyophilized to yield EC-G 0.029 g (46.7%). NMR, mass spectrometry, and HPLC were used to confirm the structure of ECG.

2.3. Synthesis of Cold Ga-ECG. $^{69}GaCl_3$ (20 mg, 0.11 mmol) in 0.2 mL H_2O was added to a solution of ECG (60 mg, 0.1 mmol) in 0.5 mL H_2O. The pH value was adjusted to 4-5 with 0.1 N NaOH (50 μL). The solution was heated for 30 min at 60°C. The product was purified by a sephadex column eluting with H_2O to yield Ga-ECG. After lyophilization, Ga-ECG was obtained as white solid (52 mg, 78.1%). NMR, mass spectrometry, and HPLC were used to confirm the structure of ^{69}Ga-ECG.

2.4. Radiosynthesis of ^{68}Ga-ECG and ^{99m}Tc-ECG. $^{68}GaCl_3$ was obtained from a ^{68}Ge/^{68}Ga generator (Eckert Ziegler, Valencia, CA) eluted with 0.1 N HCl. $^{68}GaCl_3$ (120 μL, 300 μCi) was added to the solution of ECG (1.2 mg) in 0.1 mL H_2O, and pH value was adjusted to 4-5 with $NaHCO_3$ (40 μL, 0.1 N). The solution was heated at 60°C for 15 min. Sodium pertechnetate ($Na^{99m}TcO_4$) was obtained from ^{99}Mo/^{99m}Tc generator by Covidien (Houston, TX). Radiosynthesis of ^{99m}Tc-ECG was achieved by adding ^{99m}Tc-pertechnetate (40–50 mCi) into the lyophilized residue of ECG (5 mg) and tin (II) chloride ($SnCl_2$, 100 μg). The complexation of ECG with ^{99m}Tc was carried out at pH 6.5. Radiochemical purity was determined by TLC (Waterman No. 1, Aldrich-Sigma, St. Louis, MO) eluted with saline. High-performance liquid chromatography (HPLC), equipped with a NaI detector and UV detector (210 nm), was performed on a C-18 reverse phase column (C18-extend, Agilent, Santa Clara, CA) eluted with acetonitrile/water (1 : 9, V/V) at a flow rate of 0.5 mL/min. HPLC of cold ^{69}Ga-ECG was used to confirm the structure of ^{68}Ga-ECG.

2.5. Biodistribution of Radiotracers in Mesothelioma-Bearing Rats. Female Fischer 344 rats (150 ± 25 g) (Harlan Sprague-Dawley, Indianapolis, IN) (n = 3 rats/time point) were inoculated with malignant pleural mesothelioma cells derived from the IL-45 cell line. Tumor cells (10^6 cells/rat) were injected (i.m.) into the hind legs. Studies were performed 14 to 17 days after inoculation when tumors were approximately 1 cm in diameter. In tissue distribution studies, each animal was injected (iv, 10 μCi/rat, 10 μg/rat) with ^{99m}Tc-ECG, ^{68}Ga-ECG, and ^{18}F-FDG. Rats were sacrificed at 0.5–4 hrs. The selected tissues were excised, weighed, and counted for radioactivity by using a gamma counter (Packard Instruments, Downers Grove, IL). The biodistribution of tracer in each sample was calculated as percentage of the injected dose per gram of tissue wet weight (%ID/g).

2.6. Scintigraphic Imaging Studies. Female Fischer 344 rats (150 ± 25 g) bearing malignant pleural mesothelioma (at hind legs) derived from the IL-45 cell line were used for imaging studies. Studies were performed 14 to 17 days after inoculation when tumors were approximately 1 cm in diameter. Scintigraphic images were obtained either from a micro-PET (Inveon) embedded in the gantries coordinate PET/CT data acquisition or from an M-gamma camera (Siemens Medical Systems, Inc., Hoffman Estates, IL) equipped with low-energy parallel-hole collimator. Each animal was administered with ^{99m}Tc-ECG (300 μCi/rat, iv), ^{68}Ga-ECG, and ^{18}F-FDG (400 μCi/rat, iv), and the images were obtained at 0.5–4 hrs. To demonstrate ^{68}Ga-ECG could be used for image-guided therapy, the same mesothelioma-bearing rats (n = 3) at tumor volume 1.5 cm were treated with paclitaxel (20 mg/kg, iv, single injection). Prior to treatment and postpaclitaxel treatment on day 7, the tumor-bearing rats were imaged with ^{68}Ga-ECG. Computer-outlined regions of interest (ROI) (counts per pixel) were used to determine tumor-to-background count density ratios for ^{99m}Tc-ECG. Computer outlined regions of interest (ROI) (counts per pixel) for tumor and muscle at the corresponding time interval were used to generate a dynamic plot for ^{68}Ga-ECG and ^{18}F-FDG. Dynamic plot was from 0 to 45 minutes. Paclitaxel was selected because it produced antiproliferative effects by inhibition of glucose transporters (Glut-1) in cell line studies [21]. Also, it has been reported that mesothelioma responds to paclitaxel treatment in the animal model [22].

3. Result

3.1. Chemistry. The synthetic scheme is shown in Figure 1. ECG was synthesized by two-step reactions. In the first step, thiazolidine-4-carboxylic acid (T) was reacted with 1,3,4,6-tetra-O-acetyl-2-amino-α-D-glucopyranose hydrochloride (G-$(Ac)_4$) in the presence of 1-hydroxybenzotriazole hydrate, DCC, and DMAP. After purification, the yield of product T-G-$(Ac)_4$ was 44.2%. ^{1}H NMR (D_2O, δ): 1.97–2.14 (m, 12H), 3.88 (t, 1H), 3.93 (s, 2H), 4.05–4.10 (m, 6H) 4.22–4.30 (m, 2H), 5.09 (t, 1H), 5.34 (t, 1H), 5.80 (d, 1H), 6.93 (d, 1H). ^{13}C NMR (D_2O, δ): 171.19, 171.00, 170.65, 169.35, 166.35, 141.76, 92.05, 82.45, 72.79, 72.02, 68.02, 61.73, 60.39, 53.21, 42.32, 20.84, 20.68, 20.58, 20.55. FAB MS m/z: 462.5.

In the second step, T-G-$(Ac)_4$ was reduced by sodium in liquid ammonia (Birch reduction). The crude product was purified with a sephadex column to yield ECG (46.7%). HPLC shows that purity is over 82%. ^{1}H NMR (D2O, δ): 3.15–3.20 (m, 4H), 3.78–4.05 (m, 6H), 4.08–4.15 (m, 8H), 4.2-4.3 (d, 2H), 4.68–4.73 (d, 2H), 5.19–5.21 (d, 2H). ^{13}C NMR (D_2O, δ): 174.81, 174.56, 94.95, 90.87, 90.84, 75.96, 73.91, 73.85, 71.59, 70.71, 70.66, 70.10, 69.88, 60.72, 60.62, 56.72, 54.11, 23.33, 22.23, 21.96. FAB MS m/z: 591.

NMR of cold ^{69}Ga-ECG was ^{1}H NMR (D_2O, δ): 2.94–3.38 (m, 8H), 3.43–3.65 (m, 4H), 3.50–3.80 (m, 10H), 3.92–4.02 (t, 2H), 4.23–4.34 (d, 2H), 5.15–5.34 (d, 2H), ^{13}C NMR (D_2O, δ): 175.51, 175.16, 95.55, 90.85, 90.67, 75.76, 74.90, 73.55, 71.59, 70.71, 70.66, 70.10, 69.88, 60.72, 60.62, 56.72, 54.11, 23.53, 22.83, 22.16. Radio-TLC and HPLC analyses of the purity of ^{68}Ga-ECG and ^{99m}Tc-ECG were > 96% (Figures 2–4). HPLC of cold ^{69}Ga-ECG was used to confirm the structure of ^{68}Ga-ECG (Figure 3).

3.2. In Vivo Biodistribution Studies. Tumor and tissue uptake (%ID/g) of ^{68}Ga-ECG, ^{99m}Tc-ECG and ^{18}F-FDG are shown in Tables 1, 2, and 3. The highest tumor uptake of ^{99m}Tc-ECG is 0.47 at 30 min after injection, and declined to 0.08 at 240 min after injection. Tumor uptake (%ID/g), tumor/lung, tumor/blood, and tumor/muscle count density ratios for

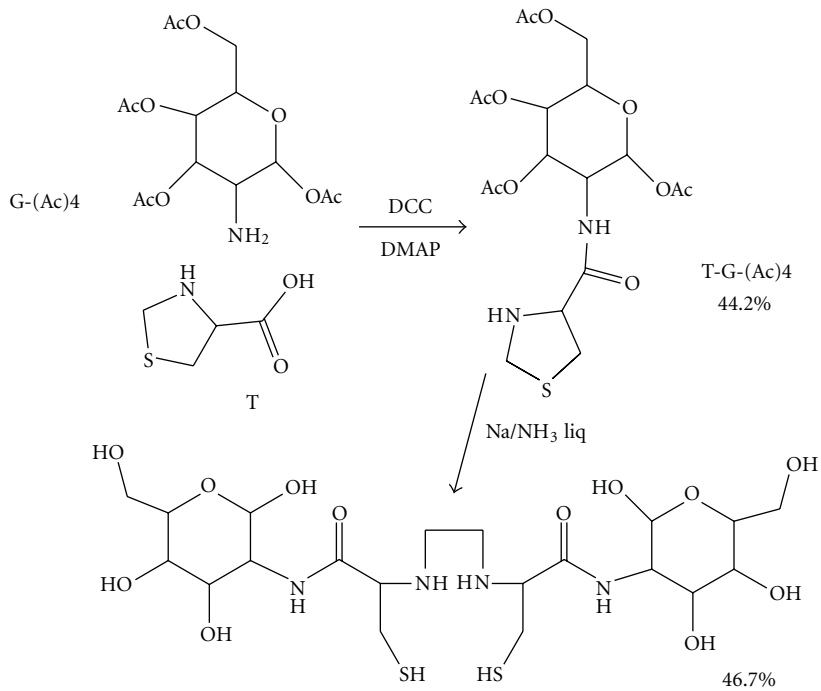

Figure 1: Efficient synthesis of ECG.

Table 1: Biodistribution of ^{68}Ga-ECG in mesothelioma-bearing rats.

	Percentage of injected dose per gram of tissue weight (n = 3/time, interval, iv)[1]		
	15 min	30 min	60 min
Blood	1.66 ± 0.06	1.54 ± 0.02	1.38 ± 0.03
Heart	0.51 ± 0.04	0.39 ± 0.04	0.40 ± 0.03
Lung	1.07 ± 0.02	0.94 ± 0.04	0.80 ± 0.04
Thyroid	0.88 ± 0.07	0.96 ± 0.11	0.83 ± 0.05
Pancreas	0.29 ± 0.02	0.28 ± 0.03	0.29 ± 0.03
Liver	0.77 ± 0.05	0.71 ± 0.07	0.78 ± 0.04
Spleen	0.41 ± 0.03	0.44 ± 0.07	0.49 ± 0.01
Kidney	1.53 ± 0.06	0.75 ± 0.04	0.70 ± 0.02
Stomach	0.29 ± 0.07	0.37 ± 0.02	0.40 ± 0.04
Intestine	0.31 ± 0.04	0.35 ± 0.05	0.53 ± 0.01
Uterus	0.87 ± 0.19	0.81 ± 0.04	0.77 ± 0.10
Tumor	0.70 ± 0.06	0.72 ± 0.06	0.92 ± 0.08
Muscle	0.18 ± 0.01	0.14 ± 0.01	0.14 ± 0.02
Bone	0.27 ± 0.02	0.51 ± 0.09	0.46 ± 0.02
Brain	0.05 ± 0.01	0.07 ± 0.01	0.08 ± 0.01
Tumor/blood	0.42 ± 0.03	0.47 ± 0.04	0.67 ± 0.07
Tumor/muscle	3.84 ± 0.52	5.63 ± 1.03	7.00 ± 1.42
Tumor/brain	11.68 ± 1.87	8.81 ± 1.54	13.20 ± 2.78
Tumor/lung	0.64 ± 0.05	0.78 ± 0.10	1.15 ± 0.08

[1] Values represent the mean ± standard deviation of data from 3 animals.

Table 2: Biodistribution of ^{99m}Tc-ECG in mesothelioma-bearing rats.

	Percentage of injected dose per gram of tissue weight (n = 3/time, interval, iv)[1]		
	30 min	2 h	4 h
Blood	0.98 ± 0.06	0.23 ± 0.03	0.16 ± 0.01
Heart	0.28 ± 0.02	0.06 ± 0.01	0.04 ± 0.00
Lung	0.65 ± 0.03	0.16 ± 0.03	0.10 ± 0.00
Thyroid	0.55 ± 0.04	0.12 ± 0.02	0.08 ± 0.00
Pancreas	0.21 ± 0.02	0.05 ± 0.01	0.04 ± 0.01
Liver	1.05 ± 0.02	0.86 ± 0.07	0.51 ± 0.02
Spleen	0.59 ± 0.05	0.61 ± 0.07	0.70 ± 0.02
Kidney	3.79 ± 0.57	2.02 ± 0.49	1.33 ± 0.10
Stomach	0.35 ± 0.03	0.07 ± 0.01	0.03 ± 0.00
Intestine	0.28 ± 0.02	0.11 ± 0.04	0.04 ± 0.01
Uterus	0.55 ± 0.04	0.15 ± 0.06	0.08 ± 0.01
Tumor	0.47 ± 0.06	0.12 ± 0.01	0.08 ± 0.00
Muscle	0.13 ± 0.01	0.03 ± 0.01	0.02 ± 0.00
Bone	0.16 ± 0.06	0.05 ± 0.01	0.03 ± 0.00
Brain	0.04 ± 0.00	0.01 ± 0.00	0.01 ± 0.00
Tumor/blood	0.47 ± 0.03	0.50 ± 0.03	0.51 ± 0.00
Tumor/muscle	3.49 ± 0.24	3.75 ± 0.44	5.06 ± 0.25
Tumor/brain	10.79 ± 0.50	10.22 ± 1.37	15.52 ± 0.89
Uterus/muscle	4.18 ± 0.23	4.49 ± 0.96	4.74 ± 0.16
Tumor/lung	0.71 ± 0.07	0.75 ± 0.10	0.85 ± 0.04

[1] Values represent the mean ± standard deviation of data from 3 animals.

Table 3: Biodistribution of ^{18}F-FDG in mesothelioma-bearing rats.

	Percentage of injected dose per gram of tissue weight (n = 3/time, interval, iv)[1]		
	30 min	90 min	180 min
Blood	0.45 ± 0.07	0.15 ± 0.01	0.07 ± 0.01
Heart	3.42 ± 1.14	1.95 ± 0.40	1.94 ± 0.45
Lung	0.60 ± 0.07	0.53 ± 0.03	0.46 ± 0.06
Thyroid	0.65 ± 0.04	0.47 ± 0.05	0.54 ± 0.04
Pancreas	0.22 ± 0.02	0.21 ± 0.02	0.21 ± 0.03
Liver	0.51 ± 0.08	0.33 ± 0.03	0.23 ± 0.03
Spleen	0.88 ± 0.08	0.87 ± 0.06	0.98 ± 0.10
Kidney	0.85 ± 0.13	0.43 ± 0.04	0.23 ± 0.01
Stomach	0.55 ± 0.03	0.40 ± 0.03	0.38 ± 0.02
Intestine	0.94 ± 0.16	1.00 ± 0.22	0.62 ± 0.07
Uterus	0.52 ± 0.06	0.57 ± 0.08	0.39 ± 0.09
Tumor	1.86 ± 0.22	1.63 ± 0.19	1.38 ± 0.35
Muscle	0.45 ± 0.14	0.23 ± 0.03	0.42 ± 0.06
Bone	0.21 ± 0.09	0.14 ± 0.07	0.24 ± 0.06
Brain	2.36 ± 0.10	2.24 ± 0.20	1.89 ± 0.35
Tumor/blood	4.19 ± 0.44	11.01 ± 1.60	19.41 ± 2.05
Tumor/muscle	5.75 ± 2.55	7.40 ± 1.67	3.33 ± 0.65
Tumor/brain	0.77 ± 0.09	0.72 ± 0.02	0.71 ± 0.05
Uterus/muscle	1.58 ± 0.69	2.50 ± 0.37	0.94 ± 0.16
Tumor/lung	3.18 ± 0.44	3.41 ± 0.43	2.92 ± 0.34

[1] Values shown represent the mean ± standard deviation of data from 3 animals.

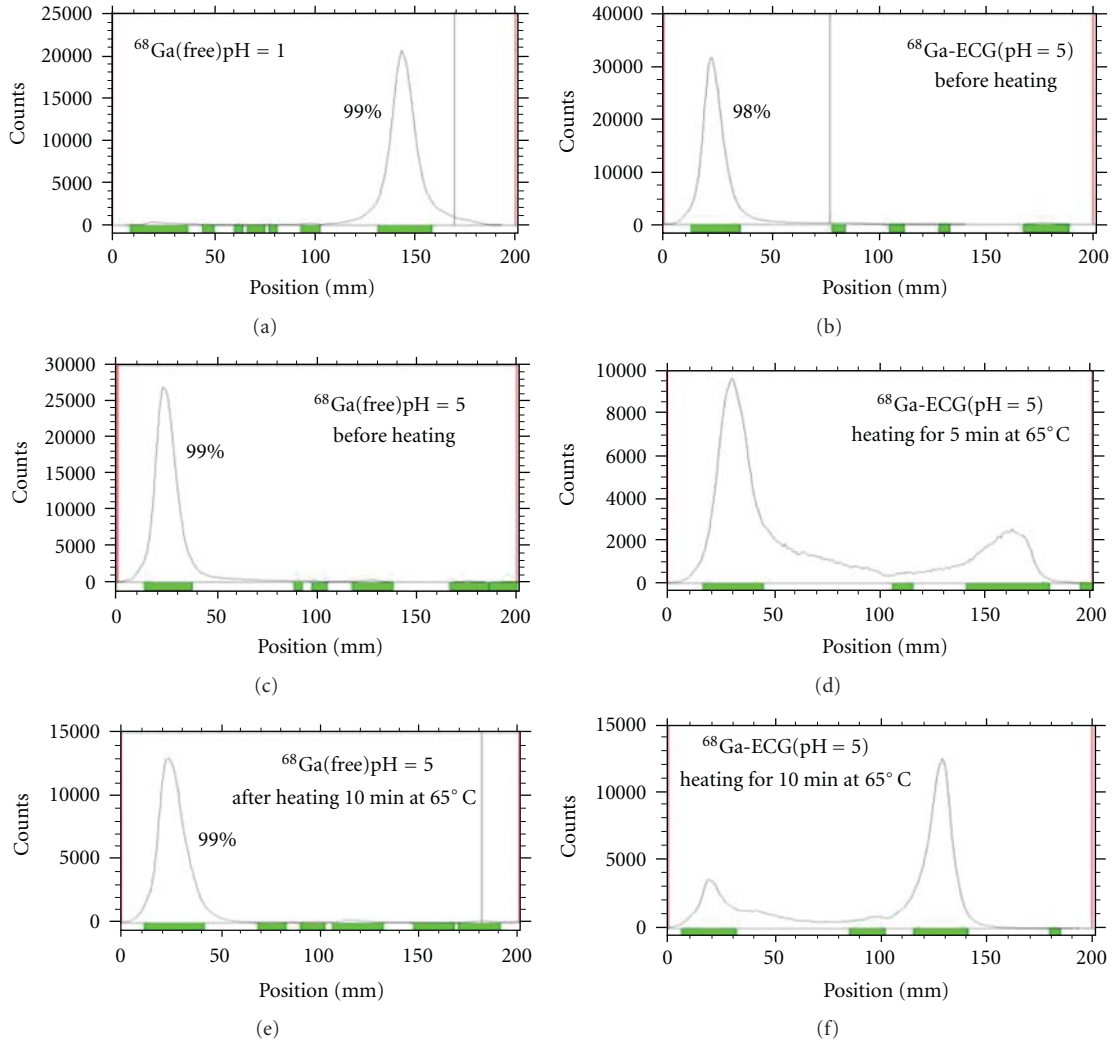

Figure 2: TLC analysis of ^{68}Ga-ECG using saline as an eluant. Radio-TLC analysis of the purity of ^{68}Ga-ECG was >96%.

^{99m}Tc-ECG (30–240 min) were 0.47 ± 0.06 to 0.08 ± 0.01, 0.71 ± 0.07 to 0.85 ± 0.04, 0.47 ± 0.03 to 0.51 ± 0.01, and 3.49 ± 0.24 to 5.06 ± 0.25; for ^{68}Ga-ECG (15–60 min) were 0.70 ± 0.06 to 0.92 ± 0.08, 0.64 ± 0.05 to 1.15 ± 0.08, 0.42 ± 0.03 to 0.67 ± 0.07, and 3.84 ± 0.52 to 7.00 ± 1.42; and for FDG (30–180 min) were 1.86 ± 0.22 to 1.38 ± 0.35, 3.18 ± 0.44 to 2.92 ± 0.34, 4.19 ± 0.44 to 19.41 ± 2.05, and 5.75 ± 2.55 to 3.33 ± 0.65, respectively. Higher kidney uptake was observed for both ^{68}Ga-ECG and ^{99m}Tc-ECG groups, presumable because EC and EC-conjugates may interact with renal tubules in the kidney [11].

3.3. Scintigraphic Imaging Studies. Scintigraphic images of rats administered ^{68}Ga-ECG, ^{99m}Tc-ECG, and ^{18}F-FDG showed that tumors could be clearly visualized at 0.5–4 hrs (Figures 5–7). Dynamic plot of tumor uptake with ^{68}Ga-ECG and ^{18}F-FDG showed similar transporter pattern (Figure 5). ^{68}Ga-ECG was able to monitor paclitaxel treatment response in the same mesothelioma-bearing rats (Figure 6). Two rats receiving ^{99m}Tc-ECG (middle and right) were randomly selected to compare to that of the rat receiving ^{99m}Tc-EC (left) under the same imaging panel. Tumor in ^{99m}Tc-ECG group showed much higher uptake than ^{99m}Tc-EC (control) group at 1 and 2 hrs (Figure 7).

4. Discussion

Previous studies have shown that ^{99m}Tc-ECG exhibits characteristics similar to ^{18}F-FDG in terms of the glucose membrane transport process and tumor uptake [11]. These glucose membrane transporters are involved in both the glycolytic pathway and the hexosamine biosynthetic pathway. Cell cycle analysis revealed that ^{99m}Tc-ECG was able to transport across the nucleus membrane and involved in proliferation activity in all phases cell cycles [14]. Moreover, the thymidine incorporation assay studies showed similar uptake patterns for both unlabeled ECG and glucose, suggesting that both ECG and glucose were involved in the proliferation/growth activity of cells, whereas unlabeled FDG was not [14].

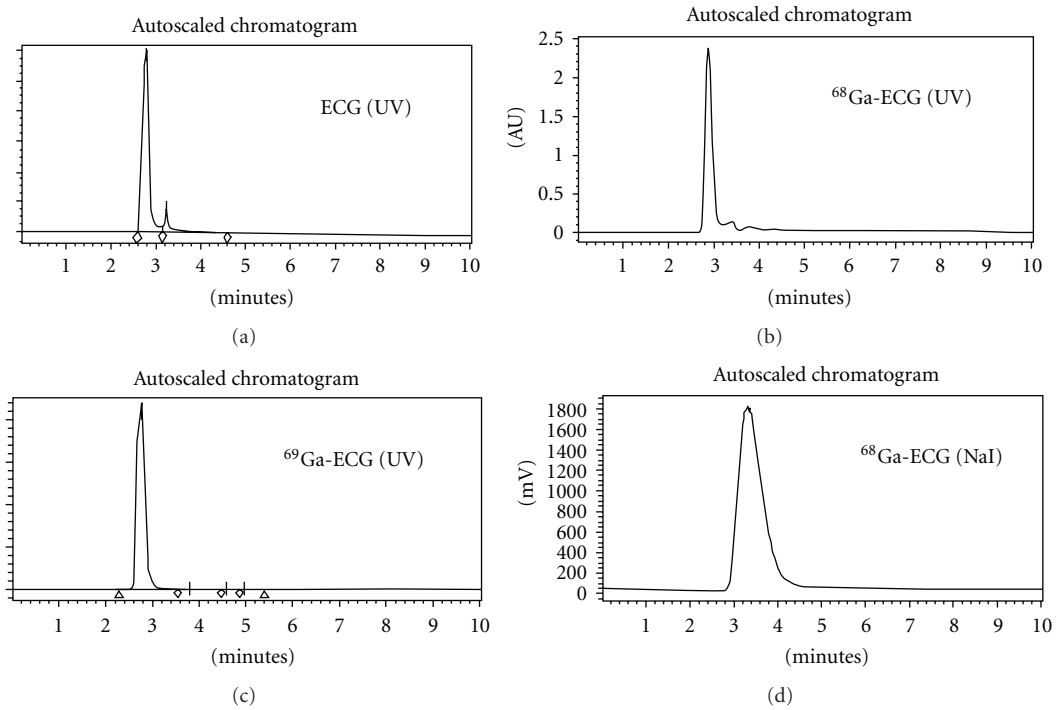

Figure 3: HPLC analysis of $^{68/69}$Ga-ECG and ECG (mobile phase: H_2O/acetonitrile, 9 : 1 V/V, flow rate: 0.5 mL/min, column: C18-extend (Agilent), UV ABS 210 nm). HPLC analysis of the purity of ^{68}Ga-ECG was >96%.

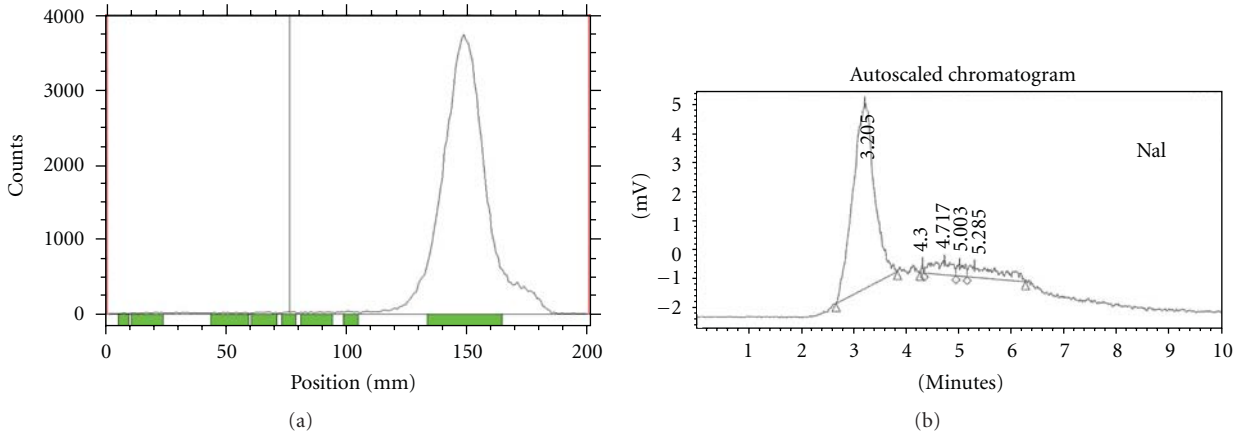

Figure 4: ITLC (a, in saline) and HPLC (b, NaI detector) analysis of ^{99m}Tc-ECG (mobile phase: H_2O/acetonitrile, 9 : 1 V/V, flow rate: 0.5 mL/min, Column: C18-extend (Agilent), UV ABS: 210 nm). Radio-TLC and HPLC analyses of the purity of ^{99m}Tc-ECG were >96%.

The lack of ^{18}F-FDG involvement in DNA proliferation is attributable to the presence of the fluorine atom at position 2 of the molecule, which prevents its metabolism and consequently its utilization in cell proliferation and growth [23]. As both molecules enter a cell and become phosphorylated by hexokinase, it can be diverted from the main glycolytic/glycogen pathways into accessory pathways. For example, under normal conditions, cells utilize 95% glucose which is transported via transporters 1 and 3 through the glycolytic pathway. ^{18}F-FDG uses transporters 1 and 3. ^{99m}Tc-ECG uses transporters 2 and 4 which are the transporters for glucosamine and transport glucose by the hexosamine pathway under normal conditions [24]. In addition, under abnormal conditions, only 3 to 5% of glucose is being utilized by the glycolytic pathway. However, in the case where an abnormal condition exists, there is a dramatic shift from 95% and above [25]. It should be noted that when the cell senses stress or a disease state occurs, the cells become hyper and glucose deficient/depleted, which in turn deactivates the glycolytic pathway. The hexosamine biosynthesis pathway then becomes active and takes over. The proliferation rates for tumors are with 100–1000x more

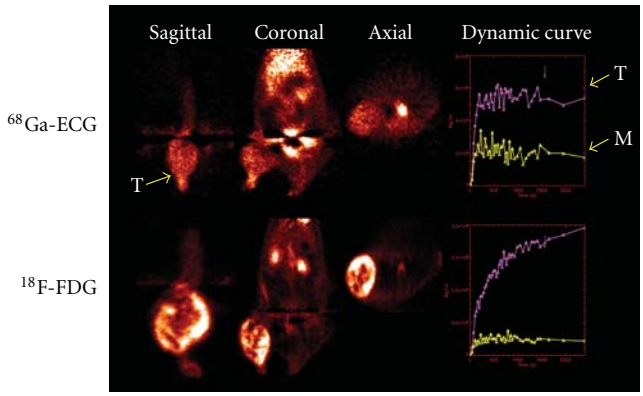

Figure 5: ^{18}F-FDG and ^{68}Ga-ECG PET imaging in mesothelioma-bearing rats (400 μCi/rat, iv, acquired 45 minutes). Computer-outlined regions of interest (ROI) (counts per pixel) for tumor and muscle at the corresponding time interval were used to generate a dynamic plot. Dynamic plot was from 0 to 45 minutes.

Image-guided therapy with ^{68}Ga-ECG in the Mesothelioma-bearing rat

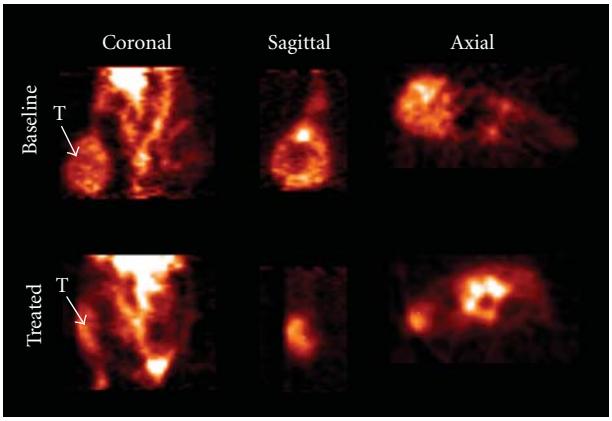

Figure 6: ^{68}Ga-ECG PET images in rat bearing mesothelioma (400 μCi/rat, iv, lower body) before and after treatment at 45 minutes. Top: baseline at tumor size 1.5 cm; bottom: treated with paclitaxel (20 mg/kg, iv, single dose on day 7). T: tumor.

than normal cells and thus a relatively greater concentration of ^{99m}Tc-ECG than normal cells. ^{99m}Tc-ECG can be utilized by cancer cells; thus the imaging studies are successful. Clinical phase 1 and 2 trials revealed that ^{99m}Tc-ECG was safe and had favorable radiation dosimetry. ^{99m}Tc-ECG was able to differentiate tumor and inflammation in lung cancer patients [26].

In the present study, we are able to place different radiometals in ECG. Both ^{99m}Tc-ECG and ^{68}Ga-ECG were able to image mesothelioma in the animal model. ^{68}Ga-ECG was able to provide image-guided therapy assessment. From biodistribution (Tables 1–3), tumor/brain count density ratios of ^{99m}Tc-ECG and ^{68}Ga-ECG were better than those of FDG. It may have advantage in brain tumor imaging than FDG. However, tumor/blood count density ratios of ^{99m}Tc-ECG and ^{68}Ga-ECG were less than that of FDG. Additional experiments such as mechanistic studies and differential diagnosis would warrant their applications in oncology.

Planar images of mesothelioma-bearing rats with ^{99m}TC-EC and ^{99m}TC-ECG

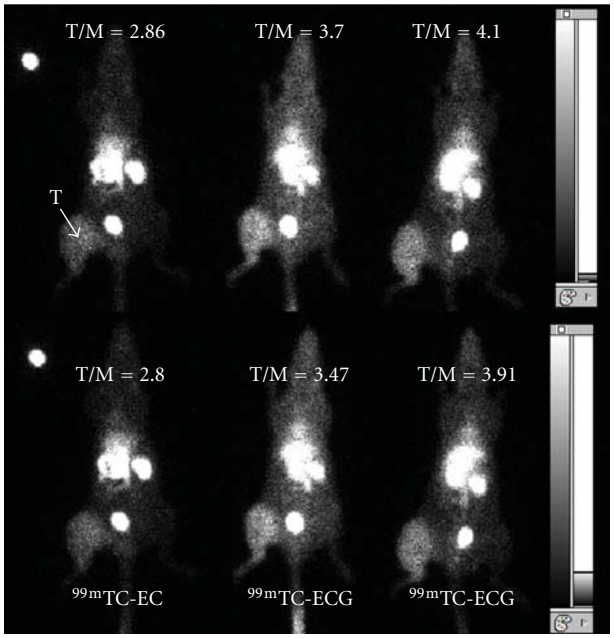

Figure 7: Planar scintigraphy of ^{99m}Tc-EC (left) and ^{99m}Tc-ECG (300 μCi/rat, iv, acquired 500,000 count) (middle and right) in mesothelioma-bearing rats. The numbers are tumor-to-muscle count density ratios at 1 hr (upper panel) and 2 hrs (lower panel). T: tumor.

In summary, efficient synthesis of ECG was achieved with high yield. ^{68}Ga-ECG and ^{99m}Tc-ECG were prepared with high radiochemical purities. Biodistribution and planar imaging studies demonstrated the pharmacokinetic distribution and feasibility of using ^{68}Ga-ECG and ^{99m}Tc-ECG to image mesothelioma. ^{68}Ga-ECG and ^{99m}Tc-ECG showed an increased uptake in mesothelioma in the model tested, indicating that they are feasible to assess tumor volume. ^{68}Ga-ECG and ^{99m}Tc-ECG may be useful for screening, diagnosing, staging, and assessing the efficacy of treatment in respect to all cancer types.

Acknowledgments

This work was supported in part by the John S. Dunn Foundation and sponsored research agreement (LS01-212) made by Cell > Point LLC at the MDACC. The animal research is supported by MD Anderson Cancer Center (CORE) Grant NIH CA-16672.

References

[1] A. Buerkle and W. A. Weber, "Imaging of tumor glucose utilization with positron emission tomography," *Cancer and Metastasis Reviews*, vol. 27, no. 4, pp. 545–554, 2008.

[2] D. Delbeke, R. E. Coleman, M. J. Guiberteau et al., "Procedure guideline for tumor imaging with ^{18}F-FDG PET/CT 1.0," *Journal of Nuclear Medicine*, vol. 47, no. 5, pp. 885–895, 2006.

[3] M. G. Buse, "Hexosamines, insulin resistance and the complications of diabetes: current status," *American Journal of Physiology*, vol. 290, pp. 1–15, 2006.

[4] S. P. N. Iyer and G. W. Hart, "Dynamic nuclear and cytoplasmic glycosylation: enzymes of O-GlcNAc cycling," *Biochemistry*, vol. 42, no. 9, pp. 2493–2499, 2003.

[5] K. Mang'era, H. Vanbilloen, B. Cleynhens et al., "Synthesis and evaluation of the ^{99m}Tc-complexes of L-cysteine acetyldiglycine (a hybrid of MAG3 and L,L-EC) and of L-β-homocysteine acetyldiglycine," *Nuclear Medicine and Biology*, vol. 27, no. 8, pp. 781–789, 2000.

[6] H. P. Vanbilloen, B. J. Cleynhens, and A. M. Verbruggen, "Synthesis and biological evaluation of the four isomers of technetium-99m labeled ethylenecysteamine cysteine (^{99m}Tc-ECC), the mono-acid derivative of ^{99m}Tc-L,L-ethylenedicysteine," *Nuclear Medicine and Biology*, vol. 27, no. 2, pp. 207–214, 2000.

[7] D. J. Yang, S. Ilgan, T. Higuchi et al., "Noninvasive assessment of tumor hypoxia with ^{99m}Tc labeled metronidazole," *Pharmaceutical Research*, vol. 16, no. 5, pp. 743–750, 1999.

[8] D. J. Yang, A. Azhdarinia, P. Wu et al., "*In vivo* and in vitro measurement of apoptosis in breast cancer cells using ^{99m}Tc-EC-annexin V," *Cancer Biotherapy and Radiopharmaceuticals*, vol. 16, no. 1, pp. 73–83, 2001.

[9] D. J. Yang, W. E. Fogler, J. L. Bryant et al., "Assessment of antiangiogenic effect using ^{99m}Tc-EC-endostatin," *Cancer Biotherapy and Radiopharmaceuticals*, vol. 17, no. 2, pp. 233–246, 2002.

[10] N. R. Schechter, D. J. Yang, A. Azhdarinia et al., "Assessment of epidermal growth factor receptor with ^{99m}Tc-ethylenedicysteine-C225 monoclonal antibody," *Anti-Cancer Drugs*, vol. 14, no. 1, pp. 49–56, 2003.

[11] D. J. Yang, C. G. Kim, N. R. Schechter et al., "Imaging with ^{99m}Tc ECDG targeted at the multifunctional glucose transport system: feasibility study with rodents," *Radiology*, vol. 226, no. 2, pp. 465–473, 2003.

[12] H. C. Song, H. S. Bom, K. H. Cho et al., "Prognostication of recovery in patients with acute ischemic stroke using brain spect with ^{99m}Tc-labeled metronidazole," *Stroke*, vol. 34, no. 4, pp. 982–986, 2003.

[13] D. J. Yang, J. Bryant, J. Y. Chang et al., "Assessment of cyclooxygense-2 expression with ^{99m}Tc-labeled celebrex," *Anti-Cancer Drugs*, vol. 15, no. 3, pp. 255–263, 2004.

[14] D. J. Yang, M. Yukihiro, C. S. Oh et al., "Assessment of therapeutic tumor response using ^{99m}Tc-Ethylenedicysteine-Glucosamine," *Cancer Biotherapy and Radiopharm*, vol. 19, no. 4, pp. 444–458, 2004.

[15] N. R. Schechter, R. E. Wendt, D. J. Yang et al., "Radiation dosimetry of ^{99m}Tc-labeled C225 in patients with squamous cell carcinoma of the head and neck," *Journal of Nuclear Medicine*, vol. 45, no. 10, pp. 1683–1687, 2004.

[16] D. J. Yang, K. Ozaki, C. S. Oh et al., "^{99m}Tc-EC-guanine: synthesis, biodistribution, and tumor imaging in animals," *Pharmaceutical Research*, vol. 22, no. 9, pp. 1471–1479, 2005.

[17] M. Ito, D. J. Yang, O. Mawlawi et al., "PET and Planar Imaging of Tumor Hypoxia With Labeled Metronidazole," *Academic Radiology*, vol. 13, no. 5, pp. 598–609, 2006.

[18] J. Gong, D. Yang, S. Kohanim, R. Humphreys, L. Broemeling, and R. Kurzrock, "Novel *In vivo* imaging shows up-regulation of death receptors by paclitaxel and correlates with enhanced antitumor effects of receptor agonist antibodies," *Molecular Cancer Therapeutics*, vol. 5, no. 12, pp. 2991–3000, 2006.

[19] H. Kurihara, D. J. Yang, M. Cristofanilli et al., "Imaging and dosimetry of ^{99m}Tc EC annexin V: preliminary clinical study targeting apoptosis in breast tumors," *Applied Radiation and Isotopes*, vol. 66, no. 9, pp. 1175–1182, 2008.

[20] K. Kayser, G. Böhm, S. Blum et al., "Glyco- and immunohistochemical refinement of the differential diagnosis between mesothelioma and metastatic carcinoma and survival analysis of patients," *The Journal of Pathology*, vol. 193, no. 2, pp. 175–180, 2001.

[21] S. Rastogi, S. Banerjee, S. Chellappan, and G. R. Simon, "Glut-1 antibodies induce growth arrest and apoptosis in human cancer cell lines," *Cancer Letters*, vol. 257, no. 2, pp. 244–251, 2007.

[22] M. D. Schulz, K. A. Zubris, J. E. Wade et al., "Paclitaxel-loaded expansile nanoparticles in a multimodal treatment model of malignant mesothelioma," *The Annals of Thoracic Surgery*, vol. 92, no. 6, pp. 2007–2013, 2011.

[23] S. Marshall, V. Bacote, and R. R. Traxinger, "Discovery of a metabolic pathway mediating glucose-induced desensitization of the glucose transport system: role of hexosamine in the induction of insulin resistance," *Journal of Biological Chemistry*, vol. 266, no. 8, pp. 4706–4712, 1991.

[24] A. Scheepers, H. G. Joost, and A. Schürmann, "The glucose transporter families SGLT and GLUT: molecular basis of normal and aberrant function," *Journal of Parenteral and Enteral Nutrition*, vol. 28, no. 5, pp. 364–371, 2004.

[25] L. Wells, K. Vosseller, and G. W. Hart, "Glycosylation of nucleocytoplasmic proteins: signal transduction and O-GlcNAc," *Science*, vol. 291, no. 5512, pp. 2376–2378, 2001.

[26] N. R. Schechter, W. D. Erwin, D. J. Yang et al., "Radiation dosimetry and biodistribution of ^{99m}Tc-ethylene dicysteine-deoxyglucose in patients with non-small-cell lung cancer," *European Journal of Nuclear Medicine and Molecular Imaging*, vol. 36, no. 10, pp. 1583–1591, 2009.

Hindawi Publishing Corporation
Journal of Biomedicine and Biotechnology
Volume 2012, Article ID 130169, 6 pages
doi:10.1155/2012/130169

Research Article

Effect of Low Tube Voltage on Image Quality, Radiation Dose, and Low-Contrast Detectability at Abdominal Multidetector CT: Phantom Study

Kun Tang,[1] Ling Wang,[2] Rui Li,[1] Jie Lin,[1] Xiangwu Zheng,[1] and Guoquan Cao[1]

[1] *Department of Radiology, The First Affiliated Hospital of Wenzhou Medical College, Zhejiang, Wenzhou 325000, China*
[2] *Department of Nuclear Medicine, Wenzhou Medical College, Zhejiang, Wenzhou 325000, China*

Correspondence should be addressed to Xiangwu Zheng, zxwu1111@sina.com

Received 5 January 2012; Revised 19 February 2012; Accepted 24 February 2012

Academic Editor: Lie-Hang Shen

Purpose. To investigate the effect of low tube voltage (80 kV) on image quality, radiation dose, and low-contrast detectability (LCD) at abdominal computed tomography (CT). *Materials and Methods*. A phantom containing low-contrast objects was scanned with a CT scanner at 80 and 120 kV, with tube current-time product settings at 150–650 mAs. The differences between image noise, contrast-to-noise ratio (CNR), and scores of LCD obtained with 80 kV at 150–650 mAs and those obtained with 120 kV at 300 mAs were compared respectively. *Results*. The image noise substantially increased with low tube voltage. However, with identical dose, use of 80 kV resulted in higher CNR compared with CNR at 120 kV. There were no statistically significant difference in CNR and scores of LCD between 120 kV at 300 mAs and 80 kV at 550–650 mAs ($P > 0.05$). The relative dose delivered at 80 kV ranged from 58% at 550 mAs to 68% at 650 mAs. *Conclusion*. With a reduction of the tube voltage from 120 kV to 80 kV at abdominal CT, the radiation dose can be reduced by 32% to 42% without degradation of CNR and LCD.

1. Introduction

There has been a remarkable increase in use of multidetector computed tomography (MDCT) since its introduction. MDCT has greater diagnostic capability and enables extended clinical applications, but it also has the potential to lead to an increase in radiation dose owing to the routine use of thinner sections, the extended volume of acquisition, and multiple-phase acquisitions. According to the literature, currently, CT represents about 7% of all radiologic examinations in the world but contributes more than 40% of the collective effective dose [1]. The theoretic risk to patients for radiation-indeed cancer from CT examination is not negligible [2–4].

In particular, the radiation dose from hepatic CT examinations has notably increased because multiple-phase dynamic-enhanced CT scan was routinely performed in patients who are suspected of having hepatic tumors. The estimated risk of cancer death for those undergoing CT is 12.5/10,000 population for each pass of the CT scan through the abdomen [5]. Therefore, concerns regarding a reduction in radiation dose have been recently raised during abdominal CT acquisitions.

Although decreasing tube current is the most means of reducing CT radiation dose [6–9], this alteration also reduces the contrast-to-noise ratio (CNR), which may affect the diagnostic outcome of the examination. This is especially true in abdominal studies, where low-contrast areas are severely affected by the CNR [10]. Some studies [11–15] suggest that scanning with low tube voltage is possible to reduce dose without markedly affecting image quality; however, there are few reports on the effect of low tube voltage on abdominal image quality and low-contrast detectability (LCD). Thus, the purpose of this study was to investigate the effect of low tube voltage with 80 kV on image noise (SD, standard deviation of CT number), CNR, radiation dose, and LCD at abdominal MDCT.

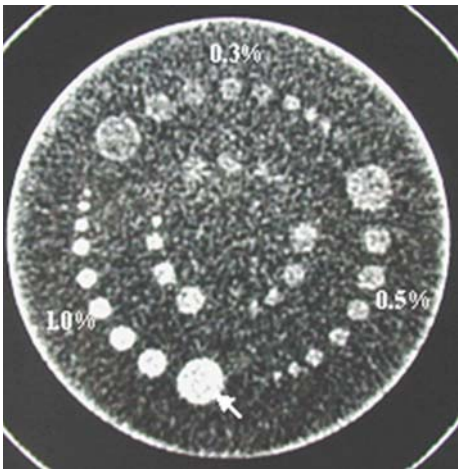

Figure 1: An axial CT image of the low-contrast module. It contains three groups of cylinders with various diameters from 2.0 to 15.0 mm. The nominal contrast levels of these groups are 0.3%, 0.5%, and 1.0%. In our study, only the 15.0 mm diameter object with a contrast difference of 1.0% (white arrow) was chosen to be analyzed.

2. Materials and Methods

The institutional review board approved this study, and informed consent was obtained from all participating radiologists.

2.1. Description of Phantom. We used a phantom (Catphan 500; Phantom Laboratory, Cambridge, NY) with an additional annulus provided by the manufacturer to simulate the X-ray absorption of a standard abdomen (giving a total test object diameter of 30 cm). The phantom contains a CTP515 module, which consists of a 40 mm thick and 200 mm diameter slice of tissue equivalent background material containing a series of cylinders of various diameters to measure low-contrast performance. The cylinders varied in diameters from 2.0 to 15.0 mm and deviated from nominal contrast levels by 0.3%, 0.5%, and 1.0% (Figure 1). In our study, in order to avoid a partial volume effect, only the 15.0 mm diameter object with a contrast difference of 1.0% (having an attenuation difference with the background of 10 HU) was chosen to be analyzed. The phantom was always positioned at the isocenter of the gantry.

2.2. CT Scanning. The phantom was scanned three times for each protocol with a 16-section MDCT scanner (LightSpeed; GE Medical Systems). The scanning parameters were configuration of 16 (detectors) ×1.5 mm (detector collimation), rotation time of 0.75 second, section thickness of 5.0 mm, section interval of 5.0 mm, pitch of 0.659, scan field of view of 50 cm, reconstruction algorithm (kernel) B30f (medium-sharp), and pixel matrix size of 512 × 512. Scanning was performed at the standard tube voltage of 120 kV and at the low tube voltage of 80 kV, with corresponding tube current-time product settings at 150, 200, 250, 300, 350, 400, 450, 500, 550, 600, and 650 mAs, respectively.

2.3. Measurement of Radiation Dose. We used the CT dose index volume (CTDIvol) based on the manufacturer's data for estimation of radiation dose. The corresponding CTDIvol of each acquisition conditions indicated on the monitor screen was recorded. The CTDIvol obtained at standard tube voltage protocol was compared with that obtained at low tube voltage protocol.

2.4. Measurement of CNR. For each scanning technique, we measured the CT number of the low-contrast object in 15 mm diameter and the background of the module. The region of interest used to perform the measurements was kept at 100 mm^2. CNRs were calculated as follows: CNR = (ROIm − ROIb)/SDb, where ROIm and ROIb are the CT numbers of the low-contrast object in a 15 mm diameter region of interest and of the background region of interest, respectively, and SDb is the standard deviation of the attenuation values of the background [16]. A CNR was calculated on the three images of each set of acquisition parameters. The measurement was repeated three times on each image, giving nine measurements for each acquisition condition. From these nine measurements, a mean CNR was calculated for each set of acquisition conditions [17].

2.5. Assessment of LCD. For the subjective assessments of LCD, we evaluated the images obtained at 120 kV and 300 mAs and the images obtained at 80 kV and 150–650 mAs. Two experienced observers who were blind to each set of scanning parameters were asked to review independently the images. The visualization of each object was graded on a 3-point scoring scale by each observer: a score of 3.0 was obtained when the object was clearly visible and appeared as a perfect circle, a score of 2.0 was obtained when the object was not clearly visible, and a score of 1.0 was obtained when the object could not be detected. A total of 36 images (twelve sets of three images each) were respectively assessed by each observer. The final score of LCD of each acquisition sets was calculated by averaging the results of the two observers. The time for reading the images was not limited, and each observer could freely adjust the window levels and window widths on the monitor screen.

2.6. Statistical Analysis. We used a two-tailed Student's t test to evaluate differences in SD, CNR, and CTDIvol between scanning performed with 80 kV and scanning performed with 120 kV. Both the relationship between SD and tube current-time product settings and the relationship between CNR and CTDIvol were investigated using the linear regression analysis and Pearson correlation coefficient (r). For subjective assessment, the Mann-Whitney U test was used to analyze differences in subjective scores between standard setting (120 kV, 300 mAs) and low tube voltage settings (80 kV, 150–650 mAs). Interobserver variation was assessed using Cohen kappa statistics. Kappa values less than 0.20 indicated poor agreement; 0.21–0.40, fair agreement; 0.41–0.60, moderate agreement; 0.61–0.80, good agreement; 0.81–1.00, excellent agreement. All statistical analyses were performed with a commercially available software package

Table 1: The CTDIvol values obtained at each set of acquisition conditions.

Tube current-time product (mAs)	CTDIvol (mGy)	
	120 kVp	80 kVp
150	10.19	3.24
200	13.59	4.33
250	16.99	5.41
300	20.39	6.49
350	23.55	7.49
400	26.91	8.57
450	30.28	9.64
500	33.64	10.71
550	37.00	11.78
600	40.37	12.85
650	43.73	13.92

(SPSS, version 15.0), and a P value of less than 0.05 was considered to be statistically significant.

3. Results

3.1. Radiation Dose. The CTDIvol obtained from each set of acquisition conditions is shown in Table 1. At equal tube current-time product settings, the CTDIvol obtained at 80 kV was approximately 32% of that at 120 kV. Compared with the CTDIvol obtained at 120 kV and 300 mAs, the relative CTDIvols obtained at 80 kV were 16% at 150 mAs, 21% at 200 mAs, 27% at 250 mAs, 32% at 300 mAs, 37% at 350 mAs, 42% at 400 mAs, 47% at 450 mAs, 53% at 500 mAs, 58% at 550 mAs, 63% at 600 mAs, and 68% at 650 mAs.

3.2. Image Quality Results. The results of CT numbers, image noise, and CNR at each scanning technique are listed in Table 2. As expected, the image noise was inversely correlative to tube current. At identical tube current, the lowest and the highest noise were seen at 120 kV and 80 kV, respectively (Figure 2). Compared with the noise obtained with 120 kV at 300 mAs, the noise obtained with 80 kV at 150–650 mAs was significantly higher ($P < 0.001$) (Table 2). There was a direct correlation between the CNR and the CTDIvol, with Pearson correlation coefficient $r = 0.95$ ($P < 0.001$) at 80 kV and $r = 0.96$ ($P < 0.001$) at 120 kV. At identical CTDIvol, use of 80 kV tube voltage resulted in higher CNR compared with CNR at 120 kV. At identical CNR, the CTDIvol at 80 kV was substantially lower than that at 120 kV (Figure 3). By using a two-tailed Student's t test, the CNRs obtained at 80 kV and 150–500 mAs were significantly lower than that at 120 kV and 300 mAs ($P < 0.05$) (Table 2). However, there was no statistically significant difference between the CNR obtained with 120 kV at 300 mAs and the CNR obtained with 80 kV at 550 mAs, 600 mAs, and 650 mAs ($P > 0.05$) (Table 2).

3.3. LCD Results. The subjective scores of LCD assigned by two observers are shown in Table 3. The mean score of the three images assigned at 120 kV and 300 mAs was 2.83 ± 0.41. At 80 kV, the mean score (1.00 ± 0.00 at 150–250 mAs, 1.83 ± 0.41 at 300 mAs, 2.00 ± 0.00 at 350 mAs, 2.33 ± 0.52 at 400–500 mAs) was significantly lower than that at 120 kV and 300 mAs ($P = 0.001$ at 150–350 mAs; $P = 0.019$ at 400–500 mAs) (Table 3). However, there was no statistically significant difference between the mean score at 120 kV and 300 mAs and the mean score assigned at 80 kV and the other tube current settings that we investigated ($P = 0.138$ at 550 mAs; $P = 0.317$ at 600 mAs; $P = 1.0$ at 650 mAs) (Table 3). Using Cohen kappa statistics, the interobserver agreement in regard to subjective assessment of LCD was good ($\kappa = 0.67$).

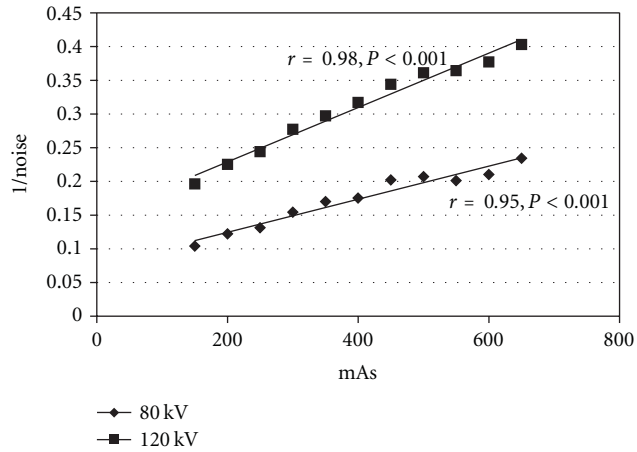

Figure 2: Graph shows inversely correlative between tube current (mAs) and image noise. At identical tube current, image noise obtained at 80 kV is higher than that at 120 kV.

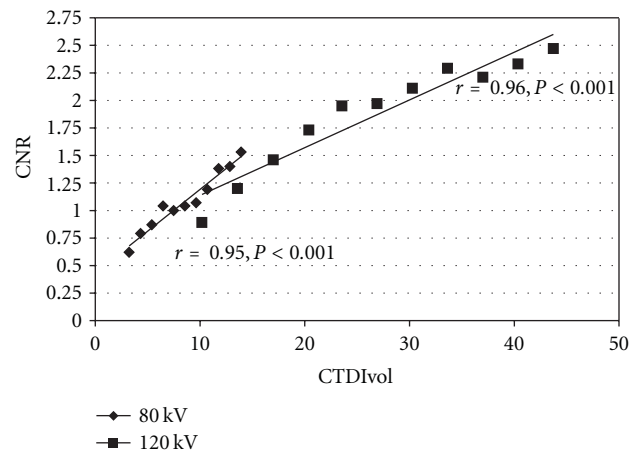

Figure 3: Graph shows relationship between CTDIvol and CNR. The Pearson correlation coefficient (r) and the corresponding P values were $r = 0.95$ and $P < 0.001$ at 80 kV and $r = 0.96$ and $P < 0.001$ at 120 kV.

4. Discussion

Improvement in MDCT technology now allows CT examinations to be easily and fast performed, leading to a possible increase of the radiation dose to patients. In particular, the radiation exposure and risk of cancer death from hepatic CT examinations have notably increased because multiple-phase

Table 2: The CT numbers, image noise, and CNR obtained at each set of acquisition conditions.

Tube current-time product (mAs)	CT number		P value	Image noise		P value*	CNR		P value*
	120 kV	80 kV		120 kV	80 kV		120 kV	80 kV	
150	56.12	27.56	<0.001	5.10	9.60	<0.001	0.89	0.62	<0.001
200	56.34	27.73	<0.001	4.45	8.20	<0.001	1.20	0.79	<0.001
250	56.21	28.17	<0.001	4.09	7.61	<0.001	1.46	0.87	0.006
300	56.76	28.35	<0.001	3.61	6.50	<0.001	1.73	1.04	0.029
350	56.93	28.21	<0.001	3.37	5.88	<0.001	1.95	1.00	0.025
400	56.77	28.41	<0.001	3.15	5.70	<0.001	1.97	1.04	0.028
450	56.69	28.43	<0.001	2.91	4.96	<0.001	2.11	1.07	0.031
500	57.00	28.36	<0.001	2.77	4.82	<0.001	2.29	1.19	0.042
550	56.78	28.68	<0.001	2.75	4.97	<0.001	2.21	1.38	0.224
600	57.14	28.78	<0.001	2.65	4.76	<0.001	2.33	1.40	0.272
650	57.14	28.86	<0.001	2.48	4.27	<0.001	2.47	1.53	0.501

*The P values are those obtained with 80 kV at the 150–650 mAs settings compared with the values obtained with 120 kV and 300 mAs.

Table 3: The subjective scores of LCD.

Tube voltage/tube current-time product	Subjective score of LCD		Mean	P value*
	Observer A	Observer B		
80 kV/150 mAs	3.0 (1.0, 1.0, 1.0)	3.0 (1.0, 1.0, 1.0)	1.00 ± 0.00	0.001
80 kV/200 mAs	3.0 (1.0, 1.0, 1.0)	3.0 (1.0, 1.0, 1.0)	1.00 ± 0.00	0.001
80 kV/250 mAs	3.0 (1.0, 1.0, 1.0)	3.0 (1.0, 1.0, 1.0)	1.00 ± 0.00	0.001
80 kV/300 mAs	5.0 (1.0, 2.0, 2.0)	6.0 (2.0, 2.0, 2.0)	1.83 ± 0.41	0.001
80 kV/350 mAs	6.0 (2.0, 2.0, 2.0)	6.0 (2.0, 2.0, 2.0)	2.00 ± 0.00	0.001
80 kV/400 mAs	7.0 (2.0, 3.0, 2.0)	7.0 (2.0, 3.0, 2.0)	2.33 ± 0.52	0.019
80 kV/450 mAs	7.0 (3.0, 2.0, 2.0)	7.0 (2.0, 2.0, 3.0)	2.33 ± 0.52	0.019
80 kV/500 mAs	8.0 (2.0, 3.0, 3.0)	6.0 (2.0, 2.0, 2.0)	2.33 ± 0.52	0.019
80 kV/550 mAs	8.0 (3.0, 3.0, 2.0)	8.0 (3.0, 2.0,3.0)	2.67 ± 0.52	0.138
80 kV/600 mAs	9.0 (3.0, 3.0, 3.0)	8.0 (2.0, 3.0, 3.0)	2.83 ± 0.41	0.317
80 kV/650 mAs	9.0 (3.0, 3.0, 3.0)	9.0 (3.0, 3.0, 3.0)	3.00 ± 0.00	1.000
120 kV/300 mAs	9.0 (3.0, 3.0, 3.0)	9.0 (3.0, 3.0, 3.0)	3.00 ± 0.00	—

*The P values are those obtained with 80 kV at the 150–650 mAs settings compared with the values obtained with 120 kV and 300 mAs. There was good agreement between observer A and observer B in regard to subjective assessment of LCD ($\kappa = 0.67$).

dynamic-enhanced CT scan is routinely performed. Managing patient dose is therefore a major concern in abdominal MDCT examinations.

In our study, we used the CT dose index volume (CTDIvol) based on the manufacturer's data for estimation of radiation dose. CTDI, expressed in terms of air kerma in milligray, was obtained at the periphery (CTDIp) and at the centre (CTDIc) of a special 100 mm long pencil-shaped ionisation chamber. The weighted CTDIw is obtained as the sum of one-third of CTDIc and two-thirds of CTDIp. The CTDIvol, which is CTDIw divided by the pitch, represents the average volume dose (air kerma) within a specified CT dosimetry phantom [18]. CTDIvol is a good measure of CT radiation dose for applications where the patient table is incremented during the scan. Adoption of CTDIvol as the intensity of the radiation dose would facilitate accurate comparisons of radiation doses used for different tube voltages. For instance, in our study, it is easy for us to compare the difference of radiation dose between 80 kV and 120 kV tube voltage. Results of our study showed that it was possible to reduce radiation exposure substantially by decreasing the tube voltage from 120 kV to 80 kV. However, it has limitations. Because the CTDIvol is an averaged dose to a homogeneous cylindrical phantom, the measurements are only an approximation of patient dose. Another limitation is that CTDIvol phantom does not provide a sufficiently long scatter path relative to the typical length of a human; hence, patient dose may be underestimated with CTDIvol [19]. Therefore, the results of radiation dose based on the CTDIvol in our study could not be accurate represented patient dose. Furthermore, the difference of the radiation dose between the central and peripheral cavities of the phantom also could not be discerned by using the CTDIvol as estimation of radiation dose.

In present study, our findings showed that there was a direct correlation between the CNR and the CTDIvol, which was consistent with previous studies [16, 20]. Although the mean CNR was decreased when CT acquisition was performed at a tube voltage of 80 kV and an identical tube current setting, CNR improved substantially when identical CTDIvol was used. Compared with CNR obtained at 120 kV

and 300 mAs, there was no statistically significant difference at 80 kV and 550 mAs, 600 mAs, and 650 mAs ($P > 0.05$). This suggest that image quality including CNR acquired at 80 kV with tube current higher than 550 mAs is equivalent to that acquired at 120 kV and 300 mAs. Furthermore, the relative radiation dose obtained at 80 kV and 550 mAs, 600 mAs, and 650 mAs was 58%, 63%, and 68% of that at 120 kVp and 300 mAs, respectively. Therefore, we postulate that scanning with a low tube voltage as low as 80 kV is feasible in abdominal CT examination without loss of diagnostic accuracy when the tube current is higher than 550 mAs allowing reduction in the radiation dose by 32% to 42%.

LCD is one of the most important factors in abdominal CT, especially when looking for small lesions in abdominal organs such as liver, spleen, pancreas, or kidneys. This LCD is not only relevant for unenhanced series but also contrast enhanced series, as contrast between normal and abnormal tissue may be only slightly increased by iodine [21]. Awai et al. [22] reported that in enhanced hepatic CT, tumor-to-liver contrast was 5–40 HU. In present study, the object with a contrast difference of 1.0% (having an attenuation difference with the background of 10 HU) was chosen to be analyzed. When the two experienced observers subjectively assessed the visibilities of low-contrast images, the subjective scores of LCD assigned at 80 kV and 550, 600, and 650 mAs did not differ significantly from those assigned at 120 kV and 300 mAs. Furthermore, the mean score of LCD obtained at 80 kV and 650 mAs was slightly higher than that at 120 kV and 300 mAs. These results suggested that a reduction from 120 kV to 80 kV also could result in up to 42% dose reduction without compromising LCD. Funama et al. [16] showed that a 35% reduction in the radiation dose could be achieved when scanning was performed at 90 kV rather than at 120 kV without degradation of LCD. Our findings agree with Funama and suggest that lower tube voltage can be used in abdominal CT thereby achieving dose reduction while maintaining acceptable image quality. In this study, we found no statistically significant difference in both CNR and LCD at 120 kV and 300 mAs compared with those at 80 kV and 550–650 mAs. This is probably because CNR and LCD are parallel to each other, which is consistent with Verdun's result [17]. He found that there was a significant correlation between the mean CNR measurements and the subjective scores of LCD ($r = 0.95$, $P < 0.05$).

The main drawback of the low tube voltage technique is the increase in image noise caused by the reduced photon flux. In our study, we found that the noise values obtained with 80 kV at the 150–650 mAs settings were significant higher than that obtained with 120 kV and 300 mAs ($P < 0.001$). As previously reported [10, 20], we found that there was an inversely correlative relationship between the image noise and the tube current. In another word, the increased noise will be obtained when the strategy of lower tube current or lower tube voltage is implemented. Image noise, however, has a greater effect on the quality of abdominal images because the abdominal region is inherently of lower contrast. Therefore, for CT scanning with low tube voltage, higher tube current settings are required to compensate for the lower number of photons. In addition, some new techniques should be developed to reduce image noise. Several articles in the last years have been reported that noise reduction filters [23–25] as well as reconstruction methods, such as adaptive statistical iterative reconstruction [26–28] could effectively help to reduce the noise on CT images with radiation dose reduction without compromise of image quality.

4.1. Study Limitations. We acknowledge that this study contains certain limitations. First, this CT scanning with low tube voltage at 80 kV was only performed in a phantom study, and the phantom did not consider variability of body composition, therefore, whether this result is suitable to clinical using needs to be further confirmed. However, Marin et al. [14] showed that a technique with low tube voltage at 80 kV could be applied to improve the conspicuity of malignant hypervascular liver tumors while significantly reducing patient radiation dose. Secondly, our investigation did not take into account differences in body sizes. Attenuation of the incident X-ray beam in CT depends on the size of body portion being evaluated; that is, greater exposure is required in corpulent patients to attain image quality equal to that in slimmer patients [29]. Although studies in patients were not part of this investigation, previous studies with a phantom suggest that the technique is effective for dose reduction of abdominal CT for relatively light weight patients whose body weight is less than 80 kg [30]. Another important aspect is that many patients present with high-attenuation implants, which can dramatically decrease image quality when low kV protocols are used routinely. Finally, we only used the CTDIvol provided by the manufacturer to estimate the radiation dose. Although the agreement between the values provided by the manufacturer and the measured values was good, with differences of less than 10% [31], there were some limitations as mentioned above.

5. Conclusions

In this CT phantom study we have shown that although image noise is increased at low tube voltage, it is possible to reduce radiation dose by up to 42% without degradation of CNR and LCD by reducing tube voltage from 120 to 80 kV and increasing tube current to more than 550 mAs. As an effective technique of reducing CT radiation dose, scanning with low tube voltage would benefit patients with relatively light weight, especially those who may need to undergo MDCT examinations for long-term followup or high-risk screening.

References

[1] F. A. Mettler Jr., M. Bhargavan, K. Faulkner et al., "Radiologic and nuclear medicine studies in the United States and worldwide: frequency, radiation dose, and comparison with other radiation sources—1950–2007," *Radiology*, vol. 253, no. 2, pp. 520–531, 2009.

[2] D. J. Brenner and C. D. Elliston, "Estimated radiation on risks potentially associated with full-body CT screening," *Radiology*, vol. 232, no. 3, pp. 735–738, 2004.

[3] D. J. Brenner, "Radiation risks potentially associated with low-dose CT screening of adult smokers for lung cancer," *Radiology*, vol. 231, no. 2, pp. 440–445, 2004.
[4] A. B. De González and S. Darby, "Risk of cancer from diagnostic X-rays: estimates for the UK and 14 other countries," *Lancet*, vol. 363, no. 9406, pp. 345–351, 2004.
[5] V. Tsapaki, M. Rehani, and S. Saini, "Radiation safety in abdominal computed tomography," *Seminars in Ultrasound, CT and MRI*, vol. 31, no. 1, pp. 29–38, 2010.
[6] S. A. Sohaib, P. D. Peppercorn, J. A. Horrocks, M. H. Keene, G. S. Kenyon, and R. H. Reznek, "The effect of decreasing mAs on image quality and patient dose in sinus CT," *British Journal of Radiology*, vol. 74, no. 878, pp. 157–161, 2001.
[7] L. M. Hamberg, J. T. Rhea, G. J. Hunter, and J. H. Thrall, "Multi-detector row CT: radiation dose characteristics," *Radiology*, vol. 226, no. 3, pp. 762–772, 2003.
[8] D. P. Frush, C. C. Slack, C. L. Hollingsworth et al., "Computer-simulated radiation dose reduction for abdominal multidetector CT of pediatric patients," *American Journal of Roentgenology*, vol. 179, no. 5, pp. 1107–1113, 2002.
[9] A. F. Kopp, M. Heuschmid, and C. D. Claussen, "Multidetector helical CT of the liver for tumor detection and characterization," *European Radiology*, vol. 12, no. 4, pp. 745–752, 2002.
[10] "Managing patient dose in computed tomography. A report of the International Commission on Radiological Protection," *Annals of the ICRP*, vol. 30, no. 4, pp. 7–45, 2000.
[11] J. Hausleiter, S. Martinoff, M. Hadamitzky et al., "Image quality and radiation exposure with a low tube voltage protocol for coronary CT angiography: results of the PROTECTION II Trial," *Cardiovascular Imaging*, vol. 3, no. 11, pp. 1113–1123, 2010.
[12] D. Marin, R. C. Nelson, H. Barnhart et al., "Detection of pancreatic tumors, image quality, and radiation dose during the pancreatic parenchymal phase: effect of a low-tube-voltage, high-tube-current CT technique—preliminary results," *Radiology*, vol. 256, no. 2, pp. 450–459, 2010.
[13] S. T. Schindera, R. C. Nelson, S. Mukundan et al., "Hypervascular liver tumors: low tube voltage, high tube current multidetector row CT for enhanced detection—phantom study," *Radiology*, vol. 246, no. 1, pp. 125–132, 2008.
[14] D. Marin, R. C. Nelson, E. Samei et al., "Hypervascular liver tumors: low tube voltage, high tube current multidetector CT during late hepatic arterial phase for detection—initial clinical experience," *Radiology*, vol. 251, no. 3, pp. 771–779, 2009.
[15] B. Bischoff, F. Hein, T. Meyer et al., "Impact of a reduced tube voltage on CT angiography and radiation dose. Results of the PROTECTION I Study," *Cardiovascular Imaging*, vol. 2, no. 8, pp. 940–946, 2009.
[16] Y. Funama, K. Awai, Y. Nakayama et al., "Radiation dose reduction without degradation of low-contrast detectability at abdominal multisection CT with a low-tube voltage technique: phantom study," *Radiology*, vol. 237, no. 3, pp. 905–910, 2005.
[17] F. R. Verdun, A. Denys, J. F. Valley, P. Schnyder, and R. A. Meuli, "Detection of low-contrast objects: experimental comparison of single- and multi-detector row CT with a phantom1," *Radiology*, vol. 223, no. 2, pp. 426–431, 2002.
[18] C. H. McCollough, M. R. Bruesewitz, M. F. McNitt-Gray et al., "The phantom portion of the American College of Radiology (ACR) Computed Tomography (CT) accreditation program: practical tips, artifact examples, and pitfalls to avoid," *Medical Physics*, vol. 31, no. 9, pp. 2423–2442, 2004.
[19] R. L. Dixon and K. E. Ekstrand, "A film dosimetry system for use in computed tomography," *Radiology*, vol. 127, no. 1, pp. 255–258, 1978.
[20] A. Waaijer, M. Prokop, B. K. Velthuis, C. J. G. Bakker, G. A. P. De Kort, and M. S. Van Leeuwen, "Circle of Willis at CT angiography: dose reduction and image quality—reducing tube voltage and increasing tube current settings," *Radiology*, vol. 242, no. 3, pp. 832–839, 2007.
[21] H. J. Brisse, J. Brenot, N. Pierrat et al., "The relevance of image quality indices for dose optimization in abdominal multidetector row CT in children: experimental assessment with pediatric phantoms," *Physics in Medicine and Biology*, vol. 54, no. 7, pp. 1871–1892, 2009.
[22] K. Awai, K. Takada, H. Onishi, and S. Hori, "Aortic and hepatic enhancement and tumor-to-liver contrast: analysis of the effect of different concentrations of contrast material at multidetector row helical CT," *Radiology*, vol. 224, no. 3, pp. 757–763, 2002.
[23] Y. Yanaga, K. Awai, Y. Funama et al., "Low-dose MDCT urography: feasibility study of low-tube-voltage technique and adaptive noise reduction filter," *American Journal of Roentgenology*, vol. 193, no. 3, pp. W220–W229, 2009.
[24] M. K. Kalra, M. M. Maher, D. V. Sahani et al., "Low-dose CT of the abdomen: evaluation of image improvement with use of noise reduction filters—pilot study," *Radiology*, vol. 228, no. 1, pp. 251–256, 2003.
[25] M. K. Kalra, M. M. Maher, M. A. Blake et al., "Detection and characterization of lesions on low-radiation-dose abdominal CT images postprocessed with noise reduction filters," *Radiology*, vol. 232, no. 3, pp. 791–797, 2004.
[26] M. Yanagawa, O. Honda, S. Yoshida et al., "Adaptive statistical iterative reconstruction technique for pulmonary CT. Image quality of the cadaveric lung on standard- and reduced-dose CT," *Academic Radiology*, vol. 17, no. 10, pp. 1259–1266, 2010.
[27] S. Singh, M. K. Kalra, M. D. Gilman et al., "Adaptive statistical iterative reconstruction technique for radiation dose reduction in chest CT: a pilot study," *Radiology*, vol. 259, no. 2, pp. 565–573, 2011.
[28] Y. Sagara, A. K. Hara, W. Pavlicek, A. C. Silva, R. G. Paden, and Q. Wu, "Abdominal CT: comparison of low-dose CT with adaptive statistical iterative reconstruction and routine-dose CT with filtered back projection in 53 patients," *American Journal of Roentgenology*, vol. 195, no. 3, pp. 713–719, 2010.
[29] J. R. Haaga, "Radiation dose management: weighing risk versus benefit," *American Journal of Roentgenology*, vol. 177, no. 2, pp. 289–291, 2001.
[30] Y. Nakayama, K. Awai, Y. Funama et al., "Abdominal CT with low tube voltage: preliminary observations about radiation dose, contrast enhancement, image quality, and noise," *Radiology*, vol. 237, no. 3, pp. 945–951, 2005.
[31] F. R. Verdun, N. Theumann, P. A. Poletti et al., "Impact of the introduction of 16-row MDCT on image quality and patient dose: phantom study and multi-centre survey," *European Radiology*, vol. 16, no. 12, pp. 2866–2874, 2006.

Hindawi Publishing Corporation
Journal of Biomedicine and Biotechnology
Volume 2012, Article ID 205818, 11 pages
doi:10.1155/2012/205818

Research Article

Usefulness of FDG, MET and FLT-PET Studies for the Management of Human Gliomas

Keisuke Miyake, Aya Shinomiya, Masaki Okada, Tetsuhiro Hatakeyama, Nobuyuki Kawai, and Takashi Tamiya

Department of Neurological Surgery, Faculty of Medicine, Kagawa University, 1750-1 Ikenobe, Miki-cho, Kita-gun, Kagawa 761-0793, Japan

Correspondence should be addressed to Keisuke Miyake, keisuke@kms.ac.jp

Received 5 January 2012; Accepted 7 February 2012

Academic Editor: David J. Yang

The use of positron imaging agents such as FDG, MET, and FLT is expected to lead the way for novel applications toward efficient malignancy grading and treatment of gliomas. In this study, the usefulness of FDG, MET and FLT-PET images was retrospectively reviewed by comparing their histopathological findings. FDG, MET, and FLT-PET were performed in 27 patients with WHO grade IV, 15 patients with WHO grade III, and 12 patients with WHO grade II during 5.5 years. The resulting PET images were compared by measuring SUVs and T/N ratios (tumor to normal tissue ratios). Although there were no significant differences in FDG-PET, there were significant differences in the T/N ratios in the MET-PET between WHO grades II and IV and in the FLT-PET between the WHO grades III and IV. In glioblastoma patients, the SUVs of the areas depicted by MRI in the MET-PET were different from those SUVs in the FLT-PET. Importantly, the areas with high SUVs in both MET-PET and FLT-PET were also high in Ki-67 index and were histologically highly malignant. PET imaging is a noninvasive modality that is useful in determining a tumor area for removal as well as improving preoperative diagnosis for gliomas.

1. Introduction

Morphological imaging using magnetic resonance imaging (MRI) is the most commonly used method for obtaining tumor information. Gd-enhanced T1-weighted MRI provides anatomical imaging with hyperintense neovascularization enclosed in a hypointense region of central necrosis. In addition, fluid-attenuated IR (FLAIR) detects the surrounding edema associated with infiltrating tumor cells [1]. The use of positron emission tomography (PET), an imaging modality providing metabolic and molecular information, can improve diagnostic procedures in malignant brain tumors. 2-Deoxy-2-[^{18}F] fluoro-D-glucose (FDG), a commonly used tracer for neoplasm detection, exhibits limited utility in brain tumor imaging, because the uptake is nonspecific and can occur in any region with increased metabolic activity. Moreover, nonspecific FDG uptake can be increased by some inflammatory diseases. In addition, FDG-PET is a marker of glycolytic metabolism and not cellular proliferation. The information it provides is therefore complementary to other imaging techniques [2–5].

L-Methyl-^{11}C-methionine (MET) is a well-established PET radiotracer for brain tumor detection and tumor delineation [6, 7]. Amino acids, including MET, readily cross the intact blood-brain barrier (BBB) through neutral amino acid transporters and are incorporated into the area with active tumor [8]. It has been shown that MET uptake in gliomas significantly correlates with the WHO tumor grade and cell proliferation determined by Ki-67 index [4, 9–11]. However, increased MET uptake in nonneoplastic lesions including inflammation, infarction, and hemorrhage may result in false positives [12, 13]. Also, the short half-life of ^{11}C (20 min) and rapid *in vivo* degradation make MET-PET less useful for routine clinical use.

A fluorinated thymidine analog, 3′-deoxy-3′-[^{18}F] fluorothymidine (FLT), has emerged as a promising PET tracer for evaluating tumor-proliferating activity in various malignant brain tumors [3, 14, 15]. FLT is phosphorylated

by thymidine kinase-1 (TK1), a principle enzyme in the salvage pathway of DNA synthesis, and trapped inside the cells. Phosphorylated FLT appears resistant to degradation and is suitable for imaging with PET. The application of FLT phosphorylation as a marker of cell proliferation is based on the assumption that cellular FLT trapping is a representation of thymidine incorporation into DNA [16, 17]. Since FLT uptake in the normal brain tissue is very low, FLT-PET provides a low-background brain image, making it an ideal PET tracer for the imaging of brain tumors. FLT-PET has been found useful for noninvasive grading of gliomas [18]. In addition, FLT-PET has been utilized in the prognostic assessment and evaluation of treatment response in malignant gliomas [19].

Despite the superior features MET and FLT offer as glioma cell tracers, they are also associated with several problems. The cut-off value of normal versus tumor cell infiltration is difficult to determine. Therefore, the purpose of this prospective study was to clarify the individual and combined roles of FDG-PET, MET-PET, and FLT-PET in tumor detection, noninvasive grading, and assessment of cellular proliferation rate in 54 newly diagnosed histologically verified gliomas of different grades.

2. Materials and Methods

2.1. Patients. From April 2006 through October 2011, 54 patients with newly diagnosed gliomas (23 men and 31 women; mean age: 52.0 ± 18.1 y; range: 22–86 y) were enrolled in this study (Table 1). The use of FDG, MET, and FLT as a PET tracer was approved by the Kagawa University School of Medicine Human Subjects Ethics Committee, and informed written consent was obtained from all patients who participated in this study. Histopathology was performed on tissue specimens obtained by biopsy or resection. All tumors were graded by the World Health Organization (WHO) grading system (malignancy scale) for CNS tumors. Tumor types and grades were distributed as follows and listed in Table 1: WHO grade II diffuse astrocytoma (n = 9), WHO grade II oligoastrocytoma (n = 2), WHO grade II oligodendroglioma (n = 1), WHO grade III anaplastic astrocytoma (n = 11), anaplastic oligoastrocytoma (n = 3), WHO grade III anaplastic oligodendroglioma (n = 1), WHO grade IV glioblastoma multiforme (n = 26), WHO grade IV gliosarcoma (n = 1).

2.2. Proliferation Analysis. Surgical specimens were fixed in 10% formalin and embedded in paraffin. Hematoxylin-and-eosin-stained specimens were checked to determine the histological tumor type. The cellular proliferation activity of the tumor was determined by measuring the Ki-67 proliferation index obtained by immunohistochemical staining with anti-Ki-67/MIB-1 antibody (Dako, Tokyo, Japan). Immunohistochemical slides were examined at high-power magnification (×400). The percentage of tumor cells which stained positively for Ki-67 antigen was measured in the area containing the largest number of positive tumor cells and was regarded as representative of the tumor proliferation activity.

2.3. PET Examination. PET studies were performed using an ECAT EXACT HR + scanner and a Biograph mCT 64 (Siemens/CTI, Knoxville, TN, USA) in three-dimensional acquisition mode. The image system enabled the simultaneous acquisition of 51 transverses per field of view (FOV), with intersection spacing of 3 mm, for a total axial FOV of 15 cm. The in-plane (transverse) reconstructed resolution was 4.7 mm full-width at half-maximum (FWHM) in the brain FOV. Images were reconstructed using the filtered backprojection method with a Hanning filter (kernel FWHM 10 mm, cutoff frequency 0.4 cycle/projection element) to generate 128 × 128 matrices.

PET radiotracers were produced using the HM-18 cyclotron (Sumitomo Heavy Industries, Tokyo, Japan). FLT was synthesized using the method described by Shields et al. [16], and the radiochemical purity of the produced FLT was >95%. MET was produced by proton bombardment of $^{14}N_2$. The resultant $^{11}CO_2$ was reduced to ^{11}C-methanol by lithium aluminum hydride and subsequently converted to $^{11}C\text{-}CH_3I$ by the addition of hydrogen iodide following the modified method described by Ishiwata et al. [20]. The radiochemical purity of the produced MET was >95%.

Each patient received the FDG, MET, and FLT one by one for a continuous 3-day course before the surgery. For the FDG-PET study, enteral and parental sources of glucose were withheld for at least 6 h before the examination. No special dietary instructions were given to the patients before the MET and FLT-PET examination. Images were acquired with patients in the supine position, resting, with their eyes closed. Using ^{68}Ge rod sources rotating around the head, transmission images of the brain were obtained for 5 min for FDG-PET, 3 min for MET-PET, and 5 min for FLT-PET. Transmission scan with ^{68}Ge rod can be replaced to CT attenuation correction in mCT64 system. A dose of 147–295 MBq (mean dose: 208 ± 39 MBq) of ^{18}F-FDG, 113–389 MBq (mean dose: 211 ± 65 MBq) of ^{11}C-MET, or 129–236 MBq (mean dose: 161 ± 25 MBq) of ^{18}F-FLT was injected intravenously. Regional emission images of the brain were obtained for 5 min, beginning 45 min after the ^{18}F-FDG injection; for 5 min, beginning 10 min after the ^{11}C-MET injection; for 10 min, beginning 40 min after the ^{18}F-FLT injection.

2.4. Image Analysis. FDG, MET, and FLT uptake in the brain tumor were semiquantitatively assessed by evaluating the standardized uptake value (SUV). A region of interest (ROI) was set manually by an observer around the hottest area of each lesion. The maximum value of SUV (SUV max) was regarded as the representative value of each tumor. To calculate the tumor-to-normal tissue count density (T/N) ratios, the ROI was set on the normal brain parenchyma (usually contralateral normal cerebral tissue excluding ventricles) and the mean value of SUV (SUV mean) was calculated. The T/N ratio was determined by dividing the SUV max of the tumor by the SUV mean of the normal brain tissue. The PET and MRI datasets were transferred to a LINUX workstation. Co-registration of FDG-PET/MET-PET/FLT-PET/MRI was undertaken on the workstation with a commercial software package (Dr. View/LINUX, version

Table 1: Patient characteristics and semiquantitative PET results for FDG, MET, and FLT. Dig: histological diagnosis, DA: diffuse astrocytoma, OA: oligoastrocytoma, O: oligodendroglioma, AA: anaplastic astrocytoma, AOA: anaplastic oligoastrocytoma, AO: anaplastic oligodendroglioma, GBM: glioblastoma multiforme, GS: gliosarcoma, SUV max maximum standardized uptake value, T/N *ratio* tumor-to-normal tissue count density.

Case	Age	Sex	Dig.	Ki-67 (%)	FDG SUV max	FDG T/N	MET SUV max	MET T/N	FLT SUV max	FLT T/N
1	49	f	DA	1.75	4.12	0.403526	2.93	1.7757576	0.13	1.1818182
2	42	f	OA	7.5	4.4	0.5231867	4.37	2.5406977	0.24	1.8461538
3	52	f	DA	1	4.96	0.5025329	3.34	1.9306358	0.55	3.6666667
4	71	m	DA	4	3.85	0.6514382	5.28	4.3278689	0.76	5.4285714
5	30	m	DA	2.5	5.65	0.495614	1.69	1	0.28	1
6	35	f	DA	2.5	5.78	0.5254545	1.57	1	0.23	1
7	30	f	DA	5	5.89	0.356	1.49	1.18254	0.18	1
8	27	f	O	2.3	5.34	0.8215385	1.38	1.5164835	0.18	1.125
9	49	f	DA	5	2.71	0.5441767	1.7	1.1971831	0.22	1.047619
10	38	f	DA	5	6.07	0.497133	2.55	1.795775	0.28	1.75
11	37	m	DA	1	23.87	2.69	4.97	2.99	0.79	2.72
12	36	m	OA	7.7	8.01	1.055336	5.26	3.094118	0.48	2.181818
13	34	f	AA	5	6.67	0.6778455	3.22	2.2517483	1.15	6.7647059
14	58	m	AA	12.5	4.46	0.566709	3.55	2.9583333	0.28	1.8666667
15	77	f	AA	35	6.98	1.8082902	5.07	3.5454545	0.9	5
16	26	m	AA	5	4.72	0.5777234	3.32	2.862069	0.32	2.6666667
17	66	f	AOA	5	3.97	0.5321716	2.93	2.4016393	0.58	3.0526316
18	60	f	AA	10	7.59	1.1587786	3.41	2.544776	0.94	3.91667
19	36	f	AA	6	4.27	0.5488432	4.81	2.829412	0.37	2.176471
20	43	f	AA	30	4.74	0.629482	8.04	4.345946	0.84	2.470588
21	71	m	AOA	50	24.02	3.1605263	5.17	4.3445378	1.45	6.3043478
22	64	m	AO	50	8.74	1.208852	8.18	6.544	2.51	9.653846
23	28	f	AOA	5	13.5	1.674938	9.02	5.401198	0.98	2.227273
24	79	f	AA	5	47.57	5.3032329	5.96	3.8701299	0.77	5.1333333
25	66	f	AA	12.5	6.23	0.7634803	2.61	1.482955	0.66	2.357143
26	31	f	AA	20	23.05	2.845679	6.49	4.570423	1.64	9.647059
27	45	m	AA	7.5	14.8	1.9865772	6.61	5.1640625	1.06	3.2121212
28	51	m	GBM	25	14.86	2.006192	20.88	5.7246377	11.18	6.0812183
29	22	f	GBM	40	12.69	1.4859485	5.21	3.196319	3.05	11.296296
30	62	m	GBM	35	7.65	0.9634761	4.55	3.64	1.19	7
31	70	f	GBM	35	5.04	0.6990291	3.44	2.3401361	1.37	6.2272727
32	81	f	GBM	50	13.05	2.8935698	5.69	3.6012658	3.74	15.583333
33	55	f	GBM	35	8.99	2.5759312	5.35	3.4294872	2.61	3.1829268
34	29	f	GBM	50	5.5	0.607064	3.57	1.9944134	1.66	8.7368421
35	77	f	GBM	45	4.6	1.281337	5.51	3.3393939	2.15	8.9583333
36	79	m	GBM	65	9.71	2.0442105	4.3	3.5833333	3.68	17.52381
37	69	f	GBM	15	15.1	2.2913505	4.98	3.254902	4.41	23.210526
38	86	f	GBM	30	10.96	1.7734627	5.91	5.472222	2.69	15.82353
39	27	f	GBM	30	6.51	1.4563758	3.83	2.992188	1.53	6.652174
40	61	m	GBM	10	6.07	1.0049669	3.68	3.2857143	1.96	7.5384615
41	53	m	GBM	25	6.61	1.0200617	3.31	3.412371	1.7	8.5
42	62	m	GBM	70	4.86	0.9382239	4.54	4.09009	1.67	15.18182
43	67	m	GBM	30	5.8	0.9148265	2.82	2.014286	1.45	9.0625
44	60	m	GBM	40	5.97	0.894615	2.9	2.788462	1.28	7.111111
45	54	m	GS	40	6.95	0.8742138	3.75	2.218935	2.9	12.6087

Table 1: Continued.

Case	Age	Sex	Dig.	Ki-67 (%)	FDG SUV max	FDG T/N	MET SUV max	MET T/N	FLT SUV max	FLT T/N
46	72	m	GBM	50	5.55	0.9771127	3.22	2.439394	2.28	16.28571
47	68	f	GBM	60	5.94	1.1020408	4.08	2.4	2.99	17.58824
48	53	f	GBM	20	4.76	0.6979472	2.63	1.992424	1.04	6.1176471
49	61	f	GBM	70	12.2	1.75	5.64	5.271028	1.58	5.8518519
50	37	m	GBM	20	10.31	1.19	14.08	9.7777778	1.73	6.1785714
51	33	m	GBM	70	20.16	2.011976	8.71	4.608466	2.85	8.6363636
52	41	f	GBM	20	24.76	3.4057771	7.04	5.1764706	2.22	17.076923
53	26	m	GBM	80	13.32	1.5857143	5.43	3.878571	2.59	4.177419
54	69	m	GBM	90	27.09	5.0166667	8.86	7.5726496	5.44	34

R2.5, AJS Inc., Tokyo, Japan) with the mutual information method. The software allowed an operator to perform manual intervention; however, required adjustment for co-registration was minimal.

The measured SUV max and T/N ratios of FDG, MET and FLT were compared with the histological diagnoses obtained by biopsy or resection. The relationships between the Ki-67 index and SUV max or T/N ratio of FDG, MET and FLT were evaluated. The relationship between FDG and MET or FLT and MET uptake were evaluated. Regarding the area with a high-intensity signal on the MRI (FLAIR) of each patient, based on a predetermined ROI, the mean SUVs of FDG, MET and FLT were used to compare the values between FDG and MET, between FLT and MET, and between FDG and FLT.

2.5. Statistical Analysis. All parametric data were expressed as mean ± standard deviation. The Mann-Whitney U test was used to assess the statistical significance in mean volumes across modalities. The Spearman correlation test was used to calculate the correlation coefficient. Statistical analysis was performed using Stat View J-5.0 for Windows.

3. Results

3.1. Patient Characteristics and Semiquantitative PET Results for FDG, MET, and FLT. Among the 54 glioma cases, the MET accumulation was observed in 51 cases (94.4%) in the MET-PET study and the FLT accumulation was observed in 50 cases (92.6%) in the FLT-PET study. Regarding the 3 cases without the MET accumulation and the 4 cases without the FLT accumulation, they were grade II gliomas. All malignant gliomas (grades III and IV) showed accumulation in both studies. Among the cases with T/N ratios higher than 1 in the FDG-PET study, there were 2 cases (16.7%) of the grade II gliomas, 8 cases (53.3%) of the grade III gliomas, and 17 cases (63.0%) of the grade IV gliomas (Table 1). In FDG-PET study, it is possible to differentiate gliomas by the WHO grade with the sensitivity of 53.3%, the specificity of 55.6%, the false positive of 44.4%, and the false negative of 46.7%. In MET-PET study, it is possible to differentiate gliomas by WHO grade with the sensitivity of 95.3%, the specificity of 9.1%, the false positive of 90.9%, and the false negative of 4.7%. In MET-PET study, it is possible to differentiate gliomas by WHO grade with the sensitivity of 93.9%, the specificity of 20%, the false positive of 80%, and the false negative of 6.1%.

3.2. Comparison of SUV max and T/N Ratios for FDG, MET, and FLT in Gliomas by WHO Grade. There were no significant differences in the SUV and T/N ratio among each group of the different WHO grades in the FDG-PET study (Figures 1(a) and 1(d)).

SUV of the normal brain in the MET-PET study was 1.52 ± 0.36 (0.92–2.62). Regarding the tumors in the MET-PET study, mean SUV max was 3.04 ± 1.56 for the grade II gliomas, 5.22 ± 2.09 for the grade III gliomas and 5.12 ± 2.44 for the grade IV gliomas (Figure 1(b)). T/N ratio was 2.03 ± 1.02 for the grade II gliomas, 3.67 ± 1.38 for the grade III gliomas and 3.76 ± 1.78 for the grade IV gliomas (Figure 1(e)). The mean SUV max and T/N ratio of the grade IV gliomas were significantly higher than that of the grade II gliomas, while there were no significant differences between the grade II gliomas and grade III gliomas. In the present study, there were some oligodendroglioma cases, which were in grade II, but their SUV max were high and ranged from 4.0 to 6.8.

SUV of the normal brain in the FLT-PET study was 0.20 ± 0.05 (0.13–0.28). Regarding the tumors in the FLT-PET study, mean SUV max was 0.36 ± 0.23 for the grade II gliomas, 0.96 ± 0.58 for the grade III gliomas, and 2.38 ± 1.07 for the grade IV gliomas (Figure 1(c)). The mean T/N ratio was 1.99 ± 1.37 for the grade II gliomas, 4.43 ± 2.61 for the grade III gliomas and 11.54 ± 6.86 for the grade IV gliomas (Figure 1(f)). There were significant differences in both SUV max and T/N ratio between the grade III gliomas and the grade IV gliomas, but, similar to the MET study, there were no significant differences between the grade II gliomas and the grade III gliomas.

3.3. The Correlations between SUV max or T/N Ratio from PET Studies and Ki-67 Index. When the accumulation of MET or FLT within the tumor and the Ki-67 index (an index for proliferation ability of tumor) were compared, linear regression analysis revealed a significant correlation between the Ki-67 index and MET SUV max ($r = 0.32$, $P = 0.02$)

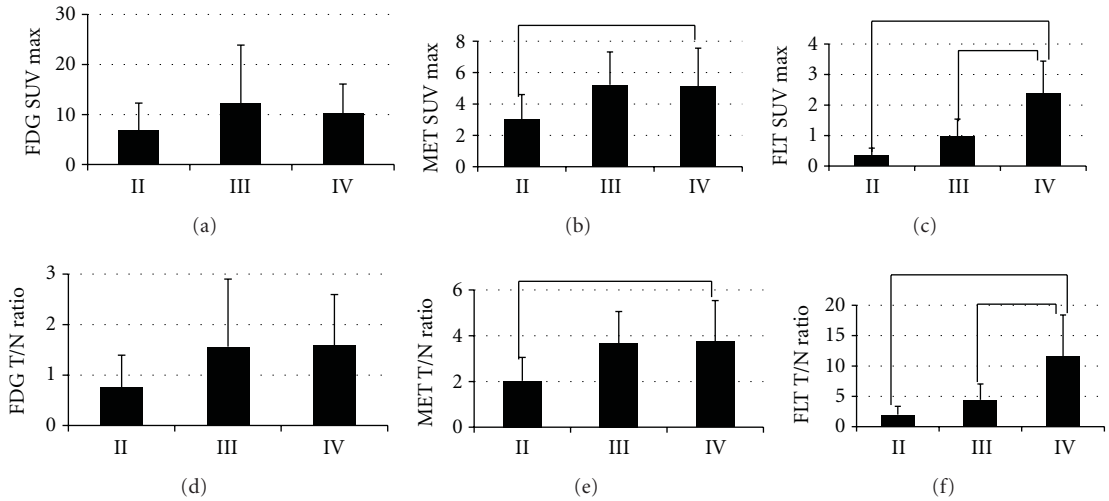

Figure 1: Comparison of SUV max and T/N ratios for FDG (a), (d) MET (b), (e) and FLT (c), (f) in gliomas by WHO grade. There were no significant differences in FDG-PET scan. The differences in MET SUV max and T/N ratio were statistically significant between grades II and IV gliomas (*$P < 0.05$), but not significant between grade II and III gliomas. The differences in FLT SUV max and T/N ratio were statistically significant between grade III and IV gliomas, grade II and grade IV ones (**$P < 0.01$).

(Figure 2(b)) or MET T/N ratio ($r = 0.39$, $P < 0.01$) (Figure 2(e)), as well as FLT SUV max ($r = 0.73$, $P < 0.001$) (Figure 2(c)) or FLT T/N ratio ($r = 0.63$, $P < 0.001$) (Figure 2(f)). FLT, compared to MET, demonstrates a significantly strong correlation with the proliferation ability. In FDG-PET study, linear regression analysis revealed no correlation between the Ki-67 index and SUV max ($r = 0.16$, $P = 0.24$) (Figure 2(a)) or T/N ratio ($r = 0.33$, $P = 0.02$) (Figure 2(d)).

3.4. Linear Regression Analysis of T/N Ratio between FDG and MET and between FLT and MET in Gliomas by WHO Grade. Regarding the area with a high intensity signal on the MRI (FLAIR) of each patient, based on a predetermined ROI, T/N ratio of FDG, MET and FLT were used to compare the values between FDG and MET, between FLT and MET and between FDG and FLT. Between FDG and MET, the T/N ratio of the MET tended to be high without correlating with increased T/N ratio of the FDG because the oligodendroglioma components were included in the grade II or grade III gliomas (Figures 3(a) and 3(b)). T/N ratio of the FDG tended to be high with correlating with low T/N ratio of the MET showing a tendency toward the focus of the epileptic changes (Figures 3(a) and 3(b) black circle). A significant but weak correlation is observed between the individual T/N ratio of FDG and MET in the grade IV gliomas ($r = 0.57$, $P = 0.03$) (Figure 3(c)). Between FLT and MET, the T/N ratio of the MET tended to be high without correlating with increased T/N ratio of the FLT because the oligodendroglioma components were included in the grade II or grade III gliomas (Figures 3(d) and 3(e)). We observed the same findings on the correlation between FDG and MET. On the other hand, no significant correlation is observed between the individual T/N ratio of FLT and MET in the grade IV gliomas ($r = 0.13$, $P = 0.61$) (Figure 3(f)). However, this relationship between FLT and MET is divided into three parts. Linear regression analysis showed a significant correlation between FLT and MET ($r = 0.21$, $P = 0.008$) in most areas and these areas appeared as astrocytic tumors (Figure 3(f), red circle). The T/N ratio of the MET tended to be high without correlating with increased T/N ratio of the FLT ($r = 0.53$, $P = 0.014$), because the oligodendroglioma components were included in the grade IV gliomas (Figure 3(f), blue circle). The T/N ratio of the MET tended to be low without correlating with increased T/N ratio of the FLT ($r = 0.12$, $P = 0.11$) because the necrotic components were included in the grade IV gliomas (Figure 3(f), green circle). A significant correlation is observed between the individual T/N ratio of FDG and FLT in the grade IV gliomas ($r = 0.54$, $P = 0.05$). Between FDG and FLT, T/N ratio of the FDG tended to be high with correlating with low T/N ratio of the FLT showing a tendency toward the focus of the epileptic changes (Figures 3(g) and 3(h) black circle). The T/N ratio of the FDG tended to be low without correlating with increased T/N ratio of the FLT, because the necrotic components were included in the grade IV gliomas (Figure 3(i), green circle).

3.5. Representative Cases. Figures 4 and 5, respectively, show representative cases of FDG, MET, and FLT-PET studies in anaplastic astrocytoma and glioblastoma.

3.5.1. Case 26: 31-Year-Old Female. She had an onset of convulsion. FLAIR showed a high-intensity lesion (Figure 4(a)), and Gd-enhanced MRI showed slightly enhanced lesion in the right frontal lobe (Figure 4(b)). FDG-PET demonstrated increased FDG uptake within the tumor (Figure 4(c)). MET-PET demonstrated increased MET uptake within the tumor (Figure 4(d)). FLT-PET demonstrated increased FLT uptake within the tumor (Figure 4(e)). Areas of different enhancement and uptake between FDG, MET and FLT are projected on the tumor, in order to perform histological sampling for further correlation during the resection (Figure 4

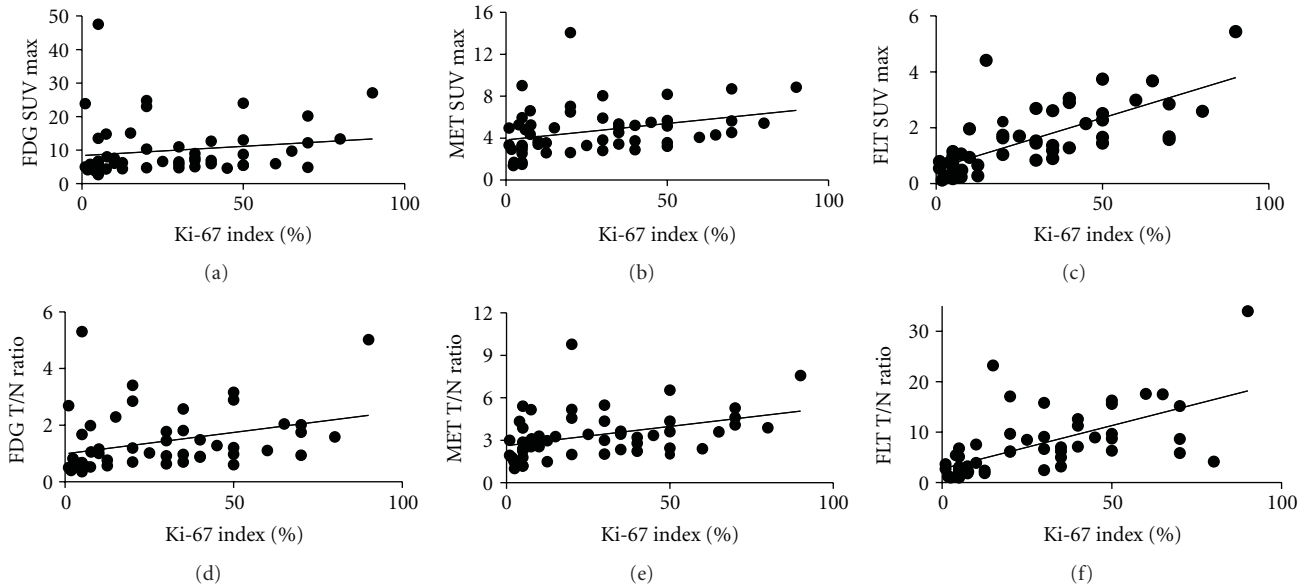

Figure 2: The correlations between SUV max (FDG (a), MET (b), and FLT (c)) and Ki-67 index were determined. Analysis indicates a more significant correlation between the Ki-67 index and FLT SUV max ($r = 0.72$, $P < 0.001$) than between the index and FDG SUV max ($r = 0.16$, $P = 0.24$) or MET SUV max ($r = 0.32$, $P = 0.02$). The correlations between T/N ratio (FDG (d), MET (e) and FLT (f)) and Ki-67 index were determined. Analysis indicates a more significant correlation between the Ki-67 index and FLT T/N ratio ($r = 0.63$, $P < 0.001$) than between the index and FDG T/N ratio ($r = 0.33$, $P = 0.02$) or MET T/N ratio ($r = 0.39$, $P < 0.01$).

yellow arrow, red arrow). Yellow arrow demonstrates anaplastic astrocytoma (Figure 4(f)) within T/N ratio of FDG-PET (2.85), MET-PET (4.57) and FLT-PET (9.65). Ki-67 index from the specimen indicated by yellow arrow was 20% (Figure 4(g)). Red arrow demonstrates diffuse astrocytoma area (Figure 4(h)) within T/N ratio of FDG-PET (0.76), MET-PET (2.08) and FLT-PET (4.65). Ki-67 index from the specimen indicated by red arrow was 8% (Figure 4(i)). She has been treated for anaplastic astrocytoma.

3.5.2. Case 28: 51-Year-Old Male. He experienced an onset of aphasia and Gerstmann's syndrome and developed glioblastoma which was recognized with a ring-like contrast in the left temporo-occipital lobe on the Gd-enhanced MRI (Figure 5(a)). The MRI study did not show a uniformed contrast, and some areas had high-intensity signal while others did not. Similar to the MRI study results, the accumulation was not uniform in MET-PET and FLT-PET studies. This relationship between MET and FLT is divided into three parts, similar to the observation described in Figure 3(f). In the blue arrow area, the contrast by MRI was not strong, but the T/N ratio of MET was 4.31 and the T/N ratio of FLT was 3.24 with a significant accumulation of MET. In the green arrow area, the contrast by MRI was strong, the T/N ratio of MET was 1.60, and the T/N ratio of FLT was 5.72 with a significant accumulation of FLT. In the red arrow area, the contrast by MRI was recognized, but the T/N ratios of MET and FLT were both high (3.27 and 5.28; resp., Figures 5(b) and 5(c)). He underwent craniotomy for histopathological diagnosis. The diagnosis revealed the blue arrow area mostly with a histological picture of oligodendroglioma (Figure 5(d)) with a Ki-67 index of 30% (Figure 5(e)) and the green arrow area mainly with a histological picture of necrotic tissues (Figure 5(f)) with a Ki-67 index of less than 10% (Figure 5(g)). As for the red arrow area displaying high accumulation of both MET and FLT, this area showed a strong nuclear atypia with megakaryocytes with a high Ki-67 index of 70% (Figures 5(h) and 5(i)). Taken together, increased accumulation of both tracers (MET and FLT) appears to indicate high-grade malignancy.

4. Discussion

Accurate tissue diagnosis of glioma is important in order to determine appropriate therapeutic strategy and predict prognosis. Final diagnosis of the grade of malignancy is carried out by surgical histopathological diagnosis. However, due to the diverse nature of gliomas within tumors, some glioma cases tend to be diagnosed less stringent than actual grade of malignancy through pathological diagnosis of a specimen taken from the tumor. The image analysis using PET has an advantage of spatial evaluation of diverse malignant gliomas [8, 21, 22]. FDG has been widely used as a PET tracer for diagnosis of malignant brain tumors. The accumulation of FDG increases in highly malignant tumors, and this method is highly specific as an image analysis and useful for predicting prognosis [23]. However, FDG uptake is high in the normal brain cortex where glucose metabolism is active, and the difference between the normal accumulation and brain tumors may not be detected. In addition, FDG uptake is low in low-grade tumors, and FDG has limitations for detecting the localization of small tumors or accurately identifying tumor area [5, 24, 25]. Extra attention is especially required for diagnosis of gliomas.

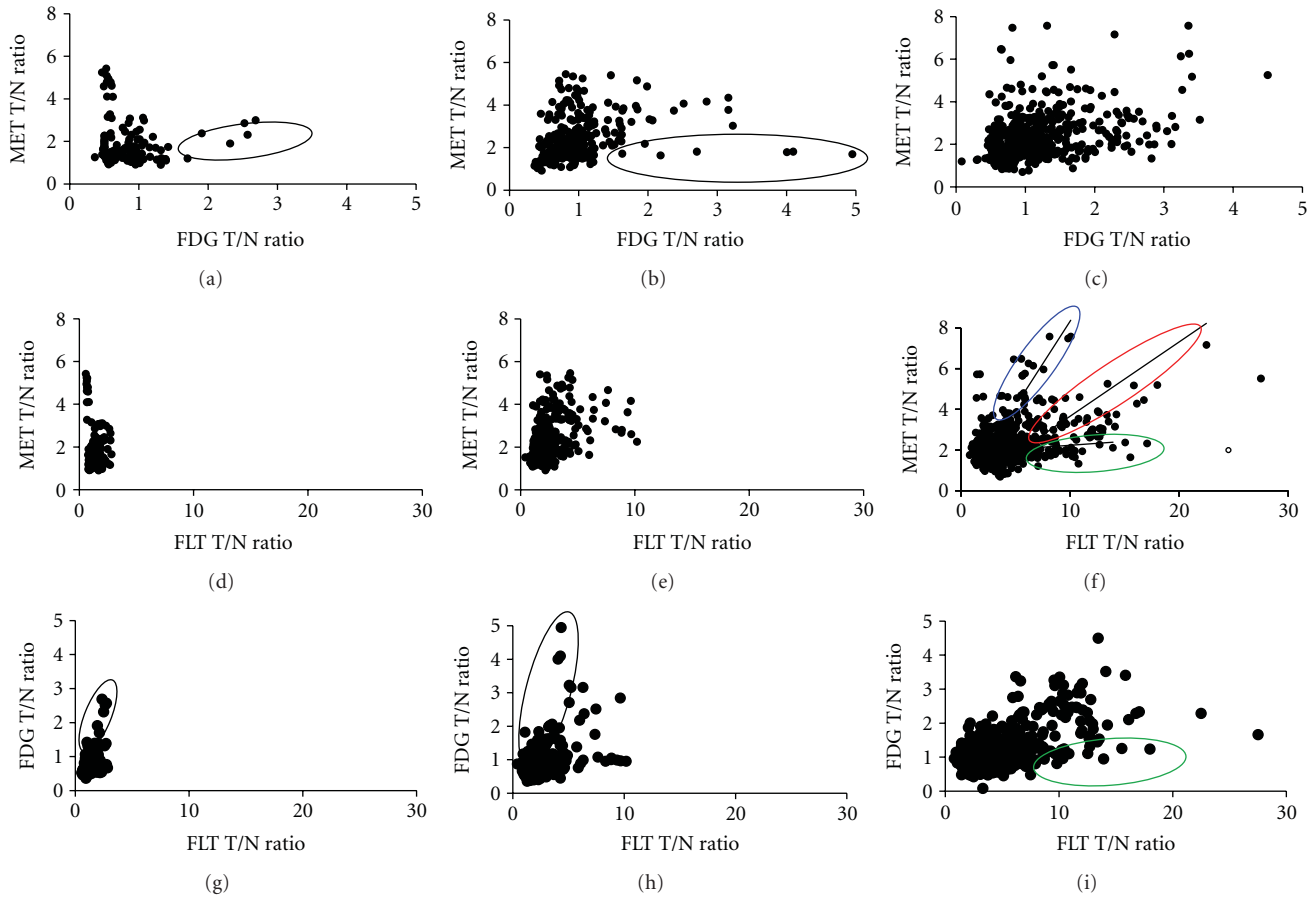

Figure 3: Linear regression analysis of T/N ratio between FDG and MET (grade II (a), grade III (b), grade IV (c)), between FLT and MET (grade II (d), grade III (e), grade IV (f)) or between FDG and FLT (grade II (g), grade III (h), grade IV (i)). A significant but weak correlation is observed between the individual T/N ratio of FDG and MET ($r = 0.57$, $P = 0.03$) (c). FDG T/N ratio tended to be high correlating with low MET T/N ratio showing a tendency toward the focus of the epileptic changes (black circle). On the other hand, no significant correlation is observed between the individual T/N ratio of FLT and MET ($r = 0.13$, $P = 0.61$) (f). This relationship between FLT and MET is divided into three parts. Linear regression analysis showed a significant correlation between FLT and MET ($r = 0.21$, $P = 0.008$) in most areas and these areas appeared as astrocytic tumors (red circle). The T/N ratio of the MET tended to be high without correlating with increased T/N ratio of the FLT ($r = 0.53$, $P = 0.014$) because the oligodendroglioma components were included (blue circle). The T/N ratio of the MET tended to be low without correlating with increased T/N ratio of the FLT ($r = 0.12$, $P = 0.11$) because the necrotic components were included (green circle). A significant correlation is observed between the individual T/N ratio of FDG and FLT in the grade IV gliomas ($r = 0.54$, $P = 0.05$) (i). Between FDG and FLT, T/N ratio of the FDG tended to be high with correlating with low T/N ratio of the FLT showing a tendency toward the focus of the epileptic changes (Figures 3(g) and 3(h) black circle). The T/N ratio of the FDG tended to be low without correlating with increased T/N ratio of the FLT, because the necrotic components were included in the grade IV gliomas (Figure 3(i), green circle).

Mixed neuronal and glial tumors and gliomas which easily cause convulsions had decreased accumulation of FDG until now [26, 27]. In our case, accumulation of FDG was high in low-grade glioma which is frequently associated with convulsions. It seems that additional attention is necessary regarding the convulsive cases and accumulation of FDG.

Recently, MET and FLT have been used as tracers with tumor specificity. MET is one of the essential amino acids and a tracer for evaluating protein synthesis. FLT is a tracer of labeled thymidine for evaluating DNA synthesis, and its accumulation is considered to reflect tumor cell proliferation activity [9, 28, 29]. In the present study, there were significant differences between the grade II gliomas and the grade IV gliomas and no significant differences between the grade II gliomas and grade III gliomas in the MET-PET study. However, the presence of tumor cells was confirmed in the area with increased accumulation of MET but poorly depicted on MRI scan and no increased accumulation of tracers in the FDG-PET and FLT-PET studies, indicating its usefulness as a testing modality to determine the presence of tumor. On the other hand, the correlation of MET uptake in the microvessel density and blood volume in tumor or with expression of vascular endothelial cells, which are amino acid transporters (LAT1) in tumor cells is suggested, and the use of MET by itself seems difficult for making diagnosis since additional factors other than proliferation activity are involved [8, 30]. Also, it has been reported that the accumulation of MET is high in oligodendroglioma due to the high cell density, and special attention is required for its differentiation [22].

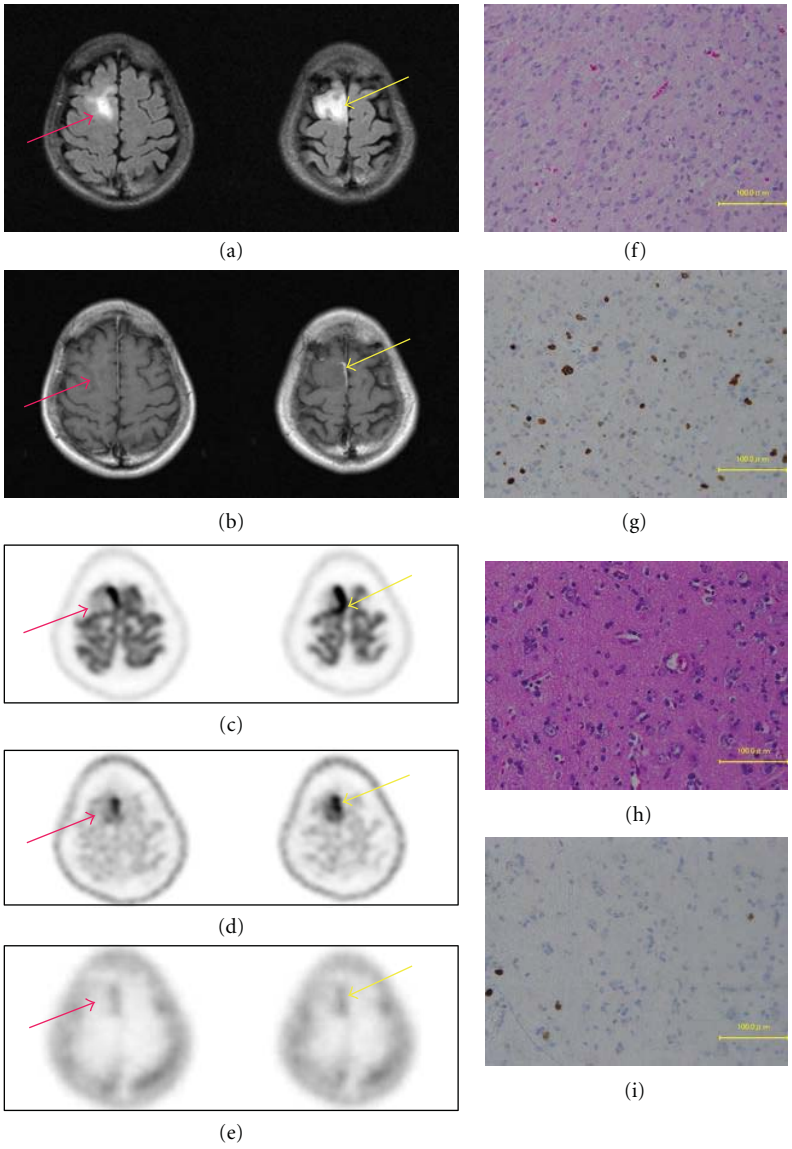

Figure 4: A 31-year-old woman with high intensity in the right frontal lobe in FLAIR MRI (a) and slightly enhanced lesion in Gd-enhanced MRI (b). FDG-PET demonstrated increased FDG uptake within the tumor (c). MET-PET demonstrated increased MET uptake within the tumor (d). FLT-PET demonstrated increased FLT uptake within the tumor (e). Areas of different enhancement and uptake between FDG, MET, and FLT are projected on the tumor, in order to perform histological sampling for further correlation during the resection (yellow arrow, red arrow). Yellow arrow demonstrates anaplastic astrocytoma (f) within T/N ratio of FDG-PET (2.85), MET-PET (4.57), and FLT-PET (9.65). Ki-67 index from the specimen indicated by yellow arrow was 20% (g). Red arrow demonstrates diffuse astrocytoma area (h) within T/N ratio of FDG-PET (0.76), MET-PET (2.08), and FLT-PET (4.65). Ki-67 index from the specimen indicated by red arrow was 8% (i).

In the FLT-PET study, there were significant differences between the grade II gliomas and the grade IV gliomas and between the grade III gliomas and grade IV gliomas. In addition, there was a significant correlation between the Ki-67 index and the FLT accumulation. There is a correlation between the Ki-67 index and the MET accumulation, but the correlation with FLT is more significant. Hence, we considered that FLT-PET was a more ideal and attractive PET tracer for glioma imaging than MET-PET. Furthermore, the uptake of FLT in normal brain tissue was lower than that of MET (SUV max, 0.20 ± 0.05 versus 1.52 ± 0.36). It means that FLT-PET provides a low-background cerebral image. One of the reasons for low uptake of FLT in normal brain tissue is that FLT allows the direct measurement of cellular TK1 activity, which has been proportional to the proliferation activity. Since, MET accumulation provides an indirect measure of LAT1 expression in the vascular endothelial cells and proliferation status as amino acid uptake, MET-PET exhibits higher background than FLT-PET in normal brain tissue. However, FLT-PET had some weak points. In our series of WHO grade II glioma, uptake of FLT was lower than that of MET (SUV max, 0.36 ± 0.23 versus 3.04 ± 1.56) and the uptake ratios for tumor to normal brain were same (T/N ratio, 1.99 ± 1.37 versus 2.03 ± 1.02). WHO grade II

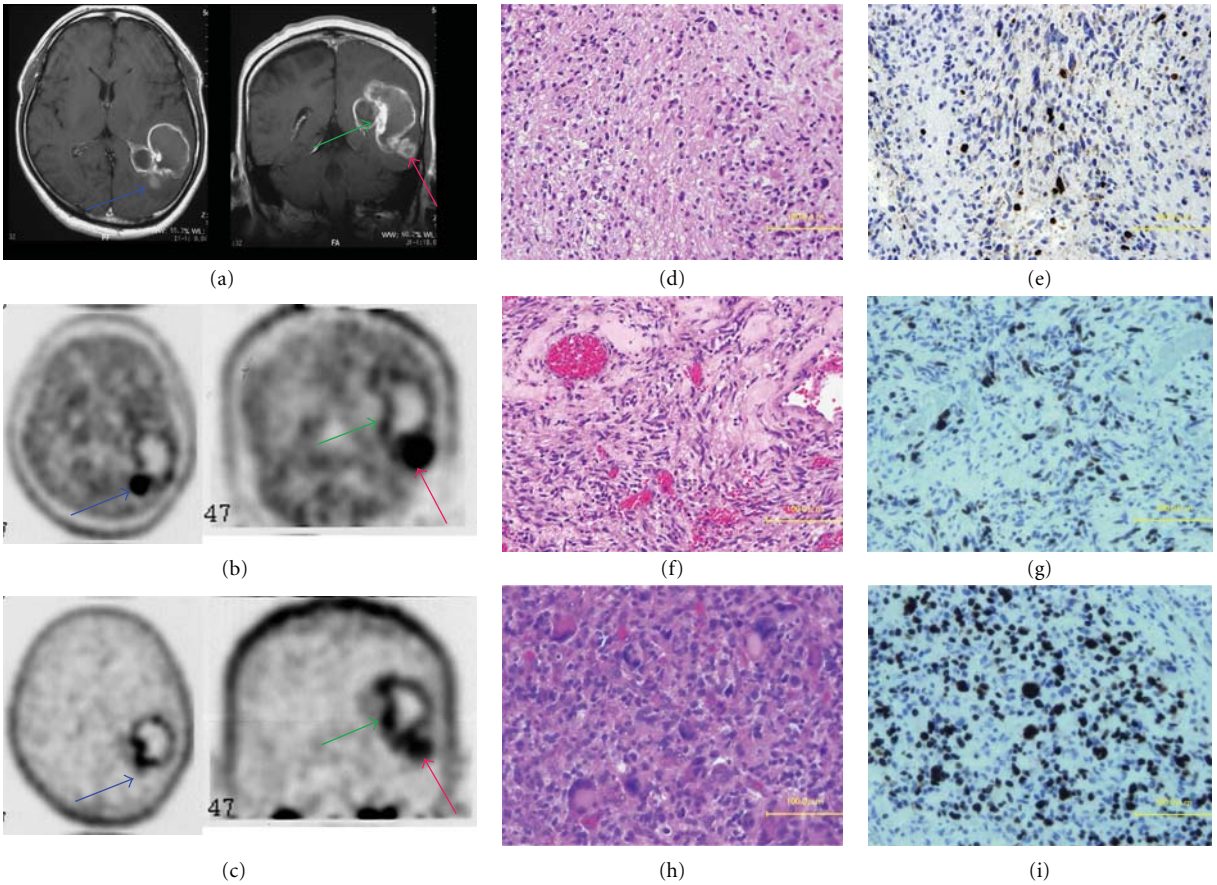

Figure 5: A 51-year-old man with glioblastoma. MRI clearly showed a ringed enhancement in the left temporo-occipital lobe (a). Areas of different enhancement and uptake between MET (b) and FLT (c) are projected on the tumor, in order to perform histological sampling for further correlation during the resection (blue arrow, green arrow, red arrow). Sample from the blue arrow demonstrates glioblastoma with oligodendroglioma (d) within high T/N ratio of MET-PET (4.31) and low T/N ratio of FLT-PET (3.24). Sample from the green arrow demonstrates necrosis area (f) within low T/N ratio of MET-PET (1.60) and high T/N ratio of FLT-PET (5.72). Sample from the red arrow demonstrates glioblastoma with multiple nuclear and large cells (h) within high T/N ratio of MET (3.27) and FLT-PET (5.28). Ki-67 index was 30% for the blue arrow (e), less than 10% for the green arrow (g), and 70% for the red arrow (i). Taken together, increased accumulation of both tracers (MET and FLT) appears to indicate high-grade malignancy.

gliomas had no contrast enhancement on Gd-enhanced MRI. FLT uptake was similar to the low levels observed in no enhanced lesions of MRI. FLT may be less useful in assessing proliferation in noncontrast-enhancing tumors regardless of the histopathology grading. Low-tracer access to the tumor tissue may limit the metabolic trapping of FLT after the phosphorylation even in proliferative tumors. The leakage of FLT was observed in the area with radiation necrosis and disrupted blood-brain barrier (BBB) that result in the increased accumulation [5, 24, 27]. We will continue the analysis of FLT with more patients as FLT can be quantified by kinetic analysis. Specifically, the kinetic analysis of FLT-PET may clarify whether the transport effect or metabolic trapping largely contribute to the increased accumulation of FLT in the tumor. As shown in Figure 5, there were differences in the accumulation of each tracer within the same tumor due to the characteristics of each tracer, which may reflect the differences in tissues by site. In other words, we can predict that there are many oligodendroglioma components in the area with high MET accumulation and low FLT accumulation, and it is likely that the area is necrotic when MET accumulation is low, but FLT accumulation is high. When both tracer accumulations are high, the area is highly malignant as a tumor site and has high proliferative ability. However, it is difficult to make differential diagnosis, determine the recurrence of tumor, and determine the presence or absence of radiation necrosis using only one type of PET studies [31, 32]. Our study indicated that the combinational uses of FDG, MET, and FLT-PET help us evaluate the differences in malignancy grade of the tissues and predict the evaluation of histopathological components. Furthermore, these analyses will be useful for preoperative planning of excision area.

5. Conclusion

PET studies using FDG, MET and FLT were conducted on 54 glioma patients. We can predict that there are many oligodendroglioma components in the area with high MET accumulation and low FLT accumulation, and it is likely

that the area is necrotic when MET accumulation is low but FLT accumulation is high. When both MET and FLT tracer accumulations are high, the area is highly malignant as a tumor site and has high proliferative ability. PET study is a noninvasive examination method, and the use of these tracers in addition to widely used FDG-PET is highly useful for accurate preoperative diagnosis of tumors and identification of tumor area for removal. We will continue these tracer analyses to elucidate the correlation with pathological diagnosis and radiological diagnosis.

Acknowledgment

The authors appreciate the excellent technical support of the radiological technologist at their institution.

References

[1] P. J. Kelly, C. Daumas-Duport, D. B. Kispert, B. A. Kall, B. W. Scheithauer, and J. J. Illig, "Imaging-based stereotaxic serial biopsies in untreated intracranial glial neoplasms," *Journal of Neurosurgery*, vol. 66, no. 6, pp. 865–874, 1987.

[2] H. J. Aronen, F. S. Pardo, D. N. Kennedy et al., "High microvascular blood volume is associated with high glucose uptake and tumor angiogenesis in human gliomas," *Clinical Cancer Research*, vol. 6, no. 6, pp. 2189–2200, 2000.

[3] W. Chen, T. Cloughesy, N. Kamdar et al., "Imaging proliferation in brain tumors with ^{18}F-FLT PET: comparison with ^{18}F-FDG," *Journal of Nuclear Medicine*, vol. 46, no. 6, pp. 945–952, 2005.

[4] S. Kim, J. K. Chung, S. H. Im et al., "^{11}C-methionine PET as a prognostic marker in patients with glioma: comparison with ^{18}F-FDG PET," *European Journal of Nuclear Medicine and Molecular Imaging*, vol. 32, no. 1, pp. 52–59, 2005.

[5] S. J. Price, "Advances in imaging low-grade gliomas," *Advances and Technical Standards in Neurosurgery*, vol. 35, pp. 1–34, 2010.

[6] K. Herholz, T. Hölzer, B. Bauer et al., "^{11}C-methionine PET for differential diagnosis of low-grade gliomas," *Neurology*, vol. 50, no. 5, pp. 1316–1322, 1998.

[7] L. W. Kracht, H. Miletic, S. Busch et al., "Delineation of brain tumor extent with [^{11}C]L-methionine positron emission tomography: local comparison with stereotactic histopathology," *Clinical Cancer Research*, vol. 10, no. 21, pp. 7163–7170, 2004.

[8] S. Okubo, H. N. Zhen, N. Kawai, Y. Nishiyama, R. Haba, and T. Tamiya, "Correlation of l-methyl-^{11}C-methionine (MET) uptake with l-type amino acid transporter 1 in human gliomas," *Journal of Neuro-Oncology*, vol. 99, no. 2, pp. 217–225, 2010.

[9] S. Ceyssens, K. van Laere, T. de Groot, J. Goffin, G. Bormans, and L. Mortelmans, "[^{11}C]methionine PET, histopathology, and survival in primary brain tumors and recurrence," *American Journal of Neuroradiology*, vol. 27, no. 7, pp. 1432–1437, 2006.

[10] T. Hatakeyama, N. Kawai, Y. Nishiyama et al., "^{11}C-methionine (MET) and ^{18}F-fluorothymidine (FLT) PET in patients with newly diagnosed glioma," *European Journal of Nuclear Medicine and Molecular Imaging*, vol. 35, no. 11, pp. 2009–2017, 2008.

[11] T. Nariai, Y. Tanaka, H. Wakimoto et al., "Usefulness of L-[methyl-^{11}C] methionine-positron emission tomography as a biological monitoring tool in the treatment of glioma," *Journal of Neurosurgery*, vol. 103, no. 3, pp. 498–507, 2005.

[12] K. Ishii, T. Ogawa, J. Hatazawa et al., "High L-methyl-[^{11}C]methionine uptake in brain abscess: a PET study," *Journal of Computer Assisted Tomography*, vol. 17, no. 4, pp. 660–661, 1993.

[13] M. Nakagawa, Y. Kuwabara, M. Sasaki et al., "^{11}C-methionine uptake in cerebrovascular disease: a comparison with ^{18}F-FDG PET and 99mTc-HMPAO SPECT," *Annals of Nuclear Medicine*, vol. 16, no. 3, pp. 207–211, 2002.

[14] S. J. Choi, J. S. Kim, J. H. Kim et al., "[^{18}F]3′-deoxy-3′-fluorothymidine PET for the diagnosis and grading of brain tumors," *European Journal of Nuclear Medicine and Molecular Imaging*, vol. 32, no. 6, pp. 653–659, 2005.

[15] T. Saga, H. Kawashima, N. Araki et al., "Evaluation of primary brain tumors with FLT-PET: usefulness and limitations," *Clinical Nuclear Medicine*, vol. 31, no. 12, pp. 774–780, 2006.

[16] A. F. Shields, J. R. Grierson, B. M. Dohmen et al., "Imaging proliferation *in vivo* with [F-18]FLT and positron emission tomography," *Nature Medicine*, vol. 4, no. 11, pp. 1334–1336, 1998.

[17] L. B. Been, A. J. H. Suurmeijer, D. C. P. Cobben, P. L. Jager, H. J. Hoekstra, and P. H. Elsinga, "[^{18}F]FLT-PET in oncology: current status and opportunities," *European Journal of Nuclear Medicine and Molecular Imaging*, vol. 31, no. 12, pp. 1659–1672, 2004.

[18] A. H. Jacobs, A. Thomas, L. W. Kracht et al., "^{18}F-fluoro-L-thymidine and ^{11}C-methylmethionine as markers of increased transport and proliferation in brain tumors," *Journal of Nuclear Medicine*, vol. 46, no. 12, pp. 1948–1958, 2005.

[19] W. Chen, S. Delaloye, D. H. S. Silverman et al., "Predicting treatment response of malignant gliomas to bevacizumab and irinotecan by imaging proliferation with [^{18}F] fluorothymidine positron emission tomography: a pilot study," *Journal of Clinical Oncology*, vol. 25, no. 30, pp. 4714–4721, 2007.

[20] K. Ishiwata, C. Kasahara, K. Hatano, S. I. Ishii, and M. Senda, "Carbon-11 labeled ethionine and propionine as tumor detecting agents," *Annals of Nuclear Medicine*, vol. 11, no. 2, pp. 115–122, 1997.

[21] K. Roessler, B. Gatterbauer, A. Becherer et al., "Surgical target selection in cerebral glioma surgery: linking methionine (MET) PET image fusion and neuronavigation," *Minimally Invasive Neurosurgery*, vol. 50, no. 5, pp. 273–280, 2007.

[22] K. Torii, N. Tsuyuguchi, J. Kawabe, I. Sunada, M. Hara, and S. Shiomi, "Correlation of amino-acid uptake using methionine PET and histological classifications in various gliomas," *Annals of Nuclear Medicine*, vol. 19, no. 8, pp. 677–683, 2005.

[23] C. Colavolpe, E. Guedj, P. Metellus et al., "FDG-PET to predict different patterns of progression in multicentric glioblastoma: a case report," *Journal of Neuro-Oncology*, vol. 90, no. 1, pp. 47–51, 2008.

[24] K. Herholz, D. Coope, and A. Jackson, "Metabolic and molecular imaging in neuro-oncology," *Lancet Neurology*, vol. 6, no. 8, pp. 711–724, 2007.

[25] C. La Fougère, B. Suchorska, P. Bartenstein, F. W. Kreth, and J. C. Tonn, "Molecular imaging of gliomas with PET: opportunities and limitations," *Neuro-Oncology*, vol. 13, no. 8, pp. 806–819, 2011.

[26] R. Talanow, P. Ruggieri, A. Alexopoulos, D. Lachhwani, and G. Wu, "PET manifestation in different types of pathology in epilepsy," *Clinical Nuclear Medicine*, vol. 34, no. 10, pp. 670–674, 2009.

[27] J. H. Phi, J. C. Paeng, H. S. Lee et al., "Evaluation of focal cortical dysplasia and mixed neuronal and glial tumors in

pediatric epilepsy patients using ^{18}F-FDG and ^{11}C-methionine pet," *Journal of Nuclear Medicine*, vol. 51, no. 5, pp. 728–734, 2010.

[28] N. Kawai, T. Hatakeyama, T. Tamiya et al., "Is it possible to differentiate between radiation necrosis and recurrence of brain tumors using positron emission tomography?" *Progress in Computed Imaging*, vol. 30, no. 1, pp. 1–11, 2008.

[29] N. Kawai, M. Kagawa, T. Hatakeyama et al., "^{11}C-methionine positron emission tomography in brain tumor," *Neurological Surgery*, vol. 36, no. 10, pp. 847–859, 2008.

[30] Y. Okita, M. Kinoshita, T. Goto et al., "^{11}C-methionine uptake correlates with tumor cell density rather than with microvessel density in glioma: a stereotactic image-histology comparison," *NeuroImage*, vol. 49, no. 4, pp. 2977–2982, 2010.

[31] Y. Terakawa, N. Tsuyuguchi, Y. Iwai et al., "Diagnostic accuracy of ^{11}C-methionine PET for differentiation of recurrent brain tumors from radiation necrosis after radiotherapy," *Journal of Nuclear Medicine*, vol. 49, no. 5, pp. 694–699, 2008.

[32] M. Kinoshita, T. Goto, H. Arita et al., "Imaging ^{18}F-fluorodeoxy glucose/^{18}C-methionine uptake decoupling for identification of tumor cell infiltration in peritumoral brain edema," *Journal of Neuro-Oncology*, vol. 106, no. 2, pp. 417–425, 2012.

Hindawi Publishing Corporation
Journal of Biomedicine and Biotechnology
Volume 2012, Article ID 368075, 8 pages
doi:10.1155/2012/368075

Research Article

^{111}In-Labeled Cystine-Knot Peptides Based on the Agouti-Related Protein for Targeting Tumor Angiogenesis

Lei Jiang,[1,2] Zheng Miao,[2] Richard H. Kimura,[2] Adam P. Silverman,[3] Gang Ren,[2] Hongguang Liu,[2] Hankui Lu,[1] Jennifer R. Cochran,[3] and Zhen Cheng[2]

[1] *Department of Nuclear Medicine, Shanghai Sixth People's Hospital, Shanghai Jiao Tong University, Shanghai 200233, China*
[2] *Molecular Imaging Program at Stanford (MIPS), Department of Radiology, Stanford Cancer Institute, and Bio-X Program, Canary Center at Stanford for Cancer Early Detection, Stanford University, Stanford, CA 94305, USA*
[3] *Department of Bioengineering, Stanford Cancer Institute, and Bio-X Program, Stanford University, Stanford, CA 94305, USA*

Correspondence should be addressed to Zhen Cheng, zcheng@stanford.edu

Received 14 December 2011; Revised 29 January 2012; Accepted 30 January 2012

Academic Editor: David J. Yang

Agouti-related protein (AgRP) is a 4-kDa cystine-knot peptide of human origin with four disulfide bonds and four solvent-exposed loops. The cell adhesion receptor integrin $\alpha_v\beta_3$ is an important tumor angiogenesis factor that determines the invasiveness and metastatic ability of many malignant tumors. AgRP mutants have been engineered to bind to integrin $\alpha_v\beta_3$ with high affinity and specificity using directed evolution. Here, AgRP mutants 7C and 6E were radiolabeled with ^{111}In and evaluated for *in vivo* targeting of tumor integrin $\alpha_v\beta_3$ receptors. AgRP peptides were conjugated to the metal chelator 1, 4, 7, 10-tetra-azacyclododecane-N, N′, N″, N‴-tetraacetic acid (DOTA) and radiolabeled with ^{111}In. The stability of the radiopeptides ^{111}In-DOTA-AgRP-7C and ^{111}In-DOTA-AgRP-6E was tested in phosphate-buffered saline (PBS) and mouse serum, respectively. Cell uptake assays of the radiolabeled peptides were performed in U87MG cell lines. Biodistribution studies were performed to evaluate the *in vivo* performance of the two resulting probes using mice bearing integrin-expressing U87MG xenograft tumors. Both AgRP peptides were easily labeled with ^{111}In in high yield and radiochemical purity (>99%). The two probes exhibited high stability in phosphate-buffered saline and mouse serum. Compared with ^{111}In-DOTA-AgRP-6E, ^{111}In-DOTA-AgRP-7C showed increased U87MG tumor uptake and longer tumor retention (5.74 ± 1.60 and 1.29 ± 0.02%ID/g at 0.5 and 24 h, resp.), which was consistent with measurements of cell uptake. Moreover, the tumor uptake of ^{111}In-DOTA-AgRP-7C was specifically inhibited by coinjection with an excess of the integrin-binding peptidomimetic c(RGDyK). Thus, ^{111}In-DOTA-AgRP-7C is a promising probe for targeting integrin $\alpha_v\beta_3$ positive tumors in living subjects.

1. Introduction

Molecular imaging is a rapidly evolving field in biomedical research and provides powerful techniques to noninvasively study a variety of important characteristics of cancers, such as tumor metabolism, proliferation, hypoxia, and receptor expression [1–3]. Therefore, novel molecular probes that target these characteristics have been under active and intensive development and investigation. Many platforms including small molecules, peptides, proteins, and nanoparticles have been explored in order to develop molecular probes to image a variety of important disease biomarkers [4, 5].

Cystine-knot peptides consist of a stable core motif of at least three disulfide bonds that are interwoven into a "knot" conformation. There is great sequence diversity among cystine-knot family members, as only the disulfide-bonded core is conserved; consequently, the loops connecting the cysteine residues are highly tolerant to substitution or incorporation of additional amino acid residues [6–8]. Previously, we used a truncated form of the Agouti-related protein (AgRP*), a 4-kDa cystine-knot peptide with four disulfide bonds and four solvent-exposed loops, as a molecular scaffold for directed evolution. In this study, high-throughput methods were used to screen a yeast-displayed

Table 1: Amino acid sequences of the AgRP* mutants 7C and 6E used in this study. DOTA was site-specific conjugated to the N-terminal amine of these peptides.

AgRP	GCVRLHESCLGQQVPCCDPAATCYCRFFNAFCYCR
AgRP-6E	GCVRLHESCLGQQVPCCDPAATCYCVERGDGNRRCYCR
AgRP-7C	GCVRLHESCLGQQVPCCDPAATCYCYGRGDNDLRCYCR

Red lines represent the disulfide bonds between Cys^1–Cys^4, Cys^2–Cys^5, Cys^3–Cys^8, and Cys^6–Cys^7 in the AgRP*-based cystine-knot peptides.

AgRP* library to identify several mutants with high affinity and specificity for $\alpha_v\beta_3$ integrin [8].

The cell adhesion receptor integrin $\alpha_v\beta_3$ is an important tumor angiogenesis factor that determines the invasiveness and metastatic ability of many malignant tumors. It is upregulated on the tumor cell surface and also overexpressed on activated endothelial cells around the tumor tissues [9–11]. Many radiolabeled probes have been developed for imaging integrin expression using positron emission tomography (PET) or single-photon emission computed tomography (SPECT) [12–15]. In our recent research, the ^{64}Cu-DOTA conjugated AgRP* mutant 7C (^{64}Cu-DOTA-AgRP-7C) was successfully developed for PET imaging of integrin $\alpha_v\beta_3$ positive tumors. This study demonstrated the potential of AgRP*-based integrin-binding peptides for use as *in vivo* molecular imaging applications and highlighted cystine-knots as promising molecules for further development as diagnostics or therapeutics against different tumor targets [13].

In the current study, to further characterize the *in vivo* performance of integrin-binding AgRP*-based peptides and also evaluate their potential use for SPECT imaging applications, two DOTA-conjugated AgRP* mutants (DOTA-AgRP-7C and DOTA-AgRP-6E; Table 1) were synthesized and radiolabeled with the gamma emitter ^{111}In ($t_{1/2}$ = 2.8 days). Tumor uptake, biodistribution, and stability of the resulting probes were evaluated in integrin $\alpha_v\beta_3$ positive human glioblastoma U87MG tumor xenograft models.

2. Materials and Methods

2.1. Chemicals, Reagents, and Instruments. DOTA-AgRP-7C and DOTA-AgRP-6E were synthesized and reported previously [13]. $^{111}InCl_3$ was purchased from PerkinElmer. All other reagents were obtained from Fisher Scientific Co. unless otherwise specified. Female athymic nude mice (nu/nu, 5-6 weeks old) were purchased from Charles River Laboratory (Wilmington, MA, USA). A CRC-15R PET dose calibrator (Capintec Inc., Ramsey, NJ, USA) was used for all radioactivity measurements. Reversed phase high performance liquid chromatography (RP-HPLC) was performed on a Dionex Summit HPLC system (Dionex Corporation, Sunnyvale, CA, USA) equipped with a 170 U 4-Channel UV-Vis absorbance detector and radioactivity detector (Carroll and Ramsey Associates, model 105S, Berkeley, CA). UV detection wavelengths were 218 nm, 254 nm, and 280 nm for all the experiments. Both semipreparative (Vydac, Hesperia, CA. 218TP510-C18, 10 mm × 250 mm) and analytical RP-HPLC columns were used. The mobile phase was solvent A, 0.1% trifluoroacetic acid (TFA)/H_2O, and solvent B, 0.1%TFA/acetonitrile.

2.2. Cell Line and Cell Culture. The human glioblastoma cell line U87MG was obtained from American Type Culture Collection (ATCC; Manassas, VA, USA). The cells were maintained as monolayer cultures in Dulbecco's Modified Eagle Medium (DMEM) containing high glucose (GIBCO, Carlsbad, CA, USA), which was supplemented with 10% fetal bovine serum (FBS; GIBCO) and 1% penicillin-streptomycin (GIBCO). The cells were expanded in tissue culture dishes and kept in a humidified atmosphere of 5% CO_2 at 37°C. The media was changed every other day. A confluent monolayer was detached with 0.5% Trypsin-EDTA, 0.01 M PBS (pH 7.4), and dissociated into a single-cell suspension for further cell culture and binding experiments.

2.3. Peptide Radiolabeling. DOTA-AgRP-7C or DOTA-AgRP-6E were radiolabeled with ^{111}In by incubating 15 μg of peptide in 37 MBq (1 mCi) $^{111}InCl_3$ and 100 μL of 0.1 N NH_4OAc (pH 5.0–5.5) buffer, at 80°C for 45 min. The radiolabeled conjugates, ^{111}In-DOTA-AgRP-7C or ^{111}In-DOTA-AgRP-6E, were purified using a PD-10 column (GE Healthcare Life Sciences, Piscataway, NJ, USA) and eluted with PBS.

2.4. In Vitro Stability Assays. Radiolabeled AgRP* peptides were incubated in 0.01 M PBS (pH 7.4) at 37°C for 24 h and monitored for degradation by HPLC. Stability was also tested by incubating 0.74 MBq (20 μCi) ^{111}In-DOTA-AgRP-7C or ^{111}In-DOTA-AgRP-6E in 400 μL of mouse serum at 37°C for 2 h. Afterward, the mixture was re-suspended in 0.5 mL of DMF containing 5 μL of Triton X-100 and centrifuged at 16,000 g for 2 min. The supernatant, which contained >95% of the starting radioactivity, was filtered using a 10 K NanoSep device (Pall Corporation, East Hills, NY, USA). Greater than 99% of the radioactive material passed through this filter. The samples were analyzed by radio-HPLC, and the percentage of intact peptide was determined by quantifying peaks corresponding to the intact peptide and to the degradation products.

2.5. In Vitro Cell Uptake Assay. Cell uptake studies were performed as previously described [16]. Briefly, U87MG cells were seeded at a density of 0.2 × 10^6 in 12-well tissue culture plates and allowed to attach overnight. After washing three times with serum-free DMEM, cells were incubated with ^{111}In-DOTA-AgRP-7C or ^{111}In-DOTA-AgRP-6E (0.5 μCi/well) with or without the integrin-binding peptidomimetic, c(RGDyK), (2 μg/well) at 37 or 4°C for 15, 60, and 120 min, respectively. Cells were washed three times with chilled PBS containing 0.2% BSA and dissolved

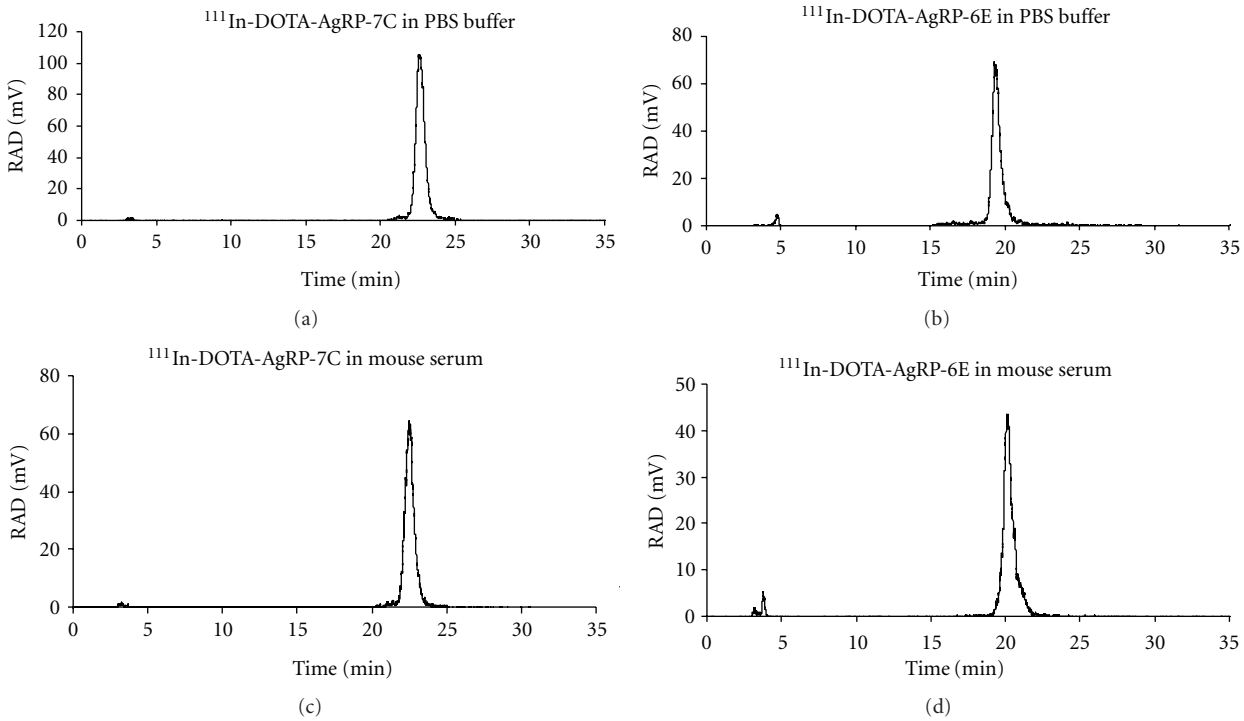

Figure 1: Stability analysis of ^{111}In-DOTA-AgRP-7C (a) and (b), and ^{111}In-DOTA-AgRP-6E (c) and (d) in PBS and mouse serum. The two radiopeptides were incubated with PBS for 24 h at room temperature, and mouse serum for 2 h at 37°C.

by treatment with 0.1 N NaOH at room temperature for 5 min. The cells' suspensions were collected and the resultant radioactivity was measured using a γ-counter (PerkinElmer 1470, Waltham, MA, USA). Cell uptake was expressed as the percentage of added radioactivity. Experiments were performed twice with triplicate wells.

2.6. Biodistribution Studies. All animal studies were carried out in compliance with federal and local institutional rules for animal experimentation. Approximately, 10^7 U87MG cells were suspended in PBS and subcutaneously implanted in the left shoulders of female athymic nu/nu mice. Tumors were allowed to grow to a size of 0.5 cm (2-3 weeks) before imaging experiments were performed. For biodistribution studies, U87MG tumor-bearing mice ($n = 3$ for each group) were injected with ^{111}In-DOTA-AgRP-7C (0.259–0.37 MBq, 7–10 Ci) or ^{111}In-DOTA-AgRP-6E (0.296–0.444 MBq, 8–12 μCi) via the tail vein and sacrificed at different time points (0.5, 2, 24, and 48 h) after injection (p.i.). Tumor and normal tissues of interest were removed and weighed, and their radioactivity was measured with a γ-counter. Radioactivity uptake was expressed as the percent injected dose per gram of tissue (%ID/g). To test the *in vivo* $\alpha_v\beta_3$ integrin targeting specificity of the probe, U87MG tumor-bearing mice ($n = 3$ for each group) were injected via the tail vein with a mixture of ^{111}In-DOTA-AgRP-7C (0.259–0.37 MBq, 7–10 μCi) and 330 μg of c(RGDyK). The mice were sacrificed at 2 h p.i. and the biodistribution of the radiolabeled peptide was measured as above.

2.7. Statistical Analysis. Quantitative data were expressed as mean ± SD. Means were compared using the Student *t*-test. A 95% confidence level was chosen to determine the significance between groups, with P values of less than 0.05 indicating significant differences.

3. Results

3.1. Radiolabeling. Due to the high thermal stability of cystine-knot peptides, DOTA-AgRP-6E and DOTA-AgRP-7C were easily labeled with $^{111}InCl_3$ by incubation in NH_4OAc buffer (pH 5.0–5.5) at 80°C for 45 min. Radiolabeled peptides were purified by PD-10 columns. The radiochemical yield for both peptides was determined by radio-HPLC to be ~50% and the radiochemical purity as also determined by radio-HPLC was greater than 99%. The specific activity of the peptides was determined to be approximately 0.25 mCi/nmol.

3.2. Peptide Stability. Both ^{111}In-DOTA-AgRP-7C and ^{111}In-DOTA-AgRP-6E were radiochemically stable after 24 h in 0.01 M PBS (pH 7.4), as determined by radio-HPLC analysis (Figures 1(a) and 1(c)). Furthermore, radio-HPLC analysis revealed that over 95% of the probes remained intact after 2 h incubation with mouse serum at 37°C (Figures 1(b) and 1(d)).

3.3. In Vitro Cell Uptake. The uptake of ^{111}In-DOTA-AgRP-7C and ^{111}In-DOTA-AgRP-6E was evaluated in U87MG

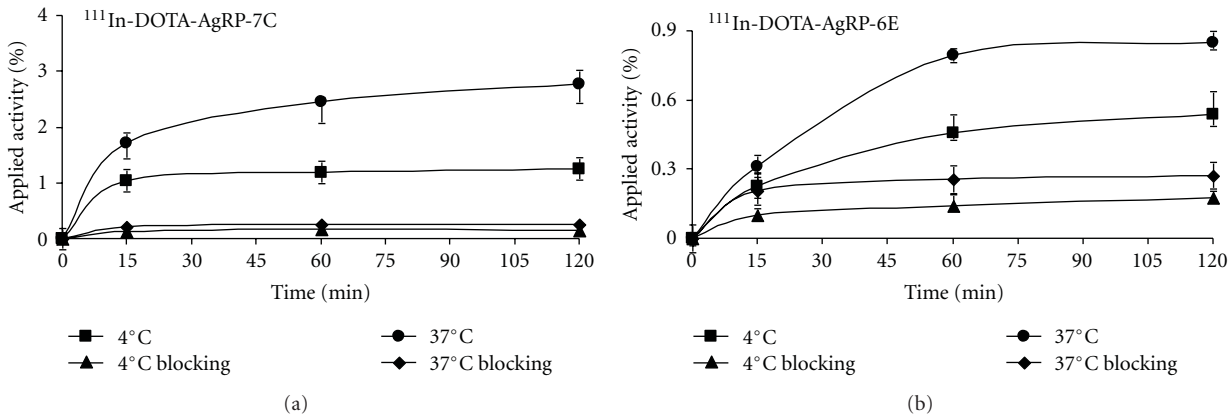

Figure 2: *In vitro* cell uptake assay of ^{111}In-DOTA-AgRP-7C (a) and ^{111}In-DOTA-AgRP-6E (b) on U87MG cells at 37°C and 4°C with or without c(RGDyK) blocking peptide ($n = 3$, mean ± SD).

cells and the results are shown in Figure 2. During the first 15 min incubation period at 37°C, ^{111}In-DOTA-AgRP-7C exhibited rapid cell accumulation, followed by a steady increase in binding and receptor-mediated uptake throughout the experiment. The cell uptake values of ^{111}In-DOTA-AgRP-7C after 15, 60 and 120 min at 37°C were 1.70 ± 0.07%, 2.46 ± 0.29%, and 2.76 ± 0.25%, and at 4°C were 1.05 ± 0.21%, 1.19 ± 0.27%, and 1.26 ± 0.38%, respectively (Figure 2(a)). Thus, a ∼2 fold greater accumulation of probe was observed in cells incubated at 37°C compared to those incubated at 4°C, which is indicative of internalization that occurs at physiological temperature. Moreover, cell surface binding and internalization were significantly inhibited by the addition of a large molar excess of the integrin-binding peptidomimetic c(RGDyK) ($P < 0.05$) (Figure 2(a)). After 1 h, cell uptake of the probe was inhibited 90% and 86% at 37°C and 4°C, respectively, demonstrating that the probe specifically targets cell surface integrin receptors.

In comparison, the U87MG cell uptake values of ^{111}In-DOTA-AgRP-6E after 15, 60, and 120 min at 37°C were 0.32 ± 0.01%, 0.85 ± 0.28% and 0.96 ± 0.07%, and at 4°C were 0.22 ± 0.04%, 0.45 ± 0.04%, and 0.50 ± 0.05%, respectively (Figure 2(b)). Similar to ^{111}In-DOTA-AgRP-7C, a ∼2-fold increase in uptake of ^{111}In-DOTA-AgRP-6E was found at 37°C compared to 4°C. Probe accumulation was blocked by the addition of c(RGDyK), with reductions in cell uptake of 38% at 37°C and 42% at 4°C after 1 h (Figure 2(b)).

3.4. Biodistribution Studies. The biodistribution of ^{111}In-DOTA-AgRP-7C was examined in nude mice bearing U87MG human glioblastoma tumors. The results of these experiments are shown in Table 2. Tumor uptake of the probe was 5.74 ± 1.60, 2.35 ± 0.36, 1.29 ± 0.02, and 0.76 ± 0.17%ID/g at 0.5, 2, 24, and 48 h, respectively, indicating relatively high tumor uptake and moderate tumor retention. The probe was found to have rapid blood clearance, with radioactivity levels of 0.68 ± 0.26 and 0.10 ± 0.02%ID/g remaining in the blood after 0.5 and 2 h p.i., respectively. Moreover, whole-body clearance of radioactivity was equally rapid. Except for the kidneys, accumulation in most organs examined were all lower than 1%ID/g at 2 h p.i. Prominent uptake was observed in the kidneys at early time points (33.93 ± 8.35%ID/g at 0.5 h), with decreasing accumulation from 2 to 48 h p.i. These data clearly indicate a renal excretion route and metabolic processing of the probe by the kidneys. With the rapid clearance of the radiotracer from blood and other normal organs, ^{111}In-DOTA-AgRP-7C exhibited high tumor-to-normal organ ratios in the blood, muscle, lung, liver, spleen, and pancreas (Table 2 and Figure 3(b)). For example, at 2 h p.i., the tumor-to-blood and tumor-to-muscle ratio of ^{111}In-DOTA-AgRP-7C was 25.8 and 39.8, respectively. To confirm *in vivo* integrin binding specificity, co-injection of ^{111}In-DOTA-AgRP-7C with a large molar excess of c(RGDyK) significantly reduced tumor uptake by ∼77% (0.54 ± 0.07 versus 2.35 ± 0.36%ID/g at 2 h p.i., $P < 0.05$) (Table 2). Significant differences were also found for probe uptake in normal tissues such as spleen upon addition of c(RGDyK) blocking peptide.

The biodistribution results of ^{111}In-DOTA-AgRP-6E are summarized in Table 3. Intermediate tumor uptake of ^{111}In-DOTA-AgRP-6E was observed at 0.5, 2, and 24 h p.i., with values of 1.76 ± 0.34, 1.21 ± 0.21, and 0.89 ± 0.06%ID/g, respectively. The probe also showed rapid blood clearance, with radioactivity levels of 1.27 ± 0.53 and 0.06 ± 0.05%ID/g remaining in the blood after 0.5 and 2 h. In addition, low normal tissue accumulation was seen with the exception of the kidneys (15.37 ± 3.19%ID/g and 14.68 ± 1.98%ID/g at 0.5 and 2 h, resp.). Finally, because of the rapid clearance of the probe from the blood and other organs, ^{111}In-DOTA-AgRP-6E also displayed high tumor-to-blood and tumor-to-muscle ratios at 2 and 24 h p.i. (Table 3).

4. Discussion

The native AgRP is a neuropeptide produced in the human brain that plays an important biological role in increasing appetite and decreasing metabolism and energy expenditure [17–19]. The C-terminus of AgRP is a cystine-knot peptide which contains a biologically active loop that naturally binds to melanocortin receptors. A truncated form of the AgRP

Table 2: Biodistribution results for ^{111}In-DOTA-AgRP-7C in nude mice bearing subcutaneous U87MG human glioblastoma xenografts. Data are expressed as the percent injected dose per gram of tissue (%ID/g) after intravenous injection of the probe (0.259–0.37 MBq, 7–10 μCi) at 0.5, 2, 24, and 48 h ($n = 3$). For 2 h blocking group, mice were coinjected with 330 μg of c(RGDyK).

Tissues	0.5 h	2 h	24 h	48 h	2 h Blocking
%ID/g					
Tumor	5.74 ± 1.60	2.35 ± 0.36	1.29 ± 0.02	0.76 ± 0.17	0.54 ± 0.07*
Brain	0.04 ± 0.02	0.02 ± 0.01	0.01 ± 0.00	0.01 ± 0.01	0.01 ± 0.00
Blood	0.68 ± 0.26	0.10 ± 0.02	0.01 ± 0.00	0.01 ± 0.00	0.07 ± 0.01
Heart	0.45 ± 0.16	0.12 ± 0.02	0.04 ± 0.01	0.03 ± 0.00	0.06 ± 0.01
Lung	2.11 ± 0.65	0.86 ± 0.20	0.26 ± 0.09	0.12 ± 0.02	0.41 ± 0.08
Liver	0.80 ± 0.19	0.43 ± 0.16	0.24 ± 0.03	0.19 ± 0.03	0.20 ± 0.04
Spleen	1.70 ± 0.62	0.88 ± 0.21	0.58 ± 0.09	0.46 ± 0.10	0.21 ± 0.03*
Kidneys	33.93 ± 8.35	30.59 ± 4.62	19.12 ± 2.17	8.47 ± 0.04	34.52 ± 4.02
Muscle	0.30 ± 0.13	0.06 ± 0.01	0.04 ± 0.01	0.02 ± 0.01	0.10 ± 0.10
Pancreas	0.42 ± 0.17	0.13 ± 0.03	0.09 ± 0.01	0.05 ± 0.01	0.13 ± 0.03
Bone	1.41 ± 0.36	0.63 ± 0.05	0.39 ± 0.07	0.24 ± 0.05	0.45 ± 0.01
Stomach	2.17 ± 0.49	0.80 ± 0.06	0.21 ± 0.01	0.14 ± 0.02	0.24 ± 0.04*
Intestine	2.02 ± 0.71	0.60 ± 0.13	0.29 ± 0.02	0.22 ± 0.03	0.25 ± 0.06*
Ratio					
Tumor-to-blood	8.90 ± 3.09	25.81 ± 10.46	127.53±30.50	144.12±36.33	8.18 ± 0.15*
Tumor-to-muscle	20.56 ± 6.40	39.83 ± 9.16	37.69 ± 9.81	41.12 ± 8.62	14.03±13.45*

*$P < 0.05$ compared with ^{111}In-DOTA-AgRP-7C without c(RGDyK) blocking at 2 h. Data are presented as mean ± SD ($n = 3$).

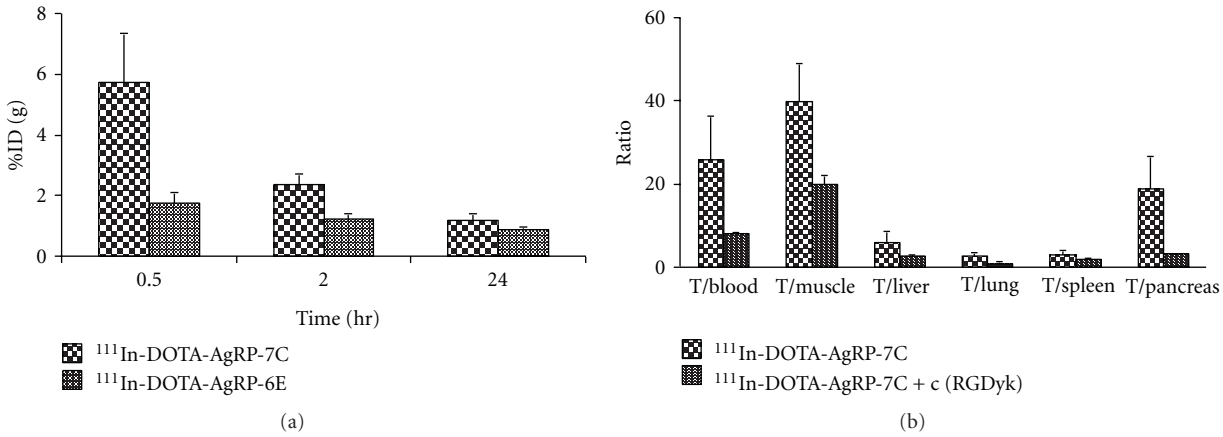

Figure 3: U87MG tumor uptake for ^{111}In-DOTA-AgRP-7C and ^{111}In-DOTA-AgRP-6E at 0.5, 2, and 24 h p.i. (a). Tumor (T)-to-normal organ ratios for ^{111}In-DOTA-AgRP-7C with or without c(RGDyK) blocking peptide at 2 h after the injection of the probe (b).

cystine knot peptide, AgRP* is emerging as a highly attractive platform for developing novel molecular imaging probes [20, 21]. AgRP* is small in size (~4 kDa) and possesses a rigid structure, yet contains four solvent-accessible loops that could be used for mutagenesis [8]. In addition, peptides based on AgRP* are likely to be nonimmunogenic due to their human origin and high thermal and proteolytic stability; Furthermore, AgRP* is amenable to recombinant and synthetic production, which will allow site-specific incorporation of labels or chemical functionality in future studies.

In our previous studies, the AgRP*-based $\alpha_v\beta_3$ integrin binder AgRP-7C was discovered and used for PET imaging of tumor angiogenesis [8, 13]. Excellent *in vivo* tumor imaging contrast was achieved which demonstrates the success of using AgRP*-based scaffolds for molecular probe development [13]. This study motivated us to further evaluate engineered AgRP*-based integrin targeting peptides for potential SPECT imaging applications. The high affinity binder DOTA-AgRP-7C (IC_{50} ~20 nM) and moderate affinity binder DOTA-AgRP-6E (IC_{50} ~130 nM) were radiolabeled with ^{111}In and tested for their ability to target tumors in living subjects.

The cystine-knot motif of AgRP* conferred high stability to the radiolabeled peptides. Compared to the reaction temperature (37°C) used for ^{64}Cu radiolabeling of AgRP-7C,

Table 3: Biodistribution results for ^{111}In-DOTA-AgRP-6E in nude mice bearing subcutaneous U87MG human glioblastoma xenografts. Data are expressed as the percent %ID/g after intravenous injection of the probe (0.296–0.444 MBq, 8–12 μCi) at 0.5, 2, and 24 h ($n = 3$).

Tissue	0.5 h	2 h	24 h
%ID/g			
Tumor	1.76 ± 0.34	1.21 ± 0.21	0.89 ± 0.06
Brain	0.06 ± 0.01	0.02 ± 0.01	0.02 ± 0.01
Blood	1.27 ± 0.53	0.06 ± 0.05	0.01 ± 0.00
Heart	0.80 ± 0.24	0.18 ± 0.06	0.12 ± 0.02
Lung	1.86 ± 0.56	0.54 ± 0.12	0.27 ± 0.02
Liver	0.87 ± 0.20	0.52 ± 0.01	0.48 ± 0.02
Spleen	1.36 ± 0.26	0.83 ± 0.05	0.65 ± 0.06
Kidneys	15.37 ± 3.19	14.68 ± 1.98	6.87 ± 1.19
Muscle	0.64 ± 0.09	0.15 ± 0.07	0.07 ± 0.01
Pancreas	0.57 ± 0.23	0.20 ± 0.06	0.14 ± 0.01
Bone	1.18 ± 0.15	0.56 ± 0.10	0.36 ± 0.04
Stomach	2.02 ± 0.47	0.87 ± 0.14	0.53 ± 0.02
Intestine	2.04 ± 0.54	1.13 ± 0.14	0.93 ± 0.04
Ratio			
Tumor-to-blood	1.71 ± 1.21	33.04 ± 23.28	142.32 ± 3.39
Tumor-to-muscle	2.75 ± 0.28	9.20 ± 3.88	13.07 ± 1.94

Data are presented as mean ± SD ($n = 3$).

^{111}In radiolabeling of DOTA-AgRP-7C and DOTA-AgRP-6E was performed at 80°C. The high reaction temperature did not appear to denature the peptides as demonstrated by the cell uptake and biodistribution studies. Similar to ^{64}Cu-DOTA-AgRP-7C, both ^{111}In-DOTA-AgRP-7C and ^{111}In-DOTA-AgRP-6E were found to be stable in PBS buffer for at least 24 h and in mouse serum for 2 h.

In biodistribution studies, ^{111}In-DOTA-AgRP-7C shows rapid tumor targeting and uptake in integrin $\alpha_v\beta_3$ expressing human glioblastoma xenografts (5.74 ± 1.60%ID/g at 0.5 h), which is significant higher than that of ^{64}Cu-DOTA-AgRP-7C (1.92 ± 0.48%ID/g at 0.5 h, $P < 0.05$). Moreover, ^{111}In-DOTA-AgRP-7C shows fast blood clearance (0.68 ± 0.26%ID/g at 0.5 h), through the kidney-urinary system. The kidney uptake of ^{111}In-DOTA-AgRP-7C is 30.59 ± 4.62%ID/g at 2 h p.i., which is much lower than that of ^{64}Cu-DOTA-AgRP-7C (60.22 ± 17.52%ID/g at 2 h). Lastly, the uptake and retention of ^{111}In-DOTA-AgRP-7C in other normal organs is low (Table 2). Overall, these data indicate that using a different radiometal (^{111}In compared to ^{64}Cu) preserves the tumor targeting ability of engineered cystine-knot peptides, but significantly improves the *in vivo* performance of the resulting probe.

Both ^{111}In and ^{64}Cu labeled DOTA-AgRP-7C exhibit high renal uptake, which is likely attributed to (1) the long residence time of radiometabolites produced by lysosomal degradation of the radiolabeled peptides within renal cells; (2) the overall positive charge of the peptides [22–25]. Several strategies previously reported that the accumulation of radiopeptide in the kidneys can be effectively reduced by coinjection of cationic amino acid such as lysine, or polylysine molecules [16, 26]. These methods could potentially be explored to reduce the radiation dose to kidney.

Biodistribution studies reveal that ^{111}In-DOTA-AgRP-7C has significant higher tumor uptake than that of ^{111}In-DOTA-AgRP-6E at different time points (0.5, 2, and 24 h) (Figure 3(a)). This could be related to the stronger integrin binding affinity of AgRP-DOTA-7C compared to AgRP-DOTA-6E (IC_{50}: 22.6 ± 3.9 nM versus 125.5 ± 16.6 nM, resp.) [27]. Both probes display good retention in tumor and low uptakes in most of normal organs (Tables 2 and 3). Interestingly, the kidney uptake of ^{111}In-DOTA-AgRP-6E was significantly lower than that of ^{111}In-DOTA-AgRP-7C (14.68 versus 30.59%ID/g at 2 h p.i.), suggesting that modification of the amino acid sequence of the engineered loop of AgRP* may help to optimize *in vivo* behavior. Because ^{111}In-DOTA-AgRP-7C showed higher tumor uptake compared to ^{111}In-DOTA-AgRP-6E, the *in vivo* integrin targeting specificity of the probe was further confirmed by a blocking study, using a peptidomimetic (c(RGDyK)) that binds to the same epitope on integrin receptors. Compared to the nonblocking group, the tumor uptake of ^{111}In-DOTA-AgRP-7C is significantly decreased upon co-injection of c(RGDyK) (2.35 ± 0.36 versus 0.54 ± 0.07%ID/g at 2 h, resp.) Table 2 and Figure 3(b), in agreement with the *in vitro* cell uptake results.

In a previous study, the tumor uptake of ^{111}In-DOTA-c(RGDfK) was reported as 6.28%ID/g at 1 h p.i. in a SKOV3 xenograft model [28]. In comparison, we show that the tumor uptake of ^{111}In-DOTA-AgRP-7C is 5.74%ID/g at 0.5 h p.i. in a U87MG xenograft model. Importantly, ^{111}In-DOTA-AgRP-7C and ^{111}In-DOTA-AgRP-6E were found to have much lower uptake and faster clearance in liver, lung, spleen and other normal tissues compared to ^{111}In-DOTA-c(RGDfK). The fast clearance of ^{111}In-labeled AgRP* mutants resulted in high tumor-to-blood and tumor-to-muscle ratios at 24 and 48 h p.i. (Tables 2 and 3,

Figure 3), demonstrating the advantages of using an AgRP*-based scaffold for imaging probe development [28, 29].

5. Conclusions

In summary, we tested the $\alpha_v\beta_3$ integrin-targeted cystine-knot peptides ^{111}In-DOTA-AgRP-6E and ^{111}In-DOTA-AgRP-7C as SPECT imaging agents in mouse tumor models. Compared to ^{111}In-DOTA-AgRP-6E, ^{111}In-DOTA-AgRP-7C exhibits higher integrin binding affinity and tumor uptake. Moreover, this probe demonstrates rapid tumor uptake, high tumor-to-normal tissue contrast, and favorable pharmacokinetics. These results suggest that AgRP* mutant 7C has potential for clinical translation as a new SPECT imaging agent for integrin $\alpha_v\beta_3$ positive tumors. Furthermore, cystine-knot peptides are a promising class of molecular scaffolds, and warrant further development and investigation for imaging applications.

Conflict of Interests

The authors declare that they have no conflict of interests.

Acknowledgments

This work was supported, in part, by National Cancer Institute (NCI) NCI 5 R01 CA119053 (to Z. Cheng), NCI *In Vivo* Cellular Molecular Imaging Center (ICMIC) Grant P50 CA114747, NCI 5K01 CA104706 (to J. R. Cochran), and a Stanford Molecular Imaging Scholars postdoctoral fellowship R25 CA118681 (to R. H. Kimura). Moreover, this work was also funded by the National Science Foundation for Young Scholars of China (Grant no. 81101072) and Shanghai Health Bureau Research Funding for Young Scholars (Grant no. 20114Y161) (to L. Jiang).

References

[1] T. Saga, M. Koizumi, T. Furukawa, K. Yoshikawa, and Y. Fujibayashi, "Molecular imaging of cancer—evaluating characters of individual cancer by PET/SPECT imaging," *Cancer Science*, vol. 100, no. 3, pp. 375–381, 2009.

[2] R. Weissleder and U. Mahmood, "Molecular imaging," *Radiology*, vol. 219, no. 2, pp. 316–333, 2001.

[3] T. F. Massoud and S. S. Gambhir, "Molecular imaging in living subjects: seeing fundamental biological processes in a new light," *Genes and Development*, vol. 17, no. 5, pp. 545–580, 2003.

[4] S. Mather, "Molecular imaging with bioconjugates in mouse models of cancer," *Bioconjugate Chemistry*, vol. 20, no. 4, pp. 631–643, 2009.

[5] W. A. Weber, "Positron emission tomography as an imaging biomarker," *Journal of Clinical Oncology*, vol. 24, no. 20, pp. 3282–3292, 2006.

[6] H. Kolmar, "Biological diversity and therapeutic potential of natural and engineered cystine knot miniproteins," *Current Opinion in Pharmacology*, vol. 9, no. 5, pp. 608–614, 2009.

[7] H. Kolmar, "Alternative binding proteins: biological activity and therapeutic potential of cystine-knot miniproteins," *FEBS Journal*, vol. 275, no. 11, pp. 2684–2690, 2008.

[8] A. P. Silverman, A. M. Levin, J. L. Lahti, and J. R. Cochran, "Engineered cystine-knot peptides that bind $\alpha_v\beta_3$ integrin with antibody-like affinities," *Journal of Molecular Biology*, vol. 385, no. 4, pp. 1064–1075, 2009.

[9] R. O. Hynes, "Integrins: versatility, modulation, and signaling in cell adhesion," *Cell*, vol. 69, no. 1, pp. 11–25, 1992.

[10] R. E. B. Seftor, E. A. Seftor, K. R. Gehlsen et al., "Role of the $\alpha_v\beta_3$ integrin in human melanoma cell invasion," *Proceedings of the National Academy of Sciences of the United States of America*, vol. 89, no. 5, pp. 1557–1561, 1992.

[11] P. C. Brooks, R. A. F. Clark, and D. A. Cheresh, "Requirement of vascular integrin $\alpha_v\beta_3$ for angiogenesis," *Science*, vol. 264, no. 5158, pp. 569–571, 1994.

[12] E. Chang, S. Liu, G. Gowrishankar et al., "Reproducibility study of [^{18}F]FPP(RGD)$_2$ uptake in murine models of human tumor xenografts," *European Journal of Nuclear Medicine and Molecular Imaging*, vol. 38, no. 4, pp. 722–730, 2011.

[13] L. Jiang, R. H. Kimura, Z. Miao et al., "Evaluation of a ^{64}Cu-labeled cystine-knot peptide based on agouti-related protein for PET of tumors expressing $\alpha_v\beta_3$ integrin," *Journal of Nuclear Medicine*, vol. 51, no. 2, pp. 251–258, 2010.

[14] J. Yang, H. Guo, and Y. Miao, "Technetium-99m-labeled Arg-Gly-Asp-conjugated alpha-melanocyte stimulating hormone hybrid peptides for human melanoma imaging," *Nuclear Medicine and Biology*, vol. 37, no. 8, pp. 873–883, 2010.

[15] Z. Xiong, Z. Cheng, X. Zhang et al., "Imaging chemically modified adenovirus for targeting tumors expressing integrin $\alpha_v\beta_3$ in living mice with mutant herpes simplex virus type 1 thymidine kinase PET reporter gene," *Journal of Nuclear Medicine*, vol. 47, no. 1, pp. 130–139, 2006.

[16] Z. Cheng, J. Chen, T. P. Quinn, and S. S. Jurisson, "Radioiodination of rhenium cyclized α-melanocyte-stimulating hormone resulting in enhanced radioactivity localization and retention in melanoma," *Cancer Research*, vol. 64, no. 4, pp. 1411–1418, 2004.

[17] M. Bäckberg, N. Madjid, S. O. Ögren, and B. Meister, "Down-regulated expression of agouti-related protein (AGRP) mRNA in the hypothalamic arcuate nucleus of hyperphagic and obese tub/tub mice," *Molecular Brain Research*, vol. 125, no. 1-2, pp. 129–139, 2004.

[18] J. R. Shutter, M. Graham, A. C. Kinsey, S. Scully, R. Lüthy, and K. L. Stark, "Hypothalamic expression of ART, a novel gene related to agouti, is up-regulated in obese and diabetic mutant mice," *Genes and Development*, vol. 11, no. 5, pp. 593–602, 1997.

[19] M. M. Ollmann, B. D. Wilson, Y. K. Yang et al., "Antagonism of Central Melanocortin receptors in vitro and in vivo by agouti-related protein," *Science*, vol. 278, no. 5335, pp. 135–138, 1997.

[20] P. J. Jackson, J. C. McNulty, Y. K. Yang et al., "Design, pharmacology, and NMR structure of a minimized cystine knot with agouti-related protein activity," *Biochemistry*, vol. 41, no. 24, pp. 7565–7572, 2002.

[21] P. J. Jackson, N. R. Douglas, B. Chai et al., "Structural and molecular evolutionary analysis of Agouti and Agouti-related proteins," *Chemistry and Biology*, vol. 13, no. 12, pp. 1297–1305, 2006.

[22] S. R. Kumar and S. L. Deutscher, "^{111}In-labeled galectin-3-targeting peptide as a SPECT agent for imaging breast tumors," *Journal of Nuclear Medicine*, vol. 49, no. 5, pp. 796–803, 2008.

[23] C. E. Mogensen and K. Solling, "Studies on renal tubular protein reabsorption: partial and near complete inhibition by certain amino acids," *Scandinavian Journal of Clinical and Laboratory Investigation*, vol. 37, no. 6, pp. 477–486, 1977.

[24] S. Silbernagl, "The renal handling of amino acids and oligopeptides," *Physiological Reviews*, vol. 68, no. 3, pp. 911–1007, 1988.

[25] J. Q. Chen, Z. Cheng, N. K. Owen et al., "Evaluation of an 111In-DOTA-rhenium cyclized α-MSH analog: a novel cyclic-peptide analog with improved tumor-targeting properties," *Journal of Nuclear Medicine*, vol. 42, no. 12, pp. 1847–1855, 2001.

[26] J. Q. Chen, Z. Cheng, T. J. Hoffman, S. S. Jurisson, and T. P. Quinn, "Melanoma-targeting properties of ^{99m}technetium-labeled cyclic α-melanocyte-stimulating hormone peptide analogues," *Cancer Research*, vol. 60, no. 20, pp. 5649–5658, 2000.

[27] L. Jiang, Z. Miao, R. H. Kimura et al., "Preliminary evaluation of ^{177}Lu-labeled knottin peptides for integrin receptor-targeted radionuclide therapy," *European Journal of Nuclear Medicine and Molecular Imaging*, vol. 38, no. 4, pp. 613–622, 2011.

[28] M. Yoshimoto, K. Ogawa, K. Washiyama et al., "$\alpha_v\beta_3$ integrin-targeting radionuclide therapy and imaging with monomeric RGD peptide," *International Journal of Cancer*, vol. 123, no. 3, pp. 709–715, 2008.

[29] M. L. Janssen, W. J. Oyen, I. Dijkgraaf et al., "Tumor targeting with radiolabeled $\alpha_v\beta_3$ integrin binding peptides in a nude mouse model," *Cancer Research*, vol. 62, no. 21, pp. 6146–6151, 2002.

Hindawi Publishing Corporation
Journal of Biomedicine and Biotechnology
Volume 2012, Article ID 259349, 14 pages
doi:10.1155/2012/259349

Review Article

Recent Advances in Imaging of Dopaminergic Neurons for Evaluation of Neuropsychiatric Disorders

Lie-Hang Shen, Mei-Hsiu Liao, and Yu-Chin Tseng

Institute of Nuclear Energy Research, Jiaan Village, Lungtan Township, Taoyuan 32546, Taiwan

Correspondence should be addressed to Yu-Chin Tseng, yctseng@iner.gov.tw

Received 15 December 2011; Accepted 27 January 2012

Academic Editor: David J. Yang

Dopamine is the most intensely studied monoaminergic neurotransmitter. Dopaminergic neurotransmission plays an important role in regulating several aspects of basic brain function, including motor, behavior, motivation, and working memory. To date, there are numerous positron emission tomography (PET) and single photon emission computed tomography (SPECT) radiotracers available for targeting different steps in the process of dopaminergic neurotransmission, which permits us to quantify dopaminergic activity in the living human brain. Degeneration of the nigrostriatal dopamine system causes Parkinson's disease (PD) and related Parkinsonism. Dopamine is the neurotransmitter that has been classically associated with the reinforcing effects of drug abuse. Abnormalities within the dopamine system in the brain are involved in the pathophysiology of attention deficit hyperactivity disorder (ADHD). Dopamine receptors play an important role in schizophrenia and the effect of neuroleptics is through blockage of dopamine D_2 receptors. This review will concentrate on the radiotracers that have been developed for imaging dopaminergic neurons, describe the clinical aspects in the assessment of neuropsychiatric disorders, and suggest future directions in the diagnosis and management of such disorders.

1. Introduction

Neuropsychiatric disorders cause severe human suffering and are becoming a major socioeconomic burden to modern society. The rapid development of noninvasive tools for imaging human brains will improve our understanding of complex brain functions and provide more insight into the pathophysiology of neuropsychiatric disorders. Neuroimaging techniques currently utilized in neuropsychiatric disorders include a variety of modalities, such as ultrasound, X-rays, computed tomography (CT), functional magnetic resonance imaging (fMRI), and nuclear medicine imaging [1].

The interactions between transporters/receptors and neurotransmitters play a key role in the diagnosis and treatment of neuropsychiatric disorders. In contrast with conventional diagnostic imaging procedures, which simply provide anatomical or structural pictures of organs and tissues, nuclear medicine imaging is the only tool to visualize the distribution, density, and activity of neurotransmitters, receptors, or transporters in the brain. Nuclear medicine imaging involves the administration of radioactively labeled tracers, which decay over time by emitting gamma rays that can be detected by a positron emission tomography (PET) or single photon emission computed tomography (SPECT) scanner [2, 3]. PET uses coincidence detection in lieu of absorptive collimation to determine the positron-electron annihilation, which produces two 511 keV photons in opposite direction. This partially explains the greater spatial resolution and sensitivity of PET. Radioisotopes used in PET imaging typically have short physical half-life and consequently many of them have to be produced with an on-site cyclotron. Radioisotopes used for labeling PET radiopharmaceuticals include ^{11}C, ^{13}N, ^{15}O, ^{18}F, ^{64}Cu, ^{62}Cu, ^{124}I, ^{76}Br, ^{82}Rb, and ^{68}Ga, with ^{18}F being the most clinically utilized. SPECT radiotracers typically have longer physical half-life than most PET tracers; thus a central radiopharmaceutical laboratory can prepare radiotracers for delivery to SPECT facilities within a radius of several hundred miles. There are a range of radioisotopes (such as ^{99m}Tc, ^{201}Tl, ^{67}Ga, ^{123}I, and ^{111}In) that can be used for labeling SPECT

radiopharmaceuticals, depending on the specific application. ^{99m}Tc is the most used radionuclide for nuclear medicine because it is readily available, relatively inexpensive, and gives lower radiation exposure [2–4].

A major advantage of nuclear medicine imaging is the extraordinarily high sensitivity: a typical PET scanner can detect between 10^{-11} mol/L to 10^{-12} mol/L concentrations, whereas MRI has a sensitivity of around 10^{-3} mol/L to 10^{-5} mol/L [4]. Because many molecules relevant to neuropsychiatric disorders are present at concentrations below 10^{-8} M, nuclear medicine imaging is currently the only available *in vivo* method capable of quantifying subtle cerebral pathophysiological changes that might occur before neurostructural abnormalities take place [5].

Radiotracers must fulfill several criteria to be successful for PET or SPECT imaging: including readily labeled with appropriate radionuclide and the labeled radiotracer being stable *in vivo* and nontoxic; sufficient affinity and high selectivity for the specific receptor combined with low nonspecific binding to brain tissue not containing the receptor of interest; rapid permeation through the blood-brain barrier permitting high access of tracers to receptors, as well as allowing high initial brain uptake and fast clearance of the activity from the brain. A large number of radiotracers have been developed for brain imaging, but most of them were utilized only *in vitro* or in experimental animals and only few have the potentiality in clinical practice. Selective radiotracers are available for the study of dopaminergic, acetylcholinergic, serotonergic, and norepinephrine systems, as well as β-amyloid plaques with promising results [5, 6].

Dopamine is the most intensely studied monoaminergic neurotransmitter. Dopaminergic neurotransmission plays an important role in regulating several aspects of basic brain function, including motor, behavior, motivation, and working memory, and is involved in the pathogenesis of several psychiatric and neurological disorders. Degeneration of the nigrostriatal dopamine system causes Parkinson's disease (PD) and related Parkinsonism. Postsynaptic receptors may be involved in neurodegenerative disorders; they are functionally changed in Parkinsonism. Dopamine is thought to be involved in drug abuse. Most drugs of abuse, with the exception of benzodiazepines, have a direct effect on increasing the dopamine reward cycle in the brain. Abnormalities within the dopamine system in the brain play a major role in the pathophysiology of attention deficit hyperactivity disorder (ADHD). Dopamine receptors also play an important role in schizophrenia and the effect of neuroleptics is through blockage of dopamine D_2 receptors [6]. Neuroimaging techniques permit us to quantify dopaminergic activity in the living human brain, which has become increasingly part of the assessment and diagnosis of neuropsychiatric disorders. To date, there are numerous PET and SPECT radiotracers available for targeting different steps in the process of dopaminergic neurotransmission. This paper will concentrate on the radiotracers that have been developed for imaging dopaminergic neurons, describe their unique strengths and limitations in the assessment of neuropsychiatric disorders, and suggest future directions in the diagnosis and management of neuropsychiatric disorders.

2. Radiotracers for Imaging Dopaminergic Neurons

Diagnosis of neurological and psychiatric disorders associated with disturbances of dopaminergic functioning can be challenging, especially in the early stages. The evolution of neuroimaging technique over the past decade has yielded unprecedented information about dopaminergic neurons. PET and SPECT techniques have been successfully employed to visualize the activity of dopamine synthesis, reuptake sites, and receptors (Table 1). The Chemical structure of various radiotracers for the assessment of dopamine system is illustrated on Figure 1. DOPA decarboxylase activity and dopamine turnover can both be measured with ^{18}F-DOPA or ^{18}F-FMT PET [7]. ^{18}F-DOPA PET was the first neuroimaging technique validated for the assessment of presynaptic dopaminergic integrity. The uptake of ^{18}F-DOPA reflects both the density of the axonal terminal plexus and the activity of the striatal aromatic amino acid decarboxylase (AADC), the enzyme responsible for the conversion of ^{18}F-DOPA to ^{18}F-dopamine. However, AADC is present in the terminals of all monoaminergic neurons, measurements of ^{18}F-DOPA uptake into extrastriatal areas provides an index of the density of the serotonergic, norepinephrinergic, and dopaminergic terminals [8–10].

Dopamine transporter (DAT) is a protein complex located in presynaptic dopaminergic nerve terminals, which serves as the primary means for removing dopamine from the synaptic cleft. The availability of presynaptic DAT can be assessed with various radiotracers, which are typically tropane based [7, 11]. Several PET tracers (^{11}C-CFT, ^{18}F-CFT, ^{18}F-FP-CIT, and ^{11}C-PE2I) and SPECT tracers such as ^{123}I-β-CIT (Dopascan), ^{123}I-FP-CIT (ioflupane, DaTSCAN), ^{123}I-altropane, ^{123}I-IPT, ^{123}I-PE2I, and ^{99m}Tc-TRODAT-1 are now available to measure DAT availability [8, 11–17]. ^{123}I-β-CIT was the first widely applied SPECT tracer in imaging DAT, however, the lack of specificity is a disadvantage. This radiotracer binds not only to DAT but also to norepinephrine transporter (NET) and serotonin transporter (SERT). Another disadvantage of ^{123}I-β-CIT is considered not convenient for routine out-patient evaluations since adequate imaging should be performed 20–30 h following the injection [11]. The faster kinetics of ^{123}I-FP-CIT is a clear advantage for clinical use, which allows adequate acquisition as early as 3 h following injection [18]. Conversely, ^{123}I-altropane SPECT images have been less extensively investigated and are more difficult to quantify owing to rapid wash out from the brain [19]. The technetium based ^{99m}Tc-TRODAT-1 has the advantage of being relatively inexpensive and available in kit form. The easy preparation of ^{99m}Tc-TRODAT-1 from lyophilized kits could be an ideal agent for daily clinical application [16]. However, its specific signal is lower than the ^{123}I-based SPECT tracers. To date, only DaTSCAN (^{123}I-FP-CIT) and ^{99m}Tc-TRODAT-1 are commercially available in the market and licensed for detecting loss of functional dopaminergic neuron terminals in the striatum.

In the brain, dopamine activates the five known types of dopamine receptors—D_1, D_2, D_3, D_4, and D_5. Dopamine

Table 1: Radiotracers available for targeting different steps in the process of dopaminergic neurotransmission and clinical applications.

Targeting	Tracer	Chemical name	Clinical studies (references)
Dopamine synthesis and turn over	^{18}F-DOPA	L-3,4-dihydroxy-6-[^{18}F]-fluorophenylalanine	PD [11, 20–23], gene therapy for PD [24–26], ADHD [27], schizophrenia [28, 29]
	^{18}F-FMT	O-[^{18}F]-fluoromethyl-D-tyrosine	Gene therapy for PD [30, 31]
Dopamine transporter	^{11}C-CFT	[^{11}C]-2β-carbomethoxy-3β-ltropane	Heroin abuse [32]
	^{11}C-altropane	2β-carbomethoxy-3β-(4-fluorophenyl)-N-((E)-3-iodo-prop-2-enyl)tropane	ADHD [33]
	^{123}I-β-CIT (Dopascan)	[^{123}I]-(1R)-2-β-carbomethoxy-3-β-(4-iodophenyl)-tropane	PD [11, 20], PM [34], PD & ET [35], cocaine abuse [36, 37], ADHD [38]
	^{123}I-FP-CIT (DaTSCAN)	[^{123}I] N-ω-fluoropropyl-2β-carbomethoxy-3β-(4-iodophenyl) nortropane	PM [39–41], PM & ET [42], PD & DLB [43], AD, PD & DLB [44], ADHD [45–47], schizophrenia [48]
	^{99m}Tc-TRODAT-1	[^{99m}Tc]technetium [2-[[2-[[[3-(4-chlorophenyl)-8-methyl-8-azabicyclo [3.2.1]oct-2-yl]-methyl](2-mercaptoethyl)amino]-ethyl]amino]ethane-thiolato(3-)-N2,N2′,S2,S2′]oxo-[1R-(exo-exo)]	PD [23, 49–51], MSA [52], PM & VP [53], DRD [54], PSP [55], genetic study of PD [51, 56], genetic study of MJD [57], cocaine abuse [58], opiate abuse [59], nicotine dependence [60, 61], ADHD [62–68]
	^{123}I-altropane	[^{123}I]-2β-carbomethoxy-3β-(4-fluorophenyl)-N-(1-iodoprop-1-en-3-yl) ortropane	PD [21], ADHD [69]
	^{123}I-IPT	[^{123}I]-N-(3-iodopropen-2-yl)-2-carbomethoxy-3beta-(4-chlorophenyl) tropane	ADHD [70]
Dopamine D_1 receptor	^{11}C-NNC 112	(+)-5-(7-Benzofuranyl)-8-chloro-7-hydroxy-3-methyl-2,3,4,5-tetrahydro-1H-3-benzazepine	Schizophrenia [71]
	^{11}C-SCH 23390	(R)-(+)-8-Chloro-2,3,4,5-tetrahydro-3-[^{11}C]methyl-5-phenyl-1H-3-benzazepin-7-ol	Schizophrenia [72, 73]
Dopamine D_2 receptor	^{11}C-Raclopride	3,5-dichloro-N-{[(2S)-1-ethylpyrrolidin-2-yl]methyl}-2-hydroxy-6-[^{11}C]methoxybenzamide	Drug abuse [74–79] cocaine abuse [80, 81], methamphetamine abuse [82], opiate abuse [83], alcohol dependence [84], ADHD [85, 86], antipsychotics [48, 87–89]
	^{123}I-IBZM	(S)-(-)-3-[^{123}I]iodo-2-hydroxy-6-methoxy-N-[(1-ethyl-2-pyrrolidinyl)methyl]benzamide	PM [40, 41], schizophrenia [90], antipsychotics [89, 91, 92]
vesicular monoamine transporter type-2	^{11}C-DTBZ	(±)-α-[^{11}C]dihydrotetrabenazine	PD [7, 11, 20]
	^{18}F-FP-DTBZ (AV-133)	9-[^{18}F]fluoropropyl-(+)-dihydrotetrabenazine	PD [93], DLB & AD [94]

Abbreviations: Parkinson's disease (PD), Parkinsonism (PM), multiple-system atrophy (MSA), progressive supranuclear palsy (PSP), essential tremor (ET), vascular Parkinsonism (VP), Machado-Joseph disease (MJD), DOPA-responsive dystonia (DRD), dementia with Lewy bodies disease (DLB), Alzheimer's disease (AD), and attention deficit hyperactivity disorder (ADHD).

receptors belong to the G-protein-coupled superfamily. The dopamine D_1 and D_5 receptor subtypes are known as D_1-like receptors and couple to inhibitory G-proteins, whereas the dopamine D_2, D_3, D_4 receptor subtypes are known as D_2-like family and couple to stimulatory G-proteins. Only dopamine D_1 and D_2 receptors have been imaged in humans. For dopamine D_1 subtype, the most commonly used radiotracers are ^{11}C-SCH23390 and ^{11}C-NNC112 [7]. As assessment of D_1-like receptors has not gained clinical significance; therefore many investigations have focused on the D_2-like receptor system in the past. Dopamine D_2 receptors are assessed most commonly with the use of benzamide radiotracers. ^{11}C-raclopride, ^{18}F-spiperone, and ^{18}F-methyl-benperidol have been developed for PET imaging; alternatively, ^{123}I-IBZM (^{123}I-iodobenzamide), ^{123}I-epidrpride, and ^{123}I-IBF have been developed for SPECT imaging. ^{11}C-raclopride is currently the gold standard PET tracer for dopamine D_2 receptors. In contrast to ^{11}C-raclopride, with a physical half-life of approximately 20 min, ^{123}I-IBZM allows shipment over considerable distances since the radiotracer has a longer physical half-life of 13.2 h [95, 96]. ^{123}I-epidrpride, displaying very high affinity to D_2/D_3 receptors, has been exploited for quantification and visualization of low density extrastriatal D_2/D_3 receptors [97].

The vesicular monoamine transporter type 2 (VMAT2) is expressed by all monoaminergic neurons and serves to pump monoamines from cytosol into synaptic vesicles thereby protecting the neurotransmitters from catabolism by cytosolic enzymes and packaging them for subsequent exocytotic release [98]. In striatum, more than 95% of

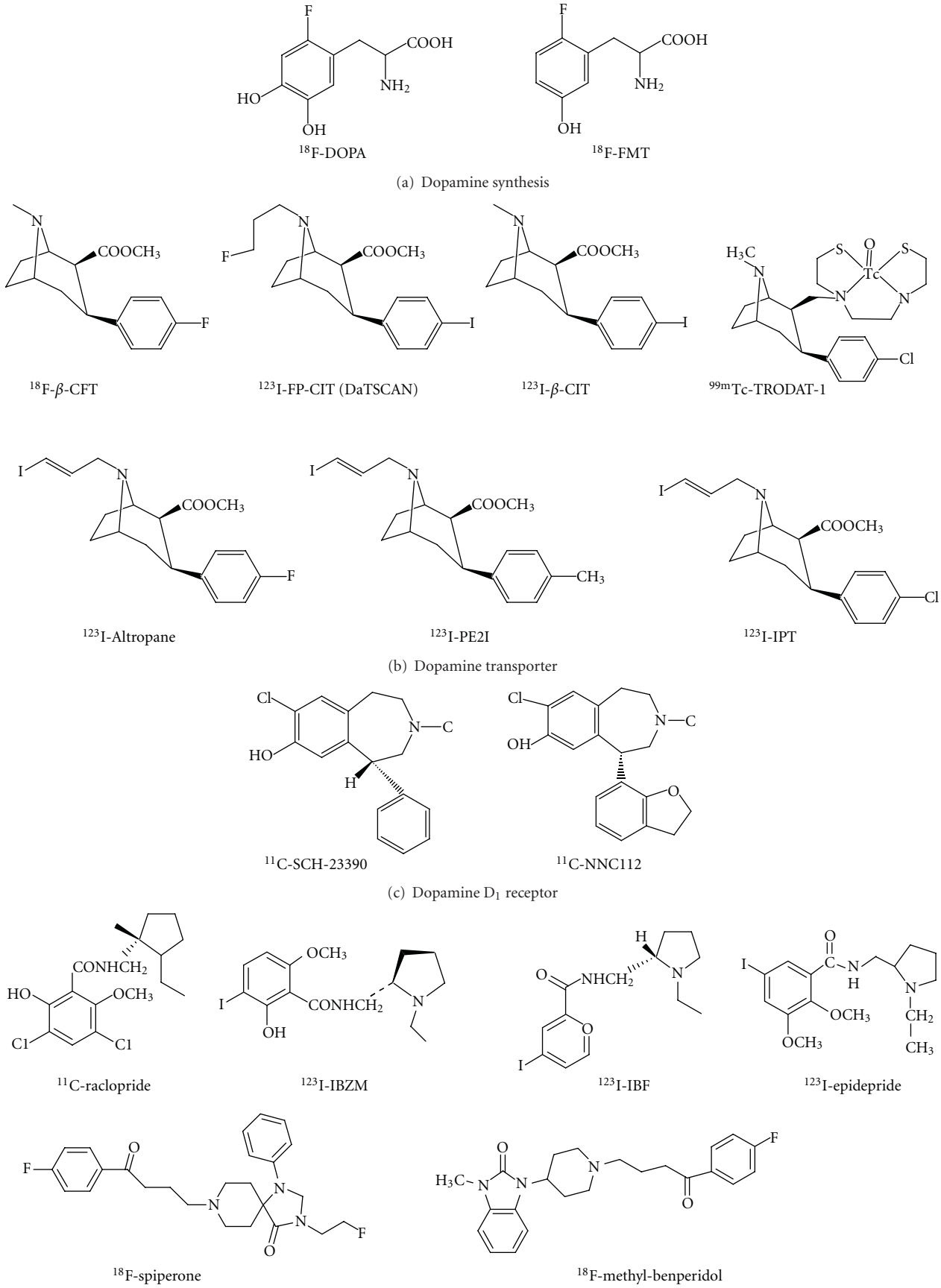

Figure 1: Continued.

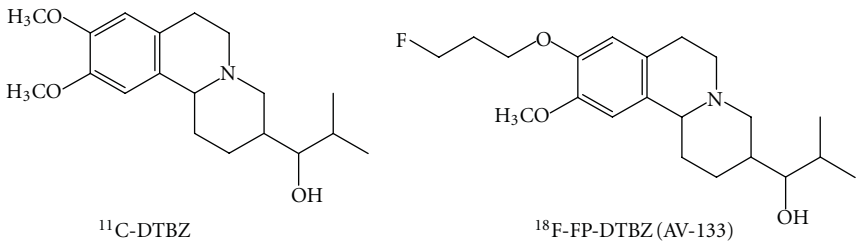

(e) Vesicular monoamine transporter type 2 (VMAT2)

Figure 1: Chemical structure of various radiotracers for the assessment of dopamine synthesis, reuptake sites, and receptors.

VMAT2 is associated with dopaminergic terminals and VAMT2 concentration linearly reflects to the concentration of dopamine in the striatum [20, 99]. The most widely used radiotracer is [^{11}C]dihydrotetrabenazine (DTBZ), which binds specifically and reversibly to VMAT2 and is amenable to quantification of striatal, diencephalic, and brain stem neurons and terminals with PET [98]. The ^{18}F-labeled VAMT2 tracer, ^{18}F-FP-DTBZ (AV-133), has been developed with the advantage of having a half-life of nearly 2 h, which allows shipment of tracers over considerable distances to PET centers without an on-site cyclotron [93, 100].

3. Parkinson's Disease and Other Movement Disorders

Parkinson's disease, the second most common neurodegenerative disorder, is characterized by severe loss of dopamine neurons, resulting in a deficiency of dopamine [101, 102]. Clinical diagnosis of Parkinson's disease relies on the presence of characteristic motor symptoms, including bradykinesia, rigidity and resting tremors, but the rate of misdiagnosis of Parkinson's disease using this method was as high as 24% according to previous studies [103–105]. Good response to dopaminergic drugs, particularly levodopa, is often used to support the clinical diagnosis of Parkinson's disease. However, some patients with pathologically confirmed Parkinson's disease have a poor response to levodopa; conversely, some patients with early multiple-system atrophy (MSA) or progressive supranuclear palsy (PSP) have beneficial responses to drug treatment [106]. Since the introduction of *in vivo* molecular imaging techniques, the diagnosis of Parkinson's disease became more reliable by assessing dopaminergic and even nondopaminergic systems [107].

Imaging of striatal denervation in Parkinson's disease was first reported with ^{18}F-DOPA PET and has been extended in imaging studies of DAT and VMAT2 [11, 13, 14, 21–23, 34, 39, 49, 94, 98, 108]. All these markers demonstrate reduced uptake in the striatum, the location of the presynaptic nigral dopamine terminal projections. More specifically, these imaging studies in Parkinson's disease patients have shown the nigral neuron loss is asymmetric, where the putamenal reductions are more profound than those in caudate [10]. Studies with ^{18}F-DOPA and DAT tracers indicated a reduction in radiotracer uptake of approximately 50–70% in the putamen in Parkinson's disease subjects [21, 34, 39, 49]. In general, all these DAT markers show similar findings in Parkinson's disease to those seen with ^{18}F-DOPA PET and are able to differentiate early Parkinson's disease from normal subjects with a sensitivity of around 90% [6, 50]. A multicenter phase III trial conducted at Institute of Nuclear Energy Research (INER) in Taiwan indicated that patients with Parkinson's disease were easily distinguished from healthy volunteers with ^{99m}Tc-TRODAT-1 SPECT, which had a sensitivity of 97.2% and a specificity of 92.6% (unpublished data).

^{18}F-DOPA PET is considered as a standard procedure for evaluating dopaminergic metabolism. However, use of ^{18}F-DOPA PET may sometimes overestimate the nigral cell reserve in Parkinson's disease, since it may show a better than actual uptake due to compensatory increased activity of dopa decarboxylase that occurs with dopamine cell terminal loss [11]. On the contrary, the striatal uptake of DAT radiotracers in early Parkinson's disease may overestimate the reduction in terminal density due to the relative downregulation of DAT in the remaining neurons as a response to nigral neuron loss, a compensatory mechanism that acts to maintain synaptic dopamine levels [23]. Additionally, DAT activity falls with age in healthy subjects, but striatal ^{18}F-DOPA uptake does not appear to be age dependent [8, 9, 22].

The signs and symptoms present in early Parkinson's disease can resemble those of many other movement disorders, particularly other forms of parkinsonism such as progressive supranuclear palsy, progressive supranuclear palsy, drug-induced Parkinsonism (DIP), vascular Parkinsonism (VP), dementia with Lewy bodies (DLB), and essential tremor (ET) [10, 40]. It is important to discriminate between idiopathic Parkinson's disease (IPD) and other neurodegenerative Parkinsonian syndromes because there are marked differences in the prognoses and therapies.

Neuroimaging studies indicate that the pattern of dopaminergic neurons loss in Parkinsonian syndromes is less region-specific than in idiopathic Parkinson's disease, the putamen and caudate are more equally effected. Moreover, left and right striatal radiotracer uptake in these disorders is also more symmetric than in idiopathic Parkinson's disease [10]. Lu et al. found DAT imaging with ^{99m}Tc-TRODAT-1 probably could provide important information to differentiate progressive supranuclear palsy from Parkinson's

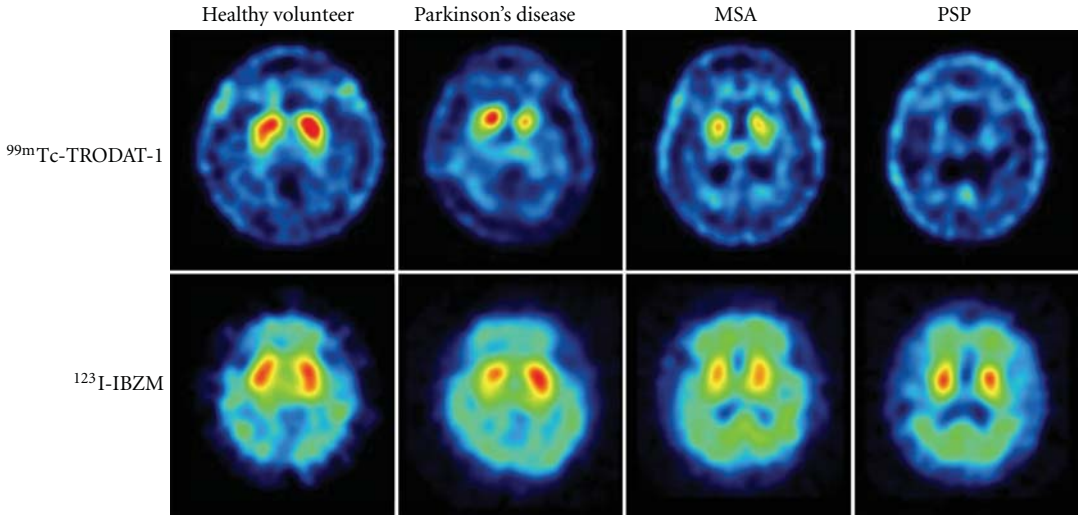

Figure 2: Dopamine transporter (DAT) imaging with ^{99m}Tc-TRODAT-1 and dopamine D_2 receptor imaging with ^{123}I-IBZM of healthy volunteer and patients with Parkinson's disease (PD), multiple-system atrophy (MSA), and progressive supranuclear palsy (PSP). The striatal DAT uptakes were significantly decreased in patients with PD, MSA, and PSP, whereas the dopamine D_2 receptor uptakes were mildly decreased in patients with PD, MSA, and PSP.

disease. The striatal binding was more symmetrically reduced in patients with progressive supranuclear palsy, in contrast to the greater asymmetric reduction in the Parkinson's disease groups [52]. Essential tremor is a condition most commonly misdiagnosed with Parkinson's disease; up to 25% of cases are initially diagnosed as having Parkinson's disease. DAT imaging using ^{123}I-β-CIT and ^{123}I-FP-CIT SPECT has been successfully proven in differentiating essential tremor from Parkinson's disease; subjects with essential tremor have normal levels of striatal uptake. Such studies have found the sensitivity and specificity for clinical diagnosis of distinguishing Parkinson's disease from essential tremor to be 95% and 93%, respectively [35, 42]. Vascular Parkinsonism is a disorder caused by cerebrovascular disease and accounts for 4.4–12% of all cases of Parkinsonism [109]. Dopaminergic imaging studies may help with the diagnosis of vascular Parkinsonism, although studies have provided conflicting results. Two studies (using ^{123}I-β-CIT or ^{99m}Tc-TRODAT-1 SPECT) found near normal DAT binding in patients with vascular Parkinsonism, differentiating them from patients with Parkinson's disease, whereas other studies have found reduced DAT binding in some patients with vascular Parkinsonism [19, 34, 53]. Dementia with Lewy bodies, characterized by severe nigrostriatal dopaminergic neuron degeneration, is the second most common form of degenerative dementia (after Alzheimer's disease, AD). Accurate diagnosis in Alzheimer's disease and dementia with Lewy bodies is particularly important in the early stage of the disease for the treatment and management of the patient. ^{18}F-DOPA, DAT, and VMAT2 markers can differentiate dementia with Lewy bodies, who display lower striatal binding in the putamen, caudate, and midbrain, from those with Alzheimer's disease, who have normal striatal binding similar to those observed in healthy controls. Mean sensitivity of ^{123}I-FP-CIT scans for a clinical diagnosis of probable dementia with Lewy bodies was 77.7%, while the mean specificity for excluding non-Lewy body dementia was 90.4%, giving overall diagnostic accuracy of 85.7% [19, 43, 44, 94]. In addition, a DAT study with ^{99m}Tc-TRODAT-1 scan in DOPA-responsive dystonia (DRD) patients, a hereditary progressive disorder with sustained response to low-dosage levodopa but entirely different prognosis from Parkinson's disease, showed significant higher DAT uptake in patients with DOPA -responsive dystonia than those in patients with young onset Parkinson disease ($P < 0.001$), suggesting a normal nigrostriatal presynaptic dopaminergic terminal in DOPA -responsive dystonia [54].

Higher diagnostic accuracy in the differential diagnosis of Parkinsonism may be achieved by combining pre- and postsynaptic quantitative information about the dopaminergic system. Previous imaging studies with the most commonly used dopamine D_2 receptor tracers, ^{11}C-raclopride and ^{123}I-IBZM, have shown that the uptake of DAT are downregulated in patients with early idiopathic Parkinson's disease, but D_2 receptors are comparable to normal subjects in medicated Parkinson's disease patients and may even be mildly increased in unmedicated patients. With the progression of Parkinson's disease, striatal D_2 receptor activity returns to normal or may fall below normal levels [98]. In contrast to Parkinson's disease, patients with atypical Parkinsonism like progressive supranuclear palsy or progressive supranuclear palsy typically show reductions in both DAT and D_2 binding [7, 40, 41]. Figure 2 illustrates the DAT scans with ^{99m}Tc-TRODAT-1 and the D_2 receptor scans with ^{123}I-IBZM of healthy volunteer and patients with Parkinson's disease, multiple system atrophy, and progressive supranuclear palsy. However, the small differences in D_2 binding failed to discriminate between idiopathic Parkinson's disease, nonidiopathic Parkinson's disease, and healthy control groups, according to a report of

a multicenter phase III trial conducted by INER (unpublished data). Nevertheless, the dopamine D_2 receptor imaging is successfully demonstrated in differentiation of the subtypes of progressive supranuclear palsy: Richardson's syndrome (RS) and progressive supranuclear palsy-parkinsonism (PSP-P). Assessment of pre- and postsynaptic dopaminergic activities in Richardson's syndrome, PSP-P, or idiopathic Parkinson's disease with ^{99m}Tc-TRODAT-1 and ^{123}I-IBZM images showed that the activities of D_2 receptor were reduced in Richardson's syndrome but not in PSP-P ($P < 0.01$), which was consistent with the clinical manifestation of PSP-P group with better prognosis and levodopa responsiveness than that of RS patients [55].

Imaging the distribution and density of single molecules in the living brain will give us straightforward information of the genetic linkages among different aspects of Parkinsonism. Genetic studies have identified at least 9 genes with mutation that cause 10% to 15% of Parkinson's disease cases [103]. *SNCA*, *Parkin*, *PINK1*, *DJ-1*, *LRRK2,* and *ATP13A2* have been identified to be the causative genes for familial and early onset Parkinson's disease (EOPD) [51]. A ^{99m}Tc-TRODAT-1 scan revealed that patients with the *PINK1* mutation displayed a rather even, symmetrical reduction of dopamine uptake, whereas patients with late-onset Parkinson's disease (LOPD) displayed a dominant decline in dopamine uptake in the putamen [56]. The contribution of genetic variants in *ATP13A2* to Parkinson's disease of Taiwanese patients was investigated with ^{99m}Tc-TRODAT-1 SPECT, showing that the striatal uptake of patients carrying the variants of G1014S and A746T were similar to that of idiopathic Parkinson's disease [51]. In addition, ^{99m}Tc-TRODAT-1 SPECT was exploited to examine the DAT activity in Machado-Joseph disease (MJD) patients and gene carriers, showing that the DAT concentration was significantly reduced in patients with Machado-Joseph disease and in asymptomatic gene carriers compared to those of healthy volunteers ($P < 0.001$) [57].

Molecular imaging is also a major tool for the evaluation of new experimental therapeutic strategies in Parkinson's disease. Cell transplantation to replace lost neurons is a recent approach to the treatment of progressive neurodegenerative diseases. Transplantation of human embryonic dopamine neurons into the brains of patients with Parkinson's disease has proved beneficial in open clinical trials [7, 24]. Several teams of investigators have reported the results from double-blind placebo-controlled trials of human embryonic dopaminergic tissue transplantation for the treatment of Parkinson's disease. Evaluations with ^{18}F-DOPA scans have shown that significant declines in the motor scores over time after transplantation ($P < 0.001$), based on the Unified Parkinson Disease Rating Scale (UPDRS), were associated with increases in putamen ^{18}F-DOPA uptake at 4 years posttransplantation followups ($P < 0.001$). Furthermore, posttransplantation changes in putamen PET signals and clinical outcomes were significantly intercorrelated ($P < 0.02$) [24, 25]. Gene therapy may be potentially useful for ameliorating the motor symptoms of Parkinson's disease. Several gene therapy studies in humans investigated transductions (with various viral vectors) of glial-derived neurotrophic factor (GDNF), neurturin (NTN), AADC, or glutamic acid decarboxylase (GAD). Brain imaging with ^{18}F-DODA or ^{18}F-FMT PET has been exploited to evaluate clinical outcomes adjunct to the UPDRS scores [26, 30, 31, 110–112].

4. Drug Abuse and Addicted Brain

Dopamine is the neurotransmitter that has been classically associated with the reinforcing effects of drug abuse. This notion reflects the fact that most of the drugs of abuse increase extracellular dopamine concentration in limbic regions including nucleus accumbens (NAc). The involvement of dopamine in drug reinforcement is well recognized but its role in drug addiction is much less clear. Imaging studies have provided evidences of how the human brain changes as an individual becomes addicted [74–77].

Cocaine is considered one of the most reinforcing drug of abuse; therefore, this drug has been extensively investigated the associated reinforcing effects in humans. Cocaine is believed to work by blocking the DAT and thereby increasing the availability of free dopamine within the brain. The relationship between DAT blockage and the reinforcement effects of cocaine abuser has been assessed with ^{11}C-cocaine PET, showing that intravenous cocaine at doses commonly abused by human (0.3–0.6 mg/kg) blocked between 60 to 77% of DAT sites in these subjects. Moreover, the magnitude of the self-reported "high" was positively correlated with the degree of DAT occupancy, and at least 47% of the transporters had to be blocked for subjects to perceive cocaine's effects [80]. When compared to normal controls, cocaine abusers showed significant decreases in dopamine D_2 receptor availability that persisted 3-4 months after detoxification. Decreases in dopamine D_2 receptor availability were associated with decreased metabolism in several regions of the frontal lobes, most markedly in orbitofrontal cortex and cingulate gyri [81]. PET studies with ^{11}C-raclopride have consistently shown that subjects with a wide variety of drug addictions (cocaine, heroin, alcohol, and methamphetamine) have significant reductions in dopamine D_2 receptor availability in the striatum that persist months after protracted detoxification [76, 78, 82–84, 113].

Since dopamine D_2 receptors are involved in the response to reinforcing properties of natural as well as drug stimuli, it has been postulated that reduced D_2 receptor levels in drug-addicted subjects would make them less sensitive to natural reinforcers. Volkow et al. compared the function of the dopamine system of 20 cocaine-dependent subjects with 23 controls using ^{11}C-raclopride PET by measuring the relative changes in extracellular dopamine induced by intravenous methylphenidate. Cocaine-dependent subjects showed reduced dopamine release in the striatum and also had a reduced "high" relative to controls, indicating that methylphenidate-induced striatal dopamine increased in cocaine abusers were significantly blunted when compared with those of controls [74, 113].

Despite the similarities between cocaine and methylphenidate in their affinity to the DAT, cocaine is much more abused than methylphenidate. Using ^{11}C labeled cocaine and methylphenidate for PET imaging, it has

been demonstrated that the regional distribution of ^{11}C-methylphenidate was identical to that of ^{11}C-cocaine and they competed with each other for the same binding site. However, these two drugs differed markedly in their pharmacokinetics. Both drugs entered the brain rapidly after intravenous administration (in less than 10 min) while the rate of clearance of ^{11}C-methylphenidate from striatum (90 min) was significantly slower than that of ^{11}C-cocaine (20 min). Therefore, it is postulated that the initial uptake of these stimulant drugs into the brain, not their steady-state presence, is necessary for drug-induced reinforcement [76, 114].

In addition to differences in bioavailability, the route of administration significantly affects the effects of stimulant drugs presumably via its effects on pharmacokinetics. This is particularly relevant to methylphenidate because it is abused when taken intravenously but rarely so when taken orally. Volkow et al. measured the dopamine changes induced by oral and intravenous administration of methylphenidate that produce equivalent DAT occupancy (about 70%). Even though the dopamine increases were comparable for oral and intravenous (approximately 20% changes in specific binding of ^{11}C-raclopride in striatum), oral methylphenidate did not induce significant increases in self-reports of "high." Intravenous administration of methylphenidate leads to fast dopamine changes, whereas oral administration increases dopamine slowly. The failure to observe the "high" with oral methylphenidate is likely to reflect the slower pharmacokinetics [76, 77, 85].

A view of DAT regulation in cocaine addicts may improve our understanding of clinical aspects of cocaine dependence, including drug-induced carving, dysphoria, and relapse. The DAT levels in the brain of cocaine-dependence were measured by ^{99m}Tc-TRODAT-1 SPECT. It has shown that there were significantly higher DAT levels in cocaine-dependent subjects compared to controls for the anterior putamen, posterior putamen, and caudate. DAT levels in these regions were 10%, 17%, and 8% higher in the cocaine dependent subjects compared to controls. This study also showed that ^{99m}Tc-TRODAT-1 uptake was negatively correlated with the duration of time since last use of cocaine [58]. Malison et al. examined the striatal DAT levels in 28 cocaine-abusing subjects with ^{123}I-β-CIT SPECT and found that striatal DAT levels were significantly increased (approximately 20%) in acutely abstinent cocaine-abusing subjects (96 h or less) [36]. Another study using ^{123}I-β-CIT SPECT also showed approximately a 14% increase in DAT availability in acutely abstinent (3.7 days on average) cocaine subjects compared to controls [37].

Human imaging studies suggest that preexisting differences in dopamine circuits may be one mechanism underlying the variability in responsiveness to drug abuse. In particular, baseline measures of striatal dopamine D_2 receptors in nonaddicted subjects have been shown to predict subjective responses to the reinforcing effects of intravenous methylphenidate treatment. Individuals describing the experience as pleasant had substantially lower levels of dopamine D_2 receptors compared with those describing methylphenidate as unpleasant [74, 79].

Methadone maintenance treatment has been demonstrated to be effective in reducing or eliminating opioid drug use. Despite its therapeutic effectiveness, relatively little is known about neuronal adaptations in the brains of methadone users. A PET study with ^{11}C-CFT has documented reduced DAT availability in patients with prolonged abstinence and with methadone maintenance treatment. Furthermore, the subjects with methadone maintenance treatment showed significant decreases of DAT uptake function in the bilateral putamen in comparison to the prolonged abstinence subjects [32]. Another study examined the differences between opioid-dependent users treated with a very low dose of methadone or undergoing methadone-free abstinence. The striatal DAT availability was significantly reduced in low-dose methadone users (0.78 ± 0.27) and methadone-free abstinence (0.94 ± 0.28) compared to controls (1.16 ± 0.26), which has demonstrated that methadone treatment or abstinence can benefit the recovery of impaired dopamine neurons. Moreover, lower midbrain SERT availability also was noted in methadone maintenance treatment and methadone-free abstinence groups, which implicated deregulation of serotoninergic neurons in opioid abuse [59].

The behavioral and neurobiological effects of tobacco smoking, in which nicotine may play an import role, are similar to those of addictive drugs. The pre- and postsynaptic activity of dopamine neuron was examined in male smokers with ^{99m}Tc-TRODAT-1/^{123}I-IBZM SPECT. A decrease in DAT availability was found in the striatum of male smokers ($P < 0.05$), suggesting cigarette smoking may alter central dopamine functions, particularly at the presynaptic sites. Moreover, the total FTND (Fagerström Test for Nicotine Dependence) scores correlated negatively with striatal DAT availability in male smokers, but not with striatal D_2 bindings [60].

5. Attention Deficit Hyperactivity Disorder

Attention deficit hyperactivity disorder (ADHD) is a common disorder of childhood characterized by inattention, excessive motor activity, impulsiveness, and distractibility. It is associated with serious disability in children, adolescents and adults. There is converging evidence that abnormalities within the dopamine system in the brain play a major role in the pathophysiology of ADHD [33, 62, 63]. Despite extensive investigation of the neuropathophysiology of ADHD by a wide array of methodologies, the mechanism underlying this disorder is still unknown.

Neuroimaging holds promise for unveiling the neurobiological causes of ADHD and provides invaluable information for management of the disease. Ernst et al. investigated the integrity of presynaptic dopaminergic function in children with ADHD through the use of ^{18}F-DOPA PET and found a 48% increase in DOPA decarboxylase activation in the right midbrain in ADHD children compared with normal controls [27].

Methylphenidate is considered as a first-line medication for ADHD in children and adults [86, 115]. This medicine

is very effective for the treatment of ADHD; it is estimated that 60–70% of ADHD subjects have favorable responses. Volkow et al. utilized ^{11}C-cocaine and ^{11}C-raclopride PET to assess the DAT and dopamine D_2 receptor occupancy for a given dose of methylphenidate. It has been proven that this drug significantly blocked DAT (60 ± 11%) and increased synaptic dopamine levels (16 ± 8%) reduction in ^{11}C-raclopride binding in the striatum [86].

It is widely accepted that the therapeutic effects of methylphenidate are through the blocking of DAT; therefore, it seems appropriate to investigate the DAT availability in patients with ADHD. The first DAT imaging study was conducted in 6 adults with ADHD by using ^{123}I-altropane SPECT, showing that the DAT levels in unmedicated patients were approximately 70% higher than those in controls [69]. However, following studies with a variety of DAT markers have shown a much smaller increase even not reaching statistical significance than that found in the first study with ^{123}I-altropane [38, 45, 64, 65, 70]. Dresel et al. investigated DAT binding in 17 treatment naïve adults with ADHD compared with 10 age- and gender-matched control subjects by using ^{99m}Tc-TRODAT-1 SPECT. Patients with ADHD exhibited a significantly increased specific DAT binding in the striatum (average 17%) compared with normal subjects ($P < 0.01$) [64]. Furthermore, Krause et al. examined DAT binding in an expanded sample of 31 adults with ADHD and 15 control subjects; the earlier findings of greater DAT binding in adults with ADHD was replicated [62]. DAT density has been compared in 9 treatment naïve children with ADHD and 6 normal children using ^{123}I-IPT SPECT, showing that mean DAT binding in the basal ganglia was significantly increased with 40% on the left and 51% on the right side compared with the controls [70]. By using ^{11}C-altropane PET, a highly selective radiotracer and technically superior imaging modality, Spencer et al. found that the overall DAT binding was increased 28% in adults with ADHD compared with controls [33]. However, the ^{123}I-β-CIT SPECT study showed no significant difference in striatal density between adult patients with ADHD and normal controls [38]. Furthermore, Hesse et al. found the striatal DAT binding ratio (specific to nondisplaceable binding) was significantly reduced in treatment naïve adults with ADHD by using ^{123}I-FP-CIT SPECT (ADHD: 5.18 ± 0.98; control: 6.36 ± 1.34) [46]. The cause of divergent findings might be the clinical heterogeneity of the ADHD phenotype rather than differences in imaging technology, applied tracer type, or outcome measurement method.

It has been shown that methylphenidate lowers DAT availability very effectively in normal subjects and in patients with ADHD. After treatment with methylphenidate (5 mg t.i.d), the specific DAT binding decreased (average 29%) significantly in all patients ($P < 0.01$), investigated by ^{99m}Tc-TRODAT-1 SPECT [64]. Vles et al. examined DAT binding in 6 treatment naïve boys with ADHD (aged 6–10 years), using ^{123}I-FP-CIT SPECT. Three months after treatment with methylphenidate, a 28–75% decrease of DAT binding in the striatum was found [47]. Generally nonresponse to methylphenidate is known to occur in approximately 30% of patients with ADHD, which may be caused by lower baseline DAT availability in these patients. Krause et al. assessed the relationship between DAT availability and treatment outcome using ^{99m}Tc-TRODAT-1 SPECT. It has shown that ADHD patients with poor response to methylphenidate had a low primary DAT availability, whereas most of patients with high DAT availability exhibited good clinical response to methylphenidate [66, 67].

Previous studies have confirmed the reduction of DAT availability by nicotine [60, 61]. Patients with ADHD and with a history of nicotine abuse displayed lower DAT availability than nonsmokers with ADHD. DAT seems to be elevated in nonsmoking ADHD patients suffering from the purely inattentive subtype of ADHD as well as in those with the combined or purely hyperactive/impulsive subtype [63, 68].

6. Schizophrenia and the Effects of Antipsychotics

Schizophrenia is a chronic mental illness characterized by disturbances of thoughts, perceptions, volition, and cognition. Manifestations of the illness are commonly divided into positive (delusions, hallucinations, thought disorganization, paranoia), negative (lack of drive and motivation, alogia, social withdrawal), and cognitive symptoms (poor performance on cognitive tasks involving attention and working memory). Positive symptoms are considered to be a result of the increased subcortical release of dopamine causing greater stimulation of D_2 receptors. The negative and cognitive symptoms are thought to arise from reduced D_1 receptor stimulation [28, 90, 116].

With the advance of brain imaging techniques, direct evidence suggestive of dysregulation of dopaminergic transmission in schizophrenia has emerged. Several lines of study have documented an increase in the striatal accumulation of ^{18}F-DOPA or ^{11}C-DOPA in patients with schizophrenia, which is consistent with increased activity of DOPA decarboxylase, an enzyme involved in dopamine synthesis [28, 90]. More recently, Howes et al. assessed striatal dopaminergic function in patients with prodromal schizophrenia using ^{18}F-DOPA PET and found elevated striatal ^{18}F-DOPA uptake, which gradually reached the level in those with schizophrenia. In addition, increased striatal ^{18}F-DOPA uptake was correlated with the severity of prodromal psychopathologic and neuropsychological impairment [29].

Since the primary target of many antipsychotic drugs is antagonism at striatal D_2 receptors, Abi-Dargham et al. compared striatal D_2 receptor availability before and during pharmacologically induced acute dopamine depletion with ^{123}I-IBZM SPECT in 18 untreated patients and 18 controls. At baselines, no difference has been found between these 2 groups. However, after depletion of endogenous dopamine, D_2 receptor availability was significantly higher in patients with schizophrenia compared with controls ($P < 0.01$). In addition, the study suggests elevated synaptic dopamine is predictive of good treatment response of positive symptoms to antipsychotic drugs [90].

PET studies with ^{11}C-SCH2390 or ^{11}C-NNC112 in drug naïve schizophrenia patients have reported divergent

findings in D_1 receptor binding and cognitive functioning. Some studies have shown a decrease in prefrontal D_1 receptor binding [72], whereas others have shown an increase in D_1 receptor binding [71] or reported no differences between patients and controls [73]. A few have shown a relationship between D_1 dysfunction and working memory performance in treatment naïve patients. The variability in the results was possibly influenced by parameters of the particular patient populations including duration of illness, symptoms and medications.

Nuclear medicine imaging technique has been widely used for the drug development in recent years. There are several approaches such as microdosing, measurement of *in vivo* receptor occupancy, and biomarkers [117]. Most imaging studies in the past have concentrated on antipsychotics. Several lines of research indicate the efficacy of antipsychotics to be related to their capacity to antagonize dopamine. Brain Imaging with PET or SPECT allows determination of dopamine D_2 receptor occupancy rate in the human brain during treatment with antipsychotics, which are associated with extrapyramidal symptoms (EPS) of antipsychotic drugs [118]. Farde et al. found that the classical antipsychotics occupied 60–85% of striatal dopamine D_2 receptor was necessary for treating positive symptoms of schizophrenia, as measured by ^{11}C-raclopride PET imaging. However, D_2 receptor occupancies above 80% were associated with a significantly higher risk of extrapyramidal symptoms [87, 118, 119].

Several new antipsychotics have been introduced to market with lower affinity for dopamine D_2 receptors, for which the term "atypical antipsychotics" had been coined. Atypical antipsychotics display with a low or nonexistent propensity of extrapyramidal symptoms as compared to classical neuroleptics [88].

Therapeutic concentrations reported from clinical studies have been confirmed by D_2 receptor imaging for classical antipsychotics and a number of atypical antipsychotics (i.e., amisulpride, clozapine, olanzapine, quetiapine, risperidone, sertindole, and zotepine). From available studies, the atypical antipsychotics clozapine and quetiapine appear to have the lowest striatal D_2 receptor occupancy rates and the typical antipsychotic haloperidol has the highest. Risperidone, sertindole, and zotepine hold an intermediate position. The incidence of EPS ranged from none with clozapine, olanzapine, quetiapine, to 80% of patients treated with haloperidol [89, 91, 92, 120]. The effect of DAT on a neuroleptic was examined by ^{123}I-FP-CIT SPECT. Mateos and coworkers found in schizophrenic patients 4 weeks of treatment with risperidone did not influence striatal DAT binding ratios significantly [48].

7. Conclusions

With the appropriate radiotracers, neuroimaging enables the visualization of the presynaptic and postsynaptic sites in the dopaminergic system. Imaging these markers provides key insights into the pathophysiology of Parkinson's disease and related neurodegenerative diseases and it becomes an important endpoint in clinical trials of potential disease-modifying therapy for Parkinson's disease such as gene therapy or cell replacement therapy. The availability of easy-to-apply diagnostic procedures such as metabolic and DAT imaging is encouraging. Nonetheless, it should also be emphasized that these results are no replacement for thorough clinical investigation. Future studies are needed in the development of new radiotracers to target nondopaminergic brain pathways and the glial reaction to disease.

Neuroimaging studies have provided evidences of how the human brain changes as an individual becomes addicted. Although available studies have mostly focused on dopamine, the interaction of dopamine with other neurotransmitters such as GABA, glutamate, and serotonin plays an important role in modulating the magnitude of the dopamine responses to drugs.

At this time, knowledge from DAT imaging studies in patients with ADHD is limited by the use of various radiotracers and small sample size. In the future, measurements of DAT with PET or SPECT should be performed in greater collectives, allowing the assignment to different subtypes of ADHD. Of further interest will be whether the DAT availability has a prognostic value for the treatment response of methylphenidate. Furthermore, since methylphenidate exerts its therapeutic efficacy is through blocking DAT and NET, the role of norepinephrinergic system in the pathophysiology of ADHD will become increasing important as the recently available of NET radiotracers.

The clinically most important contribution from neuroimaging on D_2 receptor occupancy in patients with schizophrenia is probably the identification of the optimal therapeutic window for antipsychotic drugs. Based on this concept, the striatal D_2 receptors binding profiles of typical and atypical antipsychotic agents has been determined.

In the future, the role of neuroimaging may become more significant in guiding therapy. Enhancements in image resolution and specific molecular tags will permit accurate diagnoses of a wide range of diseases, based on both structural and molecular changes in the brain. For widespread application, advances in molecular imaging should include the characterization of new radiotracers, application of modeling techniques, standardization and automation of image-processing techniques, and appropriate clinical settings in large multicenter trials. The growing field of neuroimaging is helping nuclear medicine physicians identify pathways into personalized patient care.

Acknowledgments

The authors are indebted to the research teams of Chang Gung Memorial Hospital, Tri-Service General Hospital, National Cheng Kung University Hospital, and Taipei Veterans General Hospital for carrying out the clinical studies for the neuroimaging agents developed at Institute of Nuclear Energy Research. The development of neuroimaging agents was partially supported by the Grant from National Science Council (NSC99-3111-Y-042A-013).

References

[1] D. F. Wong, G. Gründer, and J. R. Brasic, "Brain imaging research: does the science serve clinical practice?" *International Review of Psychiatry*, vol. 19, no. 5, pp. 541–558, 2007.

[2] F. A. Metter and M. J. Guiberteau, "Radioactivity, radionuclides, and radiopharmaceuticals," in *Essentials of Nuclear Medicine Imaging*, chapter 1, pp. 1–13, Saunders, Elsevier, 5th edition, 2006.

[3] F. A. Metter and M. J. Guiberteau, "Positron emission tomography (PET) imaging," in *Essentials of Nuclear Medicine Imaging*, chapter 13, pp. 359–423, Saunders, Elsevier, 5th edition, 2006.

[4] R. Weissleder and U. Mahmood, "Molecular imaging," *Radiology*, vol. 219, no. 2, pp. 316–333, 2001.

[5] M. Fumita and R. B. Innis, *Neuropsychopharmacology: The Fifth Generation of Progress*, Lippincott Williams & Wilkins, Philadelphia, Pa, USA, 1st edition, 2002.

[6] W. D. Heiss and K. Herholz, "Brain receptor imaging," *Journal of Nuclear Medicine*, vol. 47, no. 2, pp. 302–312, 2006.

[7] C. Sioka, A. Fotopoulos, and A. P. Kyritsis, "Recent advances in PET imaging for evaluation of Parkinson's disease," *European Journal of Nuclear Medicine and Molecular Imaging*, vol. 37, no. 8, pp. 1594–1603, 2010.

[8] N. Pavese and D. J. Brooks, "Imaging neurodegeneration in Parkinson's disease," *Biochimica et Biophysica Acta*, vol. 1792, no. 7, pp. 722–729, 2009.

[9] N. Pavese, L. Kiferle, and P. Piccini, "Neuroprotection and imaging studies in Parkinson's disease," *Parkinsonism and Related Disorders*, vol. 15, supplement 4, pp. S33–S37, 2010.

[10] J. P. Seibyl, "Imaging studies in movement disorders," *Seminars in Nuclear Medicine*, vol. 33, no. 2, pp. 105–113, 2003.

[11] D. J. Brooks, K. A. Frey, K. L. Marek et al., "Assessment of neuroimaging techniques as biomarkers of the progression of Parkinson's disease," *Experimental Neurology*, vol. 184, supplement 1, pp. S68–S79, 2003.

[12] J. O. Rinne, A. Laihinen, K. Någren, H. Ruottinen, U. Ruotsalainen, and U. K. Rinne, "PET examination of the monoamine transporter with [^{11}C]β-CIT and [^{11}C]β-CFT in early Parkinson's disease," *Synapse*, vol. 21, no. 2, pp. 97–103, 1995.

[13] J. O. Rinne, H. Ruottinen, J. Bergman, M. Haaparanta, P. Sonninen, and O. Solin, "Usefulness of a dopamine transporter PET ligand [^{18}F]β-CFT in assessing disability in Parkinson's disease," *Journal of Neurology Neurosurgery and Psychiatry*, vol. 67, no. 6, pp. 737–741, 1999.

[14] J. O. Rinne, E. Nurmi, H. M. Ruottinen, J. Bergman, O. Eskola, and O. Solin, "[^{18}F]FDOPA and [^{18}F]CFT are both sensitive PET markers to detect presynaptic dopaminergic hypofunction in early Parkinson's disease," *Synapse*, vol. 40, no. 3, pp. 193–200, 2001.

[15] S. K. Meegalla, K. Plössl, M. P. Kung et al., "Synthesis and characterization of technetium-99m-labeled tropanes as dopamine transporter-imaging agents," *Journal of Medicinal Chemistry*, vol. 40, no. 1, pp. 9–17, 1997.

[16] M. P. Kung, D. A. Stevenson, K. Plössl et al., "[^{99m}Tc]TRODAT-1: a novel technetium-99m complex as a dopamine transporter imaging agent," *European Journal of Nuclear Medicine*, vol. 24, no. 4, pp. 372–380, 1997.

[17] M. J. Ribeiro, M. Vidailhet, C. Loc'h et al., "Dopaminergic function and dopamine transporter binding assessed with positron emission tomography in Parkinson disease," *Archives of Neurology*, vol. 59, no. 4, pp. 580–586, 2002.

[18] J. Booij, G. Tissingh, A. Winogrodzka et al., "Practical benefit of [^{123}I]FP-CIT SPET in the demonstration of the dopaminergic deficit in Parkinson's disease," *European Journal of Nuclear Medicine*, vol. 24, no. 1, pp. 68–71, 1997.

[19] J. L. Cummings, C. Henchcliffe, S. Schaier, T. Simuni, A. Waxman, and P. Kemp, "The role of dopaminergic imaging in patients with symptoms of dopaminergic system neurodegeneration," *Brain*, vol. 134, no. 11, pp. 3146–3166, 2011.

[20] B. Ravina, D. Eidelberg, J. E. Ahlskog et al., "The role of radiotracer imaging in Parkinson disease," *Neurology*, vol. 64, no. 2, pp. 208–215, 2005.

[21] H. H. Fernandez, J. H. Friedman, A. J. Fischman, R. B. Noto, and M. C. Lannon, "Is altropane SPECT more sensitive to fluoroDOPA PET for detecting early Parkinson's disease?" *Medical Science Monitor*, vol. 7, no. 6, pp. 1339–1343, 2001.

[22] E. Nurmi, H. M. Ruottinen, J. Bergman et al., "Rate of progression in Parkinson's disease: a 6-[^{18}F]fluoro-L-dopa PET study," *Movement Disorders*, vol. 16, no. 4, pp. 608–615, 2001.

[23] W. S. Huang, Y. H. Chiang, J. C. Lin, Y. H. Chou, C. Y. Cheng, and R. S. Liu, "Crossover study of ^{99m}Tc-TRODAT-1 SPECT and ^{18}F-FDOPA PET in Parkinson's disease patients," *Journal of Nuclear Medicine*, vol. 44, no. 7, pp. 999–1005, 2003.

[24] C. R. Freed, P. E. Greene, R. E. Breeze et al., "Transplantation of embryonic dopamine neurons for severe Parkinson's disease," *New England Journal of Medicine*, vol. 344, no. 10, pp. 710–719, 2001.

[25] Y. Ma, C. Tang, T. Chaly et al., "Dopamine cell implantation in Parkinson's disease: long-term clinical and ^{18}F-FDOPA PET outcomes," *Journal of Nuclear Medicine*, vol. 51, no. 1, pp. 7–15, 2010.

[26] W. J. Marks Jr., J. L. Ostrem, L. Verhagen et al., "Safety and tolerability of intraputaminal delivery of CERE-120 (adeno-associated virus serotype 2-neurturin) to patients with idiopathic Parkinson's disease: an open-label, phase I trial," *The Lancet Neurology*, vol. 7, no. 5, pp. 400–408, 2008.

[27] M. Ernst, A. J. Zametkin, J. A. Matochik, D. Pascualvaca, P. H. Jons, and R. M. Cohen, "High midbrain [^{18}F]DOPA accumulation in children with attention deficit hyperactivity disorder," *American Journal of Psychiatry*, vol. 156, no. 8, pp. 1209–1215, 1999.

[28] N. H. Patel, N. S. Vyas, B. K. Puri, K. S. Nijran, and A. Al-Nahhas, "Positron emission tomography in schizophrenia: a new perspective," *Journal of Nuclear Medicine*, vol. 51, no. 4, pp. 511–520, 2010.

[29] O. D. Howes, A. J. Montgomery, M. C. Asselin et al., "Elevated striatal dopamine function linked to prodromal signs of schizophenia," *Archives of General Psychiatry*, vol. 66, no. 1, pp. 13–20, 2009.

[30] J. L. Eberling, W. J. Jagust, C. W. Christine et al., "Results from a phase I safety trial of *hAADC* gene therapy for Parkinson disease," *Neurology*, vol. 70, no. 21, pp. 1980–1983, 2008.

[31] S. I. Muramatsu, K. I. Fujimoto, S. Kato et al., "A phase I study of aromatic l-amino acid decarboxylase gene therapy for Parkinson's disease," *Molecular Therapy*, vol. 18, no. 9, pp. 1731–1735, 2010.

[32] J. Shi, L. Y. Zhao, M. L. Copersino et al., "PET imaging of dopamine transporter and drug craving during methadone maintenance treatment and after prolonged abstinence in heroin users," *European Journal of Pharmacology*, vol. 579, no. 1–3, pp. 160–166, 2008.

[33] T. J. Spencer, J. Biederman, B. K. Madras et al., "*In vivo* neuroreceptor imaging in attention-deficit/hyperactivity

disorder: a focus on the dopamine transporter," *Biological Psychiatry*, vol. 57, no. 11, pp. 1293–1300, 2005.

[34] N. Quinn, "A multicenter assessment of dopamine transporter imaging with DOPASCAN/SPECT in parkinsonism," *Neurology*, vol. 57, no. 4, pp. 746–747, 2001.

[35] S. Asenbaum, W. Pirker, P. Angelberger, G. Bencsits, M. Pruckmayer, and T. Brucke, "[^{123}I] β-CIT and SPECT in essential tremor and Parkinson's disease," *Journal of Neural Transmission*, vol. 105, no. 10–12, pp. 1213–1228, 1998.

[36] R. T. Malison, S. E. Best, C. H. van Dyck et al., "Elevated striatal dopamine transporters during acute cocaine abstinence as measured by [^{123}I]β-CIT SPECT," *American Journal of Psychiatry*, vol. 155, no. 6, pp. 832–834, 1998.

[37] L. K. Jacobsen, J. K. Staley, R. T. Malison et al., "Elevated central serotonin transporter binding availability in acutely abstinent cocaine-dependent patients," *American Journal of Psychiatry*, vol. 157, no. 7, pp. 1134–1140, 2000.

[38] C. H. van Dyck, D. M. Quinlan, L. M. Cretella et al., "Unaltered dopamine transporter availability in adult attention deficit hyperactivity disorder," *American Journal of Psychiatry*, vol. 159, no. 2, pp. 309–312, 2002.

[39] J. Booij, J. D. Speelman, M. W. I. M. Horstink, and E. C. Wolters, "The clinical benefit of imaging striatal dopamine transporters with [^{123}I]FP-CIT SPET in differentiating patients with presynaptic parkinsonism from those with other forms of parkinsonism," *European Journal of Nuclear Medicine*, vol. 28, no. 3, pp. 266–272, 2001.

[40] W. Koch, C. Hamann, P. E. Radau, and K. Tatsch, "Does combined imaging of the pre- and postsynaptic dopaminergic system increase the diagnostic accuracy in the differential diagnosis of parkinsonism?" *European Journal of Nuclear Medicine and Molecular Imaging*, vol. 34, no. 8, pp. 1265–1273, 2007.

[41] M. Plotkin, H. Amthauer, S. Klaffke et al., "Combined ^{123}I-FP-CIT and ^{123}I-IBZM SPECT for the diagnosis of parkinsonian syndromes: study on 72 patients," *Journal of Neural Transmission*, vol. 112, no. 5, pp. 677–692, 2005.

[42] T. S. Benamer, J. Patterson, D. G. Grosset et al., "Accurate differentiation of parkinsonism and essential tremor using visual assessment of [^{123}I]-FP-CIT SPECT imaging: the [^{123}I]-FP-CIT study group," *Movement Disorders*, vol. 15, no. 3, pp. 503–510, 2000.

[43] S. Colloby and J. O'Brien, "Functional imaging in Parkinson's disease and dementia with Lewy bodies," *Journal of Geriatric Psychiatry and Neurology*, vol. 17, no. 3, pp. 158–163, 2004.

[44] J. T. O'Brien, S. Colloby, J. Fenwick et al., "Dopamine transporter loss visualized with FP-CIT SPECT in the differential diagnosis of dementia with lewy bodies," *Archives of Neurology*, vol. 61, no. 6, pp. 919–925, 2004.

[45] R. Larisch, W. Sitte, C. Antke et al., "Striatal dopamine transporter density in drug naive patients with attention-deficit/hyperactivity disorder," *Nuclear Medicine Communications*, vol. 27, no. 3, pp. 267–270, 2006.

[46] S. Hesse, O. Ballaschke, H. Barthel, and O. Sabri, "Dopamine transporter imaging in adult patients with attention-deficit/hyperactivity disorder," *Psychiatry Research*, vol. 171, no. 2, pp. 120–128, 2009.

[47] J. S. H. Vles, F. J. M. Feron, J. G. M. Hendriksen, J. Jolles, M. J. P. G. van Kroonenburgh, and W. E. J. Weber, "Methylphenidate down-regulates the dopamine receptor and transporter system in children with Attention Deficit Hyperkinetic Disorder (ADHD)," *Neuropediatrics*, vol. 34, no. 2, pp. 77–80, 2003.

[48] J. J. Mateos, F. Lomeña, E. Parellada et al., "Lower striatal dopamine transporter binding in neuroleptic-naive schizophrenic patients is not related to antipsychotic treatment but it suggests an illness trait," *Psychopharmacology*, vol. 191, no. 3, pp. 805–811, 2007.

[49] W. S. Huang, S. Z. Lin, J. C. Lin, S. P. Wey, G. Ting, and R. S. Liu, "Evaluation of early-stage Parkinson's disease with ^{99m}Tc-TRODAT-1 imaging," *Journal of Nuclear Medicine*, vol. 42, no. 9, pp. 1303–1308, 2001.

[50] Y. H. Weng, T. C. Yen, M. C. Chen et al., "Sensitivity and specificity of ^{99m}Tc-TRODAT-1 SPECT imaging in differentiating patients with idiopathic Parkinson's disease from healthy subjects," *Journal of Nuclear Medicine*, vol. 45, no. 3, pp. 393–401, 2004.

[51] C. M. Chen, C. H. Lin, H. F. Juan et al., "ATP13A2 variability in Taiwanese Parkinson's disease," *American Journal of Medical Genetics B*, vol. 156, no. 6, pp. 720–729, 2011.

[52] C. S. Lu, Y. H. Weng, M. C. Chen et al., "^{99m}Tc-TRODAT-1 imaging of multiple system atrophy," *Journal of Nuclear Medicine*, vol. 45, no. 1, pp. 49–55, 2004.

[53] K. Y. Tzen, C. S. Lu, T. C. Yen, S. P. Wey, and G. Ting, "Differential diagnosis of Parkinson's disease and vascular parkinsonism by ^{99m}Tc-TRODAT-1," *Journal of Nuclear Medicine*, vol. 42, no. 3, pp. 408–413, 2001.

[54] C. C. Huang, T. C. Yen, Y. H. Weng, and C. S. Lu, "Normal dopamine transporter binding in dopa responsive dystonia," *Journal of Neurology*, vol. 249, no. 8, pp. 1016–1020, 2002.

[55] W. Y. Lin, K. J. Lin, Y. H. Weng et al., "Preliminary studies of differential impairments of the dopaminergic system in subtypes of progressive supranuclear palsy," *Nuclear Medicine Communications*, vol. 31, no. 11, pp. 974–980, 2010.

[56] Y. H. Weng, Y. H. W. Chou, W. S. Wu et al., "PINK1 mutation in Taiwanese early-onset parkinsonism: clinical, genetic, and dopamine transporter studies," *Journal of Neurology*, vol. 254, no. 10, pp. 1347–1355, 2007.

[57] T. C. Yen, K. Y. Tzen, M. C. Chen et al., "Dopamine transporter concentration is reduced in asymptomatic Machado-Joseph disease gene carriers," *Journal of Nuclear Medicine*, vol. 43, no. 2, pp. 153–159, 2002.

[58] P. Crits-Christoph, A. Newberg, N. Wintering et al., "Dopamine transporter levels in cocaine dependent subjects.," *Drug and Alcohol Dependence*, vol. 98, no. 1-2, pp. 70–76, 2008.

[59] T. L. Yeh, K. C. Chen, S. H. Lin et al., "Availability of dopamine and serotonin transporters in opioid-dependent users—a two-isotope SPECT study," *Psychopharmacology*, vol. 220, no. 1, pp. 55–64, 2012.

[60] Y. K. Yang, W. J. Yao, T. L. Yeh et al., "Decreased dopamine transporter availability in male smokers—a dual isotope SPECT study," *Progress in Neuro-Psychopharmacology and Biological Psychiatry*, vol. 32, no. 1, pp. 274–279, 2008.

[61] A. Newberg, C. Lerman, N. Wintering, K. Ploessl, and P. D. Mozley, "Dopamine transporter binding in smokers and nonsmokers," *Clinical Nuclear Medicine*, vol. 32, no. 6, pp. 452–455, 2007.

[62] K. H. Krause, S. H. Dresel, J. Krause, C. la Fougere, and M. Ackenheil, "The dopamine transporter and neuroimaging in attention deficit hyperactivity disorder," *Neuroscience and Biobehavioral Reviews*, vol. 27, no. 7, pp. 605–613, 2003.

[63] J. Krause, "SPECT and PET of the dopamine transporter in attention-deficit/hyperactivity disorder," *Expert Review of Neurotherapeutics*, vol. 8, no. 4, pp. 611–625, 2008.

[64] S. Dresel, J. Krause, K. H. Krause et al., "Attention deficit hyperactivity disorder: binding of [^{99m}Tc]TRODAT-1 to the

dopamine transporter before and after methylphenidate treatment," *European Journal of Nuclear Medicine*, vol. 27, no. 10, pp. 1518–1524, 2000.

[65] K. H. Krause, S. H. Dresel, J. Krause, H. F. Kung, and K. Tatsch, "Increased striatal dopamine transporter in adult patients with attention deficit hyperactivity disorder: effects of methylphenidate as measured by single photon emission computed tomography," *Neuroscience Letters*, vol. 285, no. 2, pp. 107–110, 2000.

[66] J. Krause, C. la Fougere, K. H. Krause, M. Ackenheil, and S. H. Dresel, "Influence of striatal dopamine transporter availability on the response to methylphenidate in adult patients with ADHD," *European Archives of Psychiatry and Clinical Neuroscience*, vol. 255, no. 6, pp. 428–431, 2005.

[67] C. La Fougère, J. Krause, K. H. Krause et al., "Value of ^{99m}Tc-TRODAT-1 SPECT to predict clinical response to methylphenidate treatment in adults with attention deficit hyperactivity disorder," *Nuclear Medicine Communications*, vol. 27, no. 9, pp. 733–737, 2006.

[68] K. H. Krause, S. H. Dresel, J. Krause, H. F. Kung, K. Tatsch, and M. Ackenheil, "Stimulant-like action of nicotine on striatal dopamine transporter in the brain of adults with attention deficit hyperactivity disorder," *International Journal of Neuropsychopharmacology*, vol. 5, no. 2, pp. 111–113, 2002.

[69] D. D. Dougherty, A. A. Bonab, T. J. Spencer, S. L. Rauch, B. K. Madras, and A. J. Fischman, "Dopamine transporter density in patients with attention deficit hyperactivity disorder," *The Lancet*, vol. 354, no. 9196, pp. 2132–2133, 1999.

[70] K. A. Cheon, Y. H. Ryu, Y. K. Kim, K. Namkoong, C. H. Kim, and J. D. Lee, "Dopamine transporter density in the basal ganglia assessed with [^{123}I]IPT SPET in children with attention deficit hyperactivity disorder," *European Journal of Nuclear Medicine and Molecular Imaging*, vol. 30, no. 2, pp. 306–311, 2003.

[71] A. Abi-Dargham, O. Mawlawi, I. Lombardo et al., "Prefrontal dopamine D1 receptors and working memory in schizophrenia," *Journal of Neuroscience*, vol. 22, no. 9, pp. 3708–3719, 2002.

[72] Y. Okubo, T. Suhara, K. Suzuki et al., "Decreased prefrontal dopamine D1 receptors in schizophrenia revealed by PET," *Nature*, vol. 385, no. 6617, pp. 634–635, 1997.

[73] P. Karlsson, L. Farde, C. Halldin, and G. Sedvall, "PET study of D1 dopamine receptor binding in neuroleptic-naive patients with schizophrenia," *American Journal of Psychiatry*, vol. 159, no. 5, pp. 761–767, 2002.

[74] N. D. Volkow, J. S. Fowler, and G. J. Wang, "The addicted human brain viewed in the light of imaging studies: brain circuits and treatment strategies," *Neuropharmacology*, vol. 47, supplement 1, pp. S3–S13, 2004.

[75] N. D. Volkow, J. S. Fowler, G. J. Wang, J. M. Swanson, and F. Telang, "Dopamine in drug abuse and addiction: results of imaging studies and treatment implications," *Archives of Neurology*, vol. 64, no. 11, pp. 1575–1579, 2007.

[76] N. D. Volkow, J. S. Fowler, G. J. Wang, and J. M. Swanson, "Dopamine in drug abuse and addiction: results from imaging studies and treatment implications," *Molecular Psychiatry*, vol. 9, no. 6, pp. 557–569, 2004.

[77] N. D. Volkow, J. S. Fowler, G. J. Wang, R. Baler, and F. Telang, "Imaging dopamine's role in drug abuse and addiction," *Neuropharmacology*, vol. 56, supplement 1, pp. S3–S8, 2009.

[78] N. D. Volkow, G. J. Wang, J. S. Fowler et al., "Reinforcing effects of psychostimulants in humans are associated with increases in brain dopamine and occupancy of D_2 receptors," *Journal of Pharmacology and Experimental Therapeutics*, vol. 291, no. 1, pp. 409–415, 1999.

[79] N. D. Volkow, G. J. Wang, J. S. Fowler et al., "Prediction of reinforcing responses to psychostimulants in humans by brain dopamine D_2 receptor levels," *American Journal of Psychiatry*, vol. 156, no. 9, pp. 1440–1443, 1999.

[80] N. D. Volkow, G. J. Wang, M. W. Fischman et al., "Relationship between subjective effects of cocaine and dopamine transporter occupancy," *Nature*, vol. 386, no. 6627, pp. 827–830, 1997.

[81] N. D. Volkow, J. S. Fowler, G. J. Wang et al., "Decreased dopamine D_2 receptor availability is associated with reduced frontal metabolism in cocaine abusers," *Synapse*, vol. 14, no. 2, pp. 169–177, 1993.

[82] N. D. Volkow, L. Chang, G. J. Wang et al., "Low level of brain dopamine D_2 receptors in methamphetamine abusers: association with metabolism in the orbitofrontal cortex," *American Journal of Psychiatry*, vol. 158, no. 12, pp. 2015–2021, 2001.

[83] G. J. Wang, N. D. Volkow, J. S. Fowler et al., "Dopamine D_2 receptor availability in opiate-dependent subjects before and after naloxone-precipitated withdrawal," *Neuropsychopharmacology*, vol. 16, no. 2, pp. 174–182, 1997.

[84] N. D. Volkow, G. J. Wang, J. S. Fowler et al., "Decreases in dopamine receptors but not in dopamine transporters in alcoholics," *Alcoholism: Clinical and Experimental Research*, vol. 20, no. 9, pp. 1594–1598, 1996.

[85] N. D. Volkow, G. Wang, J. S. Fowler et al., "Therapeutic doses of oral methylphenidate significantly increase extracellular dopamine in the human brain," *The Journal of Neuroscience*, vol. 21, no. 2, Article ID RC121, 2001.

[86] N. D. Volkow, G. J. Wang, J. S. Fowler et al., "Relationship between blockade of dopamine transporters by oral methylphenidate and the increases in extracellular dopamine: therapeutic implications," *Synapse*, vol. 43, no. 3, pp. 181–187, 2002.

[87] L. Farde, S. Pauli, H. Hall et al., "Stereoselective binding of 11C-raclopride in living human brain—a search for extrastriatal central D-2 dopamine receptors by PET," *Psychopharmacology*, vol. 94, no. 4, pp. 471–478, 1988.

[88] M. Nord and L. Farde, "Antipsychotic occupancy of dopamine receptors in schizophrenia," *CNS Neuroscience and Therapeutics*, vol. 17, no. 2, pp. 97–103, 2011.

[89] S. Kasper, J. Tauscher, B. Küfferle, C. Barnas, L. Pezawas, and S. Quiner, "Dopamine- and serotonin-receptors in schizophrenia: results of imaging-studies and implicationsfor pharmacotherapy in schizophrenia," *European Archives of Psychiatry and Clinical Neuroscience*, vol. 249, supplement 4, pp. S83–S89, 1999.

[90] A. Abi-Dargham, J. Rodenhiser, D. Printz et al., "Increased baseline occupancy of D_2 receptors by dopamine in schizophrenia," *Proceedings of the National Academy of Sciences of the United States of America*, vol. 97, no. 14, pp. 8104–8109, 2000.

[91] J. Tauscher, B. Küfferle, S. Asenbaum, S. Tauscher-Wisniewski, and S. Kasper, "Striatal dopamine-2 receptor occupancy as measured with [^{123}I]iodobenzamide and SPECT predicted the occurrence of EPS in patients treated with atypical antipsychotics and haloperidol," *Psychopharmacology*, vol. 162, no. 1, pp. 42–49, 2002.

[92] S. Kasper, J. Tauscher, E. Küfferle, B. Hesselmann, C. Barnas, and T. Brücke, "IBZM-SPECT imaging of dopamine D_2

receptors with typical and atypical antipsychotics," *European Psychiatry*, vol. 13, supplement 1, pp. S9–S14, 1998.

[93] N. Okamura, V. L. Villemagne, J. Drago et al., "*In vivo* measurement of vesicular monoamine transporter type 2 density in Parkinson disease with ^{18}F-AV-133," *Journal of Nuclear Medicine*, vol. 51, no. 2, pp. 223–228, 2010.

[94] V. L. Villemagne, N. Okamura, S. Pejoska et al., "*In vivo* assessment of vesicular monoamine transporter type 2 in dementia with lewy bodies and Alzheimer disease," *Archives of Neurology*, vol. 68, no. 7, pp. 905–912, 2011.

[95] H. F. Kung, Y. Z. Guo, J. Billings et al., "Preparation and biodistribution of [^{125}I]IBZM: a potential CNS D-2 dopamine receptor imaging agent," *International Journal of Radiation Applications and Instrumentation B*, vol. 15, no. 2, pp. 195–201, 1988.

[96] H. F. Kung, S. Pan, M. P. Kung et al., "In vitro and *in vivo* evaluation of [^{123}I]IBZM: a potential CNS D-2 dopamine receptor imaging agent," *Journal of Nuclear Medicine*, vol. 30, no. 1, pp. 88–92, 1989.

[97] L. H. Pinborg, C. Videbaek, M. Ziebell et al., "[^{123}I]epidepride binding to cerebellar dopamine D_2/D_3 receptors is displaceable: implications for the use of cerebellum as a reference region," *Neuroimage*, vol. 34, no. 4, pp. 1450–1453, 2007.

[98] N. I. Bohnen and K. A. Frey, "Imaging of cholinergic and monoaminergic neurochemical changes in neurodegenerative disorders," *Molecular Imaging and Biology*, vol. 9, no. 4, pp. 243–257, 2007.

[99] W. Lu and M. E. Wolf, "Expression of dopamine transporter and vesicular monoamine transporter 2 mRNAs in rat midbrain after repeated amphetamine administration," *Molecular Brain Research*, vol. 49, no. 1-2, pp. 137–148, 1997.

[100] K. J. Lin, Y. H. Weng, S. P. Wey et al., "Whole-body biodistribution and radiation dosimetry of ^{18}F-FP-(+) -DTBZ (^{18}F-AV-133): a novel vesicular monoamine transporter 2 imaging agent," *Journal of Nuclear Medicine*, vol. 51, no. 9, pp. 1480–1485, 2010.

[101] D. J. Gelb, E. Oliver, and S. Gilman, "Diagnostic criteria for Parkinson disease," *Archives of Neurology*, vol. 56, no. 1, pp. 33–39, 1999.

[102] E. Tolosa, G. Wenning, and W. Poewe, "The diagnosis of Parkinson's disease," *The Lancet Neurology*, vol. 5, no. 1, pp. 75–86, 2006.

[103] R. Pahwa and K. E. Lyons, "Early diagnosis of Parkinson's disease: recommendations from diagnostic clinical guidelines," *The American Journal of Managed Care*, vol. 16, supplement 4, pp. S94–99, 2010.

[104] A. J. Hughes, S. E. Daniel, S. Blankson, and A. J. Lees, "A clinicopathologic study of 100 cases of Parkinson's disease," *Archives of Neurology*, vol. 50, no. 2, pp. 140–148, 1993.

[105] A. H. Rajput, B. Rozdilsky, and A. Rajput, "Accuracy of clinical diagnosis in Parkinsonism—a prospective study," *Canadian Journal of Neurological Sciences*, vol. 18, no. 3, pp. 275–278, 1991.

[106] A. Antonini, "Imaging for early differential diagnosis of parkinsonism," *The Lancet Neurology*, vol. 9, no. 2, pp. 130–131, 2010.

[107] A. C. Felicio, M. C. Shih, C. Godeiro-Junior, L. A. F. Andrade, R. A. Bressan, and H. B. Ferraz, "Molecular imaging studies in Parkinson disease reducing diagnostic uncertainty," *Neurologist*, vol. 15, no. 1, pp. 6–16, 2009.

[108] A. M. M. Vlaar, T. de Nijs, A. G. H. Kessels et al., "Diagnostic value of ^{123}I-ioflupane and ^{123}I- iodobenzamide SPECT scans in 248 patients with Parkinsonian syndromes," *European Neurology*, vol. 59, no. 5, pp. 258–266, 2008.

[109] B. Thanvi, N. Lo, and T. Robinson, "Vascular parkinsonism—an important cause of parkinsonism in older people," *Age and Ageing*, vol. 34, no. 2, pp. 114–119, 2005.

[110] A. L. Berry and T. Foltynie, "Gene therapy: a viable therapeutic strategy for Parkinson's disease?" *Journal of Neurology*, vol. 258, no. 2, pp. 179–188, 2010.

[111] L. Leriche, T. Björklund, N. Breysse et al., "Positron emission tomography imaging demonstrates correlation between behavioral recovery and correction of dopamine neurotransmission after gene therapy," *Journal of Neuroscience*, vol. 29, no. 5, pp. 1544–1553, 2009.

[112] M. G. Kaplitt, A. Feigin, C. Tang et al., "Safety and tolerability of gene therapy with an adeno-associated virus (AAV) borne *GAD* gene for Parkinson's disease: an open label, phase I trial," *The Lancet*, vol. 369, no. 9579, pp. 2097–2105, 2007.

[113] N. D. Volkow, G. J. Wang, J. S. Fowler et al., "Decreased striatal dopaminergic responsiveness in detoxified cocaine-dependent subjects," *Nature*, vol. 386, no. 6627, pp. 830–833, 1997.

[114] N. D. Volkow, Y. S. Ding, J. S. Fowler et al., "Is methylphenidate like cocaine? Studies on their pharmacokinetics and distribution in the human brain," *Archives of General Psychiatry*, vol. 52, no. 6, pp. 456–463, 1995.

[115] M. V. Solanto, "Neuropsychopharmacological mechanisms of stimulant drug action in attention-deficit hyperactivity disorder: a review and integration," *Behavioural Brain Research*, vol. 94, no. 1, pp. 127–152, 1998.

[116] A. Abi-Dargham, "Do we still believe in the dopamine hypothesis? New data bring new evidence," *International Journal of Neuropsychopharmacology*, vol. 7, supplement 1, pp. S1–S5, 2004.

[117] O. Langer and C. Halldin, "PET and SPET tracers for mapping the cardiac nervous system," *European Journal of Nuclear Medicine*, vol. 29, no. 3, pp. 416–434, 2002.

[118] A. Takano, "The application of PET technique for the development and evaluation of novel antipsychotics," *Current Pharmaceutical Design*, vol. 16, no. 3, pp. 371–377, 2010.

[119] C. Hiemke, "Therapeutic drug monitoring in neuropsychopharmacology: does it hold its promises?" *European Archives of Psychiatry and Clinical Neuroscience*, vol. 258, supplement 1, pp. S21–S27, 2008.

[120] S. Kapur, R. Zipursky, C. Jones, G. Remington, and S. Houle, "Relationship between dopamine D_2 occupancy, clinical response, and side effects: a double-blind PET study of first-episode schizophrenia," *American Journal of Psychiatry*, vol. 157, no. 4, pp. 514–520, 2000.

Hindawi Publishing Corporation
Journal of Biomedicine and Biotechnology
Volume 2012, Article ID 420364, 13 pages
doi:10.1155/2012/420364

Review Article

Molecular Imaging in Tracking Tumor Stem-Like Cells

Tian Xia,[1] Han Jiang,[1,2,3,4] Chenrui Li,[5] Mei Tian,[1,2,3,4] and Hong Zhang[1,2,3,4]

[1] *Department of Nuclear Medicine, Second Affiliated Hospital of Zhejiang University, School of Medicine, 88 Jiefang Road, Hangzhou, Zhejiang 310009, China*
[2] *Zhejiang University Medical PET Center, Zhejiang University, Hangzhou 310009, China*
[3] *Institute of Nuclear Medicine and Molecular Imaging, Zhejiang University, Hangzhou 310009, China*
[4] *Key Laboratory of Medical Molecular Imaging of Zhejiang Province, Hangzhou 310009, China*
[5] *The School of Pharmacy, The Chinese University of Hong Kong, Hong Kong*

Correspondence should be addressed to Hong Zhang, hzhang21@gmail.com

Received 27 December 2011; Accepted 10 February 2012

Academic Editor: Enzhong Li

Cancer remains a major public health problem in many countries. It was found to contain a subset of cancer stem cells (CSCs) that are capable of proliferation and self-renewal, and differentiation into various types of cancer cells. CSCs often display characteristics of chemotherapy resistance and radiotherapy resistance. Numerous putative biomarkers of CSCs are currently identified including CD133, CD44, CD24, ALDH (aldehyde dehydrogenase), and ABCG2. Interestingly, no single marker is exclusively expressed by CSCs. Thus, the various combinations of different biomarkers will be possible to identify CSCs, and considerable work is being done to recognize new ones. In order to demonstrate the mechanisms of resistance and response to therapy and predict the outcome as well as prognosis, the ways to track and identify CSCs will be extremely important. The technologies of molecular imaging will reveal mechanisms of cancer progression and provide visual targets for novel therapeutics. Limited studies were investigated on the detection of various types of CSCs by molecular imaging. Although the tracking of circulating CSCs is still hampered by technological challenges, personalized diagnosis and therapies of cancers are expected to be established based on increased understanding of molecular imaging of cancer stem-like cells biomarkers.

1. Introduction

The global burden of cancer is increasing, and cancer is a major public health problem in many parts of the world, including China. Based on the American Cancer Society cancer statistics, a total of 1,596,670 new cancer cases and 571,950 deaths from cancer, corresponding to more than 1500 deaths per day, are projected to occur in the United States in 2011 [1]. Among men cancers of the prostate, lung and bronchus, and colorectum will account for approximately 52% of all newly diagnosed cancers. Breast, lung and bronchus, and colorectum will be the three most commonly diagnosed types of cancers among women this year. Cancers of the lung and bronchus, prostate, and colorectum in men, and cancers of the lung and bronchus, breast, and colorectum in women continue to be most common causes of cancer death. These four cancers account for almost half of the total cancer deaths among men and women [1].

Cancer mortality remains high, despite the recent advances made in cancer treatment and diagnosis. One possible cause for therapeutic failure is that many malignant tumors contain a subset of tumor-initiating cells termed cancer stem cells (CSCs) when multipotency and self-renewal have been demonstrated. The CSC model provides an attractive concept that help to explain why cancer cells resistant to chemo- and radiotherapies. There has been acceptance of the idea that the remaining tumor cells after anticancer therapy have a distinct molecular phenotype that confers resistance to the therapies [2, 3]. Identification and purification of the CSC population from clinical samples and cell lines have been proven successfully based on the expression of a particular cell-surface marker, as well as by functional assays. The identification of CSC has undergone rapid development in recent years.

Side population (SP) technology has been widely used to identify the cancer stem-like cells by detection of the

ability to efflux Hoechst 33342 dye through an adenosine-triphosphate-(ATP-) binding cassette (ABC) membrane transporter. In many tumors, SP cells are reported as enriched cells with tumorigenesis and are responsible for chemoresistance and tumor recurrence [4–6]. The current methods for isolation of putative CSCs depend on cell surface biomarkers and enzymatic activity detected by fluorescence-activated cell sorter (FACS). Clarified understanding and eradication of CSCs, in turn, may improve the outcome of some cancer therapy [3, 7]. One of the promising strategies is to track the CSCs and then target them for efficient treatments. Techniques required for real-time imaging and studies of tumor cells in viable fresh tissue or living animals are urgently needed.

Molecular imaging is a new and noninvasive strategy which can provide molecular and physiological information regarding cancer using various molecular-targeted imaging probes specific for cell surface biomarkers that are unique to cancer. It aims to visualize and quantify biological, physiological, and pathological processes on cellular and molecular levels. This has advantages over traditional methods, as they permit real-time tracking in vivo. Based on the biological characteristics of cancer stem cells, molecular imaging will provide a novel role for the visualization of cancer cells. Intravital imaging of CSCs could be of great importance for determining prognosis, as well as monitoring therapeutic efficacy and influencing therapeutic protocols. Cancer biomarker-based molecular imaging has become an essential element for cancer diagnosis. In most cases, the accuracy of predicting cancers depends on the specificity and signal sensitivity of molecular probes targeting genes or proteins involved in cancer growth and progression. In this paper, we will briefly discuss and summarize cancer stem biomarkers and the applications of the molecular imaging in tumor stem-like cells or tumor cells.

2. Types of Cancer Stem Cells and Its Biomarkers

CSCs have been defined as a subset of cancer cells with exclusive ability of self-renewal and to cause the heterogeneous lineages of cancer cells that comprise the tumor. Numerous putative markers are currently under investigation, and much work is being done to identify and characterize new marker. The experimental methods to identify CSCs have been developed so far as follows: (a) clonogenic assay; (b) sphere-forming assays; (c) assays to investigate the differentiation potency of isolated cells into the various differentiated cells. In addition to these analyses based on in vitro properties of CSCs, the existence of CSCs has been demonstrated by tumor initiation assays, in which the primary human tumor cells were transplanted into NOD/SCID mice [8–10] (Figure 1). Cell surface markers and enzymatic activity detected by FACS have been widely used for the prospective isolation of putative CSCs. Here, the biomarkers to identify CSCs in different types of tumor models are investigated.

2.1. Hematopoietic System: Acute Myelogenous Leukemia (AML). In 1994, Lapidot et al. showed that leukemia can be initiated in mice using a single tumorgenic cell. It implied that a single or a few malignant cells can produce tumors [11]. These leukaemia-initiating cells were found to be $CD34^+$ $CD38^-$ on the basis of the cell-surface-marker expression. Subsequently, Bonnet et al. also demonstrated that the cell capable of initiating human AML in nonobese diabetic mice with severe combined immunodeficiency disease (NOD/SCID mice), termed the SCID leukemia-initiating cell, was exclusively $CD34^+$ $CD38^-$ [12]. After the identification of rare CSCs in leukemia, numbers of molecular markers for detecting CSCs in solid tumors have also been identified. The models that have been devised to describe the CSCs are as follows.

2.2. Solid Tumors: Brain/Breast/Lung/Colorectal/Prostate/Pancreas/Liver

2.2.1. Brain. Brain tumors are the leading cause of cancer mortality in children and remain incurable despite advances in surgery and adjuvant therapies [1]. Singh et al. reported that only the $CD133^+$ brain tumor fraction contains cells that were capable of tumor-initiation in NOD-SCID mouse brains [13]. They used a xenograft assay that identified human brain tumor initiating cells that initiate tumors in vivo. In their studies, injection of 10^5 $CD133^-$ cells did not form a tumor, whereas only 100 $CD133^+$ cells produced the patient's original tumor. This identification of an in vivo tumor-initiating cell from human brain tumors provided a powerful tool to investigate the tumorigenic process in the central nervous system. Interestingly, Chiao et al. suggested that $CD133^+$ glioblastoma stem-like cells (GSCs) and $CD133^-$ GSCs shared similar efficacy in tumor formation but showed distinct intratumor vasculature [14]. Compared with $CD133^-$ GSC, a highly vascularized anaplastic tumor was found in $CD133^+$ GSC-derived tumor xenografts. Both in vitro and in vivo subsets of $CD133^+$ GSC but not $CD133^-$ GSC were capable of vascular smooth muscle-like cell differentiation. The detection of endothelium-associated CD31 gene and differentiation of vascular-like cells suggest that GSCs may contribute to form vessel-like structures and provide a blood supply for glioblastoma cells.

Additionally, Tabuse et al. found high expression of the HOXD9 gene transcript in glioma cell lines and human glioma tissues [15]. They suggested that HOXD9 would be a novel marker of GCSCs and cell proliferation and/or survival factor in gliomas and glioma cancer stem-like cells, and a potential therapeutic target (HOX genes encode a family of homeodomain-containing transcription factors involved in the determination of cell fate and identity during embryonic development. They also behave as oncogenes in some malignancies).

2.2.2. Breast. Breast cancer is the most frequently diagnosed cancer and the leading cause of cancer death among females, accounting for 23% of the total cancer cases and 14% of the cancer deaths, based on the GLOBOCAN 2008 estimates [1,

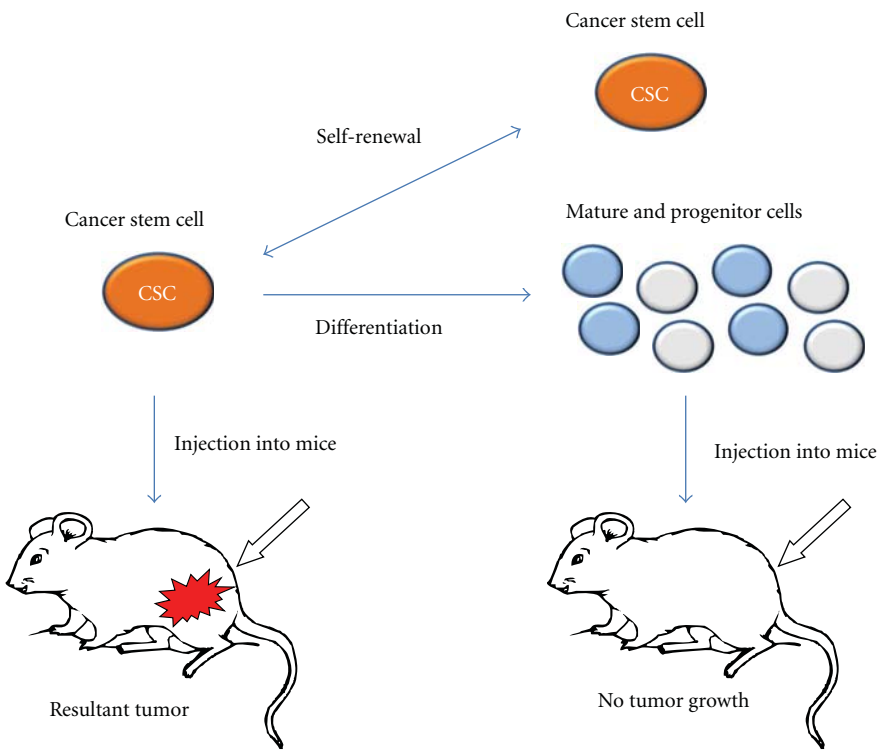

Figure 1: Three phenotypes of CSCs: self-renew, multipotentiality, and tumor-initiating capacity. Self-renewal: single-cell culture sphere-forming assay. Differentiation: flow cytometric analysis of differentiation markers and loss of stem cell markers. Tumor-initiating properties were investigated by injection of CSCs in NOD/SCID mice. The most crucial standard for a CSC is its ability to reinitiate a serially transplantable tumor that recapitulates the original heterogeneity and tumor histology. Using this standard, many so-called CSCs reported so far are based on correlative studied rather than being true CSCs.

16]. In the United States, breast cancer is expected to account for 30% (230, 480) of all new cancer cases among women in 2011 [1]. Through analysis of cell surface markers and xenotransplant models, a subpopulation of putative human breast cancer stem cells that is $CD24^-/CD44^+$ and bears high aldehyde dehydrogenase isoform 1(ALDH1) activity has been isolated in clinical samples of breast cancer tissues [3]. These cells are regarded as having the most prominent tumor-initiating activity. Cells with aldehyde dehydrogenase (ALDH) activity isolated from normal human breast have phenotypic and functional characteristics of mammary stem cells. Analyzing the expression of ALDH1 in hundreds of human breast carcinomas from two independent tumor sets indicated poor clinical outcome [17]. These findings provide support for the "cancer stem cell hypothesis" and further indicated that ALDH1 was a marker of stem/progenitor cells of the normal human breast and breast carcinomas. The ALDH1-positive cell population had a small overlap with the previously described cancer stem cell, $CD44^+/CD24^-$/lin-phenotype [18].

The overlap represented approximately 1% or less of the total cancer cell population, which bears both phenotypes appeared to be highly enriched in tumorigenic capability. It was found that as few as 20 cells were able to generate tumors. Since ALDH is also expressed in hematopoietic and neuronal stem cells, this marker may prove useful for the detection and isolation of cancer stem cells in other malignancies, thus facilitating the application of cancer stem cell biology to clinical practice. In breast CSCs, it was also showed that the activity of TAZ, a transducer of the Hippo pathway, is required to sustain self-renewal and tumor-initiation capacities. TAZ protein levels and activity, which is promoted by the epithelial-mesenchymal transition (EMT), are elevated in prospective CSCs and in poorly differentiated human tumors, which have prognostic value [19]. The Hippo transducer TAZ confers cancer stem cell-related traits on breast cancer cells.

2.2.3. Lung. Lung cancer is the third most commonly diagnosed type and third most common cause of cancer death both in male and female [1]. Similar to the limited understanding of lung stem cell biology, the identity of the cell of origin in lung tumorigenesis is also largely unknown. Lung cancer contains a rare population of $CD133^+$ cancer stem-like cells able to self-renew and generates an unlimited progeny of nontumorigenic cells. Molecular and functional characterization of such a tumorigenic population may provide valuable information to be exploited in clinic [20]. It was found that human lung CSCs also express ABCG2, c-kit receptors, embryonic markers (SSEA-3, TRA-1-81, Oct-4, and nuclear β-catenin), and low levels of the cytokeratins 8/18 (CK8/18) [21, 22].

2.2.4. Colorectal Cancer. Colorectal cancer is the third most commonly diagnosed cancer in males and the second in females [1]. Colorectal cancer incidence rates are rapidly increasing in several areas historically at low risk, of which possible reasons are a combination of factors including changes in dietary patterns, obesity, and an increased prevalence of smoking.

The existence of human colon cancer tumor-initiating cells was demonstrated by O'Brien et al. [10]. They used the renal capsule transplantation in immunodeficient NOD/SCID mice to identify a human colon cancer-initiating cell (CC-IC), which was $CD133^+$. However, the $CD133^-$ cells that comprised the majority of the tumor were unable to initiate tumour growth. They calculated by limiting dilution analysis that there was one CC-IC in 5.7×10^4 unfractionated tumor cells, whereas there was one CC-IC in 262 $CD133^+$ cells, representing >200-fold enrichment. CC-ICs within the $CD133^+$ population were able to maintain themselves as well as differentiate and reestablish tumor heterogeneity upon serial transplantation. The identification of colon cancer stem cells and the existence of tumorigenic and nontumorigenic cells within colon cancers suggested that they must target the cancer stem cells for therapeutic strategies to be effective.

Simultaneously, tumorigenic cells in colon cancer were included in the high-density $CD133^+$ population, which accounted for about 2.5% of the tumor cells [9]. The original tumor in NOD/SCID mice can be reproduced by injection of colon cancer $CD133^+$ cells. Purified CD133 and carcinoembryonic antigen-positive (CEA^+) colon cancer cells were unable to transfer the tumor into immunocompromised mice, and the tumorigenic population in colon cancer is restricted to $CD133^+$ cells. Importantly, CC-ICs need to remain undifferentiated to maintain tumorigenic potential. During the in vivo passages, the tumors were serially transplanted for several generations, and CD133+ cells did not lose their tumorigenic potential. Instead, in each of the tumors they observed progressively faster tumour growth without significant phenotypic alterations. Therefore, the small number of undifferentiated tumorigenic $CD133^+$ cells should be the target of future therapies.

Using multiple genetic markers, researchers also had evaluated the clinical significance of circulating tumor cells as a prognostic factor for overall survival (OS) and disease-free survival (DFS) in the peripheral blood (PB) of patients with colorectal cancer Dukes' stages B and C who had undergone curative surgery. OS and DFS of patients who were positive for CEA/CK/CD133mRNA were significantly worse than those of patients who were negative for these markers. Detection of CEA/CK/CD133 mRNA in PB is a useful tool for determining which patients are at high risk for recurrence and poor prognosis [23]. Moreover, in human colorectal cancer, CSCs are also defined using CD166, CD44, and CD24 cell-surface markers [24, 25].

The CSC theory suggests that the actual tumorigenic capacity of individual cancer cells may be influenced by homeostatic signals derived from their microenvironment. It was observed that high Wnt activity functionally designates the colon CSC population [26]. Nevertheless, the current data lend strong support to the influence of the niche on CSC maintenance.

2.2.5. Prostate. Prostate cancer will account for 29% (240, 890) and be most commonly diagnosed cancer in men in United States according to the American Cancer Society in 2011 [1]. There continues to be a need for new diagnostic markers and potential new therapeutic targets in prostate cancer. Studies suggested that high ALDH activity and coexpression of CD44 ($ALDH^{hi}$ $CD44^+$) cells exhibited a higher proliferative, clonogenic, and metastatic capacity in vitro and demonstrated higher tumorigenicity capacity in vivo in prostate cancer cell line. However, low ALDH activity and CD44-negative ($ALDH^{lo}$ $CD44^-$) cells were able to develop tumors, albeit with longer latency periods. In their study, ALDH activity and CD44 did not appear to identify prostate cancer stem cells; however, they did reveal increased tumorigenic and metastatic potential, indicating their potential importance for further exploration [28].

Rajasekhar et al. identified a minor subset of stem-like human prostate tumour-initiating cells (TICs) that do not express prostate cancer markers, such as androgen receptor or prostate-specific antigen [29]. The cells represent an undifferentiated subtype of basal cells and can be purified from prostate tumors based on coexpression of the human pluripotent stem cell marker TRA-1-60 with CD151 and CD166. Such triple-marker-positive TICs possess stem cell characteristics and multipotency as demonstrated by in vitro sphere formation and in vivo tumor initiation, respectively.

2.2.6. Pancreas. Pancreatic adenocarcinoma continues to be one of the deadliest cancer-related diseases in the world [30]. Little progress has been made since the past introduction of the chemotherapeutic agent gemcitabine, which remains the first-line chemotherapeutic agent in pancreatic cancer. The prognosis of patients diagnosed with pancreatic cancer remains extremely poor [31]. Emerging evidence suggests that the majority of pancreas tumors display vital functional heterogeneity in their respective cell populations. However, a small subpopulation of tumor cells that have acquired the same somatic mutations as the other tumor cells with epigenetically distinct is responsible for tumor initiation, growth, and metastasis [32, 33].

Researchers identified a highly tumorigenic subpopulation of pancreatic cancer cells expressing the cell surface markers CD44, CD24, and epithelial-specific antigen (ESA) using a xenograft model of immunocompromised mice for primary human pancreatic adenocarcinomas [34]. Pancreatic cancer cells expressing the cell surface markers CD44, CD24, and ESA had at least a 100-fold increased tumorigenic potential compared with nontumorigenic cells. The $CD44^+CD24^+ESA^+$ pancreatic cancer cells showed the stem cell properties of self-renewal, the ability to produce differentiated progeny, and increased expression of the developmental signaling molecule sonic hedgehog (SHH).

More recent data suggested an abundant expression of ALDH-1 in normal pancreas tissue [35]. It was found that a subset of adult centroacinar cells and terminal ductal epithelial (CA/TD) cells were characterized by high levels

Table 1: Comparison of the biomarkers of CSC and normal stem cell.

Cancer type	CSC marker	Normal stem cell	Marker	References
Acute myelogenous leukemia	$CD34^+CD38^-$	Mouse embryonic stem cell	Oct-4	[64]
			SSEA-1	[65]
Glioma	Nestin, HOXD9	Human embryonic stem cell	SSEA-3 SSEA-4, Oct-4	[65]
Breast	ALDH1, TAZ $CD44^+/CD24^-/lin^-$		TRA-1-60 TRA-1-81	[65]
Colon	CD166	Neural stem cell	CD133	[66]
Prostate	TRA-1-60 CD151, CD 166		Nestin	[66]
Pancreas	ESA	Hepatic stem cell	EpCAM	[43]
Liver	CD90, EpCAM CD13	Mammary stem cell	$CD49f^+EpCAM^{neg\text{-}low}$	[67]
Breast, liver, and pancreas	ALDH		ALDH1	[17, 68]
Glioma, lung, colon, pancreas, and liver	CD133			
Pancreas, colon, and liver	CD24, CD44			
Breast, pancreas, and lung	ABCG2			

CD49f: α6 integrin; Lin: Lineage surface antigen; SSEA: stage-specific embryonic antigen.

of ALDH1 enzymatic activity. CA/TD cells carry significant progenitor capacities and may contribute to the maintenance of tissue homeostasis in adult mouse pancreas. Subsequently, Kim et al. sought to determine the relationship of ALDH and CD133 whose marker best enriches for pancreatic TICs and the sufficiency of $ALDH^{hi}$ and $ALDH^{lo}$ cell populations for tumor-initiation when enriched or depleted of cell populations also expressing CD133 [36]. Finally, they demonstrated that cell populations enriched for high ALDH activity alone were more efficient and fulfill the major criteria of a CSC and efficiently recapitulate the phenotype of the original tumor independent of CD133 cell surface expression, using a strict, direct xenograft tumor system and limiting dilutions of sorted human pancreatic cancer cells injected into NOD/SCID mice [36].

It was also suggested that SP cells were enriched in CSCs of pancreas cancer and validated an intriguing regulatory mechanism of the cancer stem cell-related phenotypes, which could represent a novel therapeutic target [4, 37].

2.2.7. Liver. Hepatocellular carcinoma (HCC) accounts for over 90% of primary liver cancer in adults. The first-line treatment for HCC is liver transplantation or surgical resection [37, 38]. However, most HCCs are inoperable because patients present at advanced stages. Even after surgical resection, the long-term prognosis of HCC remains unsatisfactory due to high recurrence rates. Recently, there has been mounting evidence in support of the existence of CSCs in hepatocellular carcinoma. CD24 was found to be a functional liver tumor-initiating cell (T-IC) marker. $CD24^+$ HCC cells were found to be critical for the maintenance, self-renewal, differentiation, and metastasis of tumors and to significantly impact patients' clinical outcome [39]. In liver, CSCs can also be identified by several other cell markers, including CD44, CD133, CD90, CD13, EpCAM, OV6, and ALDH enzymatic activity, or by selecting for SP cells which express an adenosine triphosphate-binding cassette (ABC) membrane transporter, such as MDR1 and ABCG2 [40]. However, generally accepted markers of CSCs in HCC have not been identified.

In summary, recent studies indicate that the expression of the surface markers is not suitable as a universal signature to detect CSCs in cells derived from different tumor types. It is likely that a panel of markers will be required to assess the presence of reliable and true CSCs in tumors. Although the list of CSC markers is not yet finished, a method to isolate and substantially enrich CSCs for cancer research is provided (Table 1).

3. Imaging of Cancer Stem-Like (or Cancer) Cells

Noninvasive molecular imaging technology is an effective and novel approach to visualize living cells in vivo. It also plays a critical role in tracking the location and activity of CSCs [41]. Now that CSCs are being identified and characterized in different tumor types, they are postulated to be responsible for tumor development, metastasis, and relapse after conventional therapies. To date, limited studies were investigated on the detection of various types of CSCs by molecular imaging methods (Table 2).

Examples will be given for the identified biomarkers of the tumor stem-like (or tumor) cells with molecular imaging techniques. Specifically, the feasibility of molecular imaging of prostate stem cell antigen-(PSCA-) positive prostate cancer was evaluated using an intermediate size antibody fragment by micropositron emission tomography (micro-PET) imaging [42], cell tracking with magnetic resonance imaging (MRI) after the hepatic progenitor cells labeled with EpCAM microbeads [43], CD133-specific monoclonal

Table 2: Molecular imaging in tracking tumor stem-like cells.

Imaging agent	Molecular imaging	Biomarker	Model
^{64}Cu-ATSM	PET	CD 133	Colon cancer
Antibody magnetic microbead	MRI	ESA	Liver cancer
HA-MNCs	MRI	CD44	Breast cancer
Antibody AC133.1	FMT	CD133	CD133-overexpressing glioblastoma
Optical bifusion reporter genes	BLI	CD44	Breast cancer
GSC-targeting peptide	BLI	Nestin	Glioma
199b Luc-1	BLI	CD133	Medulloblastoma tumor
Adv5-199b	PET/CT		

antibody AC133.1 used for quantitative fluorescence-based optical imaging of mouse xenograft models [44], and so on.

3.1. Positron Emission Tomography (PET). PET imaging is a highly sensitive system that has advantages over traditional methods, as it permits noninvasive, real-time tracking in vivo. To our knowledge, few published studies were found to track the CICs in cancers with PET imaging. We will give an example of a generated stem cell surface marker specific probe to prostate cancer by micro-PET imaging. In the human prostate cancer LAPC-4 xenograft model, a number of candidate molecules were identified with high expression using representational difference analysis (RDA), a PCR-based subtractive hybridization strategy [45, 46]. One promising candidate, PSCA, is a prostate-specific cell surface antigen expressed strongly in both androgen-dependent and -independent LAPC-4 tumors. Elevated levels of PSCA were correlated with increased tumor stage, grade, and androgen independence [47]. PSCA located at chromosome 8, band q24.2, is a prostate-specific gene, encoding a 123-aa protein with an amino-terminal signal sequence, a carboxyl-terminal GPI-anchoring sequence, and multiple N-glycosylation sites [46]. Researchers had isolated and characterized a series of monoclonal antibodies directly against PSCA. The localization of PSCA had been detected using these antibodies.

Leyton et al. revealed a humanized radioiodinated minibody as a PET imaging agent for the detection of PSCA-expressing tumors [42]. Visualization of PSCA-positive prostate cancer is feasible using an intermediate size antibody fragment at 21 hours. The genetically engineered radioiodinated (^{124}I or ^{131}I) 2B3 minibody as a novel antibody fragment for specific targeting and potential PET imaging agent for PSCA-expressing prostate cancers was introduced [48]. Then an affinity-matured minibody that ranked second in affinity for PET imaging of PSCA-expressing tumors was selected as the best tracer [49]. Currently, this candidate is under development for evaluation in a pilot clinical imaging study. Interestingly, two antibodies, anticlaudin 4 and anti-PSCA, were radio-labeled with iodine 125 (^{125}I) for imaging pancreatic cancer xenografts in mice using gamma scintigraphy and single-photon emission computed tomography-computed tomography (SPECT/CT). It has been demonstrated that they are promising as radiodiagnostic and possibly radiotherapeutic agents for human pancreatic cancers [50]. Antibodies or their constituent parts can be conjugated with radionuclides to carry them into tumors specifically and effectively. Similar to the specific normal stem cell biomarker detected in prostate cancer, which was used as early diagnosis marker in prostate cancer, tracking the CSCs biomarkers by PET imaging is also promising.

^{64}Cu-diacetyl-bis (N4-methylthiosemicarbazone) (^{64}Cu-ATSM), a PET imaging agent, accumulated in regions of CD133^{+} high expression, which are then killed by radiation, resulting in a decrease of the percentage of CD133^{+} cells [51]. In vivo (colon 26-bearing mice) studies showed that ^{64}Cu-ATSM treatment inhibited tumor growth. The percentage of CD133^{+} cells and metastatic ability in ^{64}Cu-ATSM-treated tumors was decreased compared with that in control animals. ^{64}Cu-ATSM could be a potential internal radiotherapy agent affecting the tumor's hypoxic regions with a high density of CD133^{+} cells, designated as CSCs. Therefore, tracking CSCs biomarkers and evaluating therapy efficiency are feasible and attractive. Further studies with more kinds of CSCs biomarkers would be needed to clarify the precise applications.

3.2. Magnetic Resonance Imaging (MRI). Magnetic resonance imaging is a noninvasive modality and can provide information on the anatomy, function, and metabolism of tissues in living subjects with no ionizing radiation. This imaging technique is increasingly performed in clinical diagnostics. Epithelial cell adhesion molecule (EpCAM) also known as epithelial-specific antigen (ESA) or CD326, a cell surface antigen, is found on liver CSCs, on hepatic progenitor cells including human hepatic stem cells (hHpSCs) and hepatoblasts (hHBs), and on proliferating epithelial cells in other tissues. McClelland et al. have evaluated the feasibility of cell tracking with MRI after the hepatic progenitor cells labeled with EpCAM microbeads before or after transplantation. Then the transplanted hHpSCs could be monitored and counted repeatedly in the same host by injection of the labeled MRI probe [43]. Additionally, magnetic iron microbeads coupled with HEA-125 monoclonal antibody against the epithelial cell adhesion molecule, abbreviated as EpCAM microbeads, have been developed primarily for the positive selection or depletion of EpCAM-positive cells. The magnetic labeling methodology is applicable to other

surface antigens for which antibody magnetic microbeads are available [43]. Antibodies or their constituent parts can be conjugated with nanoparticles or other substances, to carry them more specifically and effectively into tumors. The biological effects of monoclonal antibodies are supposed to be possible if targeting antigens are present in cancer stem-like cells [52].

CD44 is a cell surface glycoprotein overexpressing in breast CSCs and plays an important role in promoting cancer cell proliferation, invasion, and tumor-associated angiogenesis [53]. First, researchers synthesized pyrenyl HA (Py-HA) conjugates as CD44-targetable surfactants capable of simultaneously encapsulating magnetic nanocrystals and targeting CD44 using HA and 1-pyrenebutyric acid (Py). Finally, Py-HA conjugates and magnetic nanocrystals were used to formulate HA-MNCs. Their study suggested that HA-MNCs can be a potent cancer-specific molecular imaging agent for effective diagnosis of CD44-overexpressing breast cancer via MR imaging [53]. Furthermore, CG-rich duplex containing prostate-specific membrane antigen (PSMA) aptamer-conjugated thermally cross-linked super paramagnetic iron oxide nanoparticles (TCL-SPIONs) was reported as prostate cancer-specific nanotheranostic agents [54]. These agents were capable of prostate tumor detection in vivo by MRI and selective delivery of drugs to the tumor tissue, simultaneously.

3.3. Optical Imaging. CD133/prominin (AC133) has been identified as a CSC marker in a variety of tumors. Tsurumi et al. showed that CD133-specific monoclonal antibody AC133.1 was used for quantitative fluorescence-based optical imaging of mouse xenograft models [44]. Near-infrared fluorescence molecular tomography (FMT), a highly sensitive and fully quantitative technology, was applied as the in vivo imaging modality. Imaging worked well using CD133 overexpressing cell line however, the implanted xenograft HCT116 cells, which express CD133 at an endogenous level, had limitations. The lower CD133 expression level of the HCT116 wild-type tumors led to a generally lower signal to noise ratio compared to CD133-overexpressing tumors. They provided the first evidence that noninvasive antibody-based in vivo imaging of tumor-associated CD133 is feasible and that CD133 antibody-based tumor targeting is efficient.

In breast cancer, it was demonstrated that with noninvasive imaging approaches, as few as 10 $CD44^+$ cells of stably labeled breast cancer stem cells (BCSCs) could be tracked in vivo by bioluminescence imaging (BLI) [41]. Imaging revealed that $CD44^+$ cells from both primary tumors and lung metastases were highly enriched for tumor-initiating cells. The BCSCs were tagged through expression of optical bifusion reporter genes to facilitate their visualization in the living human-in-mouse breast cancer xenograft model in NOD/SCID mice. Such reporters included firefly luciferase (Luc) for whole-body tracking of cells via BLI and fluorescent proteins. In order to label BCSCs, dual-function BLI-fluorescent reporter constructs constituting the Luc coding sequence (Luc2) fused to that of fluorescent proteins were used. They fused Luc2 to enhanced GFP (*eGFP*) or the red fluorescent protein td-Tomato (*Tom*), which improved detection in vivo relative to GFP. They established optimized parameters to transduce primary or passaged BCSCs with lentiviral vectors encoding Luc2-eGFP (L2G) or Luc2-Tom (L2T) fusion genes; thereby one cell in vitro and minimum of 10 cells of labeled BCSCs could be noninvasively visualized at 16 hours after implantation, thus greatly enhancing the accuracy and efficiency of tumorigenic assays compared with traditional monitoring assay. This study implied that the optimized strategy for labeling BCSCs with optical reporter genes can be applied to studies with CSCs in other tumors such as colon cancer, brain tumor, head-and-neck cancer, and leukemia, and to evaluate other putative CSC markers (e.g., CD24, CD133, EpCAM, ALDH1, etc.).

In addition, Vlashi et al. demonstrated that reduced 26S proteasome activity is a general feature of CICs for human glioma and breast cancer cells that can easily be exploited to identify, track, and target them in vitro and in vivo [55]. A fluorescent protein (ZsGreen) is a target of the 26S proteasome. The fluorescent positive cells had increased sphere-forming capacity, expressed CSC markers, and lacked differentiation markers in vitro. When injected into nude mice, ZsGreen-positive cells were approximately 100-fold more tumorigenic than the opposite cells. It was required approximately 100 ZsGreen-positive cells to form tumors in vivo. They proposed that ZsGreen-positive cells need to be further purified to obtain a pure CSC population. Tracking of CICs by fluorescence imaging in vivo may facilitate the search for novel therapeutic approaches that improve radiation therapy outcome.

Nestin, one of the most reliable stemness markers, is used to evaluate the identity of normal neural stem cells and glioma stem cells (GSCs). Samuel Beck et al. isolated a GSC-targeting (GSCT) peptide that demonstrated selective binding isotypes of Nestin proteins specifically expressed in GSCs. In human glioblastoma tissue specimens, the fluorescence-conjugated GSCT peptide could visualize putative GSC populations, showing its possible use as a diagnostic agent (Figure 2). Intravenously injected GSCT peptide effectively penetrated into tissues, specifically accumulated in gliomas that arise from implantation, and predominantly targeted Nestin-positive cells in these tumors (Figure 3) [27].

3.4. Multimodal Imaging. Molecular imaging of cancers has been characterized based on the sensitivity and selectivity of a single cancer probe targeting a cancer biomarker of a specific cancer cell line. The goal of multimodality imaging is to combine the best features of separate modalities. Researchers had designed a multimodal nanoparticle-based simultaneously multiple aptamers and RGD targeting (SMART) cancer probe targeting multiple cancer biomarkers to enhance the specificity and signal sensitivity for various cancers. The SMART probe was conjugated to a multimodal nanoparticle that is capable of concurrent fluorescence, MRI, and radionuclide imaging. Unlike a single aptamer or peptide-conjugated multimodal cancer probe targeting a single cancer biomarker, the multimodal SMART cancer probe simultaneously targets multiple cancer biomarkers in various cancer cells, resulting in enhanced targeting efficacy and signals [56].

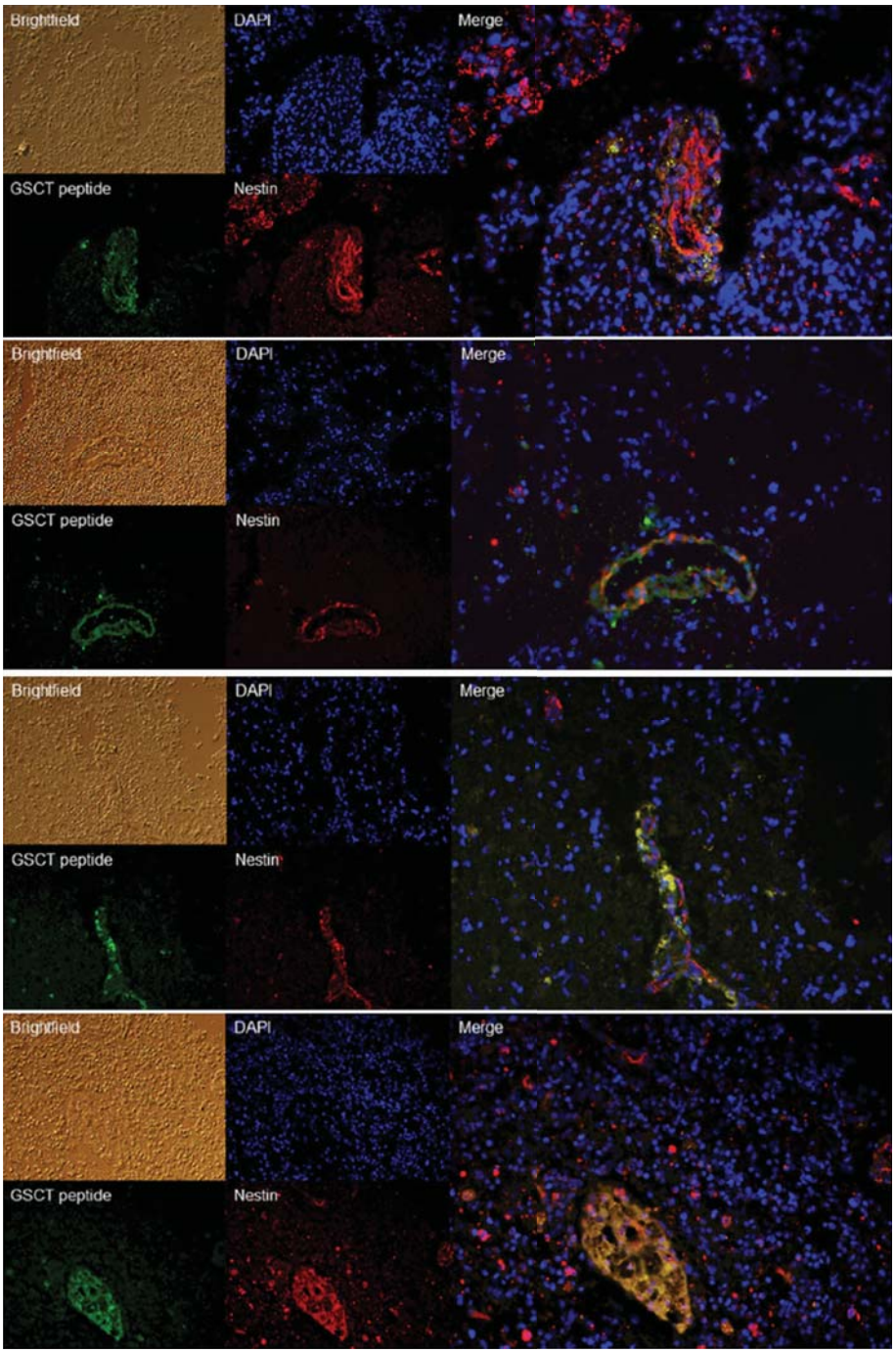

Figure 2: GSCT selectively binds Nestin-positive tumor cells in human GBM tissues. Paraffin-embedded human GBM tissue sections were stained with a biotinylated-GSCT (B-GSCT) peptide (Green) and Nestin antibody (Red). This immunofluorescence analysis revealed that most B-GSCT peptide-targeting tumor cells are colocalized with Nestin-positive tumor cells [27]. With reprint permission from Elsevier.

Garzia et al. demonstrated that miR-199b-5p overexpression blocks expression of several CSC genes and impairs the engrafting potential of medulloblastoma tumor (MB) stem-cell-like ($CD133^+$) subpopulation of cells in the cerebellum of nude mice. They used PET-CT fusion imaging to investigate the relationship between miRNAs targeting the MB tumors. The expression of miR199b-5p can deplete this tumor cell compartment, indicating the use of miRNA as an interesting therapeutic approach for the targeting of CSCs in brain tumors [57].

An important recent development is the concept of multimodality fusion reporter systems. Researchers have described fusion modality reporter genes for whole mouse body fluorescent, bioluminescent, and nuclear imaging [58].

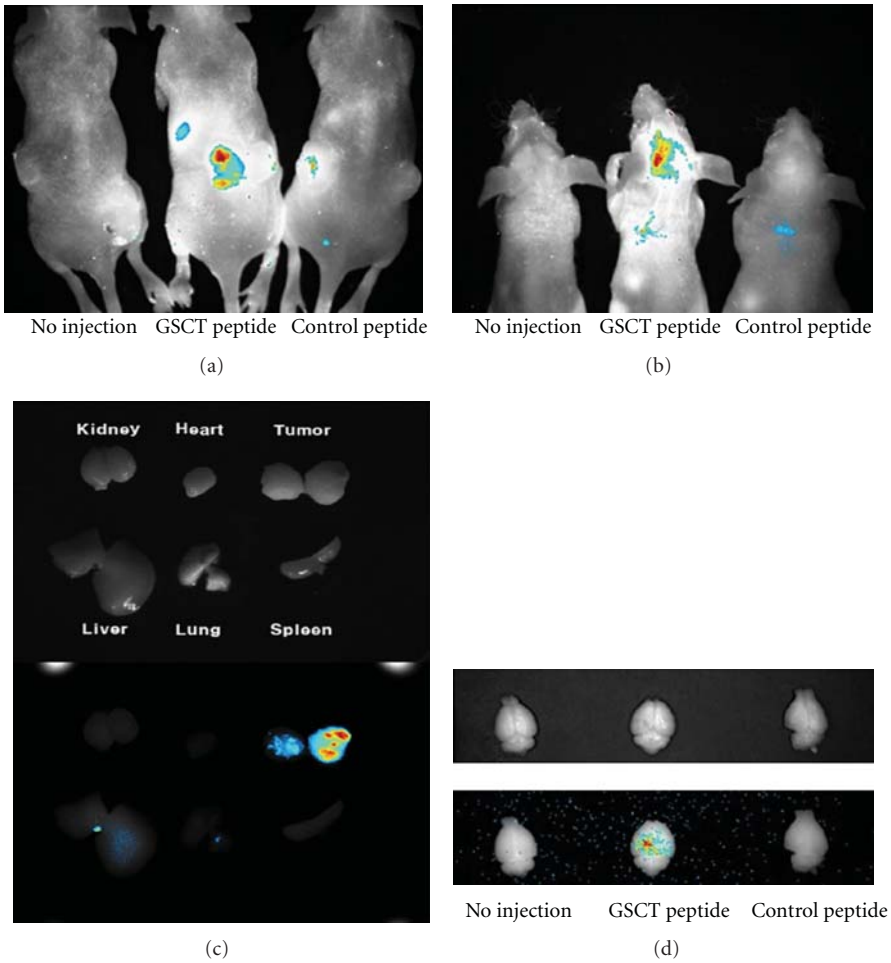

Figure 3: Homing of GSCT peptide to GSC-derived tumors in vivo [27]. (a) In vivo biodistribution of GSCT peptide was examined by intravenous injection of Q-dot 800-conjugated GSCT (QGSCT) or control peptide in mice bearing subcutaneous tumors derived from the injection of Id4-driven mouse GSCs. Whole-body biofluorescence images were obtained 24 h after injection of Q-GSCT and Q-control peptides. (b) In vivo biodistribution of Q-Dot 800-conjugated GSCT or control peptide in orthotopic brain tumor models. Whole-body biofluorescence images were obtained 4 days after injection of Q-GSCT and Q-control peptides in mice bearing orthotopic brain tumors derived from the injection of Id4-driven mouse GSCs. (c) Fluorescence images of Q-GSCT peptides in tumors and organs extracted from mice bearing subcutaneous tumors are shown in Figure 3(a). (d) Fluorescence images of Q-GSCT peptides in brains extracted from mice bearing orthotopic tumors are shown in Figure 3(b). With reprint permission from Elsevier.

The development of multifunctional reporter platforms has the potential to provide both diagnostic and therapeutic capabilities in cancer treatment.

4. Discussion

Researchers have tried for decades to understand cancer development in the context of therapeutic strategies. The CSC model provides an attractive concept to explain why cancer contains cells resistant to chemo- and radiotherapies [2, 3]. A minority population of CSCs has the ability to self-renew, whereas the majority of cancer cells have the limited or no ability to proliferate in breast and brain tumors [59]. There has been acceptance of the idea that the remaining tumor cells after anticancer therapy have a distinct molecular phenotype that confers resistance to the therapies [2, 3].

CSCs are tumorigenic and possess the metastatic phenotype. Interestingly, many studies show that cells of CSC phenotypes also express stem/progenitor-associated genes which may suggest the possible link between CSCs and normal stem cells. A comparison of the biomarkers of CSC and normal stem cell was shown in Table 1. CSCs share common features with normal stem cells, most obviously the characteristic of self-renewal. Current knowledge indicates that a specialized microenvironment, the stem cell niche, is one of the factors regulating normal stem cell maintenance and self-renewal [59]. In analogy to the normal intestinal stem cell niche, researchers conclude that there is a CSC niche that is probably composed of a combination of stromal cells and more differentiated progeny and delivers crucial signals to the CSCs. Tumors may arise through a series of mutations that disrupt normal development

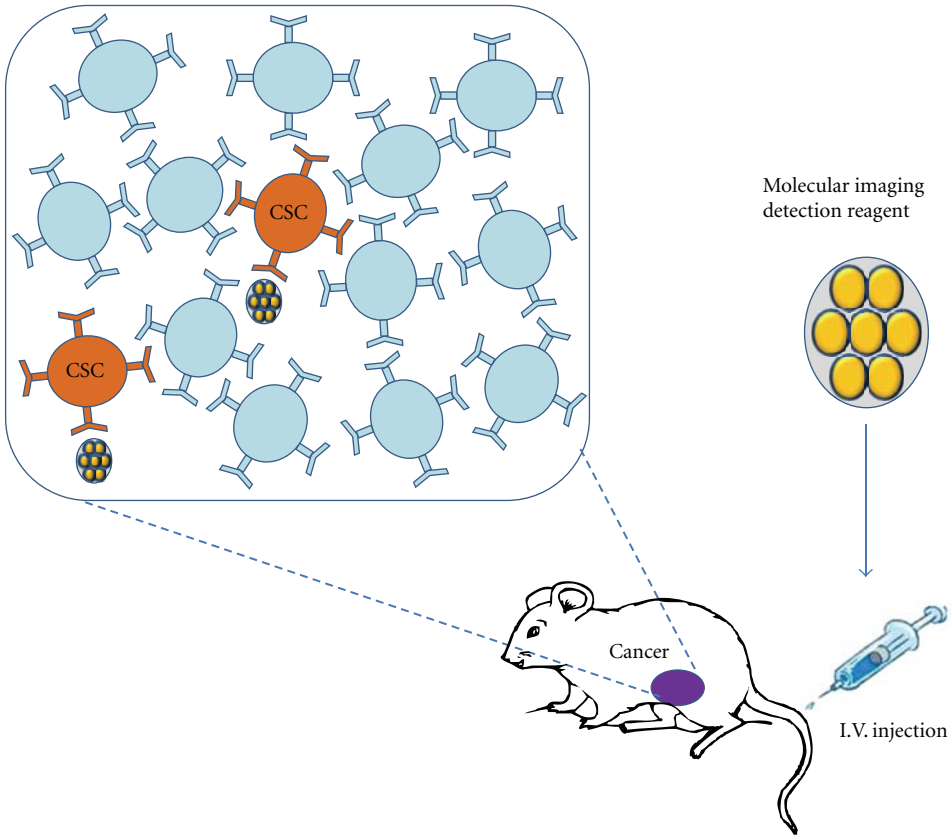

Figure 4: Paradigm of the application of molecular imaging in CSCs detection based on cancer stem cell model. Red and blue indicate cancer stem cells (CSCs) and non-CSCs, respectively.

pathways, and a population of continuously self-renewing cells must arise [59]. Genes (e.g., Bmil 1) that program self-renewal rather than differentiation are likely to be candidate oncogenes [60–62]. Exploring the mechanism regulating stemness features of CSCs in the tumorigenic process will benefit developing treatment aimed at destroying CSCs without adversely affecting normal stem cell characteristics.

CSCs may often constitute only a small population of tumor mass thus, there is a need for imaging modalities and probes that provide high-sensitivity and high-imaging resolution. Molecular imaging is emerging as a promising strategy with which to shed light on the clinical application. This technique has the potential to become a powerful technique for monitoring the history and the fate of CSCs and for evaluating response to therapy. The precise real-time imaging of CSCs in tumors at molecular and cellular levels is challenging. Single-luciferase models require animals to be injected with the luciferin substrate, and the limitation of the signal in xenograft model of human neoplasia requires expression of luciferase is at least 2,500 cells for proper detection [63]. The good option may be concurrently employing more than one fluorophore and highly sensitive detectors. MRI detects the presence of SPIO contrast agents regardless of whether the cells are alive or dead; it is also challenged to count the number of SPIO labeld cells in MRI on account of the contrast agent dilution during cell division, transfer to other cells, and the exist of other source of iron in tissue. To overcome limitations, the multimodality of imaging techniques (e.g., magnetic and optical) can be developed for applications in medicine.

For noninvasive imaging of CSCs as well as CSC-specific therapies, the targeting of cell surface proteins using antibodies or other receptor ligands is particularly relevant (Figure 4). Noninvasive imaging of CSCs would be critical in the management of malignant cancer disease, for example, for determining prognosis of patients, using as a diagnosis parameter, and monitoring therapeutic efficacy.

5. Conclusions

There is increasing evidence to support the existence of CSC that is identified by several markers, including CD133, CD44, CD24, and ALDH, or by selecting for the SP cells. Interestingly, no single marker is exclusively expressed by CSCs. Thus, in order to identify CSCs, the various combinations of different biomarkers may be possible. Targeting and elimination of the small population of CSCs hold attractive cancer treatment and avoid tumor recurrence.

Tracking of CSCs in vivo may facilitate the search for novel therapeutic approaches that improve radiation therapy outcome. The development of therapeutic agents specifically targeting CSCs together with a revised radiotherapy or chemotherapy protocol will alter the traditional poor

prognosis of tumor patients. Novel drugs that selectively target CSCs offer great promise for more completed cancer treatment; however, designing and finding such drugs remain a great challenge.

Still, much work needs to be done in order to completely understand the origin of CSCs, as well as the mechanisms regulating their stemness features in the tumorigenic process and their increased resistance to chemotherapy and radiotherapy. Although the tracking of circulating CSCs is still hampered by technological challenges, we expect personalized diagnosis and therapy of cancers to be established based on increased studies and applications of molecular imaging of biomarkers in cancer stem-like cells.

Abbreviations

CSCs:	Cancer stem cells
CICs:	Cancer initiating cells
T-ICs:	Tumor-initiating cells
SP:	Side population
PSCA:	Prostate stem cell antigen
EpCAM:	Epithelial cell adhesion molecule
ESA:	Epithelial-specific antigen
PET:	Positron emission tomography
BLI:	Bioluminescence imaging
MRI:	Magnetic resonance imaging
TCL-SPIONs:	Thermally cross-linked superparamagnetic iron oxide nanoparticles
FMT:	Near-infrared fluorescence molecular tomography.

Conflict of Interests

The authors declare that they have no conflict of interests.

Acknowledgments

This work is partly sponsored by Grants from the Zhejiang Provincial Natural Science Foundation of China (Z2110230), Health Bureau of Zhejiang Province (2010ZA075, 2011ZDA-013), National Science Foundation of China (NSFC) (nos. 81101023, 81170306, 81173468), and Ministry of Science and Technology of China (2011CB504400, 2012BAI13B06).

References

[1] R. Siegel, E. Ward, O. Brawley, and A. Jemal, "Cancer statistics, 2011: the impact of eliminating socioeconomic and racial disparities on premature cancer deaths," *CA Cancer Journal for Clinicians*, vol. 61, no. 4, pp. 212–236, 2011.

[2] J. R. Benson, I. Jatoi, M. Keisch, F. J. Esteva, A. Makris, and V. C. Jordan, "Early breast cancer," *The Lancet*, vol. 373, no. 9673, pp. 1463–1479, 2009.

[3] K. Kai, Y. Arima, T. Kamiya, and H. Saya, "Breast cancer stem cells," *Breast Cancer*, vol. 17, no. 2, pp. 80–85, 2010.

[4] A. Kabashima, H. Higuchi, H. Takaishi et al., "Side population of pancreatic cancer cells predominates in TGF-β-mediated epithelial to mesenchymal transition and invasion," *International Journal of Cancer*, vol. 124, no. 12, pp. 2771–2779, 2009.

[5] C. Hirschmann-Jax, A. E. Foster, G. G. Wulf et al., "A distinct "side population" of cells with high drug efflux capacity in human tumor cells," *Proceedings of the National Academy of Sciences of the United States of America*, vol. 101, no. 39, pp. 14228–14233, 2004.

[6] C. Hirschmann-Jax, A. E. Foster, G. G. Wulf, M. A. Goodell, and M. K. Brenner, "A distinct "side population" of cells in human tumor cells: implications for tumor biology and therapy," *Cell Cycle*, vol. 4, no. 2, pp. 203–205, 2005.

[7] C. T. Jordan, M. L. Guzman, and M. Noble, "Cancer stem cells," *New England Journal of Medicine*, vol. 355, no. 12, pp. 1253–1261, 2006.

[8] J. E. Visvader and G. J. Lindeman, "Cancer stem cells in solid tumours: accumulating evidence and unresolved questions," *Nature Reviews Cancer*, vol. 8, no. 10, pp. 755–768, 2008.

[9] L. Ricci-Vitiani, D. G. Lombardi, E. Pilozzi et al., "Identification and expansion of human colon-cancer-initiating cells," *Nature*, vol. 445, no. 7123, pp. 111–115, 2007.

[10] C. A. O'Brien, A. Pollett, S. Gallinger, and J. E. Dick, "A human colon cancer cell capable of initiating tumour growth in immunodeficient mice," *Nature*, vol. 445, no. 7123, pp. 106–110, 2007.

[11] T. Lapidot, C. Sirard, J. Vormoor et al., "A cell initiating human acute myeloid leukaemia after transplantation into SCID mice," *Nature*, vol. 367, no. 6464, pp. 645–648, 1994.

[12] D. Bonnet and J. E. Dick, "Human acute myeloid leukemia is organized as a hierarchy that originates from a primitive hematopoietic cell," *Nature Medicine*, vol. 3, no. 7, pp. 730–737, 1997.

[13] S. K. Singh, C. Hawkins, I. D. Clarke et al., "Identification of human brain tumour initiating cells," *Nature*, vol. 432, no. 7015, pp. 396–401, 2004.

[14] M. T. Chiao, Y. C. Yang, W. Y. Cheng, C. C. Shen, and J. L. Ko, "CD133$^+$ glioblastoma stem-like cells induce vascular mimicry in vivo," *Current Neurovascular Research*, vol. 8, no. 3, pp. 210–219, 2011.

[15] M. Tabuse, S. Ohta, Y. Ohashi et al., "Functional analysis of HOXD9 in human gliomas and glioma cancer stem cells," *Molecular Cancer*, vol. 10, article 60, 2011.

[16] J. Ferlay, H. R. Shin, F. Bray, D. Forman, C. Mathers, and D. M. Parkin, "Estimates of worldwide burden of cancer in 2008: GLOBOCAN 2008," *International Journal of Cancer*, vol. 127, no. 12, pp. 2893–2917, 2010.

[17] C. Ginestier, M. H. Hur, E. Charafe-Jauffret et al., "ALDH1 is a marker of normal and malignant human mammary stem cells and a predictor of poor clinical outcome," *Cell Stem Cell*, vol. 1, no. 5, pp. 555–567, 2007.

[18] M. Al-Hajj, M. S. Wicha, A. Benito-Hernandez, S. J. Morrison, and M. F. Clarke, "Prospective identification of tumorigenic breast cancer cells," *Proceedings of the National Academy of Sciences of the United States of America*, vol. 100, no. 7, pp. 3983–3988, 2003.

[19] M. Cordenonsi, F. Zanconato, L. Azzolin et al., "The hippo transducer TAZ confers cancer stem cell-related traits on breast cancer cells," *Cell*, vol. 147, no. 4, pp. 759–772, 2011.

[20] A. Eramo, F. Lotti, G. Sette et al., "Identification and expansion of the tumorigenic lung cancer stem cell population," *Cell Death and Differentiation*, vol. 15, no. 3, pp. 504–514, 2008.

[21] V. Levina, A. M. Marrangoni, R. DeMarco, E. Gorelik, and A. E. Lokshin, "Drug-selected human lung cancer stem cells: cytokine network, tumorigenic and metastatic properties," *PLoS One*, vol. 3, no. 8, Article ID e3077, 2008.

[22] M. M. Ho, A. V. Ng, S. Lam, and J. Y. Hung, "Side population in human lung cancer cell lines and tumors is enriched with

stem-like cancer cells," *Cancer Research*, vol. 67, no. 10, pp. 4827–4833, 2007.

[23] H. Iinuma, T. Watanabe, K. Mimori et al., "Clinical significance of circulating tumor cells, including cancer stem-like cells, in peripheral blood for recurrence and prognosis in patients with dukes' stage B and C colorectal cancer," *Journal of Clinical Oncology*, vol. 29, no. 12, pp. 1547–1555, 2011.

[24] L. Vermeulen, M. Todaro, F. de Sousa Mello et al., "Single-cell cloning of colon cancer stem cells reveals a multi-lineage differentiation capacity," *Proceedings of the National Academy of Sciences of the United States of America*, vol. 105, no. 36, pp. 13427–13432, 2008.

[25] P. Dalerba, S. J. Dylla, I. K. Park et al., "Phenotypic characterization of human colorectal cancer stem cells," *Proceedings of the National Academy of Sciences of the United States of America*, vol. 104, no. 24, pp. 10158–10163, 2007.

[26] L. Vermeulen, F. de Sousa E Melo, M. van der Heijden et al., "Wnt activity defines colon cancer stem cells and is regulated by the microenvironment," *Nature Cell Biology*, vol. 12, no. 5, pp. 468–476, 2010.

[27] S. Beck, X. Jin, J. Yin et al., "Identification of a peptide that interacts with Nestin protein expressed in brain cancer stem cells," *Biomaterials*, vol. 32, no. 33, pp. 8518–8528, 2011.

[28] C. Yu, Z. Yao, J. Dai et al., "ALDH activity indicates increased tumorigenic cells, but not cancer stem cells, in prostate cancer cell lines," *In Vivo*, vol. 25, no. 1, pp. 69–76, 2011.

[29] V. K. Rajasekhar, L. Studer, W. Gerald, N. D. Socci, and H. I. Scher, "Tumour-initiating stem-like cells in human prostate cancer exhibit increased NF-κB signalling," *Nature Communications*, vol. 2, article 162, 2011.

[30] P. A. Philip, M. Mooney, D. Jaffe et al., "Consensus report of the national cancer institute clinical trials planning meeting on pancreas cancer treatment," *Journal of Clinical Oncology*, vol. 27, no. 33, pp. 5660–5669, 2009.

[31] M. J. Moore, D. Goldstein, J. Hamm et al., "Erlotinib plus gemcitabine compared with gemcitabine alone in patients with advanced pancreatic cancer: a phase III trial of the National Cancer Institute of Canada Clinical Trials Group," *Journal of Clinical Oncology*, vol. 25, no. 15, pp. 1960–1966, 2007.

[32] T. Reya, S. J. Morrison, M. F. Clarke, and I. L. Weissman, "Stem cells, cancer, and cancer stem cells," *Nature*, vol. 414, no. 6859, pp. 105–111, 2001.

[33] J. Dorado, E. Lonardo, I. Miranda-Lorenzo, and C. Heeschen, "Pancreatic cancer stem cells: new insights and perspectives," *Journal of Gastroenterology*, vol. 46, no. 8, pp. 966–973, 2011.

[34] C. Li, D. G. Heidt, P. Dalerba et al., "Identification of pancreatic cancer stem cells," *Cancer Research*, vol. 67, no. 3, pp. 1030–1037, 2007.

[35] M. Rovira, S. G. Scott, A. S. Liss, J. Jensen, S. P. Thayer, and S. D. Leach, "Isolation and characterization of centroacinar/terminal ductal progenitor cells in adult mouse pancreas," *Proceedings of the National Academy of Sciences of the United States of America*, vol. 107, no. 1, pp. 75–80, 2010.

[36] M. P. Kim, J. B. Fleming, H. Wang et al., "ALDH activity selectively defines an enhanced tumor-initiating cell population relative to CD133 expression in human pancreatic adenocarcinoma," *PLoS One*, vol. 6, no. 6, Article ID e20636, 2011.

[37] B. I. Carr, "Hepatocellular carcinoma: current management and future trends," *Gastroenterology*, vol. 127, supplement 1, no. 5, pp. S218–S224, 2004.

[38] W. T. Kassahun, J. Fangmann, J. Harms, J. Hauss, and M. Bartels, "Liver resection and transplantation in the management of hepatocellular carcinoma: a review," *Experimental and Clinical Transplantation*, vol. 4, no. 2, pp. 549–558, 2006.

[39] T. K. W. Lee, A. Castilho, V. C. H. Cheung, K. H. Tang, S. Ma, and I. O. L. Ng, "CD24$^+$ liver tumor-initiating cells drive self-renewal and tumor initiation through STAT3-mediated NANOG regulation," *Cell Stem Cell*, vol. 9, no. 1, pp. 50–63, 2011.

[40] A. Hadnagy, L. Gaboury, R. Beaulieu, and D. Balicki, "SP analysis may be used to identify cancer stem cell populations," *Experimental Cell Research*, vol. 312, no. 19, pp. 3701–3710, 2006.

[41] H. Liu, M. R. Patel, J. A. Prescher et al., "Cancer stem cells from human breast tumors are involved in spontaneous metastases in orthotopic mouse models," *Proceedings of the National Academy of Sciences of the United States of America*, vol. 107, no. 42, pp. 18115–18120, 2010.

[42] J. V. Leyton, T. Olafsen, E. J. Lepin et al., "Humanized radioiodinated minibody for imaging of prostate stem cell antigen-expressing tumors," *Clinical Cancer Research*, vol. 14, no. 22, pp. 7488–7496, 2008.

[43] R. McClelland, E. Wauthier, T. Tallheden, L. M. Reid, and E. Hsu, "In Situ labeling and magnetic resonance imaging of transplanted human hepatic stem cells," *Molecular Imaging and Biology*, vol. 13, no. 5, pp. 911–922, 2011.

[44] C. Tsurumi, N. Esser, E. Firat et al., "Non-invasive in vivo imaging of tumor-associated cd133/prominin," *PLoS One*, vol. 5, no. 12, Article ID e15605, 2010.

[45] M. Hubank and D. G. Schatz, "Identifying differences in mRNA expression by representational difference analysis of cDNA," *Nucleic Acids Research*, vol. 22, no. 25, pp. 5640–5648, 1994.

[46] R. E. Reiter, Z. Gu, T. Watabe et al., "Prostate stem cell antigen: a cell surface marker overexpressed in prostate cancer," *Proceedings of the National Academy of Sciences of the United States of America*, vol. 95, no. 4, pp. 1735–1740, 1998.

[47] Z. Gu, G. Thomas, J. Yamashiro et al., "Prostate stem cell antigen (PSCA) expression increases with high gleason score, advanced stage and bone metastasis in prostate cancer," *Oncogene*, vol. 19, no. 10, pp. 1288–1296, 2000.

[48] J. V. Leyton, T. Olafsen, M. A. Sherman et al., "Engineered humanized diabodies for microPET imaging of prostate stem cell antigen-expressing tumors," *Protein Engineering, Design and Selection*, vol. 22, no. 3, pp. 209–216, 2009.

[49] E. J. Lepin, J. V. Leyton, Y. Zhou et al., "An affinity matured minibody for PET imaging of prostate stem cell antigen (PSCA)-expressing tumors," *European Journal of Nuclear Medicine and Molecular Imaging*, vol. 37, no. 8, pp. 1529–1538, 2010.

[50] C. A. Foss, J. J. Fox, G. Feldmann et al., "Radiolabeled anti-claudin 4 and anti-prostate stem cell antigen: initial imaging in experimental models of pancreatic cancer," *Molecular Imaging*, vol. 6, no. 2, pp. 131–139, 2007.

[51] Y. Yoshii, T. Furukawa, Y. Kiyono et al., "Internal radiotherapy with copper-64-diacetyl-bis (N^4-methylthiosemicarbazone) reduces CD133$^+$ highly tumorigenic cells and metastatic ability of mouse colon carcinoma," *Nuclear Medicine and Biology*, vol. 38, no. 2, pp. 151–157, 2011.

[52] O. K. Okamoto and J. F. Perez, "Targeting cancer stem cells with monoclonal antibodies: a new perspective in cancer therapy and diagnosis," *Expert Review of Molecular Diagnostics*, vol. 8, no. 4, pp. 387–393, 2008.

[53] E. K. Lim, H. O. Kim, E. Jang et al., "Hyaluronan-modified magnetic nanoclusters for detection of CD44-overexpressing breast cancer by MR imaging," *Biomaterials*, vol. 32, no. 31, pp. 7941–7950, 2011.

[54] A. Z. Wang, V. Bagalkot, C. C. Vasilliou et al., "Superparamagnetic iron oxide nanoparticle-aptamer bioconjugates for combined prostate cancer imaging and therapy," *ChemMedChem*, vol. 3, no. 9, pp. 1311–1315, 2008.

[55] E. Vlashi, K. Kim, C. Lagadec et al., "In vivo imaging, tracking, and targeting of cancer stem cells," *Journal of the National Cancer Institute*, vol. 101, no. 5, pp. 350–359, 2009.

[56] H. Y. Ko, K. J. Choi, C. H. Lee, and S. Kim, "A multimodal nanoparticle-based cancer imaging probe simultaneously targeting nucleolin, integrin $\alpha v\beta 3$ and tenascin-C proteins," *Biomaterials*, vol. 32, no. 4, pp. 1130–1138, 2011.

[57] L. Garzia, I. Andolfo, E. Cusanelli et al., "MicroRNA-199b-5p impairs cancer stem cells through negative regulation of HES1 in medulloblastoma," *PLoS One*, vol. 4, no. 3, Article ID e4998, 2009.

[58] V. Ponomarev, M. Doubrovin, I. Serganova et al., "A novel triple-modality reporter gene for whole-body fluorescent, bioluminescent, and nuclear noninvasive imaging," *European Journal of Nuclear Medicine and Molecular Imaging*, vol. 31, no. 5, pp. 740–751, 2004.

[59] M. F. Clarke and M. Fuller, "Stem cells and cancer: two faces of eve," *Cell*, vol. 124, no. 6, pp. 1111–1115, 2006.

[60] A. V. Molofsky, R. Pardal, T. Iwashita, I. K. Park, M. F. Clarke, and S. J. Morrison, "Bmi-1 dependence distinguishes neural stem cell self-renewal from progenitor proliferation," *Nature*, vol. 425, no. 6961, pp. 962–967, 2003.

[61] I. K. Park, D. Qian, M. Kiel et al., "Bmi-1 is required for maintenance of adult self-renewing haematopoietic stem cells," *Nature*, vol. 423, no. 6937, pp. 302–305, 2003.

[62] J. Lessard and G. Sauvageau, "Bmi-1 determines the proliferative capacity of normal and leukaemic stem cells," *Nature*, vol. 423, no. 6937, pp. 255–260, 2003.

[63] T. J. Sweeney, V. Mailander, A. A. Tucker et al., "Visualizing the kinetics of tumor-cell clearance in living animals," *Proceedings of the National Academy of Sciences of the United States of America*, vol. 96, no. 21, pp. 12044–12049, 1999.

[64] H. Niwa, J. I. Miyazaki, and A. G. Smith, "Quantitative expression of Oct-3/4 defines differentiation, dedifferentiation or self-renewal of ES cells," *Nature Genetics*, vol. 24, no. 4, pp. 372–376, 2000.

[65] J. A. Thomson, "Embryonic stem cell lines derived from human blastocysts," *Science*, vol. 282, no. 5391, pp. 1145–1147, 1998.

[66] C. Calabrese, H. Poppleton, M. Kocak et al., "A perivascular niche for brain tumor stem cells," *Cancer Cell*, vol. 11, no. 1, pp. 69–82, 2007.

[67] S. Pece, D. Tosoni, S. Confalonieri et al., "Biological and molecular heterogeneity of breast cancers correlates with their cancer stem cell content," *Cell*, vol. 140, no. 1, pp. 62–73, 2010.

[68] P. Eirew, J. Stingl, A. Raouf et al., "A method for quantifying normal human mammary epithelial stem cells with in vivo regenerative ability," *Nature Medicine*, vol. 14, no. 12, pp. 1384–1389, 2008.

Hindawi Publishing Corporation
Journal of Biomedicine and Biotechnology
Volume 2012, Article ID 412486, 11 pages
doi:10.1155/2012/412486

Review Article

SPECT Molecular Imaging in Parkinson's Disease

Ling Wang,[1,2,3,4,5] Qi Zhang,[2] Huanbin Li,[2] and Hong Zhang[1,3,4,5]

[1] *Department of Nuclear Medicine, Second Affiliated Hospital, School of Medicine, Zhejiang University, 88 Jiefang Road, Hangzhou, Zhejiang 310009, China*
[2] *Department of Nuclear Medicine, Wenzhou Medical College, Wenzhou, China*
[3] *Zhejiang University Medical PET Center, Zhejiang University, Hangzhou, China*
[4] *Institute of Nuclear Medicine and Molecular Imaging, Zhejiang University, Hangzhou, China*
[5] *Key Laboratory of Medical Molecular Imaging of Zhejiang Province, Hangzhou, China*

Correspondence should be addressed to Hong Zhang, hzhang21@gmail.com

Received 3 January 2012; Accepted 29 January 2012

Academic Editor: Mei Tian

Parkinson's disease (PD) is a common disorder, and the diagnosis of Parkinson's disease is clinical and relies on the presence of characteristic motor symptoms. The accuracy of the clinical diagnosis of PD is still limited. Functional neuroimaging using SPECT technique is helpful in patients with first signs of parkinsonism. The changes detected may reflect the disease process itself and/or compensatory responses to the disease, or they may arise in association with disease- and/or treatment-related complications. This paper addresses the value of SPECT in early differential diagnosis of PD and its potential as a sensitive tool to assess the pathophysiology and progression, as well as the therapeutic efficacy of PD.

1. Introduction

PD is a common neurodegenerative disorder characterized by the motor features of rigidity, tremors, akinesia, and changes in speech and gait which are associated with the loss of dopaminergic neurons in the substantia nigra pars compacta and the subsequent deficiency in striatal dopaminergic system. It has prevalence of 1-2 per 1,000 among the general population and of up to 2% among people aged over 65 years. Parkinson's causes are unknown but genetics, aging, and toxins are being researched. The pathophysiological hallmark of PD is a slow, progressive degeneration of the nigrostriatal dopaminergic system. The widely accepted subcellular factor which underlies PD neuropathology is the presence of Lewy bodies [1] with characteristic inclusions of aggregated alpha-synuclein [2–4]. A recent study revealed that PD specific brain pathology extends far beyond the nigrostriatal dopaminergic system and affects widespread brain areas, including the olfactory system, autonomic and gain setting brainstem nuclei, and the cerebral cortex [5]. Physiological imaging techniques such as positron emission tomography (PET) or SPECT provide the means for detecting *in vivo* metabolic and neurochemical changes of PD.

Motor symptoms such as tremor at rest, akinesia, rigidity, and postural instability are the cardinal signs in PD [6]. The type and severity of symptoms experienced by a person with PD vary with each individual and the stage of the disease. PD is the most common cause of parkinsonism. There are also many nonmotor features of PD including behavioral and psychiatric problems such as dementia [7], fatigue [8], anxiety [9] and depression [10], autonomic dysfunction [11], addiction and compulsion [12], psychosis [13], olfactory dysfunction [14], and cognitive impairment [10]. These clinical features also occur in other neurodegenerative diseases and by dopamine receptor antagonist drugs, which means that with this main clinical application it is hard to diagnose patients with mild, incomplete, or uncertain parkinsonism [15]. The United Kingdom Parkinson's Disease Society Brain Bank clinical diagnostic criteria can improve diagnostic accuracy [16]; still, the diagnosis and management of PD can be a challenge.

The diagnosis of PD is based on clinical criteria, but misdiagnosis is as high as 25% of cases as confirmed by anatomic-pathologic studies. Because the diagnosis of PD is entirely clinical, the diagnosis and treatment may be delayed

for years until functional disability occurs. SPECT is an aid that can help diagnosing the disease earlier.

2. Imaging Agent of SPECT for PD

The ligands used for SPECT belong to a group of compounds derived from cocaine that bind to the dopamine transporter and include IPT, TRODAT-1, and FP-CIT tagged with either iodine-123 (T1/2 = 13.2 h) or technetium-99 m (T1/2 = 6 h) radioisotopes. Tracers used for SPECT imaging of PD patients are presented in Table 1.

Specific SPECT ligands for DAT (FP-CIT, beta-CIT, IPT, TRODAT-1) imaging provide a marker for presynaptic neuronal degeneration [17]. Postsynaptic receptor density is explored with dopamine receptor ligands, notably of the D2 type [18].

Unlike PET, there is no need for an on-site cyclotron or for radiochemistry facilities due to a longer half-life. SPECT studies have the advantage of using an industrial production of tracers. The reduced cost of radiotracer synthesis permits the investigation of a larger number of patients by SPECT than by PET.

^{123}I-β-CIT. ^{123}I-β-CIT is a radiotracer which binds with nanomolar affinity to the serotonin transporter. It has a protracted period of striatal uptake enabling imaging 14–24 hours after injection for stable quantitative measures of dopamine transporters [19].

^{123}I-FP-CIT. ^{123}I-FP-CIT is an analogue of ^{123}I-β-CIT. It has been shown to achieve peak tracer uptake in the brain within hours after injection and to provide greater selectivity for the dopamine transporter. ^{123}I-FP-CIT washed out from striatal tissue is 15–20 times faster than that of ^{123}I-β-CIT [19]. A clear decline in ^{123}I-FP-CIT binding was found with aging, amounting to 9.6%/decade in the control group [20].

^{123}I-IPT. ^{123}I-IPT is a new cocaine analogue which allows the presynaptic dopamine transporters to be imaged with SPECT as early as 1-2 h after injection [21].

^{125}I/^{123}I-PE21. PE2I, a cocaine derivative, has good affinity for the DAT. ^{125}I-PE2I has revealed very intense and selective binding in the basal ganglia [22]. It is a highly potent inhibitor of cloned DAT compared with GBR 12935 and provided a useful tool for further investigations in cells transfected with cDNA encoding the DAT [23]. PE2I is a relatively new radioligand that has about 10-fold higher *in vitro* selectivity for the DAT than for the serotonin transporter (SERT) compared to ^{123}I-FP-CIT [24]. Further, ^{123}I-PE2I has faster kinetics than ^{123}I-FP-CIT. It is currently to be considered the best radioligand for imaging the DAT in the human brain with SPECT.

^{99}Tc^{m}-TRODAT-1. ^{99}Tc^{m}-TRODAT-1 is a recently developed radiotracer that selectively binds to the dopamine transporters, which are significant because loss of these transporters corresponds with a loss of dopaminergic neurons. It is a potential agent for DAT SPECT [25].

Table 1: The tracer used for SPECT in Parkinson's disease.

Biological variable	Radiotracer
Dopamine reuptake (dopamine transport)	^{123}I-β-CIT, ^{123}I-FP-β-CIT, ^{123}I-IPT (presynaptic dopamine transporter), ^{123}I-Altropane, ^{123}I-β-PE2I ^{99}Tc^{m}-TRODAT-1
D2 dopamine receptor	^{123}I-Iodospiperone, ^{123}I-Iodobenzamide (123I-IBZM), (postsynaptic dopamine D2 receptor) ^{123}I-Iodolisuride, 123I-IBF, ^{123}I-Epidepride (extrastriatal DA receptors)

^{123}I-IBZM. ^{123}I-IBZM is a central nervous system (CNS) D-2 dopamine receptor imaging agent, and it has a high concentration in basal ganglia of brain [26].

^{123}I-IBF. ^{123}I-IBF is an IBZM analogue. This agent concentrated in the striatum region and displayed a remarkably high target-to-nontarget ratio [27] and early time of peak uptake [28]. A study using P450 gene expression systems indicates that ^{123}I-IBF is enzymatically metabolized in the liver and rapidly excreted in the urine [29]. It is a potential agent for imaging D-2 dopamine receptors [30].

3. The Use of SPECT Molecular Imaging in PD

3.1. The Course and the Pathogenesis of PD. Brain SPECT imaging of DAT with specific radioligands provides a useful tool of *in vivo* investigation of the pathogenesis of PD, and it is a sensitive method for examining the integrity of the presynaptic dopaminergic system [15]. Cerebral and extracranial Lewy-body-type degeneration in PD does not develops independently from each other but develop in a strongly coupled manner. The cerebral and extracranial changes are driven by at least similar pathomechanisms [31]. Patients with PD have markedly reduced DAT levels in striatum, which correlated with disease severity and disease progression [32], whereas postsynaptic striatal D2 receptors are upregulated [33]. Similarly, another study reported that the mean ^{123}I-IBZM striatal-occipital ratio of binding was significantly higher in PD patients than in controls. In PD patients, higher values were found contralateral to the clinically most affected side, suggesting D2 receptor upregulation and the reverse was seen using ^{123}I-FP-CIT SPECT [34]. Dual isotope imaging using ^{99}Tc^{m}-TRODAT-1 and ^{123}I-IBZM is also a useful means in evaluating the changes of both pre- and postsynaptic dopamine system in a primate model of parkinsonism [35].

There was a significant association of visually analyzed shapes of the striatum in FP-CIT SPECT and clinical PD subtype. It suggested that factors other than nigrostriatal degeneration may contribute to disease severity [36]. One study including 122 patients confirmed neuropathological models for reduced dopaminergic projection to the dorsal putamen in akinetic-rigid patients as well as the lateral putamen

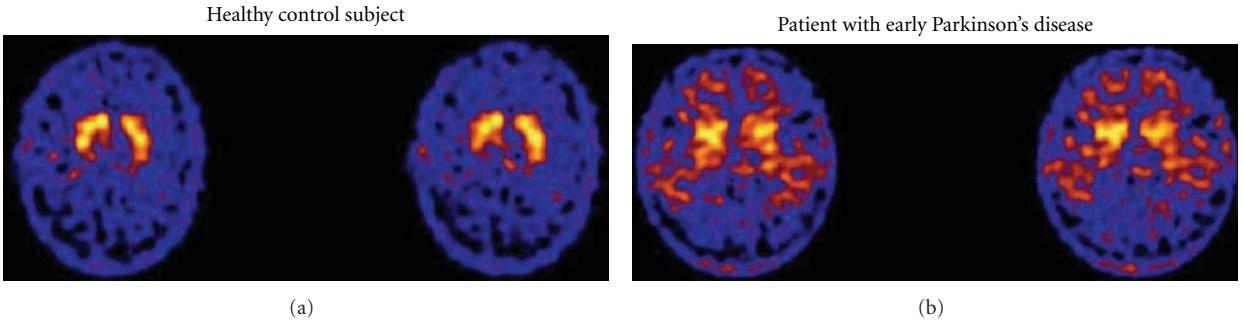

Figure 1: TRODAT-1 SPECT images of a healthy control (a) and a patient with early PD (b). The patient with early PD shows decreased TRODAT-1 uptake in the striatum compared to the control, particularly in the posterior putamen [45].

and caudate nucleus in tremor-dominant patients *in vivo* [37], and the serotonergic system is suggested to be implicated in PD [38]. Furthermore, another study showed that SERT-dependent ^{123}I-FP-CIT uptake may allow a more comprehensive assessment of neurochemical disturbances in degenerative parkinsonisms [39]; this study suggested that the neurodegenerative process extends beyond nigrostriatal system and affects serotoninergic neurons in parkinsonisms.

3.2. Early Diagnosis of PD. Since the *in vivo* molecular imaging techniques using SPECT have been introduced, the diagnosis of PD became more reliable by assessing dopaminergic and even nondopaminergic systems. SPECT is a very sensitive technique to detect nigrostriatal degeneration in PD. Various radiotracers have been used in the diagnosis of PD. DAT imaging is abnormal even in the earliest clinical presentation of PD [15]. A study using ^{123}I-β-CIT found that the relative uptake reduction in the hemi-PD patients was greater in the putamen than in the caudate in patients with early PD and suggested that it may be useful in identifying individuals with developing dopaminergic pathology before onset of motor symptoms [40].

It was reported that ^{123}I-β-CIT SPECT was 100% sensitive and specific for the diagnosis in younger patients (age <55 years). In older patients (age >55 years), specificity was substantially lower (68.5%) [41]. More recently, a prospective, longitudinal study using ^{123}I-FP-CIT had investigated 99 patients with tremor and/or parkinsonism over 3 years, and the results showed a mean sensitivity of 78% and a specificity of 97% [42]. A 2-year followed-up SPECT study using ^{99}Tc^{m}-TRODAT-1 was performed in patients with clinically unclear Parkinsonian syndromes (CUPSs) and found that the rate of disagreement of SPECT in the patients was of 20%. The sensitivity of this technique was 100%, and specificity was 70%. It indicated that TRODAT-1 helps the diagnosis of patients with CUPS [43]. DAT SPECT is sensitive enough to detect a loss of nigrostriatal neurons *in vivo* even in preclinical phases of sporadic PD.

^{123}I-FP-CIT SPECT has been successfully used to detect the loss of dopaminergic nigrostriatal neurons in Parkinson's disease at an early stage. But the results reported were controversial. Tissingh et al. reported that striatal ^{123}I-FP-CIT uptake is markedly decreased in PD, more in the putamen than in the caudate nucleus, and the mean reduction in the putamen and caudate nucleus was 57% and 29% of the control mean, respectively. However, no significant correlations were found between striatal ^{123}I-FP-CIT binding ratios and disease severity [20]. Spiegel et al. found that the striatal FP-CIT binding correlated significantly with the motor part of the unified Parkinson's disease rating scale (UPDRS) but not with age, disease duration, or gender [44]. Another study indicated that in patients with PD, the striatum, caudate, and putamen uptake was correlated with disease severity assessed by UPDRS and duration of disease [36]. More studies are needed to confirm these findings.

^{99}Tc^{m}-TRODAT-1 study including 29 patients with early PD and 38 healthy volunteers found that compared to controls, the uptake in caudate and anterior and posterior putamen values were significantly decreased in PD patients (Figure 1). Using the posterior putamen as the main region of interest resulted in the greatest accuracy sensitivity 79% and specificity 92% [45]. Patients with unilateral PD showed a bilateral loss of striatal DA transporters [46]. A study using semiquantitative ^{123}I-FP-CIT SPECT detected a bilateral dopaminergic deficit in early PD with unilateral symptoms and preclinical DAT loss in the ipsilateral striatal binding, corresponding to the side not yet affected by motor signs. It suggested that semi-quantitative analysis may be used to diagnose PD at early stage as well as to identify individuals developing bilateral dopaminergic damage [47]. The decrease of striatal uptake contralateral to the more affected side of the body was more prominent compared to the ipsilateral side [48]. Moreover, another study showed a significant loss of putaminal uptake ipsilateral to the symptoms was found in the stage I group compared with the healthy volunteers [49]. The mean reduction of binding was found in the order of putamen and caudate nucleus.

DAT imaging is a sensitive method to detect presynaptic dopamine neuronal dysfunction. Normal DAT-SPECT can be used to exclude underlying true nigrostriatal dysfunction [50].

SPECT also contributes to the assessment of the nonmotor symptoms of PD. MIBG was used in the diagnosis of damaged tissue of the heart. However, Sawada et al. [43] found that a reduction in MIBG cardiac accumulation reflects the systemic pathological process of the disease. Both

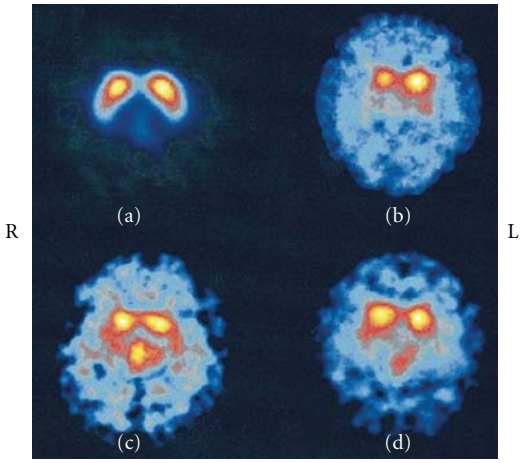

Figure 2: Transverse ^{123}I-β-CIT images. (a) The image from a healthy control. (b) in PD patient the uptake is markedly reduced, with putamen more affected than caudate, and the right striatum (opposite to the side of more severe symptoms) showing the largest dopamine transporter (DAT) loss. (c) In MSA-striatonigral degeneration (MSA-SND) patient, the uptake is significantly reduced in both caudate and putamen and indicates more symmetric loss of DAT. (d) In the MSA-Shy-Drager syndrome (SDS) patient, the uptake is also significantly reduced, with putamen more affected than caudate; the loss of DAT appears to be symmetric [64].

early and delayed images showed that the heart to mediastinum ratios were significantly lower in the PD group than in the non-PD group [51].

Sakakibara et al. [52] first reported the correlation of urinary dysfunction with nigrostriatal dopaminergic deficit in PD, which was studied by ^{123}I-β-CIT SPECT. The tracer uptake in patients with urinary dysfunction was significantly reduced than in those without urinary dysfunction

3.3. Differential Diagnosis of PD. Clinical features of PD may be shared with other disorders; thus, the differential diagnosis of PD is extensive. Idiopathic Parkinson's disease is associated with Lewy body degeneration of nigrostriatal dopaminergic neurons [53]. Atypical parkinsonian syndromes (APSs) such as multiple system atrophy (MSA), progressive supranuclear palsy (PSP), and corticobasal degeneration are characterized by poor response to antiparkinsonian medication and rapid clinical deterioration, which one often confused with PD. Other diseases, for example, drug-induced parkinsonism (DIP), essential tremor (ET), vascular parkinsonism (VP), or Dementia with Lewy bodies (DLBs) may also share common features with PD.

ET is a slowly progressive neurological disorder. DIP is developed when patients are treated with neuroleptic or dopamine receptor blocking agents. In most patients, Parkinsonism is reversible upon stopping the offending drug, though it may take several months to resolve fully but in some patients it may even persist. The differentiation between PD and DIP is difficult to assess on clinical grounds alone.

Functional imaging of the DAT defines integrity of the dopaminergic system, and a normal scan suggests an alternative diagnosis such as ET, VP (unless there is focal basal ganglia infarction), DIP, or psychogenic parkinsonism [17, 54]. Furthermore, a semiquantitative analysis with a cut-off of striatal asymmetry index greater than 14.08 could differentiate PD from VP with a 100% specificity [55]. ^{123}I-FP-CIT SPECT images demonstrate that SPECT imaging with DAT ligands is useful to determine whether parkinsonism is entirely drug induced [56] and showed high levels of accuracy [57]. Cuberas-Borrós et al. performed FP-CIT images in 3 different groups of ET, DIP, and PD patients. Lower uptake was found in the PD group in comparison with the ET and DIP groups both in the putamen and in the caudate nucleus, but the differences between DIP and ET populations were only found in the putamen. There was an optimal discrimination threshold value between the reference population and the pathologic population for the putamen ratio by using volumes of interests, (VOIs) analysis [58].

SERT-dependent ^{123}I-FP-CIT imaging showed a mild decrease in SERT levels in PD compared to ET and health control, and reduced to undetectable levels of SERT in PSP and DLB patients were displayed markedly [39]. To improve diagnostic accuracy, non-DAT tracers (i.e., D2 dopamine receptors) are necessary together with long-term clinical follow-up and rescans [59].

MSA is a neurodegenerative disorder characterized by neuropathologic demonstration of CNS alpha-synuclein-positive glial cytoplasmic inclusions with neurodegenerative changes in striatonigral or olivopontocerebellar structures [60]. Clinically, MSA is characterized by autonomic dysfunction and/or urinary dysfunction which may be associated with parkinsonian symptoms in 80% of patients (MSA-P) or with cerebellar ataxia in 20% of patients (MSA-C). It is difficult to differentiate it from other movement disorders, particularly in the early course of disease. Voxel wise analysis of ^{123}I-β-CIT SPECT revealed more widespread decline of monoaminergic transporter availability in MSA-P compared with idiopathic Parkinson's disease (IPD) [61], matching the underlying pathological features. They suggest that the quantification of midbrain DAT signal should be included in the routine clinical analysis of ^{123}I-β-CIT SPECT in patients with uncertain parkinsonism.

A combined ^{99m}Tc-ECD/^{123}I-FP-CIT brain SPECT protocols have been proven to improve the differential diagnosis of IPD and MSA as well as corticobasal degeneration and PSP [62]. SPECT with the tracer ^{123}I-Ioflupane can also give an accurate and highly sensitive measure of dopamine degeneration [63].

A study showed that the degree of loss was higher in putamen than caudate in both PD and MSA patients. However, MSA patients showed a more symmetric loss (ipsilateral versus contralateral side) of striatal DAT in both caudate and putamen than PD patients (Figure 2) [64]. It was also reported that patients with a side-to-side difference of reduced striatal ^{123}I-β-CIT binding greater than 15% are likely to suffer from IPD, while the patients with the difference between 5% and 15% are more likely to have MSA [65]. Another study showed that mean distribution volume ratios (DVRs) in the basal ganglia of MSA patients were significantly less than in controls, but generally higher than in PD patients. Furthermore, the MSA patients had significantly

increased DVRs in the posterior putamen (mean 0.49 ± 0.30) compared with PD patients (0.74 ± 0.25) [66].

Another study which used both ^{123}I-β-CIT (for DAT) and ^{123}I-IBF (for D2) reported that DAT binding in the posterior putamen was markedly reduced in all patients. However, D2 binding in posterior putamen was significantly increased in dopa-untreated PD, and it was significantly reduced in MSA. These findings suggested that DAT SPECT may be useful in differentiating parkinsonism from controls and D2 SPECT in further differentiating MSA from PD [67]. IBZM SPECT using recently introduced three dimensional automated quantification method calculating the Striatal/frontal cortex binding ratios [68] and voxel-by-voxel binding potential parametric imaging also can discriminate among extrapyramidal diseases such as PD and PSP [69].

^{123}I-IBZM SPECT is an effective diagnostic tool in the establishment of the differential diagnosis in patients with PD and Parkinson-plus syndromes. Quantification of these studies had limited utility since the overlapping of index values between normal and pathological restricts their use in individual cases [70]. Vlaar et al. reported that FP-CIT SPECT is accurate to differentiate patients with IPD from those with ET, and IPD from VP and DIP, but the accuracy of both FP-CIT and IBZM SPECT scans to differentiate between IPD and APS is low [54]. However, a study suggested that using multidimensional combination of FP-CIT, IBZM, and MIBG scintigraphy was likely to significantly increase test accuracy (94%) in differentiating PD from APS [71]. More recently, a study using ^{123}I-PE21 indicated that dopamine transporter scan has a high sensitivity and specificity in distinguishing between patients with and without striatal neurodegeneration. Calculation of the striatal anterior-posterior ratio can assist in differentiating between idiopathic PD and APS [72]. Moreover, study with ^{123}I-FP-CIT in165 patients with a clinical diagnosis of PD ($n = 120$) or APS ($n = 45$) suggested that a global and severe degeneration pattern had a high positive predictive value of APS within the first 5 years of the disease [73].

A ^{123}I-FP-CIT and ^{123}I-IBZM SPECT study, in which seven subjects were all from a Spanish family with G309D mutation in the PINK1 gene, showed that striatal DAT binding was reduced in all three PARK6 patients. But in two of the siblings, DAT binding was markedly increased. It suggested that the increased DAT binding may be an early preclinical finding [74]. SPECT is also useful for distinguishing PD from Dopa responsive dystonia (DRD), or for assessing the integrity of the nigrostriatal dopaminergic pathway in atypical cases of postural tremor or iatrogenic parkinsonian syndromes. The imaging with ^{99}Tc^{m}-TRODAT-1/^{123}I-IBZM in a 39-year-old woman with a 24-year history of DRD indicated that ^{99}Tc^{m}-TRODAT-1 is helpful in differentiating DRD from early-onset idiopathic parkinsonism and the ^{123}I-IBZM SPECT is also helpful in differentiating these two conditions in the later clinical course [75].

In IPD, two different clinical phenotypes are usually distinguished: a tremor-dominant variant (TD) and an akinetic-rigid type (ART). TD patients compared to ART patients are characterized by a slower disease progression and a minor cognitive impairment. For different phenotypes of PD, ^{123}I-FP-CIT SPECT has indicated that the dopaminergic system in ART patients is more involved compared to that in the TD patients and that this kind of difference is present from the initial stage of the disease [76–78]. There was a significantly higher FP-CIT uptake in contralateral putamen and a higher but not statistically significant uptake in all the other striatal regions in TD patients when compared to ART patients [77]. Similarly, Spiegel et al. reported a greater impairment in ART patients in all striatal regions analyzed [78]. These results suggest that further systems besides the nigrostriatal dopaminergic system may contribute to generation of parkinsonian tremor.

3.4. Monitoring the Progression of the PD. Pathologic studies investigating the rate of PD progression have been limited to patients with severe illness of long duration and rely entirely on cross-sectional data. The UPDRS or other functional clinical endpoints are used to monitor disease progression. It makes it difficult to isolate clinical change solely due to disease progression [79].

The rate of progression of dopaminergic degeneration is much faster in PD than in normal aging [80]. Patients with PD present first with unilateral symptoms that gradually progress to involve both sides [6]. Clinical progression has been investigated with SPECT, which could prove to be an objective tool for monitoring the disease progression.

^{123}I-β-CIT SPECT imaging of the dopamine transporter is a sensitive biomarker of PD onset and severity. A group of 50 early-stage PD patients was examined [81]. Two SPECT imaging series were obtained 12 months apart. The average decrease in ^{123}I-β-CIT binding ratios was about 8% in the whole striatum, 8% in the putaminal region, and 4% in the caudate region. This finding supported the feasibility of using ^{123}I-β-CIT in the evaluation of disease progression in PD [82]. Moreover, sequential SPECT scans using ^{123}I-β-CIT in PD subjects demonstrated a decline in striatal uptake of approximately 11.2%/year from the baseline scan, compared with 0.8%/year in the healthy controls [79]. Another SPECT study with ^{123}I-β-CIT demonstrated a rapid decline of striatal binding in patients with APS, exceeding the reduction in PD, and the dopaminergic degeneration in PD slows down during the course of the disease [83].

Combined ^{123}I-β-CIT and ^{123}I-IBZM SPECT studies have demonstrated that postsynaptic dopamine receptor upregulation contralateral to the presenting side occurs in untreated unilateral PD and disappears in untreated bilateral (asymmetric) PD despite a greater loss of dopamine transporter function [84]. This may be helpful in monitoring the progression of nigrostriatal dysfunction in early PD. Tatsch et al. [21] found that specific ^{123}I-IPT uptake in the caudate and putamen, and putamen to caudate ratios, decreased with increasing Hoehn and Yahr stage (H-Y). These findings indicated that ^{123}I-IPT SPECT also may be a useful technique to estimate the extent of nigrostriatal degeneration in PD patients.

Tissingh et al. reported that disease severity correlated negatively and highly significantly with the ^{123}I-β-CIT binding in patients with early PD. Tremor ratings did not cor-

relate with the ^{123}I-β-CIT uptake, whereas rigidity and bradykinesia did [46]. The striatal ^{123}I-β-CIT uptake in a large cohort of PD subjects significantly correlated with severity of PD as measured by UPDRS [79]. The mean reduction of ^{99}Tc^{m}-TRODAT-1 uptake was found in the order of putamen (contralateral side, −81%; ipsilateral side, −67%) and caudate nucleus (contralateral side, −46%; ipsilateral side, −40%), and it correlated negatively with the UPDRS and H-Y staging [85].

Winogrodzka et al. [80] used ^{123}I-FP-CIT SPECT for the assessment of the rate of dopaminergic degeneration in PD. The mean annual decrease in striatal binding ratios in PD patients was found to be about 8% of the baseline mean, indicating that ^{123}I-FP-CIT SPECT was applicable to investigate the progression of dopaminergic degeneration. The specific to nonspecific ^{123}I-FP-CIT uptake ratios were calculated for striatum, caudate, and putamen, all of which were correlated with disease severity assessed by UPDRS and the duration of disease, suggesting that tremor may origins from other systems instead of the dopamine transporter system. Meanwhile, these ratios correlated with the bradykinesia subscore but not with rigidity or tremor subscore. It suggested that factors other than nigrostriatal degeneration may contribute to disease severity [36].

3.5. Evaluation of the Treatment Effect of PD. Current therapies include drug therapy, surgical procedures, and stem cell transplantation. Drug therapy such as DA replacement therapy with levodopa fails to prevent the progression of the disease process and only alleviates the clinical symptoms. Once the diagnosis is made, the neurologist with the patient must decide whether to institute treatment at the time of diagnosis or when functional disability occurs [86]. To evaluate the effectiveness of treatment, it is critical to develop methods that can reliably measure the progression of dopaminergic degeneration.

Postsynaptic imaging has been helpful in predicting thera-peutic response to dopaminergic medication early in the course of Parkinson's disease. Studies have demonstrated that PD patients receiving treatment do better than those who do not, and those receiving treatment earlier do better in long term [87]. Schwarz et al. performed a follow-up study of 2–4 years including 55 patients with parkinsonism and prior dopaminomimetic therapy and found that IBZM-SPECT accurately predicted the response to apomorphine and levodopa, The sensitivity/specificity was 96.3%/64.7%, and 100%/75% [88]. Thus, ^{123}I-IBZM can be used routinely to identify which PD patients will benefit from dopaminergic medication [89]. Another study including 20 PD patients who undergone short-term levodopa test and SPECT imaging found there was a relationship between responsiveness to levodopa and asymmetry detected with ^{123}I-FP-CIT. This technique can predict dopaminergic responsiveness in patients with PD [90].

Recently, a ^{99}Tc^{m}-TRODAT-1 SPECT indicated that levodopa did not interfere with DAT binding, suggesting that differences between clinical assessment and radiotracer imaging in clinical trials may not be specifically related to levodopa treatment [91]. Similarly, the effect of subchronic treatment on striatal DAT was examined in patients who were not currently being treated with these medications. These results suggested that typical clinical doses of levodopa/carbidopa and L-selegiline did not induce significant occupancy of the ^{123}I-β-CIT binding site and that 4–6 weeks of treatment caused no significant modulation of DAT levels. These results supported the validity of measuring DAT levels with ^{123}I-β-CIT without the need to withdraw patients from medication treatment [92]. ^{123}I-β-CIT SPECT imaging provides a quantitative biomarker for the progressive nigrostriatal dopaminergic degeneration in PD. As new protective and restorative therapies for PD are developed, dopamine transporter imaging offers the potential to provide an objective endpoint for these therapeutic trials [79, 80].

Hwang et al. found that the PD patients with fluctuating levodopa response showed a significant decrease in ^{123}I-IBZM uptake (D2 receptor densities) than early levodopa-naive PD and chronic PD with stable levodopa response [93], which contributed to the development of motor fluctuation.

4. Discussion

It has been reported that PET using 18F-dopa represents a useful tool for detecting a reduction of dopaminergic activity in PD patients at a very early stage [94, 95]. But the uptake might be upregulated in the early phase of the disease whereas expression of DATs might be down-regulated. SPECT imaging combining both pre- and postsynaptic study as well as clinical criteria improves the diagnosis of early Parkinson's disease. The quantitative combination of presynaptic DAT and postsynaptic D2 receptor binding demonstrated higher diagnostic accuracy in the differentiation of patients with PD from patients with nonidiopathic parkinsonian syndromes than the established approach based on striatal D2 receptor binding alone [96].

The imaging of DAT with ^{99}Tc^{m}-TRODAT-1 SPECT has been recently proposed to be a valuable and feasible means of assessment of the integrity of dopamine neurons [45]. ^{123}I-FP-CIT also has been successfully used to detect the loss of dopaminergic nigrostriatal neuron in PD at an early stage [47]. The sensitivity and specificity of this technique were 100% in discriminating PD patients from healthy subjects in the age-specific (>50 y) groups [85]. A bilateral loss of striatal DA transporters in patients with unilateral PD suggests that it may identify subjects in the preclinical phase of the disease.

There was a continuous reduction in specific striatal uptake especially for the putaminal uptake of ^{99}Tc^{m}-TRODAT-1 with increasing disease severity in Parkinson's disease patients. In PD patients, presynaptic neurodegeneration may affect the putamen and caudate with different severity [20]; however, there were no significant correlations between striatal ^{123}I-FP-CIT binding ratios and disease severity as were established earlier with ^{99}Tc^{m}-TRODAT-1. Further research is necessary to interpret these findings.

The putaminal uptake contralateral to the more affected limbs was significantly reduced compared with the ipsilateral sides and the difference became greater when the posterior putaminal uptakes were compared [49], and the discriminant function analysis of both the ipsilateral and con-

tralateral putamen classified 100% of their patients correctly, whereas analysis using only the contralateral putamen classified 92% of cases correctly [46]. PET imaging using ^{18}F-DOPA also demonstrated a significant abnormality in the posterior putamen of PD patients [97]. In conclusion, the analysis using the mean of the ipsilateral and contralateral posterior putamen may result in the greatest accuracy.

The study confirms asymmetric D2 receptor upregulation in PD. However, the sensitivity of contralateral higher striatal ^{123}I-IBZM binding is only not so obvious, therefore, PD cannot be excluded in patients with parkinsonism and no contralateral upregulation of D2 receptors [34]. The exact diagnostic accuracy of this technique in parkinsonian syndromes remains controversial.

MSA and PD patients are difficult to differentiate from each other. Imaging studies using different dopamine transporters in MSA patients have reported same results: DAT binding was significantly decreased in all regions in both IPD and MSA patients as compared with healthy subjects. A study by using ^{123}I-β-CIT SPECT demonstrated that the posterior putamen is more involved than the caudate in MSA [67]. Another study using ^{99}Tc^{m}-TRODAT-1 showed MSA patients had significantly higher tracer uptake particularly in the posterior putamen compared with PD patients and significantly lower uptake compared with controls. The result suggested that the two neurodegenerative diseases have different pathophysiological processes [66].

A large retrospective study [54] on the diagnostic value of the FP-CIT and IBZM SPECT scan in patients with parkinsonian symptoms of unknown origin concluded that FP-CIT SPECT is accurate to differentiate patients with IPD from those with ET, and IPD from VP and DIP, but the two scans had low accuracy to differentiate between IPD and APS.

Age is the largest risk factor for the development and progression of PD [98]. PD may reflect a failure of the normal cellular compensatory mechanisms in vulnerable brain regions, and this vulnerability is increased by ageing. PD is one of the best examples of an age-related disease. Presynaptic imaging has demonstrated the ability to objectively measure the progression of Parkinson's disease. Although the rate of progression of the dopaminergic terminal loss in patients with PD was correlated with clinical severity, the annual percentage loss of ^{123}I-β-CIT striatal uptake did not correlate with the annual loss in measures of clinical function [79]. Striatal ^{123}I-IPT uptake was closely related to the stage of PD. The binding ratios decreased markedly from H-Y stage I to stage IV; in addition, this imaging technique has a special advantage that data can be acquired within a few hours after injection [21]. The rate of progression may be faster in APS than in PD [83]. To interprete the results well, caution must be paid in the studies in which therapeutic effects in Parkinson's disease were also monitored by serial imaging of nigrostriatal neurons [99].

For different phenotype of PD, FP-CIT striatal uptake values significantly correlated with bradykinesia and rigidity but not with tremor [78], putaminal relative sparing in TD patients could partially contribute to the slower disease progression. This fact could explain the different disease progression with a more benign course in TD group. A widespread degeneration of the nigrostriatal dopaminergic pathway might be necessary for the development of parkinsonian tremor at rest [100].

Early Parkinson's disease is dominated by a motor syndrome called parkinsonism, but as the disease develops motor complications and nonmotor problems may occur as well [6].

The results of imaging of dopamine-D2 receptors with the improvement in motor signs by the injection of apomorphine and oral dopaminomimetic therapy were compared [88]. It can be concluded that normal IBZM binding is a useful predictor of a good response to dopaminergic drugs in PD patients and a questionable response to previous dopaminomimetic therapy. However, reduced IBZM binding seems to exclude a diagnosis of PD but suggests another disorder of the basal ganglia.

To evaluate effect of treatment with drugs on striatal DAT, the imaging was performed before treatment, while on medication, and following withdrawal from medication in each patient. Thus, the results provided a measurement of DAT levels and drug occupancy following subchronic drug treatment and drug occupancy of the tracer binding site [92].

Semiquantification of striatal uptake is more correct than visual reading, but it is also time consuming and prone to error, particularly if the VOIs are positioned manually. There is a critical need to create a new technique to solve this problem. A new software tool ("IBZM tool") was presented for fully automated and standardized processing, evaluating and documenting the ^{123}I-IBZM SPECT scans [101].

MIBG may be a peripheral biological marker of PD including triplication of the a-synuclein gene. Although diagnostic accuracy of cardiac MIBG scintigram in PD is high, the sensitivity is insufficient in patients with short duration [43]. Because of its relatively lower sensitivity, cardiac ^{123}I-MIBG scintigraphy is of limited value in the diagnosis of early PD. However, because of its high specificity, it may assist in the diagnosis of PD [51]. Furthermore, Fukuyama [102] analyzed the reports about MIBG imaging in PD, and suggested that it should not be regarded as the first and best choice of diagnostic aid for PD, especially in the early stages, and careful attention should be paid for diagnosis of PD or diffused Lewy body disease.

A study showed there is an association between urinary dysfunction and degeneration of the nigrostriatal dopaminergic cells in PD [52]. The results may promote further studies of dopaminergic drug treatments on urinary dysfunction in PD.

5. Perspective

SPECT imaging has proven to be a useful tool to investigate the many facets of PD *in vivo*. This technique helps understand the pathogenesis, the differential diagnosis, and the progression of the PD.

The disadvantage of SPECT compared to PET is that it is difficult to obtain a reliable quantification. Furthermore, the resolution of images is a limitation for the visualization of basal ganglia in PD. However, SPECT is more practical as a routine procedure than PET. In the future, the technique

that provides high accuracy and new radiotracers needs to be developed to help understand the role of non-DA neurotransmitter systems in PD.

SPECT combined with other techniques such as transcranial sonography and olfaction test may have a higher accuracy in the diagnosis of PD. Imaging agents like dopamine transporter or D2 receptor ligands assess only part of aspects of the dopamine neurons. New tracers need to be synthesized to detect other aspects of dopamine neurons.

The SPECT imaging of the nigrostriatal dopaminergic pathway can be used to monitor therapeutic effects in Parkinson's disease. As new protective and restorative therapies for PD are developed, dopamine transporter imaging offers the potential to provide an objective endpoint for these therapeutic trials. Further studies are needed to evaluate the possible effects of the therapy, especially for the delayed-onset bilateral symptoms. Moreover, there is a pressing need to improve our understanding of the pathogenesis to enable development of disease modifying treatments.

Abbreviations

SPECT: Single-photon emission computed tomography
DAT: Dopamine transporter
PD: Parkinson's disease
PET: Positron emission tomography
SERT: Serotonin transporter
CNS: Central nervous system
CUPS: Clinically Unclear Parkinsonian Syndromes
UPDRS: United Parkinson's disease rating scale
APS: Atypical parkinsonian syndromes
MSA: Multiple system atrophy
PSP: Progressive supranuclear palsy
DIP: Drug induced parkinsonism
ET: Essential tremor
VP: Vascular Parkinsonism
DLB: Dementia with Lewy Bodies
VOIs: Volumes of interests
IPD: Idiopathic Parkinson's disease
DVRs: Distribution volume ratios
DRD: Dopa-responsive dystonia
TD: Tremor-dominant variant
ART: Akinetic-rigid type
H-Y: Hoehn and Yahr.

Conflict of Interests

The authors declare that they have no conflict of interests.

Acknowledgments

This work is partly sponsored by Grants from the Zhejiang Provincial Natural Science Foundation of China (Z2110230), Health Bureau of Zhejiang Province (2010ZA075, 2011ZDA013), National Science Foundation of China (NSFC) (nos. 81101023, 81170306, 81173468), and Ministry of Science and Technology of China (2011CB504400, 2012BAI13B06).

References

[1] A. J. Hughes, S. E. Daniel, L. Kilford, and A. J. Lees, "Accuracy of clinical diagnosis of idiopathic Parkinson's disease: a clinico-pathological study of 100 cases," *Journal of Neurology Neurosurgery and Psychiatry*, vol. 55, no. 3, pp. 181–184, 1992.

[2] V. Ruipérez, F. Darios, and B. Davletov, "Alpha-synuclein, lipids and Parkinson's disease," *Progress in Lipid Research*, vol. 49, no. 4, pp. 420–428, 2010.

[3] S. L. Leong, R. Cappai, K. J. Barnham, and C. L. L. Pham, "Modulation of α-synuclein aggregation by dopamine: a review," *Neurochemical Research*, vol. 34, no. 10, pp. 1838–1846, 2009.

[4] A. Bellucci, G. Collo, I. Sarnico, L. Battistin, C. Missale, and P. Spano, "Alpha-synuclein aggregation and cell death triggered by energy deprivation and dopamine overload are counteracted by D_2/D_3 receptor activation," *Journal of Neurochemistry*, vol. 106, no. 2, pp. 560–577, 2008.

[5] H. Braak, K. Del Tredici, U. Rüb, R. A. I. de Vos, E. N. H. Jansen Steur, and E. Braak, "Staging of brain pathology related to sporadic Parkinson's disease," *Neurobiology of Aging*, vol. 24, no. 2, pp. 197–211, 2003.

[6] J. P. Larsen, A. G. Beiske, S. I. Bekkelund et al., "Motor symptoms in Parkinson's disease," *Tidsskrift for den Norske Laegeforening*, vol. 128, no. 18, pp. 2068–2071, 2008.

[7] R. F. Peppard, W. R. W. Martin, G. D. Carr et al., "Cerebral glucose metabolism in Parkinson's disease with and without dementia," *Archives of Neurology*, vol. 49, no. 12, pp. 1262–1268, 1992.

[8] A. Kummer, P. Scalzo, F. Cardoso, and A. L. Teixeira, "Evaluation of fatigue in Parkinson's disease using the Brazilian version of Parkinson's Fatigue Scale," *Acta Neurologica Scandinavica*, vol. 123, no. 2, pp. 130–136, 2011.

[9] R. D. S. Prediger, F. C. Matheus, M. L. Schwarzbold, M. M. S. Lima, and M. A. B. F. Vital, "Anxiety in Parkinson's disease: a critical review of experimental and clinical studies," *Neuropharmacology*, vol. 62, no. 1, pp. 115–124, 2012.

[10] D. Aarsland, K. Brønnick, J. P. Larsen, O. B. Tysnes, and G. Alves, "Cognitive impairment in incident, untreated parkinson disease: the norwegian parkwest study," *Neurology*, vol. 72, no. 13, pp. 1121–1126, 2009.

[11] C. Magerkurth, R. Schnitzer, and S. Braune, "Symptoms of autonomic failure in Parkinson's disease: prevalence and impact on daily life," *Clinical Autonomic Research*, vol. 15, no. 2, pp. 76–82, 2005.

[12] S. S. O'Sullivan, K. Wu, M. Politis et al., "Cue-induced striatal dopamine release in Parkinson's disease-associated impulsive-compulsive behaviours," *Brain*, vol. 134, part 4, pp. 969–978, 2011.

[13] L. Morgante, C. Colosimo, A. Antonini et al., "Psychosis associated to Parkinson's disease in the early stages: relevance of cognitive decline and depression," *Journal of Neurology, Neurosurgery and Psychiatry*, vol. 83, no. 1, pp. 76–82, 2012.

[14] H. W. Berendse, D. S. Roos, P. Raijmakers, and R. L. Doty, "Motor and non-motor correlates of olfactory dysfunction in Parkinson's disease," *Journal of the Neurological Sciences*, vol. 310, no. 1-2, pp. 21–24, 2011.

[15] M. Cohenpour and H. Golan, "Nuclear neuroimaging of dopamine transporter in Parkinsonism—role in routine clinical practice," *Harefuah*, vol. 146, no. 9, pp. 698–702, 2007.

[16] J. Meara, B. K. Bhowmick, and P. Hobson, "Accuracy of diagnosis in patients with presumed Parkinson's disease," *Age and Ageing*, vol. 28, no. 2, pp. 99–102, 1999.

[17] V. Marshall and D. Grosset, "Role of dopamine transporter imaging in routine clinical practice," *Movement Disorders*, vol. 18, no. 12, pp. 1415–1423, 2003.

[18] S. Thobois, S. Guillouet, and E. Broussolle, "Contributions of PET and SPECT to the understanding of the pathophysiology of Parkinson's disease," *Neurophysiologie Clinique*, vol. 31, no. 5, pp. 321–340, 2001.

[19] J. P. Seibyl, K. Marek, K. Sheff et al., "Iodine-123-β-CIT and iodine-123-FPCIT SPECT measurement of dopamine transporters in healthy subjects and Parkinson's patients," *Journal of Nuclear Medicine*, vol. 39, no. 9, pp. 1500–1508, 1998.

[20] G. Tissingh, J. Booij, P. Bergmans et al., "Iodine-123-N-ω-fluoropropyl-2/β-carbomethoxy3β-(4-iodophenyl)tropane SPECT in healthy controls and early-stage, drug-naive Parkinson's disease," *Journal of Nuclear Medicine*, vol. 39, no. 7, pp. 1143–1148, 1998.

[21] K. Tatsch, J. Schwarz, P. D. Mozley et al., "Relationship between clinical features of Parkinson's disease and presynaptic dopamine transporter binding assessed with [^{123}I]IPT and single-photon emission tomography," *European Journal of Nuclear Medicine*, vol. 24, no. 4, pp. 415–421, 1997.

[22] P. Emond, D. Guilloteau, and S. Chalon, "PE2I: a radiopharmaceutical for in vivo exploration of the dopamine transporter," *CNS Neuroscience and Therapeutics*, vol. 14, no. 1, pp. 47–64, 2008.

[23] G. Page, S. Chalon, P. Emond, J. M. Maloteaux, and E. Hermans, "Pharmacological characterisation of (E)-N-(3-iodo–prop-2-enyl)-2β-carbomethoxy-3β-(4′-methylphenyl)nortropane (PE2I) binding to the rat neuronal dopamine transporter expressed in COS cells," *Neurochemistry International*, vol. 40, no. 2, pp. 105–113, 2002.

[24] M. Ziebell, "Evaluation of the superselective radioligand [^{123}I]PE2I for imaging of the dopamine transporter in SPECT," *Danish Medical Bulletin*, vol. 58, no. 5, Article ID B4279, 2011.

[25] W. S. Huang, Y. H. Chiang, J. C. Lin, Y. H. Chou, C. Y. Cheng, and R. S. Liu, "Crossover study of (99m)Tc-TRODAT-1 SPECT and 18F-FDOPA PET in Parkinson's disease patients," *Journal of Nuclear Medicine*, vol. 44, no. 7, pp. 999–1005, 2003.

[26] H. F. Kung, S. Pan, M. P. Kung et al., "In vitro and in vivo evaluation of [^{123}I]IBZM: a potential CNS D-2 dopamine receptor imaging agent," *Journal of Nuclear Medicine*, vol. 30, no. 1, pp. 88–92, 1989.

[27] M. P. Kung, H. F. Kung, J. Billings, Y. Yang, R. A. Murphy, and A. Alavi, "The characterization of IBF as a new selective dopamine D-2 receptor imaging agent," *Journal of Nuclear Medicine*, vol. 31, no. 5, pp. 648–654, 1990.

[28] M. S. Al-Tikriti, R. M. Baldwin, Y. Zea-Ponce et al., "Comparison of three high affinity SPECT radiotracers for the dopamine D_2 receptor," *Nuclear Medicine and Biology*, vol. 21, no. 2, pp. 179–188, 1994.

[29] H. Matsumoto, A. Tanaka, N. Suzuki, S. Kondo, M. Kato-Azuma, and Y. Yonekura, "Metabolism of ^{123}I-IBF in humans," *Kakuigaku*, vol. 36, no. 2, pp. 169–177, 1999.

[30] R. A. Murphy, H. F. Kung, M. P. Kung, and J. Billings, "Synthesis and characterization of iodobenzamide analogues: potential D-2 dopamine receptor imaging agents," *Journal of Medicinal Chemistry*, vol. 33, no. 1, pp. 171–178, 1990.

[31] J. Spiegel, D. Hellwig, W. H. Jost et al., "Cerebral and extracranial neurodegeneration are strongly coupled in Parkinson's disease," *The Open Neurology Journal*, vol. 1, pp. 1–4, 2007.

[32] J. P. Seibyl, K. L. Marchek, D. Quinlan et al., "Decreased single-photon emission computed tomographic [^{123}I]β-CIT striatal uptake correlates with symptom severity in Parkinson's disease," *Annals of Neurology*, vol. 38, no. 4, pp. 589–598, 1995.

[33] M. Ichise, Y. J. Kim, J. R. Ballinger et al., "SPECT imaging of pre- and postsynaptic dopaminergic alterations in L-dopa-untreated PD," *Neurology*, vol. 52, no. 6, pp. 1206–1214, 1999.

[34] C. C. P. Verstappen, B. R. Bloem, C. A. Haaxma, W. J. G. Oyen, and M. W. I. M. Horstink, "Diagnostic value of asymmetric striatal D_2 receptor upregulation in Parkinson's disease: an [^{123}I]IBZM and [^{123}I]FP-CIT SPECT study," *European Journal of Nuclear Medicine and Molecular Imaging*, vol. 34, no. 4, pp. 502–507, 2007.

[35] K. H. Ma, W. S. Huang, C. H. Chen et al., "Dual SPECT of dopamine system using [(99m)Tc]TRODAT-1 and [^{123}I]IBZM in normal and 6-OHDA-lesioned formosan rock monkeys," *Nuclear Medicine and Biology*, vol. 29, no. 5, pp. 561–567, 2002.

[36] H. T. S. Benamer, J. Patterson, D. J. Wyper, D. M. Hadley, G. J. A. Macphee, and D. G. Grosset, "Correlation of Parkinson's disease severity and duration with ^{123}I-FP-CIT SPECT striatal uptake," *Movement Disorders*, vol. 15, no. 4, pp. 692–698, 2000.

[37] C. Eggers, D. Kahraman, G. R. Fink, M. Schmidt, and L. Timmermann, "Akinetic-rigid and tremor-dominant Parkinson's disease patients show different patterns of FP-CIT Single photon emission computed tomography," *Movement Disorders*, vol. 26, no. 3, pp. 416–423, 2011.

[38] S. J. Kish, J. Tong, O. Hornykiewicz et al., "Preferential loss of serotonin markers in caudate versus putamen in Parkinson's disease," *Brain*, vol. 131, part 1, pp. 120–131, 2008.

[39] F. Roselli, N. M. Pisciotta, M. Pennelli et al., "Midbrain SERT in degenerative parkinsonisms: a ^{123}I-FP-CIT SPECT study," *Movement Disorders*, vol. 25, no. 12, pp. 1853–1859, 2010.

[40] K. L. Marek, J. P. Seibyl, S. S. Zoghbi et al., "[^{123}I] β-CIT/SPECT imaging demonstrates bilateral loss of dopamine transporters in hemi-Parkinson's disease," *Neurology*, vol. 46, no. 1, pp. 231–237, 1996.

[41] J. Eerola, P. J. Tienari, S. Kaakkola, P. Nikkinen, and J. Launes, "How useful is [^{123}I]β-CIT SPECT in clinical practice?" *Journal of Neurology, Neurosurgery and Psychiatry*, vol. 76, no. 9, pp. 1211–1216, 2005.

[42] V. L. Marshall, C. B. Reininger, M. Marquardt et al., "Parkinson's disease is overdiagnosed clinically at baseline in diagnostically uncertain cases: a 3-year European multicenter study with repeat [^{123}I]FP-CIT SPECT," *Movement Disorders*, vol. 24, no. 4, pp. 500–508, 2009.

[43] H. Sawada, T. Oeda, K. Yamamoto et al., "Diagnostic accuracy of cardiac metaiodobenzylguanidine scintigraphy in Parkinson disease," *European Journal of Neurology*, vol. 16, no. 2, pp. 174–182, 2009.

[44] J. Spiegel, M. O. Möllers, W. H. Jost et al., "FP-CIT and MIBG scintigraphy in early Parkinson's disease," *Movement Disorders*, vol. 20, no. 5, pp. 552–561, 2005.

[45] K. L. Chou, H. I. Hurtig, M. B. Stern et al., "Diagnostic accuracy of [(99m)Tc]TRODAT-1 SPECT imaging in early Parkinson's disease," *Parkinsonism and Related Disorders*, vol. 10, no. 6, pp. 375–379, 2004.

[46] G. Tissingh, P. Bergmans, J. Booij et al., "Drug-naive patients with Parkinson's disease in Hoehn and Yahr stages I and II show a bilateral decrease in striatal dopamine transporters as revealed by [^{123}I]β-CIT SPECT," *Journal of Neurology*, vol. 245, no. 1, pp. 14–20, 1998.

[47] L. Filippi, C. Manni, M. Pierantozzi et al., "^{123}I-FP-CIT semi-quantitative SPECT detects preclinical bilateral dopaminergic deficit in early Parkinson's disease with unilateral symptoms," *Nuclear Medicine Communications*, vol. 26, no. 5, pp. 421–426, 2005.

[48] W. S. Huang, K. H. Ma, Y. H. Chou, C. Y. Chen, R. S. Liu, and J. C. Liu, "(99m)Tc-TRODAT-1 SPECT in healthy and 6-OHDA lesioned parkinsonian monkeys: comparison with 18F-FDOPA PET," *Nuclear medicine communications*, vol. 24, no. 1, pp. 77–83, 2003.

[49] W. S. Huang, S. Z. Lin, J. C. Lin, S. P. Wey, G. Ting, and R. S. Liu, "Evaluation of early-stage Parkinson's disease with (99m)Tc-TRODAT-1 imaging," *Journal of Nuclear Medicine*, vol. 42, no. 9, pp. 1303–1308, 2001.

[50] G. Kägi, K. P. Bhatia, and E. Tolosa, "The role of DAT-SPECT in movement disorders," *Journal of Neurology, Neurosurgery and Psychiatry*, vol. 81, no. 1, pp. 5–12, 2010.

[51] K. Ishibashi, Y. Saito, S. Murayama et al., "Validation of cardiac ^{123}I-MIBG scintigraphy in patients with Parkinson's disease who were diagnosed with dopamine PET," *European Journal of Nuclear Medicine and Molecular Imaging*, vol. 37, no. 1, pp. 3–11, 2010.

[52] R. Sakakibara, H. Shinotoh, T. Uchiyama, M. Yoshiyama, T. Hattori, and T. Yamanishi, "SPECT imaging of the dopamine transporter with [^{123}I]-β-CIT reveals marked decline of nigrostriatal dopaminergic function in Parkinson's disease with urinary dysfunction," *Journal of the Neurological Sciences*, vol. 187, no. 1-2, pp. 55–59, 2001.

[53] Y. Agid, "Parkinson's disease: pathophysiology," *The Lancet*, vol. 337, no. 8753, pp. 1321–1324, 1991.

[54] A. M. M. Vlaar, T. de Nijs, A. G. H. Kessels et al., "Diagnostic value of ^{123}I-ioflupane and ^{123}I-iodobenzamide SPECT scans in 248 patients with Parkinsonian syndromes," *European Neurology*, vol. 59, no. 5, pp. 258–266, 2008.

[55] D. Contrafatto, G. Mostile, A. Nicoletti et al., "[^{123}I]FP-CIT-SPECT asymmetry index to differentiate Parkinson's disease from vascular parkinsonism," *Acta Neurologica Scandinavica*, In press.

[56] M. Loberboym, T. A. Traves, E. Melamed, Y. Lampl, M. Hellman, and R. Djaldetti, "[^{123}I]-EP/CIT SPECT imaging for distinguishing drug-induced Parkinsonism from Parkinson's disease," *Movement Disorders*, vol. 21, no. 4, pp. 510–514, 2006.

[57] F. J. Diaz-Corrales, S. Sanz-Viedma, D. Garcia-Solis, T. Escobar-Delgado, and P. Mir, "Clinical features and ^{123}I-FP-CIT SPECT imaging in drug-induced parkinsonism and Parkinson's disease," *European Journal of Nuclear Medicine and Molecular Imaging*, vol. 37, no. 3, pp. 556–564, 2010.

[58] G. Cuberas-Borrós, C. Lorenzo-Bosquet, S. Aguadé-Bruix et al., "Quantitative evaluation of striatal I-123-FP-CIT uptake in essential tremor and parkinsonism," *Clinical Nuclear Medicine*, vol. 36, no. 11, pp. 991–996, 2011.

[59] A. C. Felicio, M. C. Shih, C. Godeiro-Junior, L. A. F. Andrade, R. A. Bressan, and H. B. Ferraz, "Molecular imaging studies in Parkinson disease reducing diagnostic uncertainty," *Neurologist*, vol. 15, no. 1, pp. 6–16, 2009.

[60] S. Gilman, G. K. Wenning, P. A. Low et al., "Second consensus statement on the diagnosis of multiple system atrophy," *Neurology*, vol. 71, no. 9, pp. 670–676, 2008.

[61] C. Scherfler, K. Seppi, E. Donnemiller et al., "Voxel-wise analysis of [^{123}I]β-CIT SPECT differentiates the Parkinson variant of multiple system atrophy from idiopathic Parkinson's disease," *Brain*, vol. 128, part 7, pp. 1605–1612, 2005.

[62] G. El Fakhri and J. Ouyang, "Dual-radionuclide brain SPECT for the differential diagnosis of parkinsonism," *Methods in Molecular Biology*, vol. 680, pp. 237–246, 2011.

[63] A. Antonini, R. Benti, R. de Notaris et al., "^{123}I-Ioflupane/SPECT binding to striatal dopamine transporter (DAT) uptake in patients with Parkinson's disease, multiple system atrophy, and progressive supranuclear palsy," *Neurological Sciences*, vol. 24, no. 3, pp. 149–150, 2003.

[64] A. Varrone, K. L. Marek, D. Jennings, R. B. Innis, and J. P. Seibyl, "[^{123}I]β-CIT SPECT imaging demonstrates reduced density of striatal dopamine transporters in Parkinson's disease and multiple system atrophy," *Movement Disorders*, vol. 16, no. 6, pp. 1023–1032, 2001.

[65] G. M. Knudsen, M. Karlsborg, G. Thomsen et al., "Imaging of dopamine transporters and D_2 receptors in patients with Parkinson's disease and multiple system atrophy," *European Journal of Nuclear Medicine and Molecular Imaging*, vol. 31, no. 12, pp. 1631–1638, 2004.

[66] R. L. Swanson, A. B. Newberg, P. D. Acton et al., "Differences in [(99m)Tc]TRODAT-1 SPECT binding to dopamine transporters in patients with multiple system atrophy and Parkinson's disease," *European Journal of Nuclear Medicine and Molecular Imaging*, vol. 32, no. 3, pp. 302–307, 2005.

[67] Y. J. Kim, M. Ichise, J. R. Ballinger et al., "Combination of dopamine transporter and D_2 receptor SPECT in the diagnostic evaluation of PD, MSA, and PSP," *Movement Disorders*, vol. 17, no. 2, pp. 303–312, 2002.

[68] G. Pöpperl, P. Radau, R. Linke, K. Hahn, and K. Tatsch, "Diagnostic performance of a 3-D automated quantification method of dopamine D_2 receptor SPECT studies in the differential diagnosis of parkinsonism," *Nuclear Medicine Communications*, vol. 26, no. 1, pp. 39–43, 2005.

[69] C. Oyanagi, Y. Katsumi, T. Hanakawa et al., "Comparison of striatal dopamine D_2 receptors in Parkinson's disease and progressive supranuclear palsy patients using [^{123}I] iodobenzofuran single-photon emission computed tomography," *Journal of Neuroimaging*, vol. 12, no. 4, pp. 316–324, 2002.

[70] V. M. Poblete Garcíau, A. García Vicente, S. Ruíz Solís et al., "SPECT with ^{123}I-IBZM: utility in differential diagnosis of degenerative Parkinsonisms and establishment of quantification method," *Revista Espanola de Medicina Nuclear*, vol. 24, no. 4, pp. 234–243, 2005.

[71] M. Südmeyer, C. Antke, T. Zizek et al., "Diagnostic accuracy of combined FP-CIT, IBZM, and MIBG scintigraphy in the differential diagnosis of degenerative parkinsonism: a multidimensional statistical approach," *Journal of Nuclear Medicine*, vol. 52, no. 5, pp. 733–740, 2011.

[72] M. Ziebell, B. B. Andersen, G. Thomsen et al., "Predictive value of dopamine transporter SPECT imaging with [^{123}I]PE2I in patients with subtle parkinsonian symptoms," *European Journal of Nuclear Medicine and Molecular Imaging*, vol. 39, no. 2, pp. 242–250, 2012.

[73] D. Kahraman, C. Eggers, H. Schicha, L. Timmermann, and M. Schmidt, "Visual assessment of dopaminergic degeneration pattern in ^{123}I-FP-CIT SPECT differentiates patients with atypical parkinsonian syndromes and idiopathic Parkinson's disease," *Journal of Neurology*, vol. 259, no. 2, pp. 251–260, 2011.

[74] K. R. Kessler, N. Hamscho, B. Morales et al., "Dopaminergic function in a family with the PARK6 form of autosomal recessive Parkinson's syndrome," *Journal of Neural Transmission*, vol. 112, no. 10, pp. 1345–1353, 2005.

[75] W. J. Hwang, W. J. Yao, S. P. Wey, and G. Ting, "Clinical and [(99m)Tc]TRODAT-1/[^{123}I]IBZM SPECT imaging findings in dopa-responsive dystonia," *European Neurology*, vol. 51, no. 1, pp. 26–29, 2004.

[76] O. Schilaci, A. Chiaravaloti, M. Pierantozzi et al., "Different patterns of nigrostriatal degeneration in tremor type versus the akinetic-rigid and mixed types of Parkinson's disease at the early stages: molecular imaging with ^{123}I-FP-CIT SPECT," *International Journal of Molecular Medicine*, vol. 28, no. 5, pp. 881–886, 2011.

[77] C. Rossi, D. Frosini, D. Volterrani et al., "Differences in nigrostriatal impairment in clinical variants of early Parkinson's disease: evidence from a FP-CIT SPECT study," *European Journal of Neurology*, vol. 17, no. 4, pp. 626–630, 2010.

[78] J. Spiegel, D. Hellwig, S. Samnick et al., "Striatal FP-CIT uptake differs in the subtypes of early Parkinson's disease," *Journal of Neural Transmission*, vol. 114, no. 3, pp. 331–335, 2007.

[79] K. Marek, R. Innis, C. van Dyck et al., "[^{123}I] β-CIT SPECT imaging assessment of the rate of Parkinson's disease progression," *Neurology*, vol. 57, no. 11, pp. 2089–2094, 2001.

[80] A. Winogrodzka, P. Bergmans, J. Booij, E. A. van Royen, A. G. Janssen, and E. C. Wolters, "[^{123}I]FP-CIT SPECT is a useful method to monitor the rate of dopaminergic degeneration in early-stage Parkinson's disease," *Journal of Neural Transmission*, vol. 108, no. 8-9, pp. 1011–1019, 2001.

[81] A. Winogrodzka, P. Bergmans, J. Booij, E. A. van Royen, J. C. Stoof, and E. C. Wolters, "[^{123}I]β-CIT SPECT is a useful method for monitoring dopaminergic degeneration in early stage Parkinson's disease," *Journal of Neurology Neurosurgery and Psychiatry*, vol. 74, no. 3, pp. 294–298, 2003.

[82] J. P. Seibyl, K. Marek, K. Sheff et al., "Test/retest reproducibility of iodine-123-βCIT SPECT brain measurement of dopamine transporters in Parkinson's patients," *Journal of Nuclear Medicine*, vol. 38, no. 9, pp. 1453–1459, 1997.

[83] W. Pirker, S. Djamshidian, S. Asenbaum et al., "Progression of dopaminergic degeneration in Parkinson's disease and atypical parkinsonism: a longitudinal β-CIT SPECT study," *Movement Disorders*, vol. 17, no. 1, pp. 45–53, 2002.

[84] G. K. Wenning, E. Donnemiller, R. Granata, G. Riccabona, and W. Poewe, "^{123}I-β-CIT and ^{123}I-IBZM-SPECT scanning in levodopa-naive Parkinson's disease," *Movement Disorders*, vol. 13, no. 3, pp. 438–445, 1998.

[85] Y. H. Weng, T. C. Yen, M. C. Chen et al., "Sensitivity and specificity of (99m)Tc-TRODAT-1 SPECT imaging in differentiating patients with idiopathic Parkinson's disease from healthy subjects," *Journal of Nuclear Medicine*, vol. 45, no. 3, pp. 393–401, 2004.

[86] W. J. Weiner, "Early diagnosis of Parkinson's disease and initiation of treatment," *Reviews in Neurological Diseases*, vol. 5, no. 2, pp. 46–53, 2008, quiz 54-55.

[87] K. E. Lyons and R. Pahwa, "Diagnosis and initiation of treatment in Parkinson's disease," *International Journal of Neuroscience*, vol. 121, supplement 2, pp. 27–36, 2011.

[88] J. Schwarz, K. Tatsch, T. Gasser, G. Arnold, and W. H. Oertel, "[^{123}I]IBZM binding predicts dopaminergic responsiveness in patients with parkinsonism and previous dopaminomimetic therapy," *Movement Disorders*, vol. 12, no. 6, pp. 898–902, 1997.

[89] A. Hertel, M. Weppner, H. Baas et al., "Quantification of IBZM dopamine receptor SPET in de novo Parkinson patients before and during therapy," *Nuclear Medicine Communications*, vol. 18, no. 9, pp. 811–822, 1997.

[90] D. Contrafatto, G. Mostile, A. Nicoletti et al., "Single photon emission computed tomography striatal asymmetry index may predict dopaminergic responsiveness in Parkinson disease," *Clinical Neuropharmacology*, vol. 34, no. 2, pp. 71–73, 2011.

[91] P. O. Fernagut, Q. Li, S. Dovero et al., "Dopamine transporter binding is unaffected by L-DOPA administration in normal and MPTP-treated monkeys," *PLoS ONE*, vol. 5, no. 11, Article ID e14053, 2010.

[92] R. B. Innis, K. L. Marek, K. Sheff et al., "Effect of treatment with L-dopa/carbidopa or L-selegiline on striatal dopamine transporter SPECT imaging with [^{123}I]β-CIT," *Movement Disorders*, vol. 14, no. 3, pp. 436–442, 1999.

[93] W. J. Hwang, W. J. Yao, S. P. Wey, L. H. Shen, and G. Ting, "Downregulation of striatal dopamine D_2 receptors in advanced Parkinson's disease contributes to the development of motor fluctuation," *European Neurology*, vol. 47, no. 2, pp. 113–117, 2002.

[94] P. K. Morrish, G. V. Sawle, and D. J. Brooks, "Regional changes in [18F]dopa metabolism in the striatum in Parkinson's disease," *Brain*, vol. 119, part 6, pp. 2097–2103, 1996.

[95] K. Ito, P. K. Morrish, J. S. Rakshi et al., "Statistical parametric mapping with 18F-dopa PET shows bilaterally reduced striatal and nigral dopaminergic function in early Parkinson's disease," *Journal of Neurology Neurosurgery and Psychiatry*, vol. 66, no. 6, pp. 754–758, 1999.

[96] W. Koch, C. Hamann, P. E. Radau, and K. Tatsch, "Does combined imaging of the pre- and postsynaptic dopaminergic system increase the diagnostic accuracy in the differential diagnosis of parkinsonism?" *European Journal of Nuclear Medicine and Molecular Imaging*, vol. 34, no. 8, pp. 1265–1273, 2007.

[97] P. K. Morrish, G. V. Sawle, and D. J. Brooks, "Clinical and [(18F)]dopa PET findings in early Parkinson's disease," *Journal of Neurology Neurosurgery and Psychiatry*, vol. 59, no. 6, pp. 597–600, 1995.

[98] J. V. Hindle, "Ageing, neurodegeneration and Parkinson's disease," *Age and Ageing*, vol. 39, no. 2, pp. 156–161, 2010.

[99] J. Booij and H. W. Berendse, "Monitoring therapeutic effects in Parkinson's disease by serial imaging of the nigrostriatal dopaminergic pathway," *Journal of the Neurological Sciences*, vol. 310, no. 1-2, pp. 40–43, 2011.

[100] I. U. Isaias, R. Benti, R. Cilia et al., "[^{123}I]FP-CIT striatal binding in early Parkinson's disease patients with tremor vs. akinetic-rigid onset," *NeuroReport*, vol. 18, no. 14, pp. 1499–1502, 2007.

[101] R. Buchert, G. Berding, F. Wilke et al., "IBZM tool: a fully automated expert system for the evaluation of IBZM SPECT studies," *European Journal of Nuclear Medicine and Molecular Imaging*, vol. 33, no. 9, pp. 1073–1083, 2006.

[102] H. Fukuyama, "Is ^{123}I-MIBG cardiac scintigraphy a surrogate marker for Parkinson's disease?" *European Journal of Nuclear Medicine and Molecular Imaging*, vol. 37, no. 1, pp. 1–2, 2010.

Hindawi Publishing Corporation
Journal of Biomedicine and Biotechnology
Volume 2012, Article ID 419402, 10 pages
doi:10.1155/2012/419402

Review Article

Molecular Imaging in Therapeutic Efficacy Assessment of Targeted Therapy for Nonsmall Cell Lung Cancer

Yanni Hu,[1,2,3,4] Mei Tian,[1,2,3,4] and Hong Zhang[1,2,3,4]

[1] *Department of Nuclear Medicine, Second Affiliated Hospital of Zhejiang University School of Medicine, Hangzhou 310009, Zhejiang, China*
[2] *Medical PET Center, Zhejiang University, Hangzhou 310009, China*
[3] *Institute of Nuclear Medicine and Molecular Imaging, Zhejiang University, Hangzhou 310009, China*
[4] *Key Laboratory of Medical Molecular Imaging of Zhejiang Province, Hangzhou 310009, China*

Correspondence should be addressed to Hong Zhang, hzhang21@gmail.com

Received 28 December 2011; Accepted 30 January 2012

Academic Editor: Yasuhisa Fujibayashi

Membrane distillation is a thermally driven membrane process for seawater desalination and purification at moderate temperatures and pressures. A hydrophobic micro-porous membrane is used in this process, which separates hot and cold water, allowing water vapor to pass through; while restricting the movement of liquid water, due to its hydrophobic nature. This paper provides an experimental investigation of heat and mass transfer in tubular membrane module for water desalination. Different operating parameters have been examined to determine the mass transport mechanism of water vapor. Based on the experimental results, the effects of operating parameters on permeate flux and the heat transfer analysis have been presented and discussed in details.

1. Introduction

Lung cancer is one of the most common cancers in the world, as well as the leading cause of cancer death in men and the second leading cause in females globally [1]. Nonsmall cell lung cancer (NSCLC) accounts for more than 85% of all lung cancers [2]. The prevailing treatment options for NSCLC comprise surgery, radiotherapy, and chemotherapy, used either alone or in combination. Although local treatment modalities like surgery and radiotherapy can provide the chance for cure in early stages of NSCLC, about 54% NSCLC patients present with a metastasis disease at diagnosis, with an overall 5-year relative survival 3.8%, as estimated in 17 SEER geographic areas in America during 2001–2007 [3]. However, the option for these patients with advanced NSCLC whose lesions are mostly unresectable is limited to systemic therapy, where chemotherapy plays a predominant role. The use of chemotherapy in the treatment of this frustrating malignancy, which had a median survival measured in weeks or months in early days [4], was once a controversial issue concerning reproducible toxicity and questionable activity [4–6]. However, with validations of increasing publications of meta-analyses and randomized trials, especially with the advent of novel cytotoxic drugs with less toxicity and more activity, chemotherapy has become the mainstream of the treatment for advanced NSCLC. As an updated meta-analysis of data from 2714 patients of 16 randomized controlled trials revealed, compared with supportive care alone, chemotherapy with supportive care improves 1-year survival rate from 20% to 29% in all patients with advanced NSCLC [7]. Chemotherapy including platinum agents and the third generation drugs produces a cytotoxic effect by blocking cell division or DNA replication. Lots of randomized clinical studies in an effort to improve survival and life quality focused on the efficacy of differing combinations of chemotherapeutic drugs and revealed that variant combinations of chemotherapy agents produce similar response rate and survival [8, 9]. It is generally accepted that the efficacy of chemotherapy for advanced NSCLC has reached a plateau [10], with a response rate of 25–35%, time to progression (TTP, the time from randomization until objective tumor progression) 4–6 months, a 1-year survival

rate of 30–40%, and a median survival of 8–10 months [11]. Overall, the prognosis for advanced NSCLC remains poor.

With increasingly researches on molecular pathways of NSCLC in the last decade, aberrations in signaling pathways and molecules of tumor cells which promote tumor survival, proliferation, metastasis, and neovascularization have come to light. The advent of targeted therapy which acts selectively on the tumor-specific molecular pathways, and biomarkers detection which indicates a likely response to a specific therapy and guides the treatment choice [12], has brought the treatment strategy for NSCLC from empiricism into a new era of personalized therapy. The management of tumor is not "trial and error" modality any longer, but more predictive and efficient, with enhanced sensitivity to therapy and reduced unnecessary toxic effect and costs of likely ineffective treatment [13]. Targeted agents, composing mostly small molecule inhibitors and monoclonals antibodies, block signaling pathways by binding to intracellular domain to inhibit downstream signaling or to extracellular domain of surface receptor and activating immune mechanisms [14]. The target-signaling pathways or molecules such as epidermal growth factor receptor (EGFR) and vascular endothelial growth factor receptor (VEGFR) have already yielded significant improvements in response rate and progression-free survival (PFS, the time from randomization until objective tumor progression or death) used alone or in combination with chemotherapy compared with standard chemotherapy alone in large randomized clinical studies [15–19], and drugs of these categories such as erlotinib and bevacizumab have obtained FDA approval and have been recommended by National Comprehensive Cancer Center Network (NCCN) guidelines for subgroups of advanced and metastatic NSCLC. Many other targeted drugs acting on various pathways, for instance, heat shock protein (HSP)-90 inhibitors, insulin growth factor-1 receptor (IGF-1R) inhibitor, poly(ADP-ribose) polymerase (PARP) inhibitors, mammalian target of rapamycin (mTOR) inhibitors, histone deacetylase inhibitors and anaplastic lymphoma kinase (ALK) inhibitors, have also shown promising prospect in clinical trials [20]. Recent reviews have been published of development on these targeted therapies for NSCLC [21, 22].

Despite the ever-increasing novel drugs and differing combinations of standard drugs for the improvement of survival of the patients with advanced NSCLC, a significant proportion of patients exhibit or acquire resistance and eventually experience progression [23]. Even in patients with a positive predictive biomarker undergoing a targeted therapy that is likely to be effective, primary resistance is shown in about 30% overall, and disease recurrence occurs uniformly in patients with an initial response [24–27]. Moreover, although EGFR mutations in tumors are believed to be an important predictor of response to EGFR inhibitors, studies demonstrate that patients who benefit from EGFR inhibitors are not limited to those whose tumors have EGFR mutations [28]. Therefore, valid strategy for response prediction to help clinical management is still required.

Furthermore, after disease progression, patients often get to be unsuitable to receive further treatment due to declining performance status and increased symptom burden [29–32]. Therefore, it is of great importance to identify early whether a patient is likely to respond to the current therapy and whether a resistance has occurs, for it enables an early termination of ineffective therapy and avoidance of unnecessary toxic effect or costs for those nonresponders, as well as more chance to receive a more likely to be effective therapy. In addition, as more novel drugs come into clinical trials with inconclusive efficacy, an early and valid identification of therapeutic efficacy helps to shorten the time for assessment and reduce cost.

While improved survival has been widely accepted as the "gold standard" for establishing clinical benefit in clinical trials, as an ultimate and long-term outcome, survival is not practical for early identification of therapy effect. As a consequence, valid surrogates for shortening the time for therapeutic efficacy assessment have been applied in clinical trials, which can reflect change of tumor and help to make prediction of long-term outcomes. Like tumor markers such as CA-125 in ovarian cancer has been already used as standard markers in the objective response assessment [33], in the context of lung cancer today, imaging that can provide an insight of tumor condition has long been applied in measurement of antitumor effect. The imaging-based endpoints like objective response, PFS, and TTP are commonly used in stage II and III clinical trials. Given the importance of early assessment of therapeutic efficacy in clinical practices and investigational therapies, appropriate imaging modalities as an essential part in response assessment are essential. In this review, we will discuss the current imaging modalities, especially molecular imaging, that applied in efficacy evaluation of targeted therapy for advanced NSCLC.

2. Current Imaging Methods in Efficacy Assessment of Treatment for NSCLC

2.1. Computed Tomography (CT). With the rapid development of cytotoxic drugs since 1960s, there has been an intense need for an acknowledged standard in anti-tumor effect assessment. Since the World Health Organization (WHO) first introduced response criteria of cancer in 1979 [34] in an effort to introduce a common language to report results of investigational antitumor therapies, anatomical imaging has become the standard way to determine oncology response in solid tumors. Because of some limitations of the WHO criteria, an international working group published the Response Evaluation Criteria in Solid Tumors (RECIST) guideline in 2000, and updated it in 2009. These criteria have determined tumor response as complete response, partial response, progression disease, and stable disease, according to the change of target lesions size, and have become the main standards in clinical trials of anti-tumor therapies for NSCLC where the primary endpoints are objective response or progression.

Tumor response is believed to be an indicator of drug effect in traditional anti-tumor trials and was approved by the FDA in 1996 to be used in investigational oncological

treatments, as to accelerate approval of new anti-tumor drugs [35], for a reason that tumor is not likely to shrinkage spontaneously. Lots of trials demonstrated that objective tumor response is associated with longer survival in chemotherapy for solid tumors [36–39], yet whether tumor response can predict therapy efficacy remains an issue open to disputes [40–42]. At the same time, other endpoints such as disease control rate (consisting of CR, PR, and SD), PFS, or TTP [43] are increasingly proved to be more valid measures for therapy efficacy assessment in clinical trials [44–46]. These anatomy-based endpoints, specified by those criteria, are commonly used in investigational trials of advanced NSCLC. CT with its high resolution, moderate costs, and availability has been historically the mainstay in measurement of lung cancer sizes and still the standard method in present. In addition, it is also the recommended method in clinic for surveillance and instructs clinical management.

However, since targeted therapy came into evaluation, there are concerns about whether morphology-based criteria that was established in cytotoxic therapy trials is an appropriate metrics in efficacy assessment of targeted-therapy, where tumor shrinkage is not necessary due to an effect of delaying the tumor growth. It has been observed in diverse tumors types like metastatic renal cell cancer and GIST [47, 48], as well as NSCLC [49–51], that relationship between tumor regression and survival varied widely. Because stability of disease cannot be interpreted as ineffectiveness of a targeted therapy, the response defined in change of dimension as a measure of efficacy in targeted therapy is inappropriate. In this case, endpoints such as PFS or TTP, which focus on progression rather than regression, might be more appropriate and are commonly utilized in clinical studies of targeted therapy. However, these metrics associated with progression need regular evaluation in trials and cannot provide information about treatment efficacy before tumor enlargement occurs and hence cannot be an early predictor of treatment efficacy, which is vital to optimizing a patient's management in clinic or improving efficiency of clinical trials.

2.2. Dynamic Contrast-Enhanced CT (DCE CT). Regarding the limitation of size-based methodology, metrics other than size is also proposed to provide information about tumor response to targeted therapy. DCE CT is also known as functional CT, which can provide information about perfusion. Tumor perfusion versus whole-body perfusion can be measured on images generated following an intravenous injection of a contrast agent. A reduction in tumor perfusion is demonstrated in NSCLC patients responding to chemotherapy [52]. Similar result is also yielded in a study on targeted therapy that has an effect of antiangiogenesis for NXCLC in monitoring response of NSCLC to [53]. In this study, tumor perfusion is measured with DCE CT at week 3 and week 6 after starting treatment, and a reduction of tumor blood flow is observed at week 6. Meanwhile, tumor density used in combination with size has become a new imaging paradigm in assessment of targeted therapy for GIST [54] and metastatic renal cell carcinoma [55]. However, since there is no such study or criteria in NSCLC, whether combination of tumor density and size is a feasible metrics in evaluation of therapy for NSCLC is still unclear.

2.3. Dynamic Contrast-Enhanced Magnetic Resonance Imaging (DCE MRI). Although MRI used limitedly in imaging of NSCLC, DCE MRI has been used in evaluation of NSCLC perfusion. With this modality, quantitative parameters reflecting tumor microvessel perfusion, permeability can be obtained [56]. DCE MRI has been verified as a potential role in efficacy assessment of both cytotoxic agents and antiangiogenesis targeted-therapy for NSCLC [57, 58].

2.4. Magnetic Resonance Spectroscopy (MRS). By utilizing the special property of nuclear isotopes in a strong magnetic field, MRS gives information of tissue metabolites [59]. As a molecular imaging modality, MRS has a bright prospect in personalized medicine. It has been reported that the accuracy in discrimination between normal lung and each cancer type with proton MRS (1H MRS) was up to 81.5 to 90.7% [60]. However, there is no utilization of MRS available in response assessment area in NSCLC up to date.

2.5. Positron Emission Tomography (PET). The advent of PET brings about a totally new era of molecular imaging. By detecting the distribution of the radionuclide-labeled tracer that is involved with some specific physiological process within the body, PET makes metabolic change possible to be visualized in vivo, which is fundamentally different from conventional anatomy-based imaging modalities. Because biological features of tumor tissues are usually different from that of normal tissues, this functional imaging technology that makes qualitative, quantitative, and semiquantitative analysis available is especially useful in oncology imaging, playing a role in disease diagnosis, staging and restaging, and therapeutic response evaluation. In addition, since there are various biologic compounds participating different physiological processes, by developing diverse radionuclide-labeled tracers, we can acquire tumor information in an optimal way according to specific tumor or explore different physiologic features of tumor. While depicting an imaging on molecular characteristics of different tissues, PET can sometimes be imprecise in anatomical location. For this reason fusion of PET with traditional modality is developed and comes into application, combining molecular formations with high-resolution anatomical structures. The multimodalities of PET/CT and PET/MRI are currently in practical application with promising prospect.

The positron-emitting isotopes of oxygen, carbon, nitrogen, and fluorine which are the building components of biological substances are the commonly used labels for tracers for PET. A large spectrum of radiopharmaceuticals has been developed associating with various metabolic pathways. 2-[^{18}F] fluoro-2-deoxy-D-glucose (^{18}F-FDG) reflecting glucose metabolism is most widely used among all the tracers, with general acceptance in assessment of oncologic therapies. ^{18}F-FDG is a modified glucose molecular where the hydroxylgroup (OH) of glucose is replaced with ^{18}F, which has

a half-life of 110 minutes. Once being taken up into a cell, it cannot be further metabolized. Therefore, different levels of accumulation of ^{18}F-FDG are reflections of diverse energetic need. It is rational to consider that malignant cells will decrease glucose requirement due to direct or indirect damages. Clinical investigations have validated a reduction in ^{18}F-FDG uptake that occurs in oncological tissues after anticancer treatment in various tumors including NSCLC and is closely correlated with final outcome of therapy [61]. 3-[^{18}F] fluoro-3-deoxy-L-thymidine (^{18}F-FLT), a thymidine analogue, as a biomarker of proliferation, is another tracer often investigated in studies on NSCLC.

Radioimmunoimaging has been developed in recent years with increasing knowledge of molecular pathways of cancer cells. Based on a fundamental much alike targeted therapy, by modifying the tracer which target specific molecular of tumor cells, radioimmunoimaging helps provide tumor molecular information and thereby has a predictive value in response to targeted therapy and contributes to individualized medicine [62–64].

Since metabolic change in tumor always takes place earlier than anatomic change, PET has great advantage in early evaluation of treatment efficacy. Regarding to the widespread utilization of PET in assessment of therapy assessment, European Organization for Research and Treatment of Cancer (EORTC) and the National Cancer Institute (NCI) proposed guidelines in 1999 and 2006, respectively, intending to standardize the methodology of data acquisition and analysis of ^{18}F-FDG PET scans [65, 66]. A prospective trial assessed the relationship between PET-evaluated response and clinical outcomes by evaluating on-treatment changes in ^{18}F-FDG and ^{18}F-FLT PET imaging among patients with NSCLC treated with targeted therapy and verified that it is possible to achieve high reproducibility of scan acquisition methodology, as long as strict imaging compliance guidelines are mandated in the study protocol [67]. Furthermore, the relevance for the prediction of clinical benefit of targeted therapy using different quantitative parameters for PET with both ^{18}F-FDG and ^{18}F-FLT in patients with advanced NSCLC, early ^{18}F-FDG PET and ^{18}F-FLT PET can predict PFS regardless of the method used for standardized uptake value (SUV) calculation although several indicators like SUV_{max} measured with ^{18}F-FDG might be more robust to use for early response prediction [68]. All these efforts offer a promising prospect of robust application of this new modality in efficacy evaluation of tumors. With more targeted drugs acting on various mechanisms increasingly coming out, as well as diverse tumor metabolic characteristics, further researches are still required to offer a valid methodology for PET as a biomarker for early evaluation of targeted therapy.

While conventional imaging modalities are fraught with difficulties in early response assessment to cytostatic targeted therapy, ^{18}F-FDG PET meets these challenges both theoretically and practically. Although the reliability and powerfulness of ^{18}F-FDG PET in predicting therapeutic efficacy in NSCLC has been verified in chemotherapy in the last few years [69–72], there are fewer clinical studies on its efficiency in early prediction of outcome in targeted therapy except for gastrointestinal stromal tumor (GIST) [73–75]. However, preclinical studies have shown evidences that PET may be a promising biomarker for targeted therapies [76–79].

2.6. Single-Photon Emission-Computed Tomography (SPECT). SPECT is also a molecular imaging technique, detecting tracer labeled with radionuclide emitting single gamma rays. The dual modality of SPECT/CT has been used in lung cancer diagnosis [80]. The most investigated trace used in treatment of lung cancer is ^{99m}Tc-methoxyisobutylisonitrile (^{99m}Tc-MIBI), which is reported to play a role in recognition of chemoresistance of tumor cell [81] and thus has been used in prediction of response to chemotherapy for NSCLC. A systematic review of the literature revealed that ^{99m}Tc-MIBI SPECT can accurately identify patients with lung cancer who will respond to chemotherapy, with an overall sensitivity of 94%, specificity of 90%, and accuracy of 92% [82]. In comparison with PET, SPECT has a lower sensitivity, and the use of SPECT in assessment of treatment of NSCLC is still limited.

2.7. Ultrasound. Ultrasound generates images by detecting changes of sound speed caused by various tissue densities. Since lung is filled with air which hardly echoes, ultrasound, together with a more recent utilization as endoscopic ultrasound (EUS), is not a usual technique used in NSCLC except for mediastinal staging or guiding fine needle aspiration or a metastasis lesion evaluation.

3. Molecular Imaging in Response Evaluation of Targeted Therapy for NSCLC

Molecular imaging modalities are now under evaluation in targeted therapy for advanced NSCLC although limitedly. In various agents targeting diverse pathways of cancer cell, there are only several agents targeting EGFR, and VEGFR pathways have been evaluated by molecular imaging, entirely PET in clinical or preclinical studies.

3.1. EGFR Pathway. EGFR (also known as HER [human EGF receptor] and ErbB1) is member of the human epidermal growth factor receptor family. By triggering the downstream signaling pathways involving phosphatidylinositol-3-OH kinase (PI(3)K)/AKT/mammalian target of rapamycin (mTOR) and RAS/RAF/MEK and signal transducer and activator of transcription (STAT) [83], the activation of EGFR contributes to tumor growth and progression, including proliferation, maturation, angiogenesis, invasion, metastasis, and inhibition of apoptosis [84]. Overexpression or aberrant activation of EGFR is frequent in NSCLC [85, 86], and inhibition of EGFR is a rational anticancer strategy, which have been validated in clinical practice. EGFR is a transmembrane glycoprotein, consisting of an extracellular ligand-binding domain, a transmembrane region, and an intracellular tyrosine kinase domain [87]. Two classes of agents targeting EGFR are used in clinical practice: tyrosine kinase inhibitors (TKIs) and monoclonal antibodies.

3.1.1. EGFR TKIs. TKIs are small molecules that inhibit phosphorylation of EGFR intracellular tyrosine kinase by competing with ATP, leading to cell circle delay, inhibition of angiogenesis and apoptosis [88, 89]. In all the agents of EGFR TKIs being evaluated in clinical or preclinical studies, erlotinib is the only EGFR-targeting agent approved by FDA for the treatment of NSCLC. Gefitinib is another EGFR TKI that has been extensively investigated.

The value of ^{18}F-FDG PET in predicting efficacy of EGFR antagonist was validated in a preclinical study performed in 2006 [77]. A dramatic decrease in ^{18}F-FDG uptake was observed at as early as 2 hours after treatment in gefitinib-sensitive cell lines, while no measurable changes in ^{18}F-FDG uptake were seen in gefitinib-resistant cells.

A clinical study for early prediction of the efficacy of gefitinib for NSCLC conducted in 2007 monitored tumor response by both CT and ^{18}F-FDG PET [90]. In this study, two of the five NSCLC patients who exhibited stable disease according to RECIST criteria at 4 weeks after initiation of treatment but with long-term PFS (12.9 and 12.5 months) showed a marked decrease in ^{18}F-FDG uptake (measured by SUV_{max}) within 2 days of treatment initiation, while SUV_{max} increase on day 2 had proved progressive disease based on CT evaluation. Although conclusions can be hardly drawn due to the small sample size, it did show the potential of ^{18}F-FDG PET in early response evaluation for targeted therapy.

Another study observed an increase of SUV_{max} as measured with ^{18}F-FDG PET after discontinuation of treatment with erlotinib or gefitinib, due to progressive disease according to RECIST, and reintroduction of erlotinib or gefitinib again resulted in decreases in SUV_{max} [91]. A subsequent introduction of everolimus, the mTOR inhibitor, led to further decrease in SUV_{max} and tumor size after 3 weeks of combination therapy in 5 of the 10 patients, suggesting that some tumor cells remain sensitive to EGFR blockage after PD occurs according to RECIST.

A prospective multicenter trial evaluated response of seventy-four patients with advanced NSCLC to erlotinib treatment with only PET/CT scans [62], further verified early ^{18}F-FDG PET response is associated with improved PFS and OS, even in the absence of subsequent RECST evaluation with CT.

^{18}F-FLT PET was also applied to early detection of targeted therapy efficacy. A striking and reproducible decrease in ^{18}F-FLT uptake was exhibited in erlotinib-sensitive tumors after two days of treatment and translated into dramatic tumor shrinkage four days later [92]. Another phase II clinical trial assessed the use of ^{18}F-FDG PET and ^{18}F-FLT PET in NSCLC patients following erlotinib therapy [93]. This study enrolled thirty-four previously untreated patients, demonstrated an that early ^{18}F-FDG response (cutoff value: 30% reduction in the peak standardized uptake value) predicted significantly longer PFS, OS, and nonprogression after 6 weeks of therapy with erlotinib, while early ^{18}F-FLT response was only associated with significantly longer PFS. In particular, this study demonstrated early ^{18}F-FDG PET can identify those patients who could be benefited from erlotinib even without the knowledge of EGFR mutation.

3.1.2. Monoclonal Antibodies. EGFR-directed monoclonal antibodies exert an anticancer action by binding to the extracellular domain of the EGFR. Among all EGFR antibodies, cetuximab has been investigated extensively in treatment of NSCLC. A large phase III randomized trial shows that adding cetuximab to chemotherapy (cisplatin/vinorelbine) slightly increases overall survival (11.3 versus 10.1 months, $P = 0.04$) [94]. Other monoclonal antibodies directing EGFR are still in investigation in clinical trials.

A phase II trial evaluating ^{18}F-FDG PET and CT as endpoints for assessing efficacy of cetuximab in combination with chemotherapy for advanced gastric or gastroesophageal junction adenocarcinoma showed that ^{18}F-FDG PET could correctly differentiate responders from nonresponders, with a median TTP 16 months and 11 months, respectively [95]. No clinical studies have been performed regarding molecular imaging in treatment of NSCLC with EGFR-targeted monoclonal antibodies, but the use of ^{18}F-FLT PET has been investigated in a study of human lung cancer xenografts [96] demonstrated that SUV_{max} in tumor tissue significantly decreased versus nontreated control on day 3 after treatment with cetuximab ($P < 0.01$), while no difference in CT image was visualized until day 8.

3.2. VEGFR Pathway. VEGFR pathway plays an important role in angiogenesis, a process of endothelial cell division and migration resulting in formation of new capillaries [97]. Angiogenesis is critical to tumor growth and metastasis, and enhanced VEGF and its receptors expression is found in a variety of tumors [98]; thus, blockage of this pathway is an attractive strategy for anticancer treatment. VEGFR is a transmembrane receptor tyrosine kinase specifically expressed at the surface of endothelial cell [99]. Various antiangiogenic agents have developed in the last few years, and VEGFR-directed monoclonal antibodies and VEGFR TKI are the two classes of VEGFR agents currently used in studies of NSCLC antiangiogenesis treatment. Use of DCE MRI imaging as well as PET has been evaluated in this therapy concerning its effects on tumor vasculature. Despite the limit use of DCE MRI in evaluation of antiangiogenesis in NSCLC, DCE MRI is frequently used in other tumors. As a review exhibited, anti-angiogenic therapies do not always result in reductions of blood flow in the short term, and DCE MRI kinetic response relationships are not universally strong across all tissue sites for all drugs [100]. In treatment for patients with cancer other than NSCLC, ^{18}F-FDG PET exhibited a promising prospect in monitoring antiangiogenesis effect of VEGFR-directed pathway [100]. In VEGFR TKI no study with molecular imaging is available at present.

Bevacizumab is a humanized monoclonal antibody directed at VEGF. It gained FDA approval based on an Eastern Cooperative Oncology Group (ECOG) conducted study [101], in which an increase in survival (12.3 versus 10.3 months) was observed in selected NSCLC patients when added Bevacizumab to standard chemotherapy.

Forty-seven chemonaive patients with advanced NSCLC treated with bevacizumab and erlotinib underwent both ^{18}F-FDG PET and DCE MRI scan after 3 weeks of treatment [58], >20% decrease in SUV as measured with ^{18}F-FDG PET is well predicative for longer PFS (9.7 versus 2.8 months; $P = 0.01$), while >40% decrease in K^{trans} (the endothelial transfer constant) as assessed by DCE MRI did not predict for longer PFS though most tumors have a decrease in K^{trans} value after 3 weeks of treatment.

4. Conclusions and Future Directions

This paper reviews the currently available studies of molecular imaging used as early prediction of efficacy of targeted therapy for patients with NSCLC. For patients with advanced NSCLC, although the application of chemotherapy does prolong the OS comparing with supportive care alone [7], the prognosis of NSCLC remains poor, with a median survival of mere 8–10 months [11]. Nevertheless, it is validated that different combinations of chemotherapeutic drugs produce similar response rate and survival [7, 8] and the efficacy of chemotherapy for NSCLC is generally accepted as having reached a plateau. Targeted therapy, developing with the increasing knowledge of tumor molecular pathways, has an approach of blocking specific pathways of tumor cells instead of conventional cytotoxic effect. This new therapy for NSCLC has been investigated in many clinical trials and yielded significant improvement in RR and PFS. As a focus of current studies on therapy for NSCLC, increasing diverse targeted agents is now being investigated in clinical trials or preclinical studies. Meanwhile, the development of targeted agents highlights the need of a robust modality in efficacy assessment because the current prevailing anatomy-based criteria established on the basis of numerous previous studies on chemotherapy can no longer satisfy the requirement for early diagnosis.

Along with molecular metabolic mechanisms of tumor cells that increasingly come to light, rapid development of molecular imaging has taken place in recent years [102]. By directly visualizing and measuring the biological process in vivo [103], molecular imaging enables early assessment of response to anticancer treatment. Although molecular imaging modalities such as PET, SPECT, and MRS are involved in diagnosis of NSCLC, PET with different radiotracers is the primary modality that has been investigated in early predication of targeted therapy for NSCLC. Despite limited studies are available by now regarding the application of PET in this area, the outcome is encouraging, exhibiting utilization of PET in response evaluation, and outcome prediction is feasible and accurate. Obviously, more investigations are needed. More researches on molecular imaging in early prediction of targeted therapy efficacy should be done considering encouraging outcomes of the available studies and infinite prospect of diverse molecular imaging modalities.

Conflict of Interests

The authors declare that they have no conflict of interests.

Acknowledgment

This work is partly sponsored by Grants from the Zhejiang Provincial Natural Science Foundation of China (Z2110230), Health Bureau of Zhejiang Province (2010ZA075 and 2011ZDA013), National Science Foundation of China (NSFC) (no. 81101023, 81170306, and 81173468), and Ministry of Science and Technology of China (2011CB504400 and 2012BAI13B06).

References

[1] A. Jemal, F. Bray, M. M. Center, J. Ferlay, E. Ward, and D. Forman, "Global cancer statistics," *Cancer Journal for Clinicians*, vol. 61, no. 2, pp. 69–90, 2011.

[2] S. H. Landis, T. Murray, S. Bolden, and P. A. Wingo, "Cancer Statistics, 1999," *Ca-A Cancer Journal for Clinicians*, vol. 49, no. 1, pp. 8–31, 1999.

[3] National Cancer Institute, Surveillance, Epidemiology and End Results, http://seer.cancer.gov/.

[4] E. E. Vokes, J. D. Bitran, and N. J. Vogelzang, "Chemotherapy for non-small cell lung cancer; The continuing challenge," *Chest*, vol. 99, no. 6, pp. 1326–1328, 1991.

[5] C. M. Haskell, "Chemotherapy and survival of patients with non-small cell lung cancer; A contrary view," *Chest*, vol. 99, no. 6, pp. 1325–1326, 1991.

[6] G. Buccheri, "Chemotherapy and survival in non-small cell lung cancer; The old vexata questio," *Chest*, vol. 99, no. 6, pp. 1328–1329, 1991.

[7] S. Burdett, S. Burdett, R. Stephens et al., "Chemotherapy in addition to supportive care improves survival in advanced non-small-cell lung cancer: a systematic review and meta-analysis of individual patient data from 16 randomized controlled trials," *Journal of Clinical Oncology*, vol. 26, no. 28, pp. 4617–4625, 2008.

[8] F. Grossi, M. Aita, C. Defferrari et al., "Impact of third-generation drugs on the activity of first-line chemotherapy in advanced non-small cell lung cancer: a meta-analytical approach," *Oncologist*, vol. 14, no. 5, pp. 497–510, 2009.

[9] J. H. Schiller, D. Harrington, C. P. Belani et al., "Comparison of four chemotherapy regimens for advanced non-small-cell lung cancer," *New England Journal of Medicine*, vol. 346, no. 2, pp. 92–98, 2002.

[10] F. A. Shepherd, "Chemotherapy for non-small cell lung cancer: have we reached a new plateau?" *Seminars in Oncology*, vol. 26, supplement 4, pp. 3–11, 1999.

[11] A. Martoni, A. Marino, F. Sperandi et al., "Multicentre randomised phase III study comparing the same dose and schedule of cisplatin plus the same schedule of vinorelbine or gemcitabine in advanced non-small cell lung cancer," *European Journal of Cancer*, vol. 41, no. 1, pp. 81–92, 2005.

[12] M. J. Duffy, "Predictive markers in breast and other cancers: a review," *Clinical Chemistry*, vol. 51, no. 3, pp. 494–503, 2005.

[13] M. J. Duffy and J. Crown, "A personalized approach to cancer treatment: how biomarkers can help," *Clinical Chemistry*, vol. 54, no. 11, pp. 1770–1779, 2008.

[14] H. Francis and B. Solomon, "The current status of targeted therapy for non-small cell lung cancer," *Internal Medicine Journal*, vol. 40, no. 9, pp. 611–618, 2010.

[15] T. S. Mok, Y. L. Wu, S. Thongprasert et al., "Gefitinib or carboplatin-paclitaxel in pulmonary adenocarcinoma," *New England Journal of Medicine*, vol. 361, no. 10, pp. 947–957, 2009.

[16] D. H. Johnson, L. Fehrenbacher, W. F. Novotny et al., "Randomized phase II trial comparing bevacizumab plus carboplatin and paclitaxel with carboplatin and paclitaxel alone in previously untreated locally advanced or metastatic non-small-cell lung cancer," *Journal of Clinical Oncology*, vol. 22, no. 11, pp. 2184–2191, 2004.

[17] A. Sandler, R. Gray, M. C. Perry et al., "Paclitaxel-carboplatin alone or with bevacizumab for non-small-cell lung cancer," *New England Journal of Medicine*, vol. 355, no. 24, pp. 2542–2550, 2006.

[18] C. Gridelli, C. Butts, F. Ciardiello, R. Feld, C. Gallo, and F. Perrone, "An international, multicenter, randomized phase III study of first-line erlotinib followed by second-line cisplatin/gemcitabine versus first-line cisplatin/gemcitabine followed by second-line erlotinib in advanced non-small-cell lung cancer: treatment rationale and protocol dynamics of the TORCH trial," *Clinical Lung Cancer*, vol. 9, no. 4, pp. 235–238, 2008.

[19] M. Maemondo, A. Inoue, K. Kobayashi et al., "Gefitinib or chemotherapy for non-small-cell lung cancer with mutated EGFR," *New England Journal of Medicine*, vol. 362, no. 25, pp. 2380–2388, 2010.

[20] R. Govindan, "Summary of the proceedings from the 10th annual meeting of molecularly targeted therapy in non-small cell lung cancer," *Journal of Thoracic Oncology*, vol. 5, supplement 6, no. 12, p. S433, 2010.

[21] F. Janku, I. Garrido-Laguna, L. B. Petruzelka, D. J. Stewart, and R. Kurzrock, "Novel therapeutic targets in non-small cell lung cancer," *Journal of Thoracic Oncology*, vol. 6, no. 9, pp. 1601–1612, 2011.

[22] J. E. Larsen, T. Cascone, D. E. Gerber, J. V. Heymach, and J. D. Minna, "Targeted therapies for lung cancer: clinical experience and novel agents," *Cancer Journal*, vol. 17, no. 6, pp. 512–527, 2011.

[23] A. Chang, "Chemotherapy, chemoresistance and the changing treatment landscape for NSCLC," *Lung Cancer*, vol. 71, no. 1, pp. 3–10, 2011.

[24] A. Inoue, T. Suzuki, T. Fukuhara et al., "Prospective phase II study of gefitinib for chemotherapy-naïve patients with advanced non-small-cell lung cancer with epidermal growth factor receptor gene mutations," *Journal of Clinical Oncology*, vol. 24, no. 21, pp. 3340–3346, 2006.

[25] K. Yamazaki, I. Kinoshita, N. Sukoh et al., "A phase II trial of gefitinib as first-line therapy for advanced non-small cell lung cancer with epidermal growth factor receptor mutations," *British Journal of Cancer*, vol. 95, no. 8, pp. 998–1004, 2006.

[26] D. M. Jackman, B. Y. Yeap, N. I. Lindeman et al., "Phase II clinical trial of chemotherapy-naïve patients > or = 70 years of age treated with erlotinib for advanced non-small-cell lung cancer," *Journal of Clinical Oncology*, vol. 25, no. 7, pp. 760–766, 2007.

[27] N. Sunaga, Y. Tomizawa, N. Yanagitani et al., "Phase II prospective study of the efficacy of gefitinib for the treatment of stage III/IV non-small cell lung cancer with EGFR mutations, irrespective of previous chemotherapy," *Lung Cancer*, vol. 56, no. 3, pp. 383–389, 2007.

[28] L. V. Sequist, D. W. Bell, T. J. Lynch, and D. A. Haber, "Molecular predictors of response to epidermal growth factor receptor antagonists in non-small-cell lung cancer," *Journal of Clinical Oncology*, vol. 25, no. 5, pp. 587–595, 2007.

[29] P. M. Fidias, S. R. Dakhil, A. P. Lyss et al., "Phase III study of immediate compared with delayed docetaxel after front-line therapy with gemcitabine plus carboplatin in advanced non-small-cell lung cancer," *Journal of Clinical Oncology*, vol. 27, no. 4, pp. 591–598, 2009.

[30] T. E. Stinchcombe and M. A. Socinski, "Treatment paradigms for advanced stage non-small cell lung cancer in the era of multiple lines of therapy," *Journal of Thoracic Oncology*, vol. 4, no. 2, pp. 243–250, 2009.

[31] G. V. Scagliotti, P. Parikh, J. Von Pawel et al., "Phase III study comparing cisplatin plus gemcitabine with cisplatin plus pemetrexed in chemotherapy-naive patients with advanced-stage non-small-cell lung cancer," *Journal of Clinical Oncology*, vol. 26, no. 21, pp. 3543–3551, 2008.

[32] O. P. Joon, S. W. Kim, S. A. Jin et al., "Phase III trial of two versus four additional cycles in patients who are nonprogressive after two cycles of platinum-based chemotherapy in non-small-cell lung cancer," *Journal of Clinical Oncology*, vol. 25, no. 33, pp. 5233–5239, 2007.

[33] I. Vergote, G. J. S. Rustin, E. A. Eisenhauer et al., "Re: new guidelines to evaluate the response to treatment in solid tumors [ovarian cancer]," *Journal of the National Cancer Institute*, vol. 92, no. 18, pp. 1534–1535, 2000.

[34] World Health Organization, *WHO Handbook for Reporting Results of Cancer Treatment*, World Health Organization, Geneva, Switzerland, 1979.

[35] Food and Drug Administration, *Reinventing the Regulation of Cancer Drugs: Accelerating Approval and Expanding Access*, National Performance Review, Washington, DC, USA, 1996.

[36] A. B. Sandler, J. Nemunaitis, C. Denham et al., "Phase III trial of gemcitabine plus cisplatin versus cisplatin alone in patients with locally advanced or metastatic non-small-cell lung cancer," *Journal of Clinical Oncology*, vol. 18, no. 1, pp. 122–130, 2000.

[37] C. Sederholm, G. Hillerdal, K. Lamberg et al., "Phase III trial of gemcitabine plus carboplatin versus single-agent gemcitabine in the treatment of locally advanced or metastatic non-small-cell lung cancer: the Swedish lung cancer study group," *Journal of Clinical Oncology*, vol. 23, no. 33, pp. 8380–8388, 2005.

[38] C. M. R. Lima, N. A. Rizvi, C. Zhang et al., "Randomized phase II trial of gemcitabine plus irinotecan or docetaxel in stage IIIB or stage IV NSCLC," *Annals of Oncology*, vol. 15, no. 3, pp. 410–418, 2004.

[39] F. Grossi, F. de Marinis, V. Gebbia et al., "A randomized phase II trial of two sequential schedules of docetaxel and cisplatin followed by gemcitabine in patients with advanced non-small-cell lung cancer," *Cancer Chemotherapy and Pharmacology*, vol. 69, no. 2, pp. 369–375, 2012.

[40] K. R. Birchard, J. K. Hoang, J. E. Herndon Jr, and E. F. Patz Jr, "Early changes in tumor size in patients treated for advanced stage nonsmall cell lung cancer do not correlate with survival," *Cancer*, vol. 115, no. 3, pp. 581–586, 2009.

[41] M. Buyse and P. Piedbois, "On the relationship between response to treatment and survival time," *Statistics in Medicine*, vol. 15, no. 24, pp. 2797–2812, 1996.

[42] M. Buyse, P. Thirion, R. W. Carlson, T. Burzykowski, G. Molenberghs, and P. Piedbois, "Relation between tumour response to first-line chemotherapy and survival in advanced colorectal cancer: a meta-analysis," *The Lancet*, vol. 356, no. 9227, pp. 373–378, 2000.

[43] Administration FaD, *Guidance for Industry Clinical Trial Endpoints for the Approval of Cancer Drugs and Biologics*, Services UDoHaH, Washington, DC, USA, 2005.

[44] M. Buyse, T. Burzykowski, K. Carroll et al., "Progression-free survival is a surrogate for survival in advanced colorectal

cancer," *Journal of Clinical Oncology*, vol. 25, no. 33, pp. 5218–5224, 2007.

[45] P. N. Lara Jr, M. W. Redman, K. Kelly et al., "Disease control rate at 8 weeks predicts clinical benefit in advanced non-small-cell lung cancer: results from Southwest oncology group randomized trials," *Journal of Clinical Oncology*, vol. 26, no. 3, pp. 463–467, 2008.

[46] Q. Shi and D. J. Sargent, "Meta-analysis for the evaluation of surrogate endpoints in cancer clinical trials," *International Journal of Clinical Oncology*, vol. 14, no. 2, pp. 102–111, 2009.

[47] H. Choi, "Critical issues in response evaluation on computed tomography: lessons from the gastrointestinal stromal tumor model," *Current Oncology Reports*, vol. 7, no. 4, pp. 307–311, 2005.

[48] J. C. Yang, L. Haworth, R. M. Sherry et al., "A randomized trial of bevacizumab, an anti-vascular endothelial growth factor antibody, for metastatic renal cancer," *New England Journal of Medicine*, vol. 349, no. 5, pp. 427–434, 2003.

[49] M. Fukuoka, S. Yano, G. Giaccone et al., "Multi-institutional randomized phase II trial of gefitinib for previously treated patients with advanced non-small-cell lung cancer," *Journal of Clinical Oncology*, vol. 21, no. 12, pp. 2237–2246, 2003.

[50] M. G. Kris, R. B. Natale, R. S. Herbst et al., "Efficacy of gefitinib, an inhibitor of the epidermal growth factor receptor tyrosine kinase, in symptomatic patients with non-small cell lung cancer: a randomized trial," *Journal of the American Medical Association*, vol. 290, no. 16, pp. 2149–2158, 2003.

[51] R. Perez-Soler, "Phase II clinical trial data with the epidermal growth factor receptor tyrosine kinase inhibitor erlotinib (OSI-774) in non-small-cell lung cancer," *Clinical Lung Cancer*, vol. 6, no. 1, pp. S20–S23, 2004.

[52] J. Wang, N. Wu, M. D. Cham, and Y. Song, "Tumor response in patients with advanced non-small cell lung cancer: perfusion CT evaluation of chemotherapy and radiation therapy," *American Journal of Roentgenology*, vol. 193, no. 4, pp. 1090–1096, 2009.

[53] J. S. W. Lind, M. R. Meijerink, A. M. C. Dingemans et al., "Dynamic contrast-enhanced CT in patients treated with sorafenib and erlotinib for non-small cell lung cancer: a new method of monitoring treatment?" *European Radiology*, vol. 20, no. 12, pp. 2890–2898, 2010.

[54] H. Choi, C. Charnsangavej, S. C. Faria et al., "Correlation of computed tomography and positron emission tomography in patients with metastatic gastrointestinal stromal tumor treated at a single institution with imatinib mesylate: proposal of new computed tomography response criteria," *Journal of Clinical Oncology*, vol. 25, no. 13, pp. 1753–1759, 2007.

[55] A. D. Smith, S. N. Shah, B. I. Rini, M. L. Lieber, and E. M. Remer, "Morphology, Attenuation, Size, and Structure (MASS) criteria: assessing response and predicting clinical outcome in metastatic renal cell carcinoma on antiangiogenic targeted therapy," *American Journal of Roentgenology*, vol. 194, no. 6, pp. 1470–1478, 2010.

[56] P. S. Tofts, G. Brix, D. L. Buckley et al., "Estimating kinetic parameters from dynamic contrast-enhanced T1- weighted MRI of a diffusable tracer: standardized quantities and symbols," *Journal of Magnetic Resonance Imaging*, vol. 10, no. 3, pp. 223–232, 1999.

[57] I. Lee and K. Shogen, "Mechanisms of enhanced tumoricidal efficacy of multiple small dosages of ranpirnase, the novel cytotoxic ribonuclease, on lung cancer," *Cancer Chemotherapy and Pharmacology*, vol. 62, no. 2, pp. 337–346, 2008.

[58] A. M. Dingemans, A. J. de Langen, V. van den Boogaart et al., "First-line erlotinib and bevacizumab in patients with locally advanced and/or metastatic non-small-cell lung cancer: a phase II study including molecular imaging," *Annals of Oncology*, vol. 22, no. 3, pp. 559–566, 2011.

[59] P. F. Daly and J. S. Cohen, "Magnetic resonance spectroscopy of tumors and potential in vivo clinical applications: a review," *Cancer Research*, vol. 49, no. 4, pp. 770–779, 1989.

[60] H. Hanaoka, Y. Yoshioka, I. Ito, K. Niitu, and N. Yasuda, "In vitro characterization of lung cancers by the use of 1H nuclear magnetic resonance spectroscopy of tissue extracts and discriminant factor analysis," *Magnetic Resonance in Medicine*, vol. 29, no. 4, pp. 436–440, 1993.

[61] W. A. Weber, V. Petersen, B. Schmidt et al., "Positron emission tomography in non-small-cell lung cancer: prediction of response to chemotherapy by quantitative assessment of glucose use," *Journal of Clinical Oncology*, vol. 21, no. 14, pp. 2651–2657, 2003.

[62] L. Mileshkin, R. J. Hicks, B. G.M. Hughes et al., "Changes in ^{18}F-fluorodeoxyglucose and ^{18}F-fluorodeoxythymidine positron emission tomography imaging in patients with non-small cell lung cancer treated with erlotinib," *Clinical Cancer Research*, vol. 17, no. 10, pp. 3304–3315, 2011.

[63] A. Achmad, H. Hanaoka, H. Yoshioka et al., "Predicting cetuximab accumulation in KRAS wild-type and KRAS mutant colorectal cancer using (64) Cu-labeled cetuximab positron emission tomography," *Cancer Science*, vol. 103, no. 3, pp. 600–605, 2012.

[64] C. Wu, Z. Tang, W. Fan et al., "In vivo Positron Emission Tomography (PET) imaging of Mesenchymal - Epithelial Transition (MET) receptor," *Journal of Medicinal Chemistry*, vol. 53, no. 1, pp. 139–146, 2010.

[65] H. Young, R. Baum, U. Cremerius et al., "Measurement of clinical and subclinical tumour response using [^{18}F]- fluorodeoxyglucose and positron emission tomography: review and 1999 EORTC recommendations," *European Journal of Cancer*, vol. 35, no. 13, pp. 1773–1782, 1999.

[66] L. K. Shankar, J. M. Hoffman, S. Bacharach et al., "Consensus recommendations for the use of ^{18}F-FDG PET as an indicator of therapeutic response in patients in National Cancer Institute Trials," *Journal of Nuclear Medicine*, vol. 47, no. 6, pp. 1059–1066, 2006.

[67] D. S. Binns, A. Pirzkall, W. Yu et al., "Compliance with PET acquisition protocols for therapeutic monitoring of erlotinib therapy in an international trial for patients with non-small cell lung cancer," *European Journal of Nuclear Medicine and Molecular Imaging*, pp. 1–9, 2010.

[68] D. Kahraman, M. Scheffler, T. Zander et al., "Quantitative analysis of response to treatment with erlotinib in advanced non-small cell lung cancer using ^{18}F-FDG and 3'-deoxy-3'-^{18}F-fluorothymidine PET," *Journal of Nuclear Medicine*, vol. 52, no. 12, pp. 1871–1877, 2011.

[69] L. F. de Geus-Oei, H. F. M. Van Der Heijden, E. P. Visser et al., "Chemotherapy response evaluation with ^{18}F-FDG PET in patients with non-small cell lung cancer," *Journal of Nuclear Medicine*, vol. 48, no. 10, pp. 1592–1598, 2007.

[70] C. Nahmias, W. T. Hanna, L. M. Wahl, M. J. Long, K. F. Hubner, and D. W. Townsend, "Time course of early response to chemotherapy in non-small cell lung cancer patients with ^{18}F-FDG PET/CT," *Journal of Nuclear Medicine*, vol. 48, no. 5, pp. 744–751, 2007.

[71] L. Decoster, D. Schallier, H. Everaert et al., "Complete metabolic tumour response, assessed by 18-fluorodeoxyglucose positron emission tomography (^{18}FDG-PET), after induction chemotherapy predicts a favourable outcome in patients with locally advanced non-small cell lung cancer (NSCLC)," *Lung Cancer*, vol. 62, no. 1, pp. 55–61, 2008.

[72] Y. Imamura, K. Azuma, S. Kurata et al., "Prognostic value of SUVmax measurements obtained by FDG-PET in patients with non-small cell lung cancer receiving chemotherapy," *Lung Cancer*, vol. 71, no. 1, pp. 49–54, 2011.

[73] A. D. van den Abbeele and R. D. Badawi, "Use of positron emission tomography in oncology and its potential role to assess response to imatinib mesylate therapy in gastrointestinal stromal tumors (GISTs)," *European Journal of Cancer*, vol. 38, pp. S60–65, 2002.

[74] G. Antoch, J. Kanja, S. Bauer et al., "Comparison of PET, CT, and dual-modality PET/CT imaging for monitoring of imatinib (STI571) therapy in patients with gastrointestinal stromal tumors," *Journal of Nuclear Medicine*, vol. 45, no. 3, pp. 357–365, 2004.

[75] S. Stroobants, J. Goeminne, M. Seegers et al., "^{18}FDG-Positron emission tomography for the early prediction of response in advanced soft tissue sarcoma treated with imatinib mesylate (Glivec®)," *European Journal of Cancer*, vol. 39, no. 14, pp. 2012–2020, 2003.

[76] H. Prenen, C. Deroose, P. Vermaelen et al., "Establishment of a mouse gastrointestinal stromal tumour model and evaluation of response to imatinib by small animal positron emission tomography," *Anticancer Research*, vol. 26, no. 2, pp. 1247–1252, 2006.

[77] H. Su, C. Bodenstein, R. A. Dumont et al., "Monitoring tumor glucose utilization by positron emission tomography for the prediction of treatment response to epidermal growth factor receptor kinase inhibitors," *Clinical Cancer Research*, vol. 12, no. 19, pp. 5659–5667, 2006.

[78] S. Assadian, A. Aliaga, R. F. Del Maestro, A. C. Evans, and B. J. Bedell, "FDG-PET imaging for the evaluation of antiglioma agents in a rat model," *Neuro-Oncology*, vol. 10, no. 3, pp. 292–299, 2008.

[79] D. S. Dorow, C. Cullinane, N. Conus et al., "Multi-tracer small animal PET imaging of the tumour response to the novel pan-Erb-B inhibitor CI-1033," *European Journal of Nuclear Medicine and Molecular Imaging*, vol. 33, no. 4, pp. 441–452, 2006.

[80] O. Schillaci, "Single-Photon Emission Computed Tomography/Computed Tomography in Lung Cancer and Malignant Lymphoma," *Seminars in Nuclear Medicine*, vol. 36, no. 4, pp. 275–285, 2006.

[81] D. Piwnica-Worms, M. L. Chiu, M. Budding, J. F. Kronauge, R. A. Kramer, and J. M. Croop, "Functional imaging of multidrug-resistant P-glycoprotein with an organotechnetium complex," *Cancer Research*, vol. 53, no. 5, pp. 977–984, 1993.

[82] H. K. Mohan and K. A. Miles, "Cost-effectiveness of 99mTc-sestamibi in predicting response to chemotherapy in patients with lung cancer: systematic review and meta-analysis," *Journal of Nuclear Medicine*, vol. 50, no. 3, pp. 376–381, 2009.

[83] S. Talapatra and C. B. Thompson, "Growth factor signaling in cell survival: implications for cancer treatment," *Journal of Pharmacology and Experimental Therapeutics*, vol. 298, no. 3, pp. 873–878, 2001.

[84] J. R. Woodburn, "The epidermal growth factor receptor and its inhibition in cancer therapy," *Pharmacology and Therapeutics*, vol. 82, no. 2-3, pp. 241–250, 1999.

[85] V. Rusch, J. Baselga, C. Cordon-Cardo et al., "Differential expression of the epidermal growth factor receptor and its ligands in primary non-small cell lung cancers and adjacent benign lung," *Cancer Research*, vol. 53, no. 10, pp. 2379–2385, 1993.

[86] F. R. Hirsch, M. Varella-Garcia, P. A. Bunn et al., "Epidermal growth factor receptor in non-small-cell lung carcinomas: correlation between gene copy number and protein expression and impact on prognosis," *Journal of Clinical Oncology*, vol. 21, no. 20, pp. 3798–3807, 2003.

[87] A. Wells, "EGF receptor," *International Journal of Biochemistry and Cell Biology*, vol. 31, no. 6, pp. 637–643, 1999.

[88] D. Busse, R. S. Doughty, T. T. Ramsey et al., "Reversible G1 arrest induced by inhibition of the epidermal growth factor receptor tyrosine kinase requires up-regulation of p27(KIP1) independent of MAPK activity," *Journal of Biological Chemistry*, vol. 275, no. 10, pp. 6987–6995, 2000.

[89] A. M. Petit, J. Rak, M. C. Hung et al., "Neutralizing antibodies against epidermal growth factor and ErbB-2/neu receptor tyrosine kinases down-regulate vascular endothelial growth factor production by tumor cells in vitro and in vivo: angiogenic implications for signal transduction therapy of solid tumors," *American Journal of Pathology*, vol. 151, no. 6, pp. 1523–1530, 1997.

[90] N. Sunaga, N. Oriuchi, K. Kaira et al., "Usefulness of FDG-PET for early prediction of the response to gefitinib in non-small cell lung cancer," *Lung Cancer*, vol. 59, no. 2, pp. 203–210, 2008.

[91] G. J. Riely, M. G. Kris, B. Zhao et al., "Prospective assessment of discontinuation and reinitiation of erlotinib or gefitinib in patients with acquired resistance to erlotinib or gefitinib followed by the addition of everolimus," *Clinical Cancer Research*, vol. 13, no. 17, pp. 5150–5155, 2007.

[92] R. T. Ullrich, T. Zander, B. Neumaier et al., "Early detection of Erlotinib treatment response in NSCLC by 3′-deoxy-3′-[^{18}F]-fluoro-L-thymidine ([^{18}F]FLT) positron emission tomography (PET)," *PLoS ONE*, vol. 3, no. 12, Article ID e3908, 2008.

[93] T. Zander, M. Scheffler, L. Nogova et al., "Early prediction of nonprogression in advanced non-small-cell lung cancer treated with erlotinib by using [(18)F]fluorodeoxyglucose and [(18)F]fluorothymidine positron emission tomography," *Journal of Clinical Oncology*, vol. 29, no. 13, pp. 1701–1708, 2011.

[94] R. Pirker, J. R. Pereira, A. Szczesna et al., "Cetuximab plus chemotherapy in patients with advanced non-small-cell lung cancer (FLEX): an open-label randomised phase III trial," *The Lancet*, vol. 373, no. 9674, pp. 1525–1531, 2009.

[95] F. D. Fabio, C. Pinto, F. L. Rojas Llimpe et al., "The predictive value of ^{18}F-FDG-PET early evaluation in patients with metastatic gastric adenocarcinoma treated with chemotherapy plus cetuximab," *Gastric Cancer*, vol. 10, no. 4, pp. 221–227, 2007.

[96] S. Takeuchi, S. Zhao, Y. Kuge et al., "^{18}F-fluorothymidine PET/CT as an early predictor of tumor response to treatment with cetuximab in human lung cancer xenografts," *Oncology Reports*, vol. 26, no. 3, pp. 725–730, 2011.

[97] E. Cabebe and H. Wakelee, "Role of anti-angiogenesis agents in treating NSCLC: focus on bevacizumab and VEGFR tyrosine kinase inhibitors," *Current Treatment Options in Oncology*, vol. 8, no. 1, pp. 15–27, 2007.

[98] N. Ferrara, "The role of vascular endothelial growth factor in pathological angiogenesis," *Breast Cancer Research and Treatment*, vol. 36, no. 2, pp. 127–137, 1995.

[99] N. Weidner, J. P. Semple, W. R. Welch, and J. Folkman, "Tumor angiogenesis and metastasis - Correlation in invasive breast carcinoma," *New England Journal of Medicine*, vol. 324, no. 1, pp. 1–8, 1991.

[100] I. M. E. Desar, C. M. L. van Herpen, H. W. M. van Laarhoven, J. O. Barentsz, W. J. G. Oyen, and W. T. A. van der Graaf,

"Beyond RECIST: molecular and functional imaging techniques for evaluation of response to targeted therapy," *Cancer Treatment Reviews*, vol. 35, no. 4, pp. 309–321, 2009.

[101] A. Sandler, R. Gray, M. C. Perry et al., "Paclitaxel-carboplatin alone or with bevacizumab for non-small-cell lung cancer," *New England Journal of Medicine*, vol. 355, no. 24, pp. 2542–2550, 2006.

[102] M. A. Pysz, S. S. Gambhir, and J. K. Willmann, "Molecular imaging: current status and emerging strategies," *Clinical Radiology*, vol. 65, no. 7, pp. 500–516, 2010.

[103] D. A. Mankoff, "A definition of molecular imaging," *Journal of Nuclear Medicine*, vol. 48, no. 6, pp. 18N–21N, 2007.

Hindawi Publishing Corporation
Journal of Biomedicine and Biotechnology
Volume 2012, Article ID 957364, 8 pages
doi:10.1155/2012/957364

Review Article

Multiple Metastasis-Like Bone Lesions in Scintigraphic Imaging

Ying Zhang,[1,2,3,4] Chunlei Zhao,[1,2,3,4,5] Hongbiao Liu,[1,2,3,4] Haifeng Hou,[1,2,3,4] and Hong Zhang[1,2,3,4]

[1] *Department of Nuclear Medicine, Second Affiliated Hospital of Zhejiang University School of Medicine, Hangzhou, Zhejiang 310009, China*
[2] *Zhejiang University Medical PET Center, Hangzhou 310009, China*
[3] *Institute of Nuclear Medicine and Molecular Imaging, Zhejiang University, Hangzhou 310009, China*
[4] *Key Laboratory of Medical Molecular Imaging of Zhejiang Province, Hangzhou 310009, China*
[5] *Department of Nuclear Medicine, Hangzhou First People's Hospital, Hangzhou Cancer Hospital, Hangzhou 310009, China*

Correspondence should be addressed to Hong Zhang, hzhang21@gmail.com

Received 1 January 2012; Accepted 20 January 2012

Academic Editor: Mei Tian

Multiple benign osteolytic lesions are very hard to differentiate from disseminated bone metastasis. Whole-body bone scintigraphy (WBBS) with technetium-99m methylene diphosphonate (Tc-99m MDP) demonstrates multiple lesions with increased uptake in any bone involved. Even combined with medical history and multiple imaging results, such as MRI and CT, the clinical diagnosis of metastasis lesion remains as a challenge. These clinical characteristics are similar to multiple malignant bone metastases and therefore affect the following treatment procedures. In this paper, we analyzed multiple benign osteolytic lesions, like eosinophilic granuloma (EG), multiple myeloma (MM), disseminated tuberculosis, fibrous dysplasia, or enchondroma, occurring in our daily clinical work and concluded that additional attention should be paid before giving the diagnosis of multiple bone metastases.

1. Introduction

Radioisotopes play an important role in the diagnosis of benign and malignant bone lesions. Whole-body bone scintigraphy (WBBS) with technetium-99m methylene diphosphonate (Tc-99m MDP) is widely available and commonly used to detect metastases from malignant tumors because it is more sensitive than X-rays and allows the whole body to be surveyed. However, multiple benign osteolytic lesions are very similar with bone metastasis in findings of bone scintigraphy. Before sending out the report of multiple metastases, benign osteolytic lesions should be considered according to other imaging findings, detailed medical history, or even the preliminary pathology result.

In this pictorial review, we retrospectively studied the WBBS with Tc-99m MDP findings in 5 patients of selected multiple benign osteolytic lesions. For adult patients, 15 mCi Tc-99m MDP was administered intravenously. For pediatric patients, a smaller dose was used dependent on patient body weight: adult dose/70 $*$ patient weight (kg).

2. Eosinophilic Granuloma

A 41-year-old man with left upper arm pain for 3 months was admitted for left humerus fracture after a tumble. All of images of Tc-99m MDP WBBS (Figure 1), left shoulder joint MRI (Figure 2), and thoracic CT (Figure 3) indicated bone metastases. Left humerus resection and internal fixation were performed thereafter. EG was diagnosed definitely by histopathological examination (positive: CD1a, S-100, LCA, Ki67 (6%) and negative: CD68, CD79a, CD138, and P53). The patient received 4 courses of chemotherapy (steroids, vinca alkaloids, and antimetabolites) before discharge. Two years later, the patient was admitted again in our hospital for right femoral fracture caused by an accidental fall. Another Tc-99m MDP WBBS (Figure 4) was performed, and similar

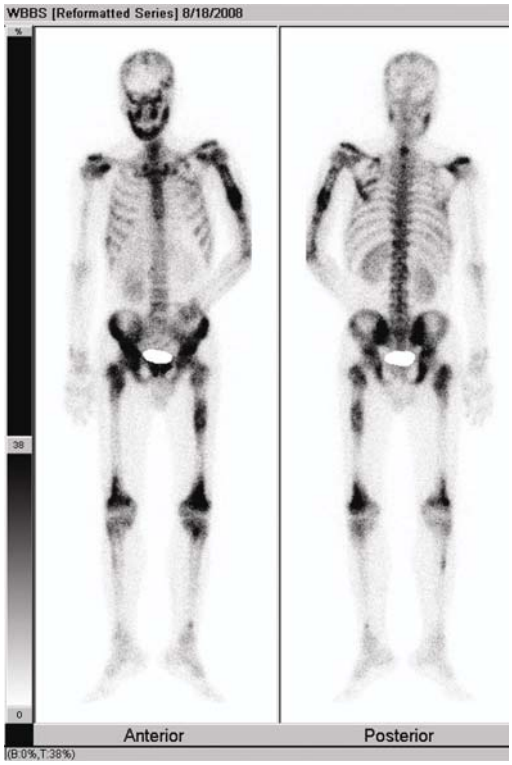

Figure 1: Tc-99m MDP WBBS of the first admission found multiple lesions with intensive radioactive accumulation in skull, mandible, left humerus, scapulas, ribs, vertebras, pelvis, femurs, and tibias.

findings (except for deterioration of right femur site) were observed as shown in the previous one (Figure 1).

3. Multiple Myeloma

A 45-year-old female patient suffered chest pain for 2 months that deteriorated recently. Blood routine examination found WBS $4.0 * 10^9$/L, Hb 43 g/L and Plt $243 * 10^9$/L. Bone marrow biopsy demonstrated plasma cell myeloma. Serum immunoglobulin (IgG) and β2-microglobulin (MG) were 43.59 g/L and 18.58 mg/L, respectively, and both were above the normal level. Tc-99m MDP WBBS (Figure 5) was performed before chemotherapy and found multiple bones accumulated the agent abnormally. Clinical diagnosis was multiple myeloma IgG stage III; then, chemotherapy of VAD regimen was given to this patient.

4. Disseminated Tuberculosis

A 25-year-old male patient suffered cough and chest pain for 1 month, and the pain extended to back and waist recently. Diffused military nodules with small cavities in both lungs, and multiple bone destructions in thoracic and lumbar vertebra were found on chest CT suggesting of disseminated tuberculosis. Tc-99m MDP WBBS (Figure 6) demonstrated high uptake in multiple bones. The patient felt remission after the treatment of antituberculosis drugs.

5. Fibrous Dysplasia

An 18-year-old female patient suffered right hip pain after long walking for this year. She received sectional resection of right femur and allograft for the reason of fibrous dysplasia when she was only 7 years old. X-ray showed benign tumor changes in upper section of right femur, considering fibrous dysplasia. WBBS (Figure 7) before operation found abnormal accumulation in right femur, tibia, and cotyle. Then operation of right femur tumor resection and internal fixation was performed.

6. Enchondroma

A 14-year-old male patient found swelling of interphalangeal joint in left middle finger 11 years ago. Then the swelling extended to left ring and little fingers. CR and MRI illustrated multiple enchondroma in left hand. Before the operation, Tc-99m MDP WBBS (Figure 8) found additional bones involvement. This patient received sectional resection of multiple lesions in left hand and allograft the next day. Histopathological examination after operation was cracked cartilage tissue which is in accordance with multiple enchondroma.

7. Discussion

EG, formerly termed histiocytosis X, is the most common and benign form of the Langerhans cell histiocytosis which

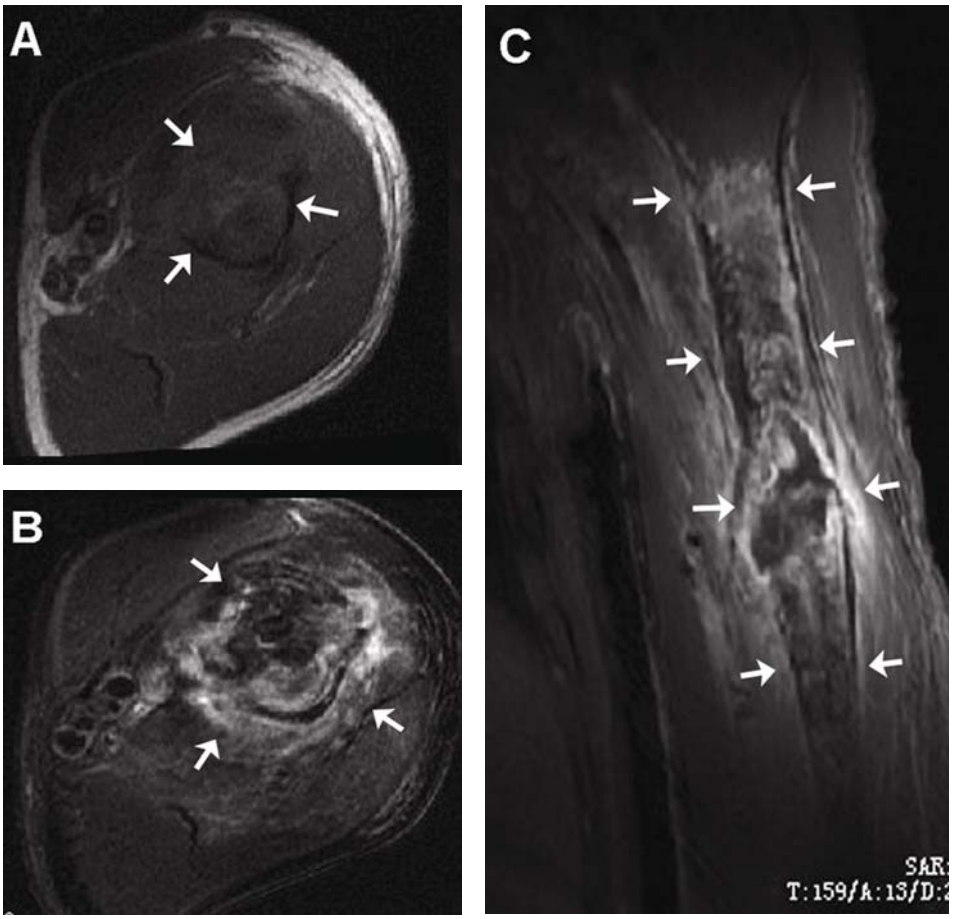

Figure 2: MRI of left shoulder demonstrated isointensity and mild-hypo-intensity signal on T1-weighted images (A), hyperintensity signal on T2-weighted images (B), and inhomogenily enhanced after Gd-DTPA administration (C) in humeral midshaft and surrounding soft tissues. These abnormal signals prompted bone malignancy and pathologic fracture.

includes another two forms: the Hand-Schüller-Christian disease (the triad of diabetes insipidus, exophthalmos, and lytic bone lesions) and the Letterer-Siwe syndrome (a rapidly-progressing multisystem disease with poor prognosis). EG predominantly affects children and adolescents although it can be found in any age. Solitary lesion is more common than multiple lesions. In our cases, a 41-year-old man with EG admitted for pathologic fracture demonstrated multiple malignant metastases like bone involvement on both scintigraphic and radiographic imaging. Although multiple bones were involved in this case with EG, we can easily differentiate it from the Hand-Schüller-Christian disease for the absence of main characteristics of diabetes insipidus and exophthalmos. The etiology of EG is still unknown. The skeletal involvement is frequent and generally demonstrates as destroyed solitary or multiple bones in any age [1–4], while the visceral involvement is rare and often occurs at age below 2 years old [5]. Localized pain is always the first symptom of bone involvement, but it can also be presented as pathologic fractures after injuries. The most commonly involved bones are skull, mandible, pelvis, spine, ribs, and long bones. Radiographic imaging is the main modality for the diagnosis of EG, although the radiographic characteristics of EG are considerably different according to the site and the activity of the lesion [6]. Bone destruction in granulation tissue forming areas of osteolysis is the main pathological characteristic of EG and may involve any portion of any bone [7].

Typical finding on Tc-99m MDP WBBS in the patients with EG is the lesion with intensive radioactive accumulation with a photopenic center [1–3], because the bone involvement in EG always begins from osteolysis that arise in the bone marrow cavity and following periosteal reaction. However, all the manifestations of the lesions with increased, decreased, or normal accumulation on Tc-99m MDP WBBS could be observed according to the amount of viable residual or reactive bone tissue. Those can significantly accumulate the radioactive tracer [6, 8]. In EG, Tc-99m MDP WBBS is generally less sensitive than radiography in the detection of osseous lesions [6]. The findings in this patient confirmed this opinion. However, Tc-99m MDP WBBS may play roles in searching additional bone lesions and monitoring therapeutic response and is helpful when the radiographs are normal or equivocal [6]. In addition, Tc-99m

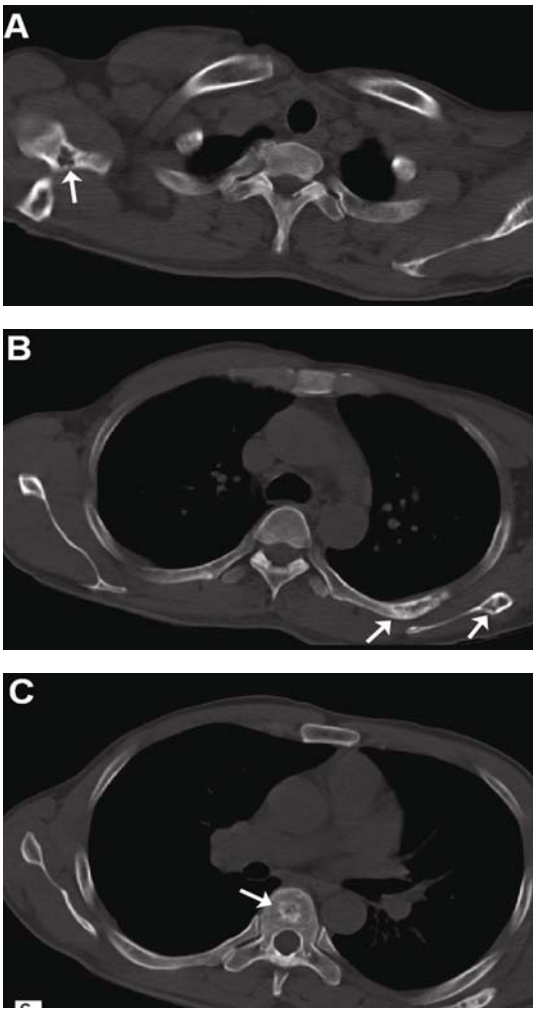

Figure 3: Chest CT of bone window showed eroded bone destruction with sclerotic edge in scapulas and ribs ((A): right scapula; (B): left scapula and the left 5th posterior rib) and patchy high density in thoracic vertebrae (C) However, the amount of the lesions was greater than that in Tc-99m MDP WBBS within the corresponding thoracic area. The bone lesions on CT with intensive Tc-99m MDP accumulation prompted multiple bone metastases.

MDP WBBS has the advantage of detecting the asymptomatic bone abnormalities possibly missed by other imaging modalities. It is suggested that combination of various imaging modalities might be helpful to make a definite diagnosis when bone biopsy or operation is not available [9]. In this patient, all images of Tc-99m MDP WBBS, MRI, and CT demonstrated the characteristics of disseminated bone metastases although EG was finally diagnosed by postoperative pathological examination. Multiple bone lesions in EG are relatively rare because solitary lesion predominates over multiple lesions, and only around 10% of solitary lesion may eventually develop into multiple lesions [2]. EG is a benign inflammatory disease, and the activity of this disease may remain stable during follow-up [1]. In this case, the Tc-99m MDP WBBS performed 2 year later revealed only mild alternations in a wide range of bone involvement as shown in the previous one except the increased radioactive accumulation in fractured right femur, confirming the benignity of EG.

Multiple myeloma is a plasma cell dyscrasia of the bone marrow. It can be mistaken radiographically for metastatic bone disease because it presents with multiple osteolytic lesions or diffuse osteopenia. WBBS often fails to demonstrate a hyperconcentration at sites of skeletal involvement by myeloma despite extensive disease by radiography. This occurs because reactive bone formation is not a feature of the disease; this might be due to release of an inactivation factor by the tumor. Multiple myeloma is a common tumor of elderly patients. It is usually confirmed by serology or bone marrow examination. Radiographs typically show either a solitary or multifocal osteolytic pattern. However, skeletal survey is not always a useful screening method, so other imaging modalities such as CT and WBBS are often used. WBBS is sensitive in 75% of patients with myeloma, but only about 10% of lesions are shown [10]. Therefore, WBBS may be helpful when there is focal pain and a negative radiograph.

Skeletal TB occurs in only very small part of patients with TB, and therefore the diagnosis is often difficult due to the nonspecific nature of the clinical presentation [11]. The spine, particularly the thoracolumbar spine, is the most common site of skeletal involvement of TB. Back pain can affect anyone and in general can originate from the bone (vertebrae), muscles, ligaments, tendons, or nerves. Tuberculosis of the spine is one of the causes for back pain, and early diagnosis and management can prevent complications. Imaging plays an important role in the diagnosis and management of spinal infections. Infection and inflammation of the spine are complex. The intense vertebra uptake on WBBS is nonspecific, so the differential diagnosis would include bone metastases from lung cancer [12]. It is important to obtain material for culture and sensitivity in the absence of confirmed pulmonary TB for a definitive diagnosis [13].

Fibrous dysplasia is a benign tumor in which masses of fibroblasts and islands of cartilage replace bone marrow in one or more locations. It is commonly found in young patients with mild bone pain or as an incidental finding, although the lesions may persist into late adulthood. The main value of WBBS in fibrous dysplasia is to show polyostotic involvement, but sometimes these lesions may show only minimal uptake or even no uptake [14]. From our case of multiple fibrous dysplasia, the differentiation from bone metastasis can be made by combining with their past medical history.

Enchondroma is a common benign lesion that appears in the medullary portion of bone and is composed chiefly of mature hyaline cartilage. The solitary enchondroma has a predilection for the phalanges and metacarpals of the hand. Multiple enchondromas, or enchondromatosis, is an anomaly usually disclosed in infancy. When one side of the body exhibits greater involvement than the other, the condition is called Ollier's disease. The combination of enchondromatosis and soft tissue hemangiomata is referred to as Maffucci's syndrome. Malignant transformation into chondrosarcoma can occur, especially in multiple enchondromatosis. Chondrosarcoma is exceedingly rare in the phalanges.

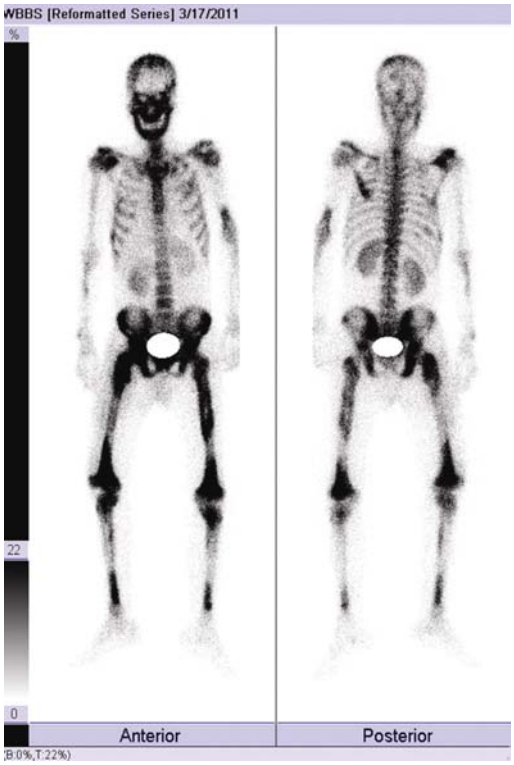

Figure 4: Tc-99m MDP WBBS of the second admission 2 years later showed multiple bone involvement observed as similar to those found in the previous Tc-99m MDP WBBS except the increased radioactive accumulation in fractured right femur.

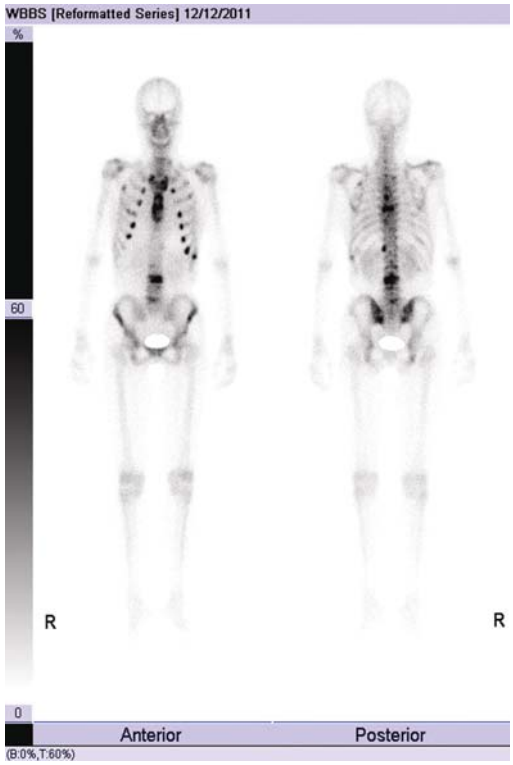

Figure 5: Tc-99m MDP WBBS before chemotherapy found a wide range of abnormal radioactive accumulation in ribs, thoracic and lumbar vertebra, sacrum, and pelvis.

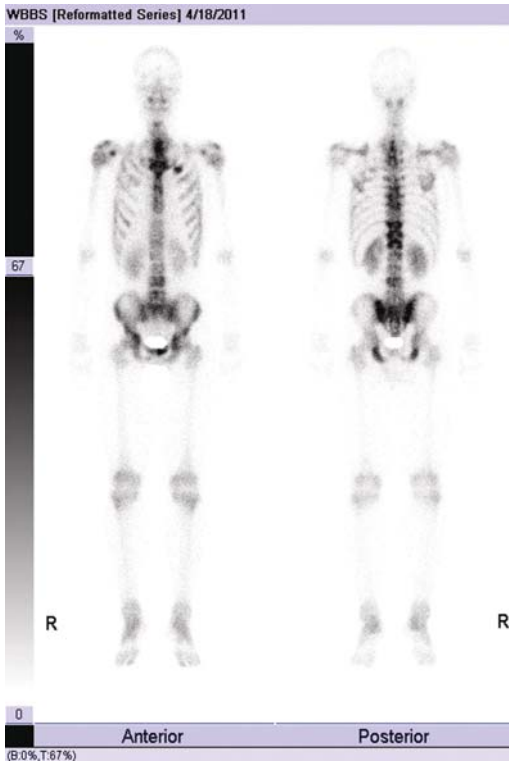

Figure 6: Tc-99m MDP WBBS showed ribs, spine, and pelvis intensively accumulated the agent and was very similar to the changes of multiple bone metastasis.

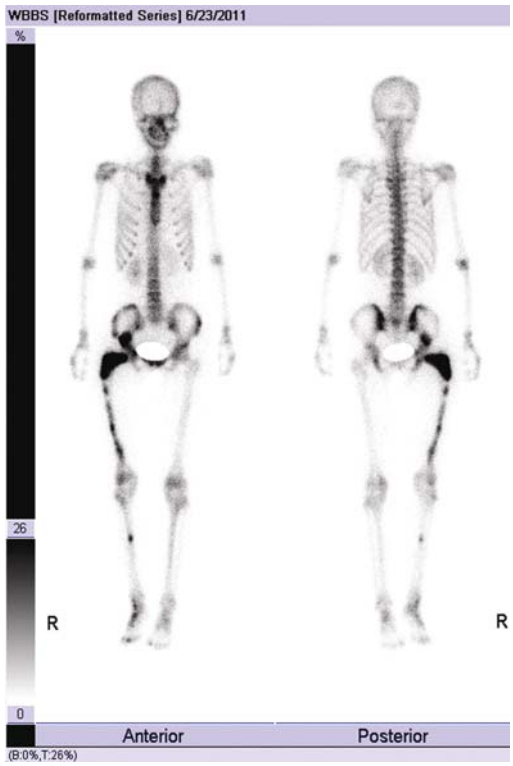

Figure 7: Tc-99m MDP WBBS found abnormal intensive accumulation in right femur, tibia, and cotyle suggesting tumor, and decreased accumulation in upper right femur due to the previous operation.

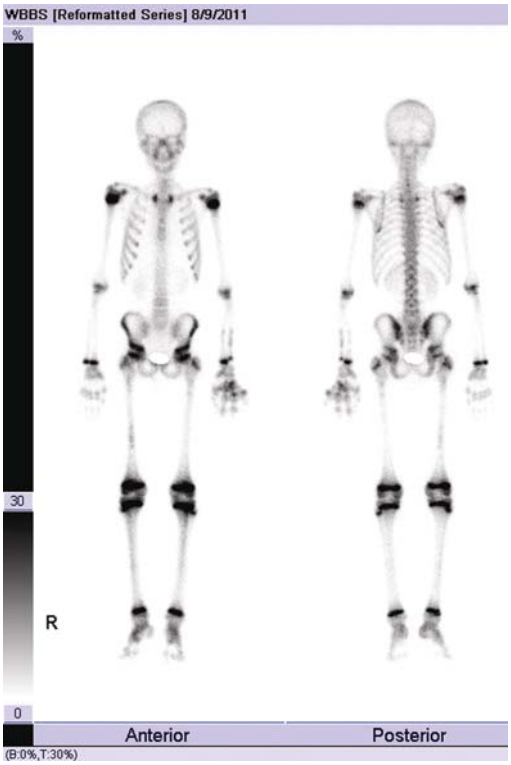

Figure 8: Tc-99m MDP WBBS before operation demonstrated intensive radioactive accumulation in multiple metacarpophalangeal and interphalangeal joints of left hand, left ulna, left radius, and right femur.

Enchondroma can have high FDG and MDP uptake on scintigraphic imaging and occasionally may mimic metastatic lesions in patients being screened for metastatic disease [15]. Taking one with another, WBBS is an effective and economic method in detecting multiple enchondromatosis.

8. Conclusion

WBBS is that of intense radioactive imaging agent uptake in the osteolytic lesions. Given the low specificity of Tc-99m MDP WBBS and its sensitivity to increased bone remodeling from any cause, whether benign or malignant, the presence of multiple benign osteolytic lesions renders the interpretation indistinguishable from malignant metastasis. Therefore, we should be watchful of giving the diagnosis of disseminated bone metastasis during our daily work; furthermore, detailed past medical history and various laboratory results might be helpful for accurate diagnosis.

Acknowledgments

This work is partly sponsored by Grants from the Zhejiang Provincial Natural Science Foundation of China (Z2110230), Health Bureau of Zhejiang Province (2010ZA075, 2011ZDA013), National Science Foundation of China (NSFC) (no. 81101023, 81170306, 81173468), and Ministry of Science and Technology of China (2011CB504400, 2012BAI13B06).

References

[1] L. G. Flores, H. Hoshi, S. Nagamachi et al., "Thallium-201 uptake in eosinophilic granuloma of the frontal bone: comparison with technetium-99 m-MDP imaging," *Journal of Nuclear Medicine*, vol. 36, no. 1, pp. 107–110, 1995.

[2] M. Yoshikawa, Y. Sugawara, T. Kikuchi et al., "Two cases of pediatric bone disease (Eosinophilic Granuloma and Brodie's abscess) showing similar scintigraphic and radiographic findings," *Clinical Nuclear Medicine*, vol. 25, no. 12, pp. 986–990, 2000.

[3] S. Solav, "Bone Scintiscanning in Osteolytic Lesions," *Clinical Nuclear Medicine*, vol. 29, no. 1, pp. 12–20, 2004.

[4] B. D. Nguyen, M. C. Roarke, and S. F. Chivers, "Multifocal Langerhans cell histiocytosis with infiltrative pelvic lesions: PET/CT imaging," *Clinical Nuclear Medicine*, vol. 35, no. 10, pp. 824–826, 2010.

[5] J. Donadieu, "A multicentre retrospective survey of Langerhans' cell histiocytosis: 348 cases observed between 1983 and 1993," *Archives of Disease in Childhood*, vol. 75, no. 1, pp. 17–24, 1996.

[6] K. Wang, L. Allen, E. Fung, C. C. Chan, J. C. S. Chan, and J. F. Griffith, "Bone scintigraphy in common tumors with osteolytic components," *Clinical Nuclear Medicine*, vol. 30, no. 10, pp. 655–671, 2005.

[7] G. B. Greenfield, *Radiology of Bone Disease*, Lippincott Company, Philadelphia, Pa, USA, 3rd edition, 1980.
[8] S. Antonmattei, M. R. Tetalman, and T. V. Lloyd, "The multiscan appearance of eosinophilic granuloma," *Clinical Nuclear Medicine*, vol. 4, no. 2, pp. 53–55, 1979.
[9] R. Naumann, B. Beuthien-Baumann, R. Fischer et al., "Simultaneous occurrence of Hodgkin's lymphoma and eosinophilic granuloma: a potential pitfall in positron emission tomography imaging," *Clinical Lymphoma*, vol. 3, no. 2, pp. 121–124, 2002.
[10] W. Dahnert, "Bone and soft-tissue disorders," in *Radiology Review Manual*, W. Dahnert, Ed., vol. 122, Lippincott Company, Philadelphia, Pa, USA, 5th edition, 2002.
[11] L. Cormican, R. Hammal, J. Messenger, and H. J. Milburn, "Current difficulties in the diagnosis and management of spinal tuberculosis," *Postgraduate Medical Journal*, vol. 82, no. 963, pp. 46–51, 2006.
[12] N. Khattry, S. Thulkar, A. Das, S. A. Khan, and S. Bakhshi, "Spinal tuberculosis mimicking malignancy: atypical imaging features," *Indian Journal of Pediatrics*, vol. 74, no. 3, pp. 297–298, 2007.
[13] A. I. de Backer, K. J. Mortelé, I. J. Vanschoubroeck et al., "Tuberculosis of the spine: CT and MR imaging features," *Journal Belge de Radiologie*, vol. 88, no. 2, pp. 92–97, 2005.
[14] J. Han, J. S. Ryu, M. J. Shin, G. H. Kang, and H. K. Lee, "Fibrous dysplasia with barely increased uptake on bone scan: a case report," *Clinical Nuclear Medicine*, vol. 25, no. 10, pp. 785–788, 2000.
[15] N. Dobert, C. Menzel, R. Ludwig et al., "Enchondroma: a benign osseous lesion with high F-18 FDG uptake," *Clinical Nuclear Medicine*, vol. 27, no. 10, pp. 695–697, 2002.

Hindawi Publishing Corporation
Journal of Biomedicine and Biotechnology
Volume 2012, Article ID 854524, 5 pages
doi:10.1155/2012/854524

Research Article

Reduced Striatal Dopamine Transporters in People with Internet Addiction Disorder

Haifeng Hou,[1,2,3,4] Shaowe Jia,[5] Shu Hu,[5] Rong Fan,[5] Wen Sun,[5] Taotao Sun,[5] and Hong Zhang[1,2,3,4]

[1] *Department of Nuclear Medicine, Second Affiliated Hospital of Zhejiang University School of Medicine, Hangzhou, Zhejiang 310009, China*
[2] *Zhejiang University Medical PET Center, Hangzhou 310009, China*
[3] *Institute of Nuclear Medicine and Molecular Imaging, Zhejiang University, Hangzhou 310009, China*
[4] *Key Laboratory of Medical Molecular Imaging of Zhejiang Province, Hangzhou 310009, China*
[5] *Department of Nuclear Medicine, Peking University Shenzhen Hospital, Shenzhen 310009, China*

Correspondence should be addressed to Hong Zhang, hzhang21@gmail.com

Received 5 January 2012; Accepted 31 January 2012

Academic Editor: Mei Tian

In recent years, internet addiction disorder (IAD) has become more prevalent worldwide and the recognition of its devastating impact on the users and society has rapidly increased. However, the neurobiological mechanism of IAD has not bee fully expressed. The present study was designed to determine if the striatal dopamine transporter (DAT) levels measured by ^{99m}Tc-TRODAT-1 single photon emission computed tomography (SPECT) brain scans were altered in individuals with IAD. SPECT brain scans were acquired on 5 male IAD subjects and 9 healthy age-matched controls. The volume (V) and weight (W) of bilateral corpus striatum as well as the ^{99m}Tc-TRODAT-1 uptake ratio of corpus striatum/the whole brain (Ra) were calculated using mathematical models. It was displayed that DAT expression level of striatum was significantly decreased and the V, W, and Ra were greatly reduced in the individuals with IAD compared to controls. Taken together, these results suggest that IAD may cause serious damages to the brain and the neuroimaging findings further illustrate IAD is associated with dysfunctions in the dopaminergic brain systems. Our findings also support the claim that IAD may share similar neurobiological abnormalities with other addictive disorders.

1. Introduction

The use of the internet has expanded incredibly across the world over the last few years. The internet provides remote access to others and abundant information in all areas of interest. However, maladaptive use of the internet has resulted in impairment of the individual's psychological well-being, academic failure, and reduced work performance and, especially leaded to internet addiction disorder (IAD) [1–4]. IAD was first raised in 1990s [5] and according to the Beard's definition of IAD, "an individual is addicted when an individual's psychological state, which includes both mental and emotional states, as well as their scholastic, occupational, and social interactions, is impaired by the overuse of the medium." [6]

In recent years, IAD has become more prevalent worldwide; the recognition of its devastating impact on the users and society has rapidly increased [7]. Importantly, recent studies have found dysfunctions of IAD are similar to other types of addictive disorders, such as substance abuse disorders and pathological gambling [7–10]. People experiencing IAD showed clinical features such as craving, withdrawal and tolerance [7, 8], increased impulsiveness [9], and impaired cognitive performance in tasks involving risky decision-making [10].

As similar with the abnormalities in the dopaminergic neural system in individuals with substance-related addiction [11], the role of dopaminergic neural system in IAD also has been elucidated in a few researches [12–14]. In a recent study, people with IAD were found to have altered

resting-state glucose metabolism in several brain regions including the major dopamine projection areas such as the striatum and orbitofrontal region [12]. Moreover, another study found that adolescents with increased genetic polymorphisms in genes coding for the dopamine D2 receptor and dopamine degradation enzyme were more susceptible to excessive internet gaming compared with an age-matched cohort of controls [14]. In a positron emission tomography (PET) imaging study, reduced levels of dopamine D2 receptor in subdivisions of the striatum including the bilateral dorsal caudate and right putamen were found in the individuals with IAD [13]. Taken together, these findings suggest that IAD may also be partly due to impaired dopaminergic neural systems similar to substance-related addiction [15].

Dopamine transporter (DAT) is a protein situated in the presynaptic terminal and striatal DAT is responsible for the active dopamine reuptake into the presynaptic neuron and plays a critical role in the regulation of striatal synaptic dopamine levels [16–18]. Altered DAT concentration in the striatum following chronic substance administration has been reported previously [19–24]. However, whether the abnormality of DAT also exists in IAD has not been illustrated before.

In recent years, imaging of DAT has been used as an important tool in clinical settings to display changes in the brain structure of patients with substance-related addiction [21–24]. In addition, the radiotracer ^{99m}Tc-TRODAT-1, a technetium-99 m (^{99m}Tc) labeled tropane derivative (technetium,2-[[2-[[[3-(4-chlorophenyl)-8-methyl-8-azabicyclo [3, 2, 1]oct-2-yl]-methyl](2-mercaptoethyl)amino]ethyl]-amino]ethanethiolato(3-)]-oxo-[1R-(exo-exo)]-), is regarded as a safe and suitable imaging agent for monitoring DAT status for human imaging studies [21, 25, 26]. In the present study, we used single photon emission tomography (SPECT) with the radiotracer ^{99m}Tc-TRODAT-1 to investigate striatal DAT density to identify potential presynaptic abnormalities in IAD subjects compared to age-matched healthy controls. This study aims to test the hypothesis that the altered availability of DAT is associated with the pathogenesis of IAD.

2. Materials and Methods

2.1. Diagnosed Criteria of IAD. IAD was assessed using Young's Internet Addiction Diagnostic Questionnaire (IADDQ) [4] and Goldberg's Internet addictive Disorder Diagnostic Criteria (IADDC) [27]. All of the questions of IADDQ and IADDC were translated into Chinese. To be eligible, participants in the IAD group were asserted that five or more "yes" responses to the eight questions of IADDQ and to satisfy three or more of IADDC (i.e., tolerance, withdrawal, craving and unplanned use, failure to reduce use, excessive use, sacrificing social activities to use, and physical and psychological problems associated with use).

2.2. Subjects. Five men (mean ± SD, 20.40 ± 2.30 years old) with IAD were randomly selected from the patients seeking treatment at the Peking University Shenzhen Hospital. The IAD subjects used the internet almost everyday, and spend more than 8 hours (mean ± SD, 10.20 ± 1.48 hours) everyday in front of the monitor, mostly for chatting with cyber friends, playing online games, and watching online pornographies or adult movies. These subjects were initially familiar with internet mostly at the early stage of their adolescence (mean age ± SD, 12.80 ± 1.92 years old) and had the indications of IAD for more than 6 years (mean ± SD, 7.60 ± 1.52 years).

Nine age-matched controls (mean ± SD, 20.44 ± 1.13 years old) recruited through advertisement participated in this study. No statistical difference was found for the ages of the participants between the two groups ($P = 0.96$). The participants in the control group used Internet occasionally or frequently but spent no more than 5 hours a day on the line (mean ± SD, 3.81 ± 0.76 hours) and did not satisfy the diagnosed criteria of IAD [4, 27].

All the recruited participants were native Chinese speakers, never used illegal substances (sometimes, a few of the participants smoked or drink alcohol, but none of them meet the diagnosis criteria of substance-related disorders [28]), had no history of significant medical, neurological or psychiatric diseases, and were right-handed. All the participants gave written informed consent before participation after the nature of the procedure was fully explained, including possible risks and side effects. All procedures for this study were approved by the ethics committee of the Peking University Shenzhen Hospital.

2.3. Imaging. TRODAT-1 ligand (liquid) was supplied by the Department of Chemistry, Beijing Normal University (Beijing, China). The radiotracer ^{99m}Tc-TRODAT-1, 740 MBq (20 mCi) with purity >90% was synthesized as described previously [25]. And SPECT studies with ^{99m}Tc-TRODAT-1 were carried out using a Siemens DIACAM/E.CAM/ICON double detector SPECT with lower-energy all-purpose collimator (Siemens, Erlangen, Germany). The imaging method was performed as described previously [25, 29]. Subjects were injected intravenously with 740 MBq (20 mCi) of ^{99m}Tc-TRODAT-1. Imaging was performed 2.5 h after the administration of ^{99m}Tc-TRODAT-1. The acquisition parameters included 64 views over 18 s per view and a 128 × 128 matrix over 360° with a rotation in 5.6° increments. Transverse reconstruction backprojection was applied to the raw data. A Butterworth filter was then applied with an order of 15 and a cutoff of 0.33 Nyquist frequency. Photon attenuation correction was performed using Chang's first order correction method using an attenuation coefficient of 0.15 cm^{-1} [30]. The transverse image thickness was 2.7 mm (1 pixel). All images were processed and reconstructed using the same procedure.

2.4. Image Analysis. Image analysis was done using the region ratio software of the E-Cam. Regions of interest (ROIs) were drawn on 12 transverse images, the pixels were extracted and counts of whole brain and bilateral corpus striatum were carried out. The volume (V) and weight (W) of bilateral corpus striatum as well as the ratio of

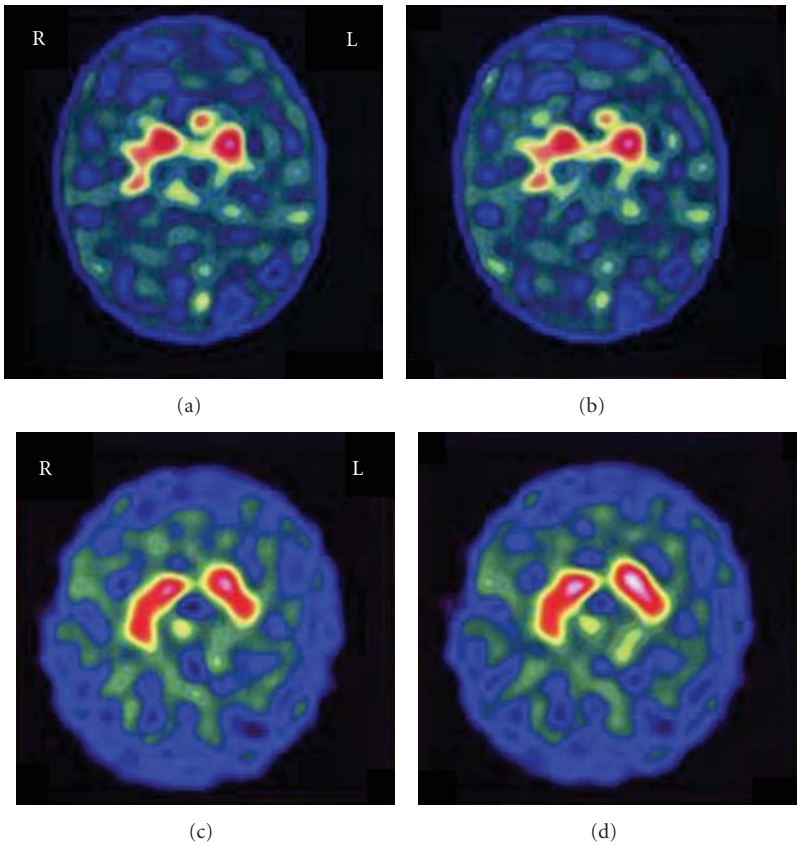

Figure 1: (a,b) representative ^{99m}Tc-TRODAT-1 SPECT images of an IAD subject in comparison with an age-matched healthy control ((a) a 20-year-old male IAD subject; (b) a 20-year-old male healthy control). Left hemisphere is on right side of image. The IAD subject demonstrates a significant decrease in binding of ^{99m}Tc-TRODAT-1 to the DAT in the striatum and the bilateral corpus striatum is much smaller and more irregular than that in the control.

corpus striatum/the whole brain (Ra) was calculated using the mathematical models as described in the previous paper [21, 31].

2.5. Data Analysis. Data in the present paper are presented as means ± standard (mean ± SD). Statistical Program for the Social Sciences for Windows, version 11 (SPSS 13.0, SPSS Inc, Chicago, USA) was used to analyze the data. Differences between the groups were assessed by Student's t-test. For all of the tests conducted, the criterion for significance was set at $P < 0.05$.

3. Results

The DAT images of the bilateral corpus striatum in the control group showed a panda-eye shape and DATs were distributed uniformly and symmetrically in the corpus striatum. The bilateral corpus striatum was situated on 8–12 layers, as shown in Figure 1(b). However, the DAT images of the IAD subjects displayed different levels of abnormity, in which the corpus stratums were much smaller and showed different shapes, dumbbell, thin strip, lunate shape, or sporadic spot (Figure 1(a)).

As shown in Figure 1 and Table 1, DAT expression level of striatum was significantly decreased in IAD subjects. Briefly, in comparison with the controls, there were significantly lower values of V (cm^3), W (g) and Ra of corpus striatum in the IAD group, suggesting that decreased ^{99m}Tc-TRODAT-1 bound to DAT or impairment as well as dysfunction of corpus striatum occurred. No statistical difference was found as comparing V or W of the bilateral corpus striatum (left side and right side) either in the IAD group ($P = 0.67$ and $P = 0.68$ resp.) or in the health control group ($P = 0.10$ and $P = 0.11$ resp.).

4. Discussion

IAD resulted in impaired individual psychological well-being, academic failure, and reduced work performance, especially among adolescents [1–4]. However, there is currently no standardized treatment targeted for IAD. To develop effective methods for intervention and treatment of IAD, it will first require establishing a clear understanding of the underlying neurobiological mechanisms. In the present study, we assessed the DAT expression level in IAD subjects and healthy controls using ^{99m}Tc-TRODAT-1 SPECT. We found that DAT expression level of striatum was significantly

Table 1: Comparison of corpus striatum V (cm^3), W (g), and Ra between IAD subjects and the controls.

	Volume of corpus striatum V (cm^3)		Weight of corpus striatum W (g)		Ratio of corpus striatum/whole brain
	VL (left side)	VR (right side)	WL (left side)	WR (right side)	Ra (%)
Controls ($n = 9$)	16.69 ± 1.63	18.17 ± 2.00	17.53 ± 1.71	19.08 ± 2.10	7.93 ± 0.75
IAD subjects ($n = 5$)	11.72 ± 3.13*	12.51 ± 2.53**	12.30 ± 3.28*	13.14 ± 2.10**	5.38 ± 0.77**

Values are expressed as mean ± SD with $^*P < 0.05$ and $^{**}P < 0.01$.

decreased and the values of V, W, and Ra of the corpus striatum in IAD subjects were greatly reduced. The imaging results provided the direct-viewing proof of altered availability of DAT in brain of people with IAD.

DATs play a critical role in the regulation of striatal synaptic dopamine levels [16–18] and have been used as markers of the dopamine terminals [32]. A reduced number of cell membrane DATs may possibly reflect pronounced striatal dopamine terminal loss or the brain dopaminergic function impairment which has been found in substance-related addiction [21–23]. PET imaging studies have found increased release of dopamine in the striatum during the video game [33]. Patients with pathological gambling also demonstrated high level of dopamine in the ventral striatum during gambling [34]. Because increased extracellular dopamine in the striatum is associated with subjective descriptors of reward (high, euphoria) [11, 35], individuals with IAD may also experience euphoria as the extracellular dopamine in the striatum increases. However, long-time and high concentrations of dopamine have been shown to cause a selective lesion of dopamine terminals [32, 36] and decreased size of dopaminergic cell bodies [20]. Taken together, the reduced DATs found in our study may indicate the neuropathologic damage to the dopaminergic neural system caused by IAD.

According to our knowledge, this is the first imaging study to examine the abnormality of DAT in the brain of IAD subjects. Furthermore, the imaging results of the present study provide the objective proofs that long-term maladaptive use internet might cause serious problems. However, for complete interpretation of the results of the present study, some limitations should be noted. Firstly, the small sample size of our study may limit the generalizability of our results. Those positive associations in our study might have been due to chance or a stratification effect in the sample collection, and further studies in independent samples or a larger population are required. Secondly, the IAD subjects in the present study reported different desired activities when they are sitting in front of the monitor (including chatting with cyber friends, playing online games, watching online pornographies or adult movies, etc.). Our study can not determine whether the different types of Internet behaviors may cause different brain DAT changes. Therefore, the present study can only be recognized as exploratory and primary, and more research work should be done before we get the most definitive conclusion.

5. Conclusion

The results from this study provide evidence that IAD may induce significant DAT losses in the brain and these findings suggest that IAD is associated with dysfunctions in the dopaminergic brain systems and are consistent with previous reports in various types of addictions either with or without substances [21–23, 37]. Our findings support the claim that IAD may share similar neurobiological abnormalities with other addictive disorders [15].

Author's contribution

H. Hou and S. Jia are contributed equally to this work.

Acknowledgments

This work is partly sponsored by Grants from the Zhejiang Provincial Natural Science Foundation of China (Z2110230), Health Bureau of Zhejiang Province (2010ZA075, 2011ZDA013), National Science Foundation of China (NSFC) (no. 81101023, 81170306, 81173468), and Ministry of Science and Technology of China (2011CB504400, 2012BAI13B06).

References

[1] C. H. Ko, J. Y. Yen, S. H. Chen, M. J. Yang, H. C. Lin, and C. F. Yen, "Proposed diagnostic criteria and the screening and diagnosing tool of Internet addiction in college students," *Comprehensive Psychiatry*, vol. 50, no. 4, pp. 378–384, 2009.

[2] C. Flisher, "Getting plugged in: an overview of Internet addiction," *Journal of Paediatrics and Child Health*, vol. 46, no. 10, pp. 557–559, 2010.

[3] M. A. Moreno, L. Jelenchick, E. Cox, H. Young, and D. A. Christakis, "Problematic internet use among US youth: a systematic review," *Archives of Pediatrics and Adolescent Medicine*, vol. 165, no. 9, pp. 797–805, 2011.

[4] K. S. Young, "Internet addiction: the emergence of a new clinical disorder," *Cyberpsychology and Behavior*, vol. 1, no. 3, pp. 237–244, 1998.

[5] S. Byun, C. Ruffini, J. E. Mills et al., "Internet addiction: meta-synthesis of 1996–2006 quantitative research," *Cyberpsychology and Behavior*, vol. 12, no. 2, pp. 203–207, 2009.

[6] K. W. Beard, "Internet addiction: a review of current assessment techniques and potential assessment questions," *Cyberpsychology and Behavior*, vol. 8, no. 1, pp. 7–14, 2005.

[7] J. J. Block, "Issues for DSM-V: internet addiction," *American Journal of Psychiatry*, vol. 165, no. 3, pp. 306–307, 2008.

[8] E. Aboujaoude, L. M. Koran, N. Gamel, M. D. Large, and R. T. Serpe, "Potential markers for problematic internet use: a telephone survey of 2,513 adults," *CNS Spectrums*, vol. 11, no. 10, pp. 750–755, 2006.

[9] N. A. Shapira, T. D. Goldsmith, P. E. Keck, U. M. Khosla, and S. L. McElroy, "Psychiatric features of individuals with problematic internet use," *Journal of Affective Disorders*, vol. 57, no. 1–3, pp. 267–272, 2000.

[10] D. L. Sun, Z. J. Chen, N. Ma, X. C. Zhang, X. M. Fu, and D. R. Zhang, "Decision-making and prepotent response inhibition functions in excessive internet users," *CNS spectrums*, vol. 14, no. 2, pp. 75–81, 2009.

[11] N. D. Volkow, J. S. Fowler, G. J. Wang, R. Baler, and F. Telang, "Imaging dopamine's role in drug abuse and addiction," *Neuropharmacology*, vol. 56, no. 1, pp. 3–8, 2009.

[12] H. S. Park, S. H. Kim, S. A. Bang, E. J. Yoon, S. S. Cho, and S. E. Kim, "Altered regional cerebral glucose metabolism in internet game overusers: a 18F-fluorodeoxyglucose positron emission tomography study," *CNS Spectrums*, vol. 15, no. 3, pp. 159–166, 2010.

[13] S. H. Kim, S.-H. Baik, C. S. Park, S. J. Kim, S. W. Choi, and S. E. Kim, "Reduced striatal dopamine D2 receptors in people with Internet addiction," *NeuroReport*, vol. 22, no. 8, pp. 407–411, 2011.

[14] D. H. Han, Y. S. Lee, K. C. Yang, E. Y. Kim, I. K. Lyoo, and P. F. Renshaw, "Dopamine genes and reward dependence in adolescents with excessive internet video game play," *Journal of Addiction Medicine*, vol. 1, no. 3, pp. 133–138, 2007.

[15] M. N. Potenza, "Should addictive disorders include non-substance-related conditions?" *Addiction*, vol. 101, no. 1, pp. 142–151, 2006.

[16] W. Schultz, "Predictive reward signal of dopamine neurons," *Journal of Neurophysiology*, vol. 80, no. 1, pp. 1–27, 1998.

[17] T. Dohi, S. Kitayama, K. Kumagai, W. Hashimoto, and K. Morita, "Pharmacology of monoamine neurotransmitter transporters," *Folia Pharmacologica Japonica*, vol. 120, no. 5, pp. 315–326, 2002.

[18] J. C. Dreher, P. Kohn, B. Kolachana, D. R. Weinberger, and K. F. Berman, "Variation in dopamine genes influences responsivity of the human reward system," *Proceedings of the National Academy of Sciences of the United States of America*, vol. 106, no. 2, pp. 617–622, 2009.

[19] R. Simantov, "Chronic morphine alters dopamine transporter density in the rat brain: possible role in the mechanism of drug addiction," *Neuroscience Letters*, vol. 163, no. 2, pp. 121–124, 1993.

[20] S. J. Kish, K. S. Kalasinsky, P. Derkach et al., "Striatal dopaminergic and serotonergic markers in human heroin users," *Neuropsychopharmacology*, vol. 24, no. 5, pp. 561–567, 2001.

[21] S. W. Jia, W. Wang, Y. Liu, and Z. M. Wu, "Neuroimaging studies of brain corpus striatum changes among heroin-dependent patients treated with herbal medicine, U'finer capsule," *Addiction Biology*, vol. 10, no. 3, pp. 293–297, 2005.

[22] J. Shi, L. Y. Zhao, M. L. Copersino et al., "PET imaging of dopamine transporter and drug craving during methadone maintenance treatment and after prolonged abstinence in heroin users," *European Journal of Pharmacology*, vol. 579, no. 1–3, pp. 160–166, 2008.

[23] H. Hou, S. Yin, S. Jia et al., "Decreased striatal dopamine transporters in codeine-containing cough syrup abusers," *Drug and Alcohol Dependence*, vol. 118, no. 2-3, pp. 148–151, 2011.

[24] P. Crits-Christoph, A. Newberg, N. Wintering et al., "Dopamine transporter levels in cocaine dependent subjects.," *Drug and Alcohol Dependence*, vol. 98, no. 1-2, pp. 70–76, 2008.

[25] H. F. Kung, H. J. Kim, M. P. Kung, S. K. Meegalla, K. Plössl, and H. K. Lee, "Imaging of dopamine transporters in humans with technetium-99m TRODAT-1," *European Journal of Nuclear Medicine*, vol. 23, no. 11, pp. 1527–1530, 1996.

[26] M. P. Kung, D. A. Stevenson, K. Plössl et al., "[^{99m}Tc]TRODAT-1: a novel technetium-99m complex as a dopamine transporter imaging agent," *European Journal of Nuclear Medicine*, vol. 24, no. 4, pp. 372–380, 1997.

[27] I. Goldberg, "Internet Addictive Disorder (IAD) Diagnostic Criteria," 1996, http://www.psycom.net/iadcriteria.html.

[28] American-Psychiatric-Association, *Diagnostic and Statistical Manual of Mental Disorders*, American Psychiatric Press, Washington DC, USA, 4th edition, 1994.

[29] P. Danos, S. Kasper, F. Grünwald et al., "Pathological regional cerebral blood flow in opiate-dependent patients during withdrawal: a HMPAO-SPECT study," *Neuropsychobiology*, vol. 37, no. 4, pp. 194–199, 1998.

[30] L. T. Chang, "A method for attenuation correction in radionuclide computed tomography," *IEEE Transactions on Nuclear Science*, vol. 25, no. 1, pp. 638–643, 1977.

[31] S. W. Jia, Z. M. Wu, H. E. Luo et al., "The value of dopamine transporter [^{99m}Tc] TRODAT-1 imaging for evaluating the therapeutic effects of Junfukang capsule on prevention and cure of drug addiction recurrence," *Chinese Journal of Nuclear Medicine*, vol. 24, no. 3, pp. 155–157, 2004.

[32] N. D. Volkow, L. Chang, G. J. Wang et al., "Loss of dopamine transporters in methamphetamine abusers recovers with protracted abstinence," *Journal of Neuroscience*, vol. 21, no. 23, pp. 9414–9418, 2001.

[33] M. J. Koepp, R. N. Gunn, A. D. Lawrence et al., "Evidence for striatal dopamine release during a video game," *Nature*, vol. 393, no. 6682, pp. 266–268, 1998.

[34] T. D. L. Steeves, J. Miyasaki, M. Zurowski et al., "Increased striatal dopamine release in Parkinsonian patients with pathological gambling: a [11C] raclopride PET study," *Brain*, vol. 132, no. 5, pp. 1376–1385, 2009.

[35] W. C. Drevets, C. Gautier, J. C. Price et al., "Amphetamine-induced dopamine release in human ventral striatum correlates with euphoria," *Biological Psychiatry*, vol. 49, no. 2, pp. 81–96, 2001.

[36] M. J. LaVoie and T. G. Hastings, "Dopamine quinone formation and protein modification associated with the striatal neurotoxicity of methamphetamine: evidence against a role for extracellular dopamine," *Journal of Neuroscience*, vol. 19, no. 4, pp. 1484–1491, 1999.

[37] R. Cilia, J. H. Ko, S. S. Cho et al., "Reduced dopamine transporter density in the ventral striatum of patients with Parkinson's disease and pathological gambling," *Neurobiology of Disease*, vol. 39, no. 1, pp. 98–104, 2010.

Hindawi Publishing Corporation
Journal of Biomedicine and Biotechnology
Volume 2012, Article ID 783739, 8 pages
doi:10.1155/2012/783739

Review Article

PET/CT in the Staging of the Non-Small-Cell Lung Cancer

Fangfang Chao[1, 2, 3, 4] and Hong Zhang[1, 2, 3, 4]

[1] *Department of Nuclear Medicine, Second Affiliated Hospital of Zhejiang University School of Medicine, Hangzhou, Zhejiang 310009, China*
[2] *Zhejiang University Medical PET Center, Zhejiang University, Hangzhou 310009, China*
[3] *Institute of Nuclear Medicine and Molecular Imaging, Zhejiang University, Hangzhou 310009, China*
[4] *Key Laboratory of Medical Molecular Imaging of Zhejiang Province, Hangzhou 310009, China*

Correspondence should be addressed to Hong Zhang, hzhang21@gmail.com

Received 1 January 2012; Accepted 20 January 2012

Academic Editor: Mei Tian

Lung cancer is a common disease and the leading cause of cancer-related death in many countries. Precise staging of patients with non-small-cell lung cancer plays an important role in determining treatment strategy and prognosis. Positron emission tomography/computed tomography (PET/CT), combining anatomic information of CT and metabolic information of PET, is emerging as a potential diagnosis and staging test in patients with non-small-cell lung cancer (NSCLC). The purpose of this paper is to discuss the value of integrated PET/CT in the staging of the non-small-cell lung cancer and its health economics.

1. Introduction

Lung cancer, with 80–85% being non-small-cell lung cancer (NSCLC), is the leading cause of cancer-related death in both men and women in the western world [1]. In 2008, 215,020 new cases are expected and 161,840 persons are projected to die from the disease in the United States [2]. Adequate therapeutic planning and prognosis is largely depended on the early diagnosis and precise staging. Computed tomography (CT) as a conditional and standard method of diagnosis and staging lung cancer provides excellent morphological information, but it has significant limitations in differentiating between benign and malignant lesions either in an organ or in lymph nodes [3]. Positron emission tomography (PET) is a unique imaging technique that provides details of functional processes in the body. However, the pool anatomic details obtained with PET make it hard to locate lesions, which can lead to errors in the diagnosis and staging of NSCLC. The combination of the 2 imaging procedures provided by integrated PET/CT scanners is relatively new, which was introduced into clinical practice in 1998 [4]. Advances in positron emission tomography combined with computed tomography (PET/CT) strive to solve these problems by allowing the acquisition of both functional and anatomical information of the whole body in a single study and has gained wide acceptance over the last few years, especially in North America and Western Europe, and its clinical utility is expected to continue to rise [5]. The purpose of this paper is to discuss the value of integrated PET/CT in the staging of the non-small-cell lung cancer and its health economics.

2. Imaging Technique

A very small amount of a biological compound labeled with a positron-emitting radionuclide, which is produced in a cyclotron and has a very short half live, is injected intravenously. A PET scanner measures the localization of the tracer in tissue. The most commonly used radionuclide is Fluoride (^{18}F) for its relatively long half-life (110 min). Glucose which is usually used to provide energy for our body, is the most commonly used biologic agent. Glucose is labeled with ^{18}F to create the glucose analog ^{18}F-fluorodeoxyglucose (^{18}F-FDG) that is the most widely used radionuclide in oncology because cancer cells have greater metabolic activity compared with normal cells. The radionuclides used in PET emit positrons as they decay. These positrons annihilate after encountering an electron and produce a pair of

photons that travel in opposite directions, which are then detected by the PET scanner. The PET scan detects these annihilation photons and is able to construct tomography images including coronal, sagittal, and transverse manners, which embody quantitative physiological, pathological, or pharmacological information [6].

Cancer cells are capable of greater intracellular uptake of FDG because of increased glucose transporters on the cell membrane and increased activity of enzymes involved in the glycolytic pathway. FDG is phosphorylated to FDG-6-phosphate which, cannot be further metabolized and remains trapped in the cells. Therefore, the uptake and accumulation of malignant regions will be greater than normal tissue cells and they will be displayed as abnormal strong gather areas.

Due to the relatively poor spatial resolution of PET, disease localization usually proved to be hard. To solve this problem, anatomic and functional imaging has been integrated into one diagnostic modality that is known as image fusion. Image fusion can be performed at 3 different levels [7]: visual fusion, software fusion, and hardware fusion. In traditional visual image fusion, the physician compares 2 separate imaging modalities viewed next to each other. The fusion takes place in his or her mind. In software image fusion, PET and CT imaging are fused using software-based algorithms, which creates 2D and 3D fusion images. As far as integrated PET/CT is considered, hardware fusion using a single detector provides the best coregistration of physiologic and anatomic detail.

Hardware fusion is the most advanced and can make best anatomic registration, but it is the most expensive and the least accessible method. In the integrated PET/CT study, low-dose CT, diagnostic CT and PET scans are all obtained in a single time. Low-dose CT obtained at quiet respiration for attenuation correction results in a lower noise emission scan and faster examinations (reduction of whole body scan times by at least 40%) and, thus, fewer motion artifacts and a higher throughput [8]. The diagnostic CT, obtained with the administration of contrast material, provides excellent anatomic data. Fusion obtained using external software, which creates 2D and 3D fusion images [9].

3. Staging

Accurate staging of patients with non-small-cell lung cancer is critical in determining treatment strategy and predicting prognosis. Nowadays we usually take TNM staging system, which is maintained by the American Joint Committee on Cancer and the International Union Against Cancer [10]. TNM staging system is based on a combination of findings: the location and extent of the primary tumor (T), the presence or absence of intrapulmonary, hilar or mediastinal lymph node metastases (N), and the presence or absence of extrathoracic metastases (M) [11, 12]. The combination of T, N, and M staging is then used to give the tumor an overall stage (I–IV), with the aim of grouping patients into stages with similar prognosis. Survival rate and treatment options also vary from stage to stage [10].

Based on adequate diagnosis and staging, personalized treatment strategies can be selected to gain best prognosis and to be cost-effective. The recommended therapy [13] for stage I disease is surgical resection, with stereotactic body radiation therapy (SBRT) [14, 15] reserved for those who are medically inoperable. Stage II disease is also treated with surgery followed by adjuvant chemotherapy to prevent disease recurrence. Stage IIIA disease has multiple treatment options determined by the extent of regional (nodal) involvement. Stage IIIA disease is often treated with concurrent chemotherapy and radiation, adding surgical resection (trimodality therapy) for those who are medically fit and have responded well to initial concurrent therapy. Stage IIIB disease is treated with concurrent chemotherapy and radiation. Stage IV disease is treated with systemic therapy, chemotherapy, and/or molecular targeted agents, in addition to radiotherapy for alleviating of painful lesions or brain metastasis. Many studies have demonstrated that integrated PET/CT is more accurate than CT alone, PET alone [16, 17], and visually correlated PET/CT in evaluating, the TNM status [18].

3.1. T Staging. T staging describes the location, size, and extension of the primary tumor and the presence or absence of satellite nodules. CT is an important imaging modality for the evaluation of the primary tumor because of its excellent anatomical resolution. But it is difficult for it to evaluate the invasion of the chest wall or involvement of the mediastinum and differentiate tumors from postobstructive atelectasis correctly [19].

FDG-PET gives more information about the metabolic changes of the neoplasm but offers little application in the T staging of non-small-cell lung cancer, because of its limited ability for precise anatomic location and size measurement. PET is limited in detecting microscopic tumor deposits, correctly evaluating extension of tumor and biological low metabolism tumor, such as bronchoalveolar cell carcinoma, carcinoid tumors, and some adenomas [18]. It is striking that PET alone are both upstaging and understaging for the T staging of patients with NSCLC.

It has been shown that integrated PET/CT provided more than the sum of PET and CT [20]. In particular, it improves T staging [21]. Due to precise CT correlation with the extent of ^{18}F-FDG uptake, the location of the primary tumor can be exactly defined. It has been demonstrated that integrated PET/CT provides important information on mediastinal infiltration, chest wall infiltration, and differentiation between tumor and peritumoral atelectasis [3]. It has been found in many literatures [21] that PET/CT is the best noninvasive imaging technique for the accurate prediction of T staging. In one study of Wever et al. [18], integrated PET/CT correctly predicted the T staging in patients with NSCLC in 86% of cases versus 68% with CT, 46% with PET, 72% with visually correlated PET/CT.

3.2. N Staging. Accurate mediastinal staging is particularly important, as in many cases the status of these nodes will determine whether surgical resection of lung cancer is

Table 1: Recent studies evaluating N staging with PET/CT compared with PET and CT.

Ref.	Sensitivity (%)			Specificity (%)			PPV (%)			NPV (%)			Accuracy (%)		
	PET/CT	PET	CT	PET/CT	PET	CT	PET/CT	PET	CT	PET/CT	PET	CT	PET/CT	PET	CT
[25]	70			94			64			95					
[26]				95		77							87		69
[27]	54			92			74			82			81		
[28]	65			97			79			90			92		
[29]	86		69	85		71	64		43	95		88	85		71
[18]	83	83	83	84	81	68	75	71	60	90	89	88	84	82	74
[30]	84		84	85		61							85		74
[31]	56		65	100		89							90		83
[20]	85		70	84		69							84		69
Average	73	83	74	91	81	73	71	71	52	90	89	88	86	82	73

possible [3]. The accuracy of CT for determining N staging remains limited, because nodal staging with CT is based on morphological characteristics. Lymph node size is used as the only criterion to determine metastatic disease. The current consensus considers a lymph node with a short-axis diameter greater than 1 cm as a predictor for metastasis [22]. However, if postobstructive pneumonitis is present, little correlation exists between the size of the mediastinal lymph nodes and tumor involvement [23]. Normal-sized regional lymph nodes may prove to be metastasizing upon histological examination, and nodal enlargement can be due to reactive hyperplasia or other nonmalignant conditions. PET has been reported to increase diagnostic accuracy in the differentiation of benign and malignant lesions and to improve identification of nodal metastasis. Functional scans obtained with FDG PET not only are complementary to those obtained with conventional modalities but also may be more sensitive because alterations in tissue metabolism generally precede anatomic change [24]. However, its poor spatial detail and FDG being nonspecific tracer can lead to inaccuracies, particularly in the areas of normal physiologic uptake.

By integrating functional and anatomic data, PET/CT improved N staging compared with PET or CT alone. Indeed the benefit of PET/CT compared with PET in nodal staging appears to lie in a moderate increase in specificity and positive predictive value for its additional exactly anatomic information. Because of attaching metabolism information of lymph node, PET/CT improves accuracy compared with CT. Initial studies demonstrated a pooled average sensitivity, specificity, positive predictive value, negative predictive value, and accuracy of PET/CT for detecting metastatic lymph nodes of, respectively, 73%, 91%, 71%, 90%, and 86% versus 83%, 81%, 71%, 89%, 82% of PET alone and 74%, 73%, 52%, 88%, 73% of CT alone. The results of these studies are summarised in Table 1 [18, 20, 25–31].

In one study performed by Darling et al. [25], of 22 patients with a PET/CT interpreted as positive for mediastinal nodes, 8 did not have tumor. Based on PET/CT alone, eight patients would have been denied potentially curative surgery if the mediastinal abnormalities detected by PET/CT had not been evaluated with an invasive mediastinal procedure. PET/CT assessment of the mediastinum is associated with a clinically relevant false-positive rate. When positive mediastinal lymph nodes are detected, invasive mediastinal staging must be performed [25]. While mediastinal lymph nodes is negative, surgery can be done directly because of its high negative predict value.

There is an ongoing controversy whether PET/CT scan can reduce further invasive mediastinal staging. The general consensus is that PET/CT can reduce mediastinoscopy for high negative predict value. Perigaud et al. [32] reported the specificity is high: patients with negative integrated ^{18}F-FDG PET/CT can be operated upon directly without invasive mediastinal staging. While one study of Metin et al. [33] showed that PET/CT does not reduce the need for invasive procedures in detecting lymph node metastasis in aortopulmonary window. By integrating functional and anatomic data, PET/CT is the best noninvasive method for the detection of nodal metastasis, but mediastinoscopy remains the gold standard [25, 33]. The results of imaging are not conclusive and the probability of mediastinal involvement is high (based on tumor size and location), which are the indications for mediastinoscopy. Therefore, mediastinoscopy is appropriate for patients with T2 and T3 lesions even if the PET/CT scan does not suggest mediastinal node involvement. Mediastinoscopy may also be appropriate to confirm mediastinal node involvement in patients with a positive PET/CT scan [12]. In general, the biopsy of the lymph node with the highest stage by endoscopic bronchial ultrasound (EBUS) or mediastinoscopy is sufficient for further treatment decisions. However, not all mediastinal lymph nodes are routinely reachable by EBUS or mediastinoscopy (paraaortic region, aortopulmonary window). Recently, it has been demonstrated that PET can assist mediastinoscopy [3].

3.3. M Staging. Despite radical surgical treatment of potentially curable NSCLC the overall 5-year survival rate remains low (20–40%). One reason for this is undetected extrathoracic metastases, which cause underestimation of the tumor

stage [3]. NSCLC most metastasizes to the brain, bones, liver, and adrenal glands [34].

Radionuclide bone scanning with ^{99m}Tc-methylene diphosphonate is usually used in the detection of occult skeletal metastases; however, it has high false-positive rate [35]. The accuracy of bone scintigraphy to detect bone metastases was 87% versus 98% of ^{18}F-FDG PET. PET scanning is more sensitive and accurate than bone scanning for the detection of skeletal metastases (91% and 94% versus 75% and 85%, resp.), with a high PPV of 98% if the findings on PET/CT scanning are concordant, but decreases to 61% if the CT scan is negative [36].

Adrenal metastases from lung cancer are common, found in approximately 33% of patients at autopsy [12]. In patients with NSCLC, however, many solitary adrenal masses are not malignant. So it is very critical in distinguishing between a metastatic lesion and an adenoma. Diagnostic CT evaluates adrenal metastases based on tumor size and attenuation value, which may lead to false negative or false positive results. Any adrenal mass found on a preoperative CT scan in a patient with lung cancer should be biopsied to rule out benign adenoma. For magnetic resonance imaging (MRI), the ability to distinguish metastases from adenomas has improved considerably with the introduction of more sophisticated MR imaging techniques such as fat-saturated, chemical shift and dynamic gadolinium-enhanced MR imaging. One group of investigators correlated the MR imaging findings with histological results in 114 patients with 134 adrenal masses. Combined chemical shift and dynamic gadolinium-enhanced MR imaging was found to have a sensitivity of 91% and a specificity of 94% for differentiating benign from malignant adrenal masses [37]. In fact, PET scanning is useful in distinguishing benign from malignant adrenal masses detected on CT scanning [35, 38]. In some studies, integrated PET/CT is a useful diagnostic modality for adrenal gland imaging in cancer patients, since it allows early detection and accurate localization of adrenal lesions and differentiation of metastatic nodules from benign lesions, thereby facilitating treatment planning [39, 40]. However, some adenoma may show increased FDG, which will produce false positive results. Hemorrhage, necrosis [37, 41], and subcentimeter metastatic lesions may have low FDG uptake, which will lead to produce false negative results. In one study performed by Perri et al. [42], they demonstrated that the combination of standardized uptake value (SUV) and CT histogram analysis allowed us to significantly improve the PET/CT diagnostic accuracy for characterizing adrenal lesions, leading to a significant reduction in the number of false positive cases. In another study, Chong et al. [43] reported that fine-needle aspiration biopsy should be performed only if clinical and imaging studies are inconclusive.

In the newly adopted 7th edition of the TNM classification for lung cancer, NSCLC metastatic is subdivided into M1a for those cases with pleural nodules or malignant pleural or pericardial effusion and additional pulmonary nodules in the contralateral lung and M1b for those cases with other distant metastases disease [44]. The presence of pleural or pericardial nodules on CT can confirm the diagnosis of M1a disease, but these findings are often absent. PET can usually suggest the diagnosis of malignant pleural disease by showing increased focal or diffuse FDG uptake, but localization to the pleura or pericardium is not always clear for its poor resolution. Statistically, PET/CT has proven to be superior to either technique the in evaluation of metastatic pleural disease.

PET/CT has a low sensitivity in detecting brain metastases because of brain cells with high glucose uptake in nature. Therefore, in patients with neurological symptoms, an MRI of the brain should be performed, because of its high resolution, while Salskov et al. reported that PET using ^{18}F-fluorothymidine (^{18}F-FLT) for its low physiological uptake in brain can be used in detecting brain metastases [45].

PET/CT can improve the accuracy in the staging of non-small-cell lung cancer. For N staging, PET/CT scanning possessing high negative predict value can reduce unnecessary mediastinoscopy. Although some authors found no significant reduction in the number of avoidable thoracotomies performed when employing additional PET imaging in NSCLC, the general consensus is that PET can reduce needless thoracotomy rates. In one study of Fischer et al. [46], a total of 189 patients were enrolled and randomly assigned to either the PET/CT group (98 patients) or the conventional-staging group (91 patients). After staging, 60 patients in the PET/CT group (61%) and 73 patients in the conventional-staging group (80%) were considered to have operable disease and underwent thoracotomy ($P = 0.004$), while a total of 21 of 98 patients in the PET/CT group (21%) and 38 of 91 in the conventional-staging group (42%) underwent a futile thoracotomy. In other words, for every five PET/CT scans, one futile thoracotomy was avoided. Therefore, they reported that the use of PET/CT for preoperative staging of NSCLC reduced both the total number of thoracotomies and the number of futile thoracotomies. Two randomized trials have assessed the clinical effect of PET alone. A trial by van Tinteren et al. [47] showed that the number of futile thoracotomies was significantly reduced in 19/82 patients compared to 29/96 patients, based on the addition of ^{18}F-FDG PET to the diagnostic algorithm. A randomized trial, however, did not show that adding PET reduced the number of thoracotomies [48]. We have to notice that imaging strategies based on PET/CT may help identify advanced disease and prevent futile thoracotomies in patients with NSCLC, but it also has false positive results that incorrectly upstage disease in some patients.

Despite an extensive literature documenting the sensitivity and specificity of PET/CT scanning, rarely publications exist to demonstrate an increased survival of patients with NSCLC due to the use of PET scanning. The studies of Fontaine et al. [49] showed that the introduction of routine PET scanning did not result in improved survival in the short or long term for patients undergoing resections for stage IA, IB and stage II, while a significant increased survival for stage III primary lung cancer ($P = 0.03$). They concluded that patients with stage III non-small-cell lung cancer should undergo PET scanning prior to surgical resection.

While in the study of Fischer et al. [46] 98 patients were assigned to PET/CT group, 91 patients were assigned

to the conventional-staging group. They found that there were no significant differences in survival between the two groups; median survival was 31 months in the PET/CT group and 49 months in the conventional-staging group ($P = 0.29$). Therefore, they reported that the use of PET/CT for preoperative staging of NSCLC did not improve overall survival rate.

4. The Cost-Effectiveness of PET/CT in NSCLC Staging

A diagnostic effectiveness of PET/CT for staging NSCLC and superiority to conventional cancer imaging modalities has been demonstrated by many studies [18, 20, 50, 51]. However, whether this technology should be widely applied in the staging of NSCLC remains at debate for its high examination costs. In addition, this may be offset in part by improvements in staging accuracy and examination times [52]. In recent years, incremental cost-effectiveness ratios (ICER), quality-adjusted life year (QALY) et al., were used to evaluate healthy economic of this technology. Several cost-effectiveness analyses have been published evaluating PET in lung cancer staging, though data specifically on PET/CT is absence.

In a randomized trial performed by van Tinteren et al. [47], 96 patients were randomly assigned conventional workup (CWU) and 92 conventional workup and PET (CWU + PET). In the CWU group, 39 (41%) patients had futile thoracotomies, compared with 19 (21%) in the CWU + PET group (relative reduction 51%, $P = 0.003$). The addition of PET to CWU prevented futile surgery in one out of five patients with suspected NSCLC. Despite the additional PET costs, the total costs were lower in the PET group, mainly due to a reduction in the number of futile operations and general hospital days especially intensive care days. The additional use of PET in the staging of patients with NSCLC is feasible and safe, and it saves costs from a clinical and an economic perspective.

A study performed in Canada showed that PET for staging NSCLC without CT coregistration, compared with CT alone, led to a cost savings of $1,455 combined with an increase in life expectancy of 3.1d [53]. Recently, the diagnostic value and cost-effectiveness have also been approved by the German health care system [54].

In one study based on 172 NSCLC patients who underwent diagnostic, contrast-enhanced helical CT and integrated PET/CT, Schreyögg et al. [55]reported that the incremental cost-effectiveness ratios (ICER) per correctly staged patient were $3,508 for PET/CT versus CT alone. The ICER per quality-adjusted life year (QALY) gained were $79,878 for PET/CT versus CT alone, decreasing to $69,563 assuming a reduced loss of utility (0.10 QALY) due to surgical morbidity. The study showed that costs for PET/CT are within the commonly accepted range for diagnostic tests, therapies, or staging from the payer's perspective.

Søgaard et al. [56] performed a randomized clinical trial in which 189 patients were allocated to conventional staging ($n = 91$) or conventional staging + PET/CT ($n = 98$) and followed for 1 year after which the numbers of futile thoracotomies in each group were monitored. They showed that implementation of PET/CT into the diagnostic algorithm of staging NSCLC is cost-effective. The ICER was calculated to be 19,314 €, meaning that PET/CT is cost-effective if the provider's willingness to pay (WTP) is 50,000 € per avoided futile thoracotomy. Including comorbidity-related costs, we found that the cost-effectiveness of PET/CT for staging NSCLC depends on the WTP in order to avoid a futile thoracotomy for which there is no true threshold value. A futile thoracotomy can be futile either because it is performed in patients with a benign lung lesion or because it is performed in patients with unresectable, end-stage cancer.

5. The Limitation of PET/CT in Staging of Non-Small-Cell Lung Cancer

Although PET/CT is an accurate and noninvasive method in the staging of non-small-cell lung cancer, many pitfalls exist. Imprecise physiologic and anatomic registration, most common adjacent to the diaphragm and heart, can lead to misregistration artifact [57]. Misregistration occurs as a result of differences in the position of the patient during the CT and PET examination. This may occur either as a result of voluntary motion of the patient during the examination or more commonly because of discrepancies in the phases of the patient's respiratory cycle during the CT and PET examinations [52]. Misregistration can lead to incorrect anatomical registration of PET and CT images, which can affect the accurate localization of uptake within pulmonary masses or lymph nodes. Cohade et al. [58] reported the mean discrepancy between the location of pulmonary lesions on PET and CT was approximately 7 mm, with better registration at the lung apices than bases. These misregistrations can make micro-lesions missed, resulting in false negative results.

As a general rule uptake of SUV(max) ≥ 2.5 was considered to indicate a malignant lesion, and SUV(max) < 2.5 was considered to indicate a benign lesion [59]. Many processes with increased metabolic activities show increased FDG uptake on PET/CT imaging. Several benign lesions that have increased glucose metabolism can accumulate FDG and can be misinterpreted as malignant, such as infection, inflammation, and infarct [10]. In addition, physiological uptake of FDG usually found in the brain, heart, gastrointestinal and genitourinary tracts, and striated muscles show increased FDG uptake on PET/CT imaging. Iatrogenic causes of focal or diffuse FDG uptake include, granulation tissue, healing wounds, chest tubes and gastrotomy tubes, percutaneous needle biopsy, and mediastinoscopy [60]. These increased FDG uptake can lead to false positive results. There is some evidence to suggest that "dual-time-point" imaging may be helpful in differentiating malignant versus inflammatory and infectious processes [61].

False-negative FDG uptake includes technological limitations of PET/CT and inherent properties of neoplasm. Lesions that measure less than two to three times than the spatial resolution of the scanner will appear less active

and a lower SUV due to the partial volume effect. Lesions containing little cells, low metabolic neoplasm, and highly differentiated tumors can lead to false negative results. It is important for us to know these potential pitfalls in order to get more accuracy staging of non-small-cell lung cancer.

6. Conclusion

The accurate staging of NSCLC is important in determining optimal treatment strategy and getting a better prognosis. Integrated PET/CT combining the benefits of PET and CT and minimizing their limitations is a potential tool in the staging of non-small-cell lung cancer. It reduces futile treatment and its associated morbidity and cost, improving the quality of life and being cost-effectiveness.

Abbreviations

PET/CT:	Positron emission tomography/computed tomography
NSCLC:	Non-small-cell lung cancer
CT:	Computed tomography
PET:	Positron emission tomography
^{18}F-FDG:	^{18}F-fluorodeoxyglucose
MRI:	Magnetic resonance imaging
EBUS:	Endoscopic bronchial ultrasound
^{99m}Tc-MDP:	^{99m}Tc-methylene diphosphonate
SUV:	Standardized uptake value
FLT:	^{18}F-fluorothymidine
ICER:	Incremental cost-effectiveness ratios
QALY:	Quality-adjusted life year
CWU:	Conventional workup
CWU + PET:	Conventional workup and PET
WTP:	Willingness to pay.

Acknowledgments

This work is partly sponsored by grants from the Zhejiang Provincial Natural Science Foundation of China (Z2110230), Health Bureau of Zhejiang Province (2010ZA075), National Science Foundation of China (NSFC) (no. 81101023, 81170306, 81173468), and Ministry of Science and Technology of China (2011CB504400).

References

[1] D. Morgensztern, B. Goodgame, M. Q. Baggstrom, F. Gao, and R. Govindan, "The effect of FDG-PET on the stage distribution of non-small cell lung cancer," *Journal of Thoracic Oncology*, vol. 3, no. 2, pp. 135–139, 2008.

[2] A. Jemal, R. Siegel, E. Ward et al., "Cancer statistics, 2008," *CA: A Cancer Journal for Clinicians*, vol. 58, no. 2, pp. 71–96, 2008.

[3] H. C. Steinert, "PET and PET-CT of lung cancer," *Methods in Molecular Biology*, vol. 727, pp. 33–51, 2011.

[4] W. De Wever, J. Coolen, and J. A. Verschakelen, "Integrated PET/CT and cancer imaging," *JBR-BTR*, vol. 92, no. 1, pp. 13–19, 2009.

[5] S. Y. Low, P. Eng, G. H. W. Keng, and D. C. E. Ng, "Positron emission tomography with CT in the evaluation of non-small cell lung cancer in populations with a high prevalence of tuberculosis," *Respirology*, vol. 11, no. 1, pp. 84–89, 2006.

[6] P. McQuade, D. J. Rowland, J. S. Lewis, and M. J. Welch, "Positron-emitting isotopes produced on biomedical cyclotrons," *Current Medicinal Chemistry*, vol. 12, no. 7, pp. 807–818, 2005.

[7] W. V. Vogel, W. J. Oyen, J. O. Barentsz, J. H. Kaanders, and F. H. Corstens, "PET/CT: panacea, redundancy, or something in between?" *Journal of Nuclear Medicine*, vol. 45, supplement 1, pp. 15S–24S, 2004.

[8] Y. Y. Yau, W. S. Chan, Y. M. Tam et al., "Application of intravenous contrast in PET/CT: does it really introduce significant attenuation correction error?" *Journal of Nuclear Medicine*, vol. 46, no. 2, pp. 283–291, 2005.

[9] S. Kligerman and S. Digumarthy, "Staging of non-small cell lung cancer using integrated PET/CT," *American Journal of Roentgenology*, vol. 193, no. 5, pp. 1203–1211, 2009.

[10] S. Tsim, C. A. O'Dowd, R. Milroy, and S. Davidson, "Staging of non-small cell lung cancer (NSCLC): a review," *Respiratory Medicine*, vol. 104, no. 12, pp. 1767–1774, 2010.

[11] R. Rami-Porta, J. J. Crowley, and P. Goldstraw, "The revised TNM staging system for lung cancer," *Annals of Thoracic and Cardiovascular Surgery*, vol. 15, no. 1, pp. 4–9, 2009.

[12] L. L. Carr, J. H. Finigan, and J. A. Kern, "Evaluation and treatment of patients with non-small cell lung cancer," *Medical Clinics of North America*, vol. 95, no. 6, pp. 1041–1054, 2011.

[13] D. S. Ettinger, W. Akerley, G. Bepler et al., "Non-small cell lung cancer: clinical practice guidelines in oncology," *Journal of the National Comprehensive Cancer Network*, vol. 8, no. 7, pp. 740–801, 2010.

[14] J. P. C. Grutters, A. G. H. Kessels, M. Pijls-Johannesma, D. De Ruysscher, M. A. Joore, and P. Lambin, "Comparison of the effectiveness of radiotherapy with photons, protons and carbon-ions for non-small cell lung cancer: a meta-analysis," *Radiotherapy and Oncology*, vol. 95, no. 1, pp. 32–40, 2010.

[15] R. Timmerman, R. Paulus, J. Galvin et al., "Stereotactic body radiation therapy for inoperable early stage lung cancer," *JAMA*, vol. 303, no. 11, pp. 1070–1076, 2010.

[16] D. Lardinois, W. Weder, T. F. Hany et al., "Staging of non-small-cell lung cancer with integrated positron-emission tomography and computed tomography," *The New England Journal of Medicine*, vol. 348, no. 25, pp. 2500–2507, 2003.

[17] B. M. Fischer and J. Mortensen, "The future in diagnosis and staging of lung cancer: positron emission tomography," *Respiration*, vol. 73, no. 3, pp. 267–276, 2006.

[18] W. Wever, S. Ceyssens, L. Mortelmans et al., "Additional value of PET-CT in the staging of lung cancer: comparison with CT alone, PET alone and visual correlation of PET and CT," *European Radiology*, vol. 17, no. 1, pp. 23–32, 2007.

[19] W. R. Webb, C. Gatsonis, E. A. Zerhouni et al., "CT and MR imaging in staging non-small cell bronchogenic carcinoma: report of the Radiologic Diagnostic Oncology Group," *Radiology*, vol. 178, no. 3, pp. 705–713, 1991.

[20] S. S. Shim, K. S. Lee, B. T. Kim et al., "Non-small cell lung cancer: prospective comparison of integrated FDG PET/CT and CT alone for preoperative staging," *Radiology*, vol. 236, no. 3, pp. 1011–1019, 2005.

[21] S. Pauls, A. K. Buck, K. Hohl et al., "Improved non-invasive T-Staging in non-small cell lung cancer by integrated 18F-FDG PET/CT," *NuklearMedizin*, vol. 46, no. 1, pp. 9–14, 2007.

[22] J. A. Verschakelen, W. De Wever, and J. Bogaert, "Role of computed tomography in lung cancer staging," *Current Opinion in Pulmonary Medicine*, vol. 10, no. 4, pp. 248–255, 2004.

[23] K. M. Kerr, D. Lamb, C. G. Wathen, W. S. Walker, and N. J. Douglas, "Pathological assessment of mediastinal lymph nodes in lung cancer: implications for non-invasive mediastinal staging," *Thorax*, vol. 47, no. 5, pp. 337–341, 1992.

[24] N. C. Gupta, W. J. Tamim, G. G. Graeber, H. A. Bishop, and G. R. Hobbs, "Mediastinal lymph node sampling following positron emission tomography with fluorodeoxyglucose imaging in lung cancer staging," *Chest*, vol. 120, no. 2, pp. 521–527, 2001.

[25] G. E. Darling, D. E. Maziak, R. I. Inculet et al., "Positron emission tomography-computed tomography compared with invasive mediastinal staging in non-small cell lung cancer: results of mediastinal staging in the early lung positron emission tomography trial," *Journal of Thoracic Oncology*, vol. 6, no. 8, pp. 1367–1372, 2011.

[26] T. Y. Jeon, K. S. Lee, C. A. Yi et al., "Incremental value of PET/CT over CT for mediastinal nodal staging of non-small cell lung cancer: comparison between patients with and without idiopathic pulmonary fibrosis," *American Journal of Roentgenology*, vol. 195, no. 2, pp. 370–376, 2010.

[27] A. Billé, E. Pelosi, A. Skanjeti et al., "Preoperative intrathoracic lymph node staging in patients with non-small-cell lung cancer: accuracy of integrated positron emission tomography and computed tomography," *European Journal of Cardio-Thoracic Surgery*, vol. 36, no. 3, pp. 440–445, 2009.

[28] B.-J. Liu, J.-C. Dong, C.-Q. Xu et al., "Accuracy of 18F-FDG PET/CT for lymph node staging in non-small-cell lung cancers," *Chinese Medical Journal*, vol. 122, no. 15, pp. 1749–1754, 2009.

[29] W. F. Yang, G. Z. Tan, Z. Fu, and J. M. Yu, "[Evaluation of the diagnostic value of (18)F-FDG PET-CT and enhanced CT for staging of lymph node metastasis in non-small cell lung cancer]," *Chinese Journal of Oncology*, vol. 31, no. 12, pp. 925–928, 2009.

[30] K. G. Tournoy, S. Maddens, R. Gosselin, G. Van Maele, J. P. Van Meerbeeck, and A. Kelles, "Integrated FDG-PET/CT does not make invasive staging of the intrathoracic lymph nodes in non-small cell lung cancer redundant: a prospective study," *Thorax*, vol. 62, no. 8, pp. 696–701, 2007.

[31] C. A. Yi, K. S. Lee, B. T. Kim et al., "Efficacy of helical dynamic CT versus integrated PET/CT for detection of mediastinal nodal metastasis in non-small cell lung cancer," *American Journal of Roentgenology*, vol. 188, no. 2, pp. 318–325, 2007.

[32] C. Perigaud, B. Bridji, J. C. Roussel et al., "Prospective preoperative mediastinal lymph node staging by integrated positron emission tomography-computerised tomography in patients with non-small-cell lung cancer," *European Journal of Cardio-Thoracic Surgery*, vol. 36, no. 4, pp. 731–736, 2009.

[33] M. Metin, N. Citak, A. Sayar et al., "The role of extended cervical mediastinoscopy in staging of non-small cell lung cancer of the left lung and a comparison with integrated positron emission tomography and computed tomography: does integrated positron emission tomography and computed tomography reduce the need for invasive procedures?" *Journal of Thoracic Oncology*, vol. 6, no. 10, pp. 1713–1719, 2011.

[34] L. E. Quint, S. Tummala, L. J. Brisson et al., "Distribution of distant metastases from newly diagnosed non-small cell lung cancer," *Annals of Thoracic Surgery*, vol. 62, no. 1, pp. 246–250, 1996.

[35] M. T. Truong, C. Viswanathan, and J. J. Erasmus, "Positron emission tomography/computed tomography in lung cancer staging, prognosis, and assessment of therapeutic response," *Journal of Thoracic Imaging*, vol. 26, no. 2, pp. 132–146, 2011.

[36] A. V. Taira, R. J. Herfkens, S. S. Gambhir, and A. Quon, "Detection of bone metastases: assessment of integrated FDG PET/CT imaging," *Radiology*, vol. 243, no. 1, pp. 204–211, 2007.

[37] G. Heinz-Peer, S. Hönigschnabl, B. Schneider, B. Niederle, K. Kaserer, and G. Lechner, "Characterization of adrenal masses using MR imaging with histopathologic correlation," *American Journal of Roentgenology*, vol. 173, no. 1, pp. 15–22, 1999.

[38] S. Jana, T. Zhang, D. M. Milstein, C. R. Isasi, and M. D. Blaufox, "FDG-PET and CT characterization of adrenal lesions in cancer patients," *European Journal of Nuclear Medicine and Molecular Imaging*, vol. 33, no. 1, pp. 29–35, 2006.

[39] M. S. Yon, S. L. Kyung, B. T. Kim et al., "18F-FDG PET versus 18F-FDG PET/CT for adrenal gland lesion characterization: a comparison of diagnostic efficacy in lung cancer patients," *Korean Journal of Radiology*, vol. 9, no. 1, pp. 19–28, 2008.

[40] C. Ansquer, S. Scigliano, E. Mirallié et al., "18F-FDG PET/CT in the characterization and surgical decision concerning adrenal masses: a prospective multicentre evaluation," *European Journal of Nuclear Medicine and Molecular Imaging*, vol. 37, no. 9, pp. 1669–1678, 2010.

[41] M. Yun, W. Kim, N. Alnafisi, L. Lacorte, S. Jang, and A. Alavi, "18F-FDG PET in characterizing adrenal lesions detected on CT or MRI," *Journal of Nuclear Medicine*, vol. 42, no. 12, pp. 1795–1799, 2001.

[42] M. Perri, P. Erba, D. Volterrani et al., "Adrenal masses in patients with cancer: PET/CT characterization with combined CT histogram and standardized uptake value PET analysis," *American Journal of Roentgenology*, vol. 197, no. 1, pp. 209–216, 2011.

[43] S. Chong, S. L. Kyung, Y. K. Ha et al., "Integrated PET-CT for the characterization of adrenal gland lesions in cancer patients: diagnostic efficacy and interpretation pitfalls," *Radiographics*, vol. 26, no. 6, pp. 1811–1824, 2006.

[44] P. Goldstraw, J. Crowley, K. Chansky et al., "The IASLC lung cancer staging project: proposals for the revision of the TNM stage groupings in the forthcoming (seventh) edition of the TNM classification of malignant tumours," *Journal of Thoracic Oncology*, vol. 2, no. 8, pp. 706–714, 2007.

[45] A. Salskov, V. S. Tammisetti, J. Grierson, and H. Vesselle, "FLT: measuring Tumor Cell Proliferation In Vivo With Positron Emission Tomography and 3′-Deoxy-3′-[^{18}F]Fluorothymidine," *Seminars in Nuclear Medicine*, vol. 37, no. 6, pp. 429–439, 2007.

[46] B. Fischer, U. Lassen, J. Mortensen et al., "Preoperative staging of lung cancer with combined PET-CT," *The New England Journal of Medicine*, vol. 361, no. 1, pp. 32–39, 2009.

[47] H. van Tinteren, O. S. Hoekstra, E. F. Smit et al., "Effectiveness of positron emission tomography in the preoperative assessment of patients with suspected non-small-cell lung cancer: the PLUS multicentre randomised trial," *The Lancet*, vol. 359, no. 9315, pp. 1388–1392, 2002.

[48] R. C. Viney, M. J. Boyer, M. T. King et al., "Randomized controlled trial of the role of positron emission tomography in the management of stage I and II non-small-cell lung cancer," *Journal of Clinical Oncology*, vol. 22, no. 12, pp. 2357–2362, 2004.

[49] E. Fontaine, J. McShane, M. Carr et al., "Does positron emission tomography scanning improve survival in patients undergoing potentially curative lung resections for non-small-cell lung cancer?" *European Journal of Cardio-Thoracic Surgery*, vol. 40, no. 3, pp. 642–646, 2011.

[50] A. K. Buck, K. Herrmann, T. Stargardt, T. Dechow, B. J. Krause, and J. Schreyögg, "Economic evaluation of PET and PET/CT in oncology: evidence and methodologic approaches," *Journal of Nuclear Medicine Technology*, vol. 38, no. 1, pp. 6–17, 2010.

[51] T. L. Allen, A. T. K. Kendi, M. O. Mitiek, and M. A. Maddaus, "Combined contrast-enhanced computed tomography and 18-fluoro-2-deoxy-D-glucose-positron emission tomography in the diagnosis and staging of non-small cell lung cancer," *Seminars in Thoracic and Cardiovascular Surgery*, vol. 23, no. 1, pp. 43–50, 2011.

[52] A. Devaraj, G. J. R. Cook, and D. M. Hansell, "PET/CT in non-small cell lung cancer staging-promises and problems," *Clinical Radiology*, vol. 62, no. 2, pp. 97–108, 2007.

[53] J. S. Sloka, P. D. Hollett, and M. Mathews, "Cost-effectiveness of positron emission tomography for non-small cell lung carcinoma in Canada," *Medical Science Monitor*, vol. 10, no. 5, pp. MT73–MT80, 2004.

[54] A. K. Buck, K. Herrmann, and J. Schreyögg, "PET/CT for staging lung cancer: costly or cost-saving?" *European Journal of Nuclear Medicine and Molecular Imaging*, vol. 38, no. 5, pp. 799–801, 2011.

[55] J. Schreyögg, J. Weller, T. Stargardt et al., "Cost-effectiveness of hybrid PET/CT for staging of non-small cell lung cancer," *Journal of Nuclear Medicine*, vol. 51, no. 11, pp. 1668–1675, 2010.

[56] R. Søgaard, B. M. B. Fischer, J. Mortensen, L. Højgaard, and U. Lassen, "Preoperative staging of lung cancer with PET/CT: cost-effectiveness evaluation alongside a randomized controlled trial," *European Journal of Nuclear Medicine and Molecular Imaging*, vol. 38, no. 5, pp. 802–809, 2011.

[57] M. D. Gilman, A. J. Fischman, V. Krishnasetty, E. F. Halpern, and S. L. Aquino, "Optimal CT breathing protocol for combined thoracic PET/CT," *American Journal of Roentgenology*, vol. 187, no. 5, pp. 1357–1360, 2006.

[58] C. Cohade, M. Osman, L. T. Marshall, and R. L. Wahl, "PET-CT: accuracy of PET and CT spatial registration of lung lesions," *European Journal of Nuclear Medicine and Molecular Imaging*, vol. 30, no. 5, pp. 721–726, 2003.

[59] M. Okada, T. Shimono, Y. Komeya et al., "Adrenal masses: the value of additional fluorodeoxyglucose-positron emission tomography/computed tomography (FDG-PET/CT) in differentiating between benign and malignant lesions," *Annals of Nuclear Medicine*, vol. 23, no. 4, pp. 349–354, 2009.

[60] T. F. Hany, J. Heuberger, and G. K. von Schulthess, "Iatrogenic FDG foci in the lungs: a pitfall of PET image interpretation," *European Radiology*, vol. 13, no. 9, pp. 2122–2127, 2003.

[61] S.-J. Kim, Y.-K. Kim, I. J. Kim, Y. D. Kim, and M. K. Lee, "Limited predictive value of dual-time-point F-18 FDG PET/CT for evaluation of pathologic N1 status in NSCLC patients," *Clinical Nuclear Medicine*, vol. 36, no. 6, pp. 434–439, 2011.

Hindawi Publishing Corporation
Journal of Biomedicine and Biotechnology
Volume 2012, Article ID 671708, 9 pages
doi:10.1155/2012/671708

Research Article

Development of Tyrosine-Based Radiotracer ^{99m}Tc-N4-Tyrosine for Breast Cancer Imaging

Fan-Lin Kong,[1] Mohammad S. Ali,[1] Alex Rollo,[1] Daniel L. Smith,[2] Yinhan Zhang,[1] Dong-Fang Yu,[1] and David J. Yang[1]

[1] *Department of Experimental Diagnostic Imaging, The University of Texas MD Anderson Cancer Center, Houston, TX 77030, USA*
[2] *Department of Imaging Physics, The University of Texas MD Anderson Cancer Center, Houston, TX 77030, USA*

Correspondence should be addressed to Fan-Lin Kong, kongfanlin2007@gmail.com

Received 11 November 2011; Accepted 13 December 2011

Academic Editor: Lie-Hang Shen

The purpose of this study was to develop an efficient way to synthesize ^{99m}Tc-*O*-[3-(1,4,8,11-tetraazabicyclohexadecane)-propyl]-tyrosine (^{99m}Tc-N4-Tyrosine), a novel amino acid-based radiotracer, and evaluate its potential in breast cancer gamma imaging. Precursor N4-Tyrosine was synthesized using a 5-step procedure, and its total synthesis yield was 38%. It was successfully labeled with ^{99m}Tc with high radiochemical purity (>95%). Cellular uptake of ^{99m}Tc-N4-Tyrosine was much higher than that of ^{99m}Tc-N4 and the clinical gold standard ^{18}F-2-deoxy-2-fluoro-glucose (^{18}F-FDG) in rat breast tumor cells *in vitro*. Tissue uptake and dosimetry estimation in normal rats revealed that ^{99m}Tc-N4-Tyrosine could be safely administered to humans. Evaluation in breast tumor-bearing rats showed that although ^{99m}Tc-N4-Tyrosine appeared to be inferior to ^{18}F-FDG in distinguishing breast tumor tissue from chemical-induced inflammatory tissue, it had high tumor-to-muscle uptake ratios and could detect breast tumors clearly by planar scintigraphic imaging. ^{99m}Tc-N4-Tyrosine could thus be a useful radiotracer for use in breast tumor diagnostic imaging.

1. Introduction

^{18}F-2-deoxy-2-fluoro-glucose (^{18}F-FDG), an ^{18}F-labeled glucose analog, is a gold standard for positron emission tomography (PET) in cancer diagnosis. However, ^{18}F-FDG-PET has several limitations that can result in false positive or negative diagnoses, and its ability to predict tumor response to chemotherapy or radionuclide therapy is poor [1]. For instance, ^{18}F-FDG cannot distinguish tumor tissue from inflammatory or normal brain tissues because each type of tissue has high glucose consumption. Therefore, radiolabeled amino acids have been developed as an alternative to ^{18}F-FDG in diagnostic imaging of cancer. Their use in tumor detection is based on an increased uptake of amino acids in tumor cells, which is assumed to reflect enhanced amino acid transport, metabolism, and protein synthesis [2].

Among all radiolabeled amino acids, aromatic ones such as tyrosine and its derivatives are more suitable for use in cancer diagnostic imaging given their readily alterable chemistry and favorable biological characteristics. To date, tyrosine and its α-methyl-substituted analog α-methyl tyrosine (AMT) have been successfully labeled with ^{11}C, ^{18}F, and $^{124/125}$I for PET imaging, as well as $^{123/131}$I for single-photon emission computed tomography (SPECT) imaging, respectively [2–7]. Most of these radiolabeled tyrosine analogs show promise in preclinical and clinical research in diagnostic tumor imaging, especially for brain tumors. They have also been successfully applied to imaging breast cancer, which is the most common malignancy among women in the world. For instance, ^{11}C-labeled tyrosine appears to be better than ^{18}F-FDG for breast cancer imaging because of its lower uptake in noncancerous fibrocystic disease [8].

However, most existing radiolabeled tyrosine derivatives require an on-site cyclotron to produce the radioisotope, which is inconvenient and costly. In addition to that, the radioisotopes have either a too short (e.g., 20 minutes for ^{11}C) or too long (e.g., 57.4 days for ^{125}I) half-life, making them impractical for clinical use. Furthermore,

iodine-labeled compounds are not stable *in vivo* because of deiodination. So far, ^{18}F has the most appropriate half-life (110 minutes); however, the radiosynthesis yield of ^{18}F-labeled radiotracers is relatively low, apparently because of the electrophilic fluorination and tedious purification of ^{18}F. Therefore, a radiotracer with simpler chemistry and an affordable isotope that can be used clinically in most major medical facilities is needed.

Technetium-99 m (^{99m}Tc) is an ideal radioisotope for diagnostic imaging studies because of its favorable physical characteristics. It emits a 140 keV gamma ray in 89% abundance, which is commonly used in gamma and SPECT imaging. The half-life of ^{99m}Tc is 6.02 hours, allowing serial images and, thus, overcoming a drawback of ^{18}F [9]. Unlike most cyclotron-produced radionuclides, which use covalent chemistry for labeling, ^{99m}Tc requires a chelator to conjugate the radioisotope with the target ligand. The combinations of nitrogen, oxygen, and sulfur appear to be stable chelators for ^{99m}Tc [10–12]. In fact, this chelator could allow the same target ligand to be labeled with several different radioisotopes, such as gallium-68, indium-111, or rhenium-188, for future diagnostic and therapeutic applications.

Here, we report the synthesis of ^{99m}Tc-labeled tyrosine using 1,4,8,11-tetra-azacyclotetradecane (N4) cyclam as a chelator and evaluate its potential in gamma imaging using *in vitro* and *in vivo* breast tumor models.

2. Materials and Methods

All chemicals of analytical grade and solvents of high-performance liquid chromatography (HPLC) grade were obtained from Sigma-Aldrich (St. Louis, MO, USA). Nuclear magnetic resonance (NMR) was performed on a Bruker 300-MHz spectrometer (Bruker BioSpin Corporation, Billerica, MA, USA), and mass spectra were performed on a Waters Q-TOF Ultima mass spectrometer (Waters, Milford, MA, USA) at the chemistry core facility at The University of Texas MD Anderson Cancer Center (Houston, TX, USA). Sodium pertechnetate ($Na^{99m}TcO_4$) was obtained from a ^{99}Mo/^{99m}Tc generator (Mallinckrodt, Hazelwood, MO, USA). ^{18}F-FDG was obtained from the Department of Nuclear Medicine at MD Anderson.

2.1. Synthesis of Precursor N4-Tyrosine

2.1.1. N-t-Butoxycarbonyl-O-[3-Br-propyl]-L-tyrosine Methyl Ester (Compound 1). N-*t*-Butoxycarbonyl-L-tyrosine methyl ester (25.00 g; 0.085 mol) was dissolved in acetone (300 mL). 1,3-Dibromopropane (17.3 mL; 0.169 mol) and K_2CO_3 (58.00 g; 0.420 mol) were added under a nitrogen atmosphere. The reaction mixture was refluxed at 80°C overnight. After the mixture was cooled and filtered, the solvent was removed under reduced pressure and the residue was dissolved in chloroform. The residue was washed with water and dried with anhydrous $MgSO_4$. The product was purified by column chromatography using a silica gel column eluted with hexane: ethyl acetate (2 : 1, v/v). Yield: 33.30 g (94.60%). Ms (m/z) = 440.09 $[M+Na]^+$.

2.1.2. N^1,N^4-Dioxylyl-1,4,8,11-tetraazabicyclotetradecane (N^1,N^4-Cyclooxamide) (Compound 2). N4 cyclam (15.00 g; 74.88 mmol) was dissolved in 150 mL of anhydrous ethanol, and diethyl oxalate (10.94 g; 74.88 mmol) was added. The reaction mixture was refluxed for 18 hours at 75°C. The solvent was rotary evaporated, and the crude product was dissolved in minimum quantity of ethanol and filtered and recrystallized in 400 mL of acetone/ethanol to yield white crystals of compound 2. Yield: 13.64 g (71.62%). Ms (m/z) 255.19 $[M]^+$.

2.1.3. N-t-Butoxycarbonyl-O-[3-(N^1,N^4-dioxylyl-1,4,8,11-tetraazabicyclotetradecane)-propyl]-tyrosine Methyl Ester (Compound 3). Compound 2 (0.63 g; 2.46 mmol) was dissolved in 20 mL of anhydrous dimethylformamide; it was reacted with a solution of compound 1 (1.06 g; 2.46 mmol) in 40 mL of dimethylformamide under a nitrogen atmosphere. The mixture was refluxed at 75°C for 18 hours and then cooled to room temperature. The reaction mixture was filtered, and the solvent was removed *in vacuo*. The crude compound was purified via silica gel column using chloroform: methanol solution (9 : 1, v/v). Yield: 0.65 g (1.05 mmol; 42.76%). Ms (m/z) 591.31 $[M]^+$.

2.1.4. O-[3-(N^1,N^4-Dioxylyl-1,4,8,11-tetraazabicyclotetradecane)-propyl]-tyrosine Methyl Ester (Compound 4). To deprotect N-*t*-butoxycarbonyl group, Compound 3 (0.60 g; 1.00 mmol) was dissolved in anhydrous dichloromethane (15 mL), and 2.5 mL of trifluoroacetic acid was added to it. The solution was stirred overnight at room temperature, and the solvents were then removed *in vacuo*. The crude compound was purified by chromatography over silica gel (chloroform: methanol 9 : 1, v/v) giving an off-white solid. Yield: 0.18 g (90%). Ms (m/z) 490.31 $[M]^+$.

2.1.5. O-[3-(1,4,8,11-Tetraazabicyclohexadecane)-propyl]-tyrosine (Compound 5, N4-Tyrosine). Compound 4 (0.25 g; 0.50 mmol) was dissolved in 5 mL of water, and 2.5 mL of 10 N NaOH was added to it. The solution was stirred and refluxed overnight at 90°C, and the solvent was evaporated *in vacuo*. The crude compound was then dissolved in 5 mL of water, and the pH of the solution was neutralized to pH 7 by adding 5 M HCl. The final solution was lyophilized overnight to obtain white powder, which was then dissolved in 25 mL of anhydrous methanol, filtered, evaporated, and lyophilized to obtain off-white powder. Yield: 0.19 g (88.78%). = Ms (m/z) 422.31 $[M]^+$.

2.2. Radiolabeling of N4-Tyrosine with ^{99m}Tc. N4-Tyrosine (1 mg) was dissolved in 0.2 mL of sterile water, and tin (II) chloride (0.1 mL, 1 mg/mL) was added. The required amount of $Na^{99m}TcO_4$ was added to the N4-Tyrosine solution at the room temperature. Radiochemical purity was determined by radio-HPLC using an C-18 reverse column (Waters), eluted with a 7 : 3 acetonitrile: water solution (v/v) at a flow rate of 0.5 mL/minute.

2.3. Determination of the Partition Coefficient. To determine the lipophilicity, 20 μL of ^{99m}Tc-N4-Tyrosine was added into an equal volume mixture of 1-octanol and sterile water in a centrifuge tube. The mixture was vortexed at room temperature for 1 minute and then centrifuged at 5,000 rpm for 5 minutes to allow phase separation. From each phase, 0.1 mL of the aliquot was taken out, and the radioactivity was measured by gamma counter (Cobra Quantum, Packard, MN, USA). The measurement was repeated 3 times, and care was taken to avoid cross-contamination between the phases. The partition coefficient value, expressed as log P, was calculated using the following equation:

$$\text{Log}\,P = \log\left(\frac{\text{radioactivity in 1-octanol layer}}{\text{radioactivity in sterile water layer}}\right) \quad (1)$$

2.4. In Vitro Cellular Uptake. Rat breast tumor cell line 13762 (American Type Culture Collection, Rockville, MD, USA) was used for both *in vitro* studies and to create the animal model for *in vivo* evaluation. All cells were maintained in Dulbecco's modified Eagle's medium and nutrient mixture F-12 Ham (DMEM/F12; GIBCO, Grand Island, NY) at 37°C in a humidified atmosphere containing 5% CO_2.

For *in vitro* cellular uptake analysis, cells were plated onto 6-well tissue culture plates (2×10^5 cells/well) 48 hours before adding the radiotracers and incubated with ^{99m}Tc-N4-Tyrosine (0.05 mg/well, 8 μCi/well), ^{99m}Tc-N4 (0.025 mg/well, 8 μCi/well), or ^{18}F-FDG (8 μCi/well) for 0–4 hours. After incubation, cells were washed with ice-cold phosphate-buffered solution twice and detached using a treatment of 0.5 mL of trypsin for 5 minutes. Cells were then collected, and the radioactivity of the cells was measured in triplicate with a gamma counter (Cobra Quantum). Radioactivity was expressed as mean ± standard deviation (SD) percent of cellular uptake (%Uptake).

2.5. Blood Clearance. All animal work was carried out in the Small Animal Imaging Facility at MD Anderson under a protocol approved by the Institutional Animal Care and Use Committee. For blood clearance analysis, 3 normal female Fischer 344 rats (150 ± 25 g; Harlan Sprague-Dawley, Indianapolis, IN, USA) were intravenously injected with 30 μCi of ^{99m}Tc-N4-Tyrosine. Blood samples ($n = 3$/rat) were drawn from each rat through the lateral tail vein by microliter pipette (10 μL) at several time points between 5 minutes and 24 hours after injection. The blood samples were measured for radioactivity by gamma counter, and the radioactivity was expressed as a percentage of the injected dose per gram of blood (%ID/g).

2.6. Tissue Distribution. Tissue distribution studies of ^{99m}Tc-N4-Tyrosine were conducted using normal female Fischer 344 rats (150 ± 25 g, $n = 9$). The rats were divided into 3 groups, and each rat was injected intravenously with 25 ± 0.5 μCi of ^{99m}Tc-N4-Tyrosine. Each group was examined at 1 of 3 time points (0.5, 2, or 4 hours after injection). At each time point, the rats were killed, and the selected tissues were excised, weighed, and measured for radioactivity by gamma counter. For each sample, radioactivity was expressed as mean percentage of the injected dose per gram of tissue wet weight (%ID/g). Counts from a 1/10 diluted sample of the original injection were used as a reference.

2.7. OLINDA/EXM Dosimetry Estimates. Rat absorbed dose estimates for ^{99m}Tc-N4-Tyrosine were computed from biodistribution data. Individual organ and whole-body time-activity curves were fitted to exponential functions using OLINDA/EXM software (version 1.1; Vanderbilt University, Nashville, TN, USA). These functions were then integrated analytically to determine the area under the curve to yield the residence time of ^{99m}Tc-N4-Tyrosine in each organ. It was assumed that the injected activity of ^{99m}Tc-N4-Tyrosine was uniformly distributed throughout the body immediately following injection. Mass correction factors were used to account for the different ratios of organs to total body weight and different scaling of residence times between rats and humans [13]. Residence times were then used to calculate target organ absorbed radiation doses for a 70 kg standard man model using the OLINDA/EXM software.

2.8. Planar Scintigraphic Imaging in Breast Tumor-Bearing Rats. Cells from the breast tumor cell line 13762, suspended in phosphate-buffered solution (10^5 cells/0.1 mL solution per rat), were injected subcutaneously into the right calf muscle of female Fischer 344 rats ($n = 9$). Planar scintigraphic imaging of ^{99m}Tc-N4-Tyrosine was performed 12–14 days after inoculation when tumors reached approximately 1 cm in diameter. The breast tumor-bearing rats ($n = 3$/time point) were anesthetized and injected intravenously with ^{99m}Tc-N4-Tyrosine (0.3 mg/rat, 300 μCi/rat), and images were acquired at 30, 120, and 240 minutes after administration of tracers. Planar scintigraphic images were obtained using M-CAM (Siemens Medical Solutions, Hoffman Estates, IL, USA) equipped with a low-energy high-resolution collimator. Computer-outlined regions of interest (ROIs in counts per pixel) between tumor and muscle tissue were used to calculate tumor-to-muscle (T/M) ratios. Percent of injected dose (%ID) in the tumor was also calculated from the reference standard, which was 1/10 of the original injection activity of ^{99m}Tc-N4-Tyrosine.

2.9. Tumor and Inflammation Uptake Comparison. To investigate whether ^{99m}Tc-N4-Tyrosine can differentiate tumor tissue from inflammatory tissue, a rat model bearing both a mammary tumor and tissue with turpentine oil-induced inflammation was created. Rat breast tumor cells (from cell line 13762; 10^5 cells/0.1 mL phosphate-buffered solution per rat) were injected into the right calf muscles of 3 female Fischer 344 rats. After the tumors reached 1 cm in diameter, turpentine oil (0.1 mL/rat) was injected into the left calf muscles of the rats to induce inflammation. The anesthetized rats were injected intravenously with ^{99m}Tc-N4-Tyrosine 24 hours after the turpentine injection. Planar scintigraphic images were acquired at 30, 120, and 240 minutes after the ^{99m}Tc-N4-Tyrosine injection, and ROIs of the tumor, inflamed tissue, and muscle were used to

calculate the tumor-to-muscle ratios (T/Ms), inflammation-to-muscle ratios (I/Ms), and tumor-to-inflammation ratios (T/Is), respectively. The same animal model was used to evaluate ^{18}F-FDG. Micro-PET imaging of ^{18}F-FDG was performed using an R4 micro-PET scanner (Concorde Microsystems, Knoxville, TN, USA). Three breast tumor- and inflammation-bearing rats were injected intravenously with ^{18}F-FDG (500 μCi/rat), and dynamic PET scans with a spatial resolution of 2.2 mm were obtained at 30, 60, and 90 minutes after ^{18}F-FDG injection. PET images were reconstructed by using the ordered subset expectation maximization (OSEM) algorithm. T/M, I/M, and T/I ratios were calculated using the regional radioactivity concentrations (μCi/cm^3) that were estimated from the average pixels within ROIs drawn around the tumor, inflamed tissue, or muscle on transverse slices of the reconstructed image sets.

3. Results and Discussion

As mentioned previously, radiolabeled amino acid analogues have shown great potentials in cancer imaging by targeting the increased amino acids uptake in tumor cells. In the present study, we report the synthesis of ^{99m}Tc-labeled tyrosine using (N4) cyclam as a chelator and evaluate its potential in breast cancer diagnosis using the breast tumor models *in vitro* and *in vivo*.

3.1. Chemistry and Radiochemistry. The total synthesis yield of precursor N4-Tyrosine via our 5-step procedure was 38%. The synthetic scheme is shown in Figure 1. The structure and purity of N4-Tyrosine were confirmed by ^{1}H- and ^{13}C-NMR, mass spectra, and HPLC. The ^{1}H-NMR results (D_2O δ, ppm) were as follows: 7.18 (d, 2H, phenyl ring), 6.95 (d, 2H, phenyl ring), 4.073 (t, 2H, O-CH_2), 3.43 (t, 1H, CHN), 2.28–3.00 (m, 2OH, OCH_2 and NCH_2-), 1.87–1.91(m, 2H, C-CH_2-C), and 1.68–1.79 (m, 4H, C-CH_2-C). ^{13}C- NMR results (D_2O δ, ppm) were as follows: 162.88, 156.72, 130.76, 117.57, 115.25, 68.55, 57.29, 53.91, 51.56, 49.95, 49.17, 48.96, 48.24, 48.03, 46.80, 45.73, 45.35, 39.27, 24.90, 24.31, and 23.87. Because the starting material, N-*t*-butoxycarbonyl-L-tyrosine methyl ester, was commercially available, the synthetic yield of N4-Tyrosine in our study was much higher (38%) than that of its α-methyl derivative N4-AMT (14%), which was reported in a previous study [14].

For the radiolabeling, the top and middle panels of Figure 2 show the ultraviolet absorbance of ^{99m}Tc-N4-Tyrosine at 210 nm and 274 nm, while the bottom panel indicates the peak from NaI detector that only detects the radioactivity. Since precursor N4-Tyrosine has a unique ultraviolet absorbance at 274 nm, we selected 274 nm for one of the ultraviolet detectors. On the other hand, the 210 nm detector can detect almost every molecule; therefore, we were able to detect any impurities in our compound. The retention time of three detectors matched very well, which indicated precursor N4-Tyrosine was labeled with ^{99m}Tc successfully with high radiochemical purity (>95%). Because ^{99m}Tc-N4-Tyrosine is a kit product and labeled without any further purification, its radiochemical yield was assumed to be identical to its radiochemical purity. For the partition coefficient value, the log P of ^{99m}Tc-N4-Tyrosine was -2.83 ± 0.082, which was lower than that of its α-methyl derivative ^{99m}Tc-N4-AMT (-2.02 ± 0.168). Since the log P value is positively correlated with lipophilicity of the compound, we found that the lipophilicity of the tyrosine-based radiotracer could be increased by adding a methyl group on its α-carbon.

3.2. In Vitro Cellular Uptake Evaluation. The cellular uptake kinetics of ^{99m}Tc-N4-Tyrosine, ^{99m}Tc-N4, and ^{18}F-FDG in rat breast tumor cells is shown in Figure 3. The uptake for ^{99m}Tc-N4-Tyrosine increased dramatically up to 240 minutes, but this was not true for the ^{99m}Tc-N4 chelator, suggesting that ^{99m}Tc-N4-Tyrosine can enter tumor cells specifically and accumulate rapidly. In addition, the mean %Uptake of ^{99m}Tc-N4-Tyrosine was much higher than that of ^{18}F-FDG, which indicated that ^{99m}Tc-N4-Tyrosine had better imaging potential than ^{18}F-FDG in this *in vitro* breast cancer model.

3.3. In Vivo Evaluation in Normal Fischer 344 Rats. The blood clearance curve for ^{99m}Tc-N4-Tyrosine in normal Fischer 344 rats is shown in Figure 4. The plasma half-life of the distribution phase ($t_{1/2\alpha}$) was 9.31 ± 0.759 minutes, and the plasma half-life of the elimination phase ($t_{1/2\beta}$) was 90.14 ± 1.901 minutes, indicating that ^{99m}Tc-N4-Tyrosine had relatively fast blood clearance in normal rats.

Tissue distribution of ^{99m}Tc-N4-Tyrosine in normal Fischer 344 rats is shown in Table 1. Low thyroid and stomach uptake of ^{99m}Tc-N4-Tyrosine was observed, suggesting that ^{99m}Tc-N4-Tyrosine has high stability *in vivo*. High uptake was found in the kidneys, which was consistent with the planar scintigraphic imaging findings in the breast tumor-bearing rats (see Figure 5). This high kidney uptake may be a result of the low lipophilicity of ^{99m}Tc-N4-Tyrosine, or it may be related to the biological characteristics of ^{99m}Tc-labeled tyrosine because similar results were also observed in the previously developed tyrosine-based radiotracers ^{99m}Tc-N4-AMT, ^{99m}Tc-EC-AMT, and ^{99m}Tc-EC-Tyrosine [14, 15].

To estimate the maximum dose of ^{99m}Tc-N4-Tyrosine that could be safely administered to humans, individual organ absorbed radiation doses were calculated using OLINDA/EXM software. Estimates of the doses per unit administered are shown in Table 2. The kidneys received the highest absorbed dose (4.86*E*-02 mSv/MBq or 1.80*E*-01 rem/mCi), which made it the dose-limiting organ. Other organs with relatively high absorbed radiation doses included the heart wall, spleen, and liver. According to the US Food and Drug Administration regulations, human exposure to radiation from the use of "radioactive research drugs" should be limited to 3 rem per single administration and 5 rem per year to the whole body, blood-forming organs (red marrow, osteogenic cells, spleen), the lens of the eye, and gonads (testes and uterus); the limit for other organs is 5 rem per single administration and 15 rem annually. Total rem of ^{99m}Tc-N4-Tyrosine absorbed by each organ was below these limits at the proposed injection of 15 mCi per patient.

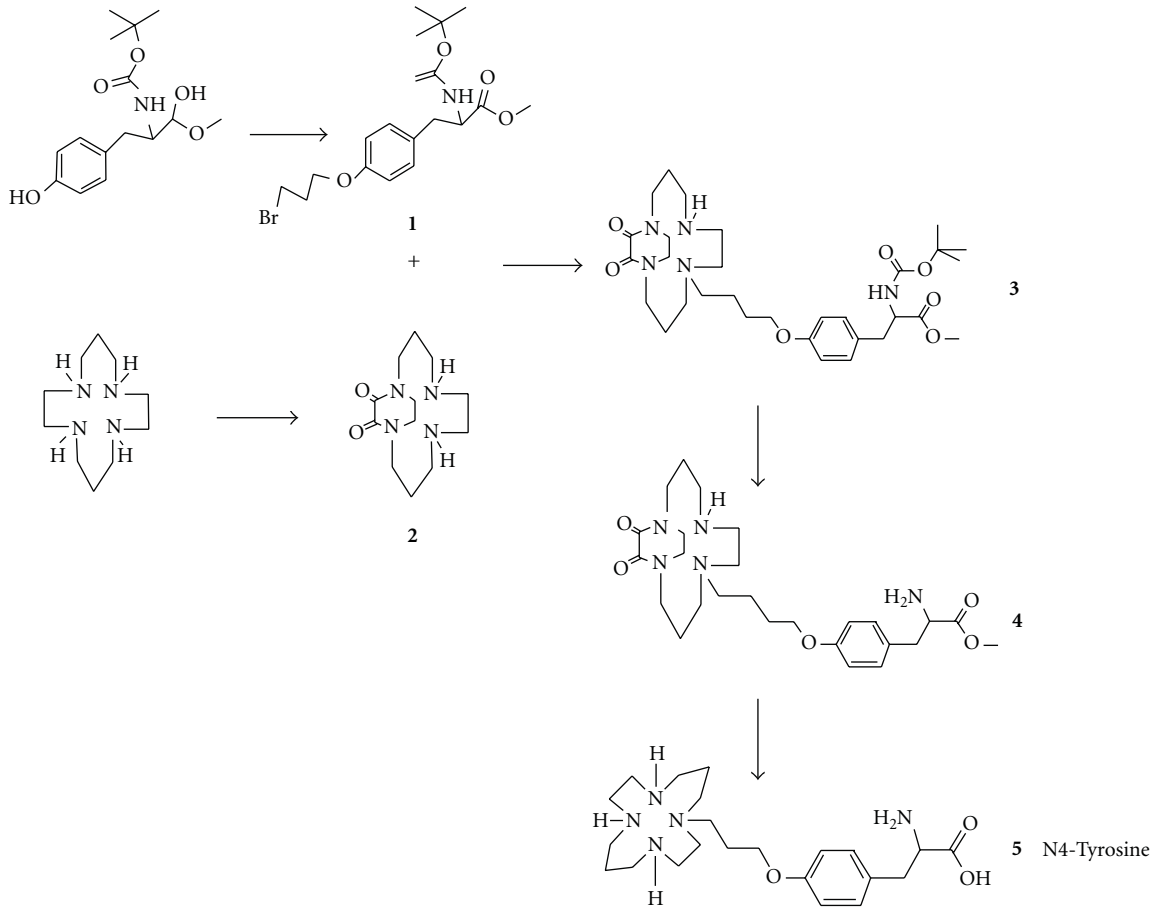

Figure 1: Synthetic scheme of precursor N4-Tyrosine.

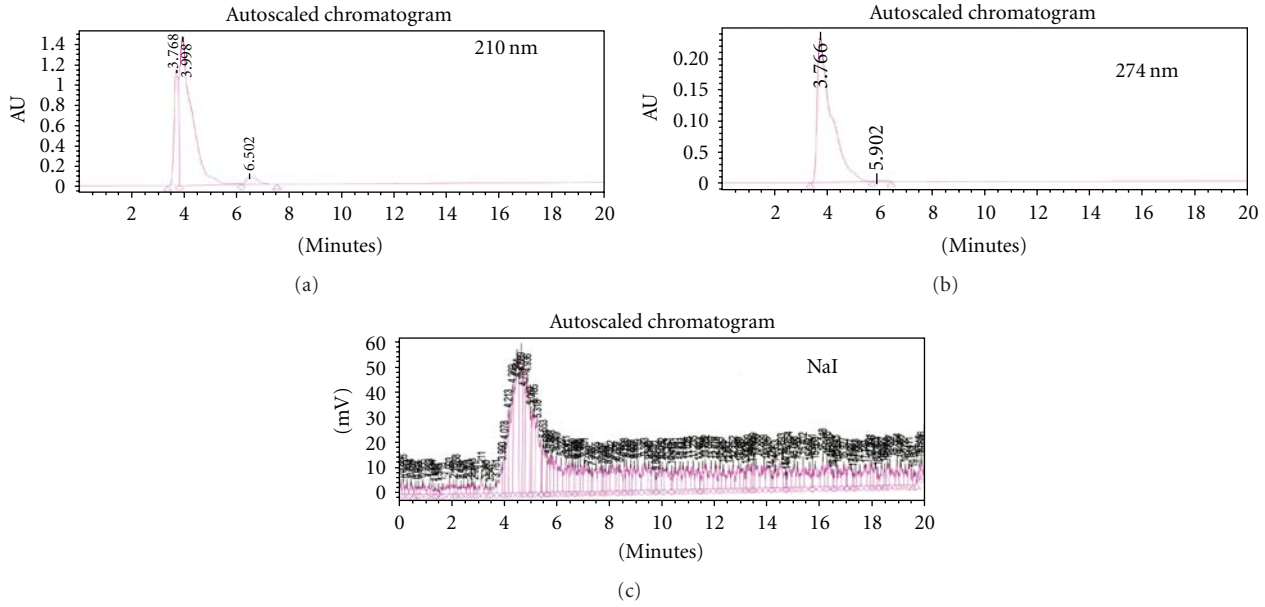

Figure 2: High-performance liquid chromatographic analysis of ^{99m}Tc-N4-Tyrosine at a flow rate of 0.5 mL/minute using a C-18 reverse column under ultraviolet absorbance of 210 nm (a) and 274 nm (b), as well as under a NaI radioactivity detector (c).

Table 1: *In vivo* tissue distribution of ^{99m}Tc-N4-Tyrosine in normal Fischer 344 rats ($n = 3$) at 30, 120, and 240 minutes after injection.

Organ	30	MIN	120	MIN	240	MIN
Blood	0.88	±0.040	0.20	±0.018	0.17	±0.009
Heart	0.21	±0.022	0.06	±0.003	0.05	±0.003
Lung	0.50	±0.023	0.19	±0.011	0.14	±0.006
Thyroid	0.34	±0.019	0.10	±0.010	0.09	±0.006
Pancreas	0.17	±0.017	0.07	±0.012	0.05	±0.002
Liver	1.15	±0.059	0.70	±0.040	0.67	±0.044
Spleen	0.94	±0.089	0.76	±0.032	0.63	±0.051
Kidney	11.05	±0.783	12.34	±0.502	12.40	±0.405
Stomach	0.20	±0.018	0.08	±0.003	0.06	±0.002
Intestine	0.34	±0.057	0.13	±0.010	0.11	±0.006
Muscle	0.07	±0.007	0.03	±0.002	0.02	±0.001
Bone and joint	0.24	±0.021	0.15	±0.008	0.12	±0.008
Brain	0.03	±0.001	0.02	±0.001	0.01	±0.001

Each value indicates the percent of injected dose per gram of wet weight (%ID/g, $n = 3$/time point). Each data represents mean of three measurements with standard deviation.

Table 2: Absorbed radiation dose estimates (dose per unit injected into a 70 kg adult man) for ^{99m}Tc-N4-Tyrosine.

Target organ	Absorbed radiation dose estimates		Human dose (15 mCi)
	mSv/MBq	rem/mCi	rem
Adrenals	$4.65E-03$	$1.72E-02$	$2.58E-01$
Brain	$4.69E-04$	$1.74E-03$	$2.61E-02$
Breasts	$1.27E-03$	$4.72E-03$	$7.08E-02$
Gallbladder wall	$3.79E-03$	$1.40E-02$	$2.10E-01$
Lower large intestine wall	$1.62E-03$	$6.00E-03$	$9.00E-02$
Small intestine	$2.70E-03$	$1.00E-02$	$1.50E-01$
Stomach wall	$2.49E-03$	$9.21E-03$	$1.38E-01$
Upper large intestine wall	$2.44E-03$	$9.04E-03$	$1.36E-01$
Heart wall	$8.51E-03$	$3.15E-02$	$4.73E-01$
Kidneys	$4.86E-02$	$1.80E-01$	$2.70E+00$
Liver	$5.52E-03$	$2.04E-02$	$3.06E-01$
Lungs	$2.27E-03$	$8.41E-03$	$1.26E-01$
Muscle	$1.34E-03$	$4.96E-03$	$7.44E-02$
Ovaries	$1.76E-03$	$6.53E-03$	$9.80E-02$
Pancreas	$3.76E-03$	$1.39E-02$	$2.09E-01$
Red marrow	$1.91E-03$	$7.07E-03$	$1.06E-01$
Osteogenic cells	$5.21E-03$	$1.93E-02$	$2.90E-01$
Skin	$8.91E-04$	$3.30E-03$	$4.95E-02$
Spleen	$5.66E-03$	$2.09E-02$	$3.14E-01$
Testes	$7.91E-04$	$2.93E-03$	$4.40E-02$
Thymus	$2.29E-03$	$8.47E-03$	$1.27E-01$
Thyroid	$1.25E-03$	$4.61E-03$	$6.92E-02$
Urinary bladder wall	$1.39E-03$	$5.14E-03$	$7.71E-02$
Uterus	$1.77E-03$	$6.53E-03$	$9.80E-02$
Total Body	$1.98E-03$	$7.32E-03$	$1.10E-01$
Effective dose equivalent	$5.71\ E-03$	$2.11E-02$	$3.17E-01$
Effective dose	$2.19\ E-03$	$8.11E-03$	$1.22E-01$

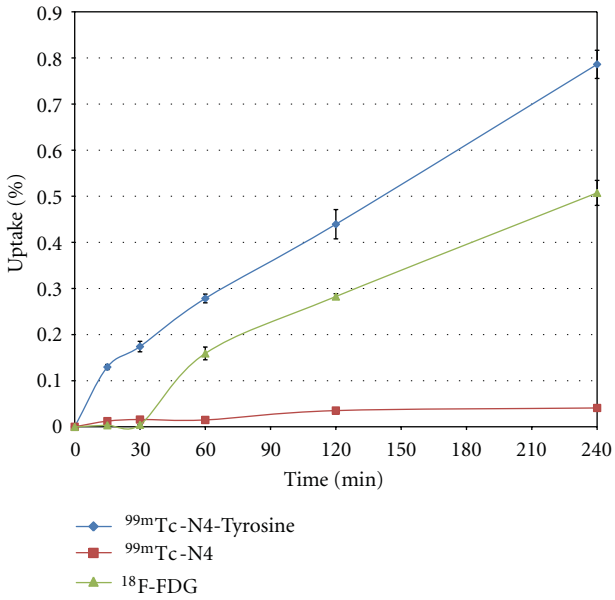

Figure 3: *In vitro* cellular uptake of ^{99m}Tc-N4-Tyrosine, ^{99m}Tc-N4, and ^{18}F-FDG in cells from rat breast tumor cell line 13762. Data are expressed as mean percent of cellular uptake ± standard deviation (%Uptake ± SD) measured at 15, 30, 60, 120, and 240 minutes after coincubation with ^{99m}Tc-N4-Tyrosine.

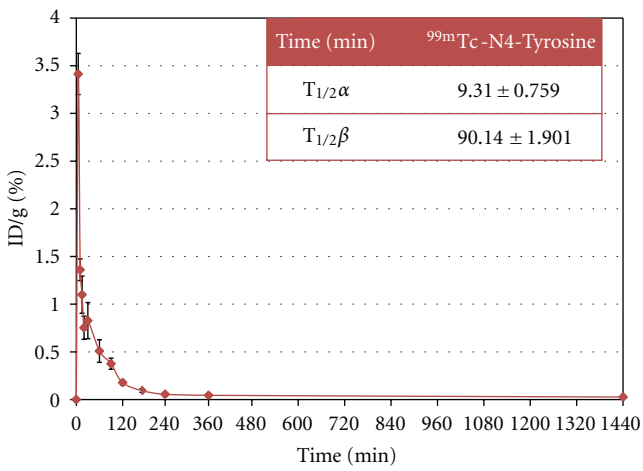

Figure 4: Blood clearance curve of ^{99m}Tc-N4-Tyrosine in normal female Fischer 344 rats ($n = 3$). Mean radioactivity is expressed as mean percentage of the injected dose per gram of blood ± standard deviation (%ID/g ± SD).

3.4. In Vivo Evaluation in Breast Tumor-Bearing Rats. The selected planar scintigraphic images of breast tumor-bearing rats at 30, 120, and 240 minutes after ^{99m}Tc-N4-Tyrosine injection are shown in Figure 5. The T/M ratios at 30, 120, and 240 minutes were 5.12, 4.88, and 5.20, respectively. Tumor %ID at these three time points were 1.82%, 1.87%, and 1.71%, respectively. Tumors could be clearly detected by ^{99m}Tc-N4-Tyrosine at all time points.

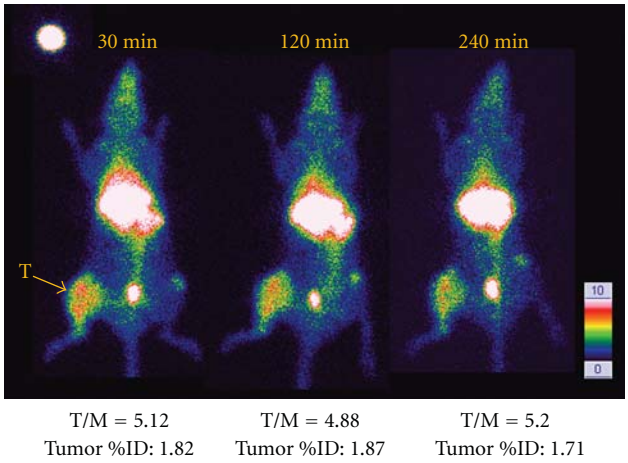

Figure 5: The selected planar scintigraphic images of breast tumor-bearing rats at 30, 120, and 240 minutes after ^{99m}Tc-N4-Tyrosine injection (T indicates tumor; T/M, tumor-to-muscle ratio; tumor %ID, percent of injected dose in the tumor).

The selected planar scintigraphic images of breast tumor- and inflammation-bearing rats at 30, 120, and 240 minutes after ^{99m}Tc-N4-Tyrosine injection, as well as micro-PET images at 30, 60, and 90 minutes after ^{18}F-FDG injection, are shown in Figure 6. The T/M ratio of ^{99m}Tc-N4-Tyrosine was relatively higher than I/M ratio at each time point. Although T/I ratios were greater than 1 at all time points for both ^{99m}Tc-N4-Tyrosine and ^{18}F-DFG, indicating that the tumor had higher uptake than the inflammation site, the T/I ratios for ^{99m}Tc-N4-Tyrosine were lower than those for ^{18}F-FDG. This suggests that ^{99m}Tc-N4-Tyrosine was inferior to ^{18}F-FDG in differentiating tumor from inflammation in this breast tumor-bearing rat model. However, we used turpentine to induce inflammation chemically in this model. It may be worth testing ^{99m}Tc-N4-Tyrosine in another animal model using radiation to induce inflammation so that the model better mimics patients undergoing radiation therapy.

4. Conclusion

In summary, N4-Tyrosine was synthesized and labeled efficiently with ^{99m}Tc with high radiochemical purity. Although it appears to inferior ^{18}F-FDG in distinguishing breast tumor tissue from chemical-induced inflammatory tissue, ^{99m}Tc-N4-Tyrosine has high tumor-to-muscle uptake ratios and can detect breast tumor tissue clearly by gamma camera. By taking the advantage of chelator N4 cyclam, we could label N4-Tyrosine with gallium-68 for PET imaging and, furthermore, labeled with rhenium-188 for radionuclide therapy for breast cancer treatment in future.

Authors' Contribution

F. -L. Kong and M S. Ali contributed equally to this work.

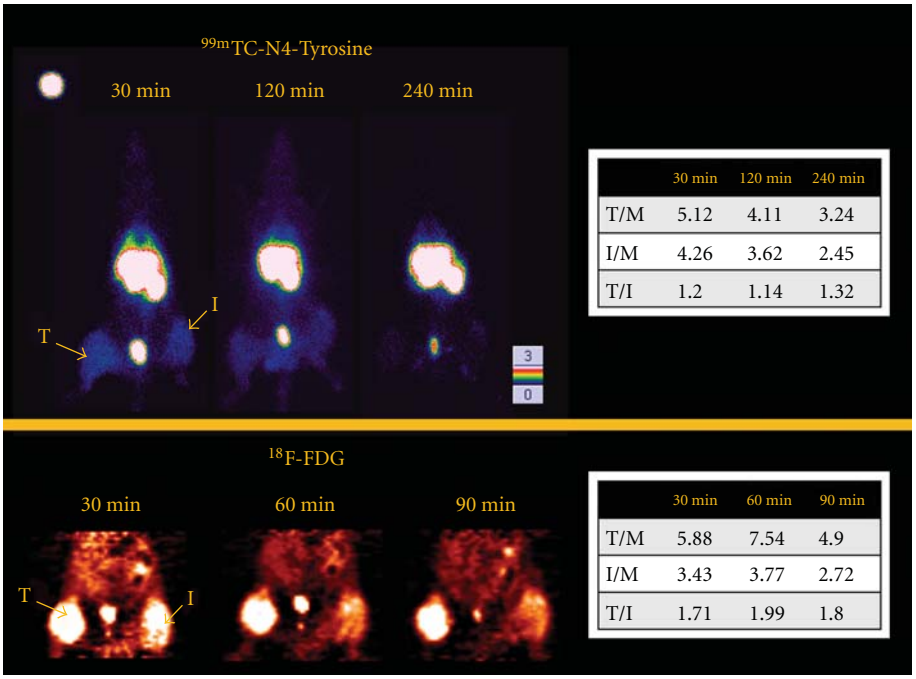

	30 min	120 min	240 min
T/M	5.12	4.11	3.24
I/M	4.26	3.62	2.45
T/I	1.2	1.14	1.32

	30 min	60 min	90 min
T/M	5.88	7.54	4.9
I/M	3.43	3.77	2.72
T/I	1.71	1.99	1.8

Figure 6: The selected planar scintigraphic images of breast tumor- and inflammation-bearing rats at 30, 120, and 240 minutes after ^{99m}Tc-N4-Tyrosine injection and micro-PET images at 30, 60, and 90 minutes after ^{18}F-FDG injection (T indicates tumor; I, inflammation). Tumor-to-muscle (T/M), inflammation-to-muscle (I/M), and tumor-to-inflammation (T/I) ratios are shown in the tables.

Acknowledgments

This work was supported in part by a sponsored research agreement with Cell > Point L.L.C. (MDA LS2005-00012803PL) and the John S. Dunn Foundation. The NMR, mass spectrometry, and animal research were supported by the MD Anderson Cancer Center Support Grant CA016672 from the National Institutes of Health.

References

[1] S. J. Rosenbaum, T. Lind, G. Antoch, and A. Bockisch, "False-positive FDG PET uptake—the role of PET/CT," *European Radiology*, vol. 16, no. 5, pp. 1054–1065, 2006.

[2] P. L. Jager, W. Vaalburg, J. Pruim, E. G. de Vries, K. J. Langen, and D. A. Piers, "Radiolabeled amino acids: basic aspects and clinical applications in oncology," *Journal of Nuclear Medicine*, vol. 42, no. 3, pp. 432–445, 2001.

[3] K. J. Langen, K. Hamacher, M. Weckesser et al., "*O*(2-[^{18}F]fluoroethyl)-L-tyrosine: uptake mechanisms and clinical applications," *Nuclear Medicine and Biology*, vol. 33, no. 3, pp. 287–294, 2006.

[4] K. J. Langen, D. Pauleit, H. H. Coenen et al., "3-[^{123}I]Iodo-α-methyl-L-tyrosine: uptake mechanisms and clinical applications," *Nuclear Medicine and Biology*, vol. 29, no. 6, pp. 625–631, 2002.

[5] R. Boni, H. Steinert, R. Huch Boni et al., "Radioiodine-labelled alpha-methyl-tyrosine in malignant melanoma: cell culture studies and results in patients," *British Journal of Dermatology*, vol. 137, no. 1, pp. 96–100, 1997.

[6] K. Kaira, N. Oriuchi, Y. Otani et al., "Fluorine-18-α-methyltyrosine positron emission tomography for diagnosis and staging of lung cancer: a clinicopathologic study," *Clinical Cancer Research*, vol. 13, no. 21, pp. 6369–6378, 2007.

[7] H. Tsukada, K. Sato, D. Fukumoto, S. Nishiyama, N. Harada, and T. Kakiuchi, "Evaluation of D-isomers of *O*-^{11}C tyrosine and *O*-^{18}F tyrosine as tumor-imaging agents in tumor-bearing mice: comparison with L- and D-^{11} C-methionine," *Journal of Nuclear Medicine*, vol. 47, no. 4, pp. 679–688, 2006.

[8] A. C. Kole, O. E. Nieweg, J. Pruim et al., "Standardized uptake value and quantification of metabolism for breast cancer imaging with FDG and L-[1-^{11}C]tyrosine PET," *Journal of Nuclear Medicine*, vol. 38, no. 5, pp. 692–696, 1997.

[9] S. Jurisson, C. Cutler, and S. V. Smith, "Radiometal complexes: characterization and relevant in vitro studies," *Quarterly Journal of Nuclear Medicine and Molecular Imaging*, vol. 52, no. 3, pp. 222–234, 2008.

[10] J. David, J. L. B. Yang, and E. Edmund Kim, "Chelator-based imaging technology: new molecular imaging agents provide answers," *Imaging Economics*, 2006.

[11] C. J. Anderson, C. S. John, Y. J. Li et al., "N, N′-Ethylene-di-L-cysteine (EC) complexes of Ga(III) and In(III): molecular modeling, thermodynamic stability and in vivo studies," *Nuclear Medicine and Biology*, vol. 22, no. 2, pp. 165–173, 1995.

[12] S. Liu, "Bifunctional coupling agents for radiolabeling of biomolecules and target-specific delivery of metallic radionuclides," *Advanced Drug Delivery Reviews*, vol. 60, no. 12, pp. 1347–1370, 2008.

[13] D. J. Macey, L. E. Williams, H. B. Breitz, A. Liu, T. K. Johnson, and P. B. Zanzonico, *A Primer for Radioimmunotherapy and Radionuclide Therapy*, 2001.

[14] F. L. Kong, M. S. Ali, Y. Zhang et al., "Synthesis and evaluation of amino acid-based radiotracer ^{99m}TcTc-N4-AMT for breast

cancer imaging," *Journal of Biomedicine and Biotechnology*, vol. 2011, Article ID 276907, 2011.

[15] F. L. Kong, Y. Zhang, M. S. Ali et al., "Synthesis of ^{99m}TcTc-EC-AMT as an imaging probe for amino acid transporter systems in breast cancer," *Nuclear Medicine Communications*, vol. 31, no. 8, pp. 699–707, 2010.